Investigating the Static Corrosion of T91 for Lead-Bismuth Eutectic Reactors at the Atomic Scale

Minyi Zhang

Kellogg College

University of Oxford

A thesis submitted for the degree of

Doctor of Philosophy

Trinity Term 2024

Abstract

T91 steel is a candidate material for structural components in lead-bismuth-eutectic (LBE) cooled systems, for example, fast reactors and solar power plants. However, the corrosion mechanisms of T91 in LBE remain poorly understood. In this study, we have analysed the static corrosion of T91 in liquid LBE using a range of characterisation techniques at increasingly smaller scales. Both the corrosion in reducing and oxidising environments are considered. Several different corrosion mechanisms are identified and the effect of oxygen content on LBE corrosion is investigated.

Oxygen concentration strongly influences the corrosion pattern. In a reducing environment (low oxygen content), the physical dissolution of elements (e.g. Fe, Cr) in LBE is the main factor with slight oxidation happening at the interface of T91 and LBE. A unique pattern of liquid metal intrusion is observed that does not appear to correlate with the grain boundary network. Atomic scale elemental redistribution and 3D morphology of the corrosion interface are revealed using scanning transmission electron microscope (STEM) and atom probe tomography (APT). A thin surface oxide layer (presumably wüstite) is observed at the LBE-steel interface.

In an oxidising environment (high oxygen content), preferential oxidation at grain boundaries is the dominant process, with LBE penetration into materials happening more locally. Complex oxide structures are identified with the use of STEM and APT. Moreover, the quality of the oxide layer may directly influence the protection effect.

Upon closer inspection, electron backscatter diffraction (EBSD) reveals a change in the morphology of grains at the LBE-exposed surface for both reducing and oxidising environments, suggesting a local phase transition. Energy dispersive X-ray (EDX) maps show that Cr is depleted in the T91 material near the LBE interface. The dissociation of Cr carbides and the overall Cr depletion adjacent to the corrosion interface show a potential correlation to the phase change observed in this region. High-resolution electron backscatter diffraction (HR-EBSD) and micro-

beam Laue X-ray diffraction measurements further support the results. Based on this detailed nano-scale information from STEM and APT, a potential mechanism of Cr depletion, Cr carbide dissociation, and phase change in T91 induced by LBE corrosion is proposed.

Preface

The work presented in this doctoral thesis has been carried out at the Department of Materials, University of Oxford from October 2020 to July 2024, under the supervision of Prof. Michael P. Moody, Prof. Felix Hofmann and Dr. Paul A.J. Bagot. All the research carried out for this thesis is original and where the work of others has been included it has been referenced and acknowledged. No part of this thesis has been submitted for a degree or any other university. Some of this work has been published in peer-reviewed journals and presented at conferences as detailed below:

Publications:

1. **Zhang, Minyi**, Guanze He, Mark Lapington, Weiyue Zhou, Michael P. Short, Paul AJ Bagot, Felix Hofmann, and Michael P. Moody. "Nano-scale corrosion mechanism of T91 steel in static lead-bismuth eutectic: A combined APT, EBSD, and STEM investigation." Acta Materialia (2024): 119883.
2. **Zhang, Minyi**, Mark Lapington, Weiyue Zhou, Michael P. Short, Paul AJ Bagot, Michael P. Moody, and Felix Hofmann. "Analyzing the Static Corrosion of T91 in Liquid Lead and Bismuth Eutectic at the Atomic Scale." Microscopy and Microanalysis 28, no. S1 (2022): 2094-2096.
3. Lapington, M. T., **M. Zhang**, M. P. Moody, W. Y. Zhou, M. P. Short, and F. Hofmann. "Characterisation of corrosion damage in T91/F91 steel exposed to static liquid lead-bismuth eutectic at 700–715° C." Journal of Nuclear Materials 586 (2023): 154687.
4. **Zhang, Minyi**, Guanze He, Robert James Scales, Kay Song, Mark Lapington, Weiyue Zhou, Zhiyuan Ding et al. "Correlated Chromium Carbide Dissociation and Phase Changes in Liquid Lead-Bismuth Eutectic Corroded T91 Steel." *Available at SSRN 4999045*.

Conference Presentations:

1. **Minyi Zhang**, Zhiyuan Ding, Guanze He, Houzhi Liu, Weiyue Zhou, Michael P. Short, Paul A.J. Bagot, Felix Hofmann, and Michael P. Moody. *The static corrosion of T91 in lead bismuth eutectic with different oxygen level. PICO,* Vaals, Netherlands. April 2024.

2. **Minyi Zhang**, Guanze He, Kay Song, Mark Lapington, Weiyue Zhou, Michael P. Short, Paul A.J. Bagot, Felix Hofmann, and Michael P. Moody. *An analysis of T91 corrosion in liquid lead-bismuth by correlating APT with Electron microscopy.* APT&M, Leuven, Belgium. September 2023.

3. **Minyi Zhang**, Guanze He, Mark Lapington, Weiyue Zhou, Michael P Short, Paul AJ Bagot, Michael P Moody, and Felix Hofmann. *Atomic scale corrosion behaviour of T91 steel in static lead-bismuth eutectic*. TMS, San Diego, United States. March 2023.

4. **Minyi Zhang**, Guanze He, Mark Lapington, Weiyue Zhou, Michael P. Short, Paul A.J. Bagot, Michael P. Moody, and Felix Hofmann. *Static corrosion of T91 steel in liquid lead-bismuth eutectic.* Nuclear Materials, Ghent, Belgium. November 2022.

5. **Minyi Zhang**, Mark Lapington, Weiyue Zhou, Michael P. Short, Paul A.J. Bagot, Michael P. Moody, and Felix Hofmann. *Analyzing the Static Corrosion of T91 in Liquid Lead and Bismuth Eutectic at the Atomic Scale.* Microscopy and Microanalysis, Portland, United States. July 2022.

Acknowledgements

I would like to express my gratitude to all my supervisors. A special thank you to Prof. Michael P. Moody, Prof. Felix Hofmann, and Dr. Paul A.J. Bagot for allowing me to be involved in this project and for their immense support throughout my DPhil studies. They have been instrumental not only in guiding me through my academic journey but also in shaping my personal growth. Their support and mentorship have provided me with invaluable knowledge and skills, while their wisdom and advice have had a profound impact on my perspective and decisions in life. The influence they've had on both my professional and personal development is something I will always cherish.

I am deeply grateful to the wonderful ladies in our office, including Dr. Laura Wheatley, Laura Lain, Ruiying, and Megan Jones. We often discussed research and shared our thoughts on current events, making our office a gathering spot for conversations among the women in the group. The positive and supportive atmosphere of the APT group, particularly toward female researchers, had a significant and uplifting impact on my DPhil experience.

This project involved everything from corrosion testing to various material characterisations, and it would have been impossible to complete without the help of many individuals. I would like to express my gratitude to Michael P. Short and Dr. Weiyue Zhou, who not only provided the corroded samples but also contributed through numerous insightful discussions. I am thankful to Dr. Mark Lapington for training and supervising me on FIB, and to Dr. Guanze He and Zhiyuan Ding for their assistance with TEM analyses. I also appreciate Dr. Kay Song's help with X-ray analyses and Robert Scale's support with GND calculations and MTEX analysis. Houzhi Liu provided valuable assistance with TEM sample preparation, and I am grateful to Prof. Sergio Lozano-Perez for the helpful discussions and guidance on low-energy EDX analyses. I would like to thank everyone in APT group and Hofmann's group. They all made significant contributions to my research.

I would like to thank my family, who have always supported me and given me the strength to keep going. I am also grateful to my friends for bringing me so many wonderful memories throughout my DPhil journey. A special thanks to Dr. Yanru Ren, Xinya Niu, and Yumeng Yin for their companionship and unwavering support.

Finally, I would like to express my deepest gratitude to my beloved husband, Zhiyuan Ding. With you, I have found unwavering support, boundless love, and the constant gift of encouragement. Your ability to always offer positive emotional feedback has been a guiding light through both the challenging and joyful moments of this journey. You have transformed marriage into the most precious part of my life. With you, love is not just a dream, but a beautiful and enduring reality.

I dedicate this dissertation to you, my dearest husband.

Acronyms

AFM: Atomic force microscopy

AMU: Atomic mass unit

APT: Atom probe tomography

BSE: Backscattered electron

EBSD: Electron backscatter diffraction

EDX: Energy dispersive X-ray spectroscopy

GBs: Grain boundaries

GFR: Gas-cooled fast reactor

HAADF: High-angle annular dark field

HR-EBSD: High-resolution electron backscatter diffraction

HR-TKD: High-resolution transmission Kikuchi diffraction

LAADF: Low-angle annular dark field

Laue: Synchrotron X-ray micro-beam Laue diffraction

LBE: Lead-bismuth eutectic

LBEFR: Lead-bismuth eutectic-cooled fast reactor

LFR: Lead-cooled fast reactor

MFM: Magnetic force microscopy

MSR: Molten salt-cooled reactor

PAGBs: Prior austenite grain boundaries

PKA: Primary knock-on atom

RIS: Radiation-induced segregation

SCWR: Supercritical water-cooled reactor

SEM: Scanning electron microscope

SFR: Sodium-cooled fast reactor

SPPs: Secondary particle precipitates

STEM: Scanning transmission electron microscopy

T-EBSD: Transmission electron backscatter diffraction

TEM: Transmission electron microscopy

TKD: Transmission Kikuchi diffraction

VHTR: Very high-temperature reactor

Contents

Chapter I

Introduction

Carbon dioxide (CO_2) is a major greenhouse gas that contributes to global warming. To limit climate change, reducing the production of CO_2 is of vital importance. The combustion of fossil fuels to produce electricity is still the main source of CO_2 emissions. At the same time, the overuse of non-renewable energy (including coal, oil, and natural gas) also requires the exploration of new resources. Nuclear fission power is an attractive alternative because of its efficiency, sustainability and lower environmental impact [1].

Fast reactors are considered an important technology for improving the sustainability of nuclear energy, as they can help utilize existing nuclear waste and reduce the long-term radiotoxicity of spent fuel [2]. A fast reactor is a type of nuclear reactor that uses fast neutrons to sustain the nuclear fission reaction. Unlike thermal reactors, which slow down neutrons using moderators (such as water or graphite) to increase the probability of fission, fast reactors do not use a moderator. One potential Gen IV nuclear fission reactor concept is the lead-bismuth-eutectic-cooled fast reactor (LBEFR), as shown in Fig.1.1. It would use lead-bismuth eutectic (LBE) as the coolant due to its favourable properties, including low neutron moderation and capture, low melting point, low vapour pressure, wide margin to boiling, excellent gamma radiation shielding, and relatively low reactivity with water or air. These are significant advantages over other potential coolants: in high-pressure water, the reactor could not realistically be run with a fast spectrum because of the operation pressure and moderation; or Sodium (Na) and sodium-potassium alloys (NaK), which ignite spontaneously in air and react explosively with water [3-5].

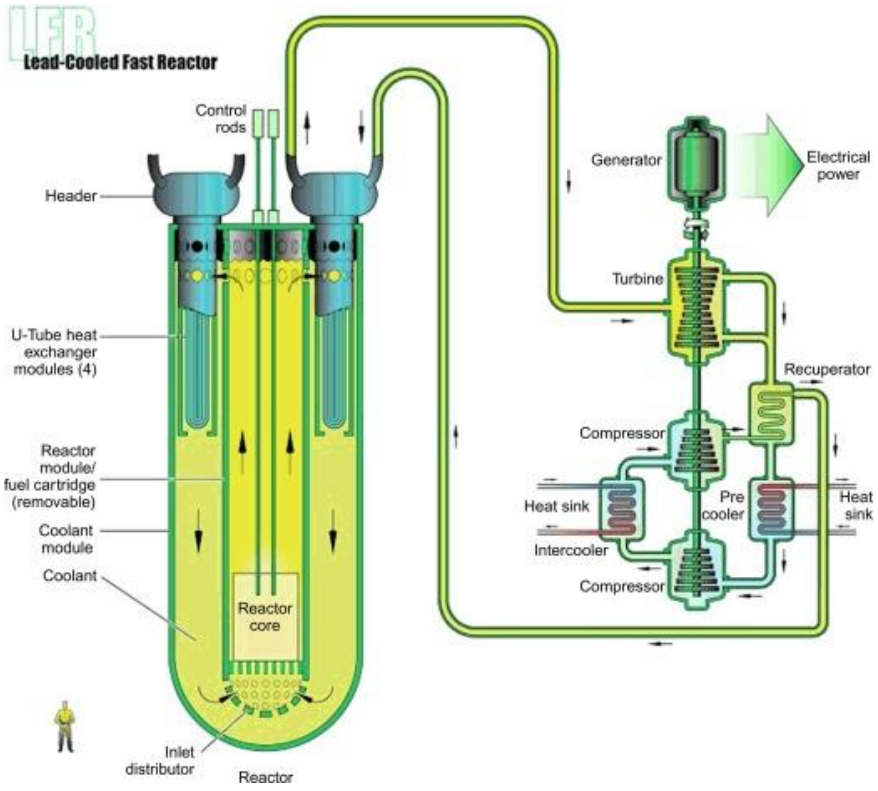

Fig. 1.1. The schematic of LBEFR [6]. Reprinted with permission from Elsevier.

The structural materials used in nuclear reactors significantly influence their mechanical properties, which, in turn, affect reactor performance and safety. 9Cr-1Mo steels, often denoted T91 or F91, have been proposed as structural components for LBEFRs. In particular, as a ferritic/martensitic (F/M) steel, T91 has excellent resistance to irradiation-induced void swelling [7]. It also has low thermal expansion, high thermal conductivity and a mature supply chain with ASME nuclear qualification [8]. Compared to martensitic steels with higher Cr content, the irradiation-induced ductile-to-brittle transition temperature shift of T91 is lower [9]. Compared to austenitic steels, F/M steels avoid the concern of fast corrosion when temperature is increased above 500℃ promoting ferritization of the austenite [10]. However, liquid metal embrittlement of F/M steel in liquid LBE is a major concern that impedes the use of F/M steels in reactors [11-13]. Liquid metal embrittlement is the reduction in the elongation-to-failure that can be produced when normally ductile solid metals are stressed while in contact with a liquid

metal [14]. Because of this, the Multi-purpose Hybrid Research Reactor for High-tech Applications (MYRRHA), designed by SCK-CEN in Belgium, will use 316L austenitic stainless steel as the structural material [15]. When considering the liquid metal embrittlement (LME) of F/M steels in LBE, stress and temperature are the main factors. Liquid metal embrittlement becomes important when the threshold stress is exceeded, for example, for T91 with temperature 350-400℃, the threshold stress is 680 MPa [16]. Normally it is most prominent just above the melting point of the liquid metal, and as temperature increases further the ductility will gradually return. According to previous studies, for LBE, the LME mainly happens in the temperature range of 300℃ to 500℃ [17].

This thesis focuses on the corrosion of T91 in static LBE, specifically, its mechanism as evidenced by morphological observations of corrosion, to help predict its onset and extent. Corrosion of containment and structural materials remains the main critical issue for LBEFR design [18]. Lead alloys are more corrosive to structural steels than other potential fast reactor coolants like helium or sodium as discussed in more detail in section 2.2.1. Furthermore, because of the higher solubility of Fe, Cr, and Ni in liquid LBE compared to liquid lead, material dissolution problems are more severe in LBE than in lead at similar temperatures [19]. Higher temperatures are also known to exacerbate corrosion further [20-22]. When considering the influence of the enhanced effects of LBE, detrimental phase changes, and magnetite/wüstite oxide phase transition regardless of the type of steel selected, whether it be austenitic or F/M, the operation temperature of the reactor generally has to be restricted to ~550℃ or below. This restriction in turn limits the reactor's power density and thus the economic benefits LBEFR promised For example, the Russian LBEFR, SVBR, is limited to 390℃ and the MYRRHA reactor is designed to operate at 400℃ [23]. To help break this bottleneck, and better understand the processes involved, this study investigates T91 samples exposed to static LBE corrosion at 700 ℃ for oxidising environment and 715℃ for reducing environment. At this temperature liquid metal embrittlement could be largely avoided, however, these conditions are also known to be highly

corrosive to the material. Few studies have investigated LBE corrosion of T91 under these conditions.

Several previous investigations have shown that during corrosion in an oxidising environment (i.e. oxygen levels sufficient to oxidise iron) an oxide layer is formed at the T91 and LBE interface [24, 25]. However, even in a reducing environment, an oxide layer with a thickness of around tens of nanometres at the corrosion interface has been observed in a model Fe-12Cr-2Si alloy though it mainly consisted of Si oxide [26]. This is important, as the oxide layer prevents direct contact between the liquid LBE and underlying metals, thereby potentially offering some protection against LBE corrosion. However, according to these previous studies, for FeCr alloys, even in an oxygen-saturated environment, the effective protection of the oxide layer (mainly CrO) will reduce with increasing temperatures. The oxide phase transition from dense magnetite to porous wüstite could be a reason for this [27]. At the same time, oxygen content will also influence the protection. Since passivation is not easily achievable at higher temperatures (for this study, it is 715 ℃), operating under reducing conditions is a potential alternative. Interestingly a previous study observed shallower LBE ingress into T91 under reducing conditions than in an oxidising environment [28]. Moreover, even in an oxidising environment, avoiding locations with lower oxygen contents is practically challenging. As such, a detailed understanding of LBE corrosion of T91 under reducing conditions is important.

According to previous studies, the corrosion of materials in LBE with low oxygen levels is driven by the dissolution of alloying elements in the liquid LBE [29, 30]. A better understanding of how different elements behave near the lead-steel interface is essential to disentangle the most important mechanisms for degradation and develop strategies to mitigate corrosion.

Though it is difficult to reach passivation with the temperature set in this experiment, the formation of surface oxides is still one of the most popular ways of enhancing the corrosion performance of structural materials. A better understanding of how the material corroded in an

oxidising environment in LBE may provide new thoughts for using oxide layers to protect at a high-temperature range. For example, the adjustment of material composition, better control of the dissolved oxygen in LBE, and the compromised operation temperature.

To this end, high-resolution characterisation is required. However, thus far the corrosion of F/M steels in liquid LBE or lead has mostly been studied at the microscale [10, 24, 31, 32]. There is little research on the lead corrosion mechanisms within steel at the atomic scale. In this study we consider T91 steel samples exposed to static corrosion in liquid LBE for various lengths of time (70, 245, or 506 hours) in both reducing and oxidising environments at 715℃ and 700℃, respectively. Characterisation methods including Atom probe tomography (APT) transmission electron microscopy (TEM), scanning transmission electron microscopy (STEM), electron energy loss spectroscopy (EELS), energy-dispersive x-ray spectroscopy (EDX), scanning electron microscopy (SEM), and electron backscatter diffraction (EBSD) will be used. As a result, investigation of the static corrosion of T91 steel in LBE of both oxidising and reducing environments can be conducted across multiple length scales, and some of the most prominent mechanisms are identified.

This thesis consists of 9 main chapters with the introduction and literature review presenting the background information and importance of this research; the materials and methods chapter and the atom probe tomography operating condition and data analysis techniques chapter showing the test conditions for the data collection; three result chapters including (corrosion mechanism of T91 steel in static lead-bismuth eutectic in reducing environment; the correlation of Cr carbides dissociation and phase change observed in liquid lead-bismuth eutectic corroded T91; corrosion mechanism of T91 steel in static lead-bismuth eutectic in the oxidising environment) show the main research results and discussions; the last two chapters are the conclusion and future work which introduce the main results shown in the thesis and several interesting, unresolved questions that would be exciting to address in future research.

Chapter II

Literature Review

2.1 Overview

Nuclear fission power is a promising approach to alleviating environmental and resource pressures [1]. Generation IV (GenIV) reactors represent the most advanced nuclear power systems currently under development [33]. Six reactor designs have been chosen for consideration: gas-cooled fast reactor (GFR), lead-cooled fast reactor (LFR), molten salt–cooled reactor (MSR), sodium-cooled fast reactor (SFR), supercritical water-cooled reactor (SCWR), and very high-temperature reactor (VHTR). These systems do not follow a natural evolutionary progression from the widely established water-cooled nuclear reactors. Instead, they are designed to meet more ambitious goals, including improved safety, enhanced resistance to nuclear proliferation, greater economic efficiency, and long-term sustainability [34].

Furthermore, these GenIV reactors can solve the shortage of usable uranium. Additionally, GenIV reactors offer a solution to the looming shortage of usable uranium. Current reactors (GenI-III) are limited to using uranium-235, which has a natural abundance of only 0.720%. Given the global rate of uranium consumption, it is estimated that uranium-235 supplies will be depleted in approximately 130 years [35]. By contrast, uranium-238, which makes up 99.244% of natural uranium, is far more abundant. Notably, four of the six GenIV reactor designs—including the liquid lead and lead-bismuth eutectic (LBE) cooled fast reactor—can utilize uranium-238 due to their "fast" neutron energy spectrum [36].

Among the Generation IV reactor concepts, liquid lead and LBE-cooled fast reactors stand out for their potential to improve the power density and economic viability of nuclear fission. These reactors benefit from the exceptional physical and chemical properties of lead-based alloys,

including low neutron moderation and capture, high neutron spallation yields, excellent thermodynamic properties, a low melting point, low vapor pressure, a wide margin to boiling, and reduced reactivity with water or air compared to liquid sodium. These properties make lead alloys particularly promising for the development of advanced nuclear systems [3, 4].

Figure 2.1 illustrates the Pb-Bi phase diagram [37], and Table 2.1 summarizes several thermodynamic properties of lead (Pb), bismuth (Bi), and LBE [3].

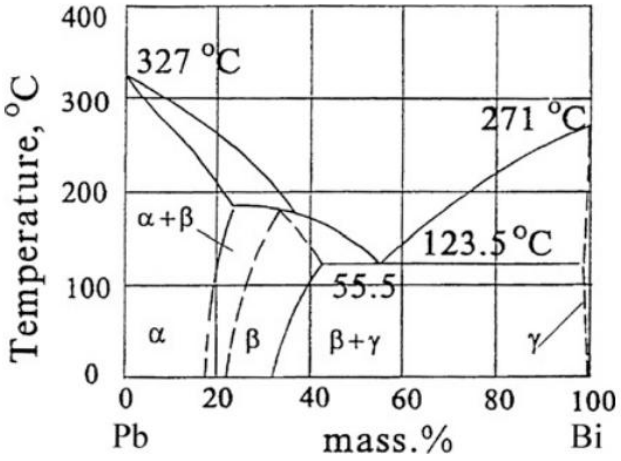

Fig. 2.1. Pb-Bi phase diagram from the Institute of Physics and Power Engineering, Obninsk, Russia. α is Pb, β is Pb_7Bi_3, and γ is Bi [37]. Reprinted with permission from IOP Science.

Despite these advantages, corrosion and its dependence on irradiation remain significant challenges for the development of lead-cooled fast reactors (LFRs) and lead-bismuth eutectic-cooled fast reactors (LBEFRs). To address these issues, researchers have employed various methods to replicate operating conditions and uncover the mechanisms underlying material property changes. The following sections provide a detailed overview of the current state of knowledge in this area.

Table 2.1. Thermodynamic properties of lead, bismuth and LBE [3]. Reprinted with permission from Elsevier.

Parameter	Units	Lead	Bismuth	LBE
Atomic weight	g/mol	207.18	208.98	208.18
Neutron (th) absorption	Barn	0.17		
Melting temperature	°C	327.4	271.0	123.5
Latent heat of melting	kJ/kg	23	50.2	38.1
Volume change at melting	%	+3.5	-3.32	0.0
Density[a]	kg/m^3	10430	9910	10200
Thermal expansion[a]	1/K	1.12×10^{-4}		
Heat capacity[a]	J/kg/K	147		146.5
Thermal conductivity	W/m/K	15.4	13.3	13.2
Kinetic viscosity[a]	m^2/s	1.76×10^{-7}	1.42×10^{-3}	
Surface tension[a]	N/m	0.44		
Solubility of Fe[a]	at.%	2.72×10^{-4}		
Boiling temperature	°C	1745	1490	1670
Latent heat of boiling	kJ/kg	860	855.2	856.7
Saturation pressure	bar	5.1×10^{-6}		

[a] $T = 500$ °C

2.2 Challenges in Selecting Structural Materials for LFRs and LBEFRs

The corrosion of structural materials remains one of the primary challenges in the design of lead-cooled fast reactors (LFRs) and lead-bismuth eutectic-cooled fast reactors (LBEFRs) [4, 18]. The selection of suitable structural materials largely depends on the operating temperature of the system.

For lower-temperature applications, metallic materials are the preferred choice. In contrast, for higher-temperature environments, silicon carbide composites have emerged as the leading candidates [19]. The choice of materials also depends on the radiation dose. Austenitic stainless steels are generally used in low-dose reactors, whereas ferritic-martensitic steels are favoured for high-dose reactors due to their superior resistance to void swelling under irradiation [38].

2.2.1 Corrosion

One of the primary challenges in designing and applying liquid metal or alloy coolant systems in advanced nuclear reactors is ensuring that structural materials can withstand corrosion. Liquid metal corrosion is a critical issue in high-temperature systems and has been extensively studied since liquid metals and alloys were first proposed as potential coolants for nuclear fast reactors.

Unlike corrosion by aqueous media, which is predominantly an electrochemical process, corrosion caused by liquid metals such as liquid lead and LBE is largely a physical or physico-chemical process. This involves the dissolution of material constituents, their transport between solid and liquid phases, and reactions between corrosion products and impurities [39].

Liquid metal corrosion has been shown to alter the microstructure, composition, and surface morphology of structural materials. These changes degrade the mechanical and physical properties of the materials, potentially leading to system failure. As a result, liquid metal corrosion is recognized as a significant failure mechanism for structural materials in advanced

nuclear reactor systems, driven by the high-temperature physical and chemical interactions between the liquid metals, alloys, and containment materials [40].

Corrosion is affected by various factors, including the type of coolant, oxygen concentration, liquid flow rate, and temperature gradient. Each of these factors plays a role in determining how materials corrode [10].

2.2.1.1 Coolant type influence on corrosion

Cathcart and Manly [41] investigated 24 types of metals and alloys subjected to corrosion in liquid lead, finding that only molybdenum (Mo) and niobium (Nb) exhibited high resistance to mass transfer caused by lead-induced corrosion. Oak Ridge National Laboratory (ORNL) [42] reported that alloys with high nickel content, such as Ni–Cr–Fe alloys and 347 stainless steel, exhibited lower resistance to liquid lead corrosion compared to alloys with no nickel content. Additionally, Ali-Khan [43] showed that the corrosion rate increases with external stress applied to the materials. For instance, corrosion at the bend region of a U-shaped sample was significantly higher than in other parts of the specimens.

Liquid bismuth exhibits significantly higher corrosive properties compared to liquid lead. The corrosion rate of identical materials in liquid bismuth is approximately 40 times greater than in liquid lead under the same operational conditions [44]. Research by James and Trotman [44] demonstrated that steels with high concentrations of Ni and Mn exhibited notably poor corrosion resistance in liquid bismuth, due to the high solubility of these elements. They also suggest corrosion rate increases with the Cr content. However, this trend is only applicable in the presence of clear bismuth or oxygen getters, such as Mg. When oxygen is present in the liquid, the oxide layer that forms on the material's surface can provide protective benefits, resulting in an inverse trend where the corrosion rate decreases as the Cr content increases, as reported by Wilson [45].

The corrosion rate of steel exposed to liquid lead–bismuth alloy depends on the liquid composition. The corrosion rate of the same steel increases with the content of Bi, due to the higher solubility of Fe, Cr, and Ni in liquid Bi compared to liquid lead [19, 46]. A comparison of the solubility of different elements in liquid lead and LBE is shown in Fig. 2.2. It is evident that, at the same temperature, elements display significantly higher solubility in LBE compared to pure lead [47].

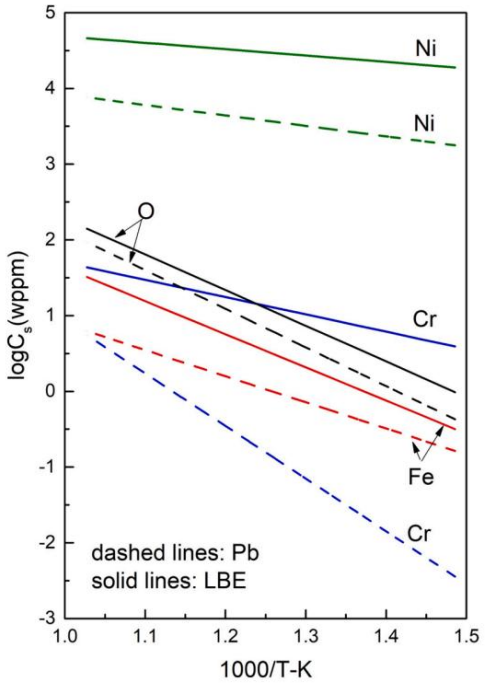

Fig. 2.2. Solubility curves of Fe, Cr, Ni, and O in liquid lead and LBE environment [47]. Reprinted with permission from Elsevier.

2.2.1.2 Steel type influence on corrosion

Both ferritic and martensitic (F/M) steels, such as T91 and HT9, and austenitic stainless steels, like SS304 and SS316, are widely used in the design of LFRs and LBEFRs *[47]*. F/M steels offer excellent resistance to irradiation-induced void swelling, low thermal expansion, and high thermal conductivity [7, 8]. In contrast, austenitic steels exhibit significantly lower susceptibility

to liquid metal embrittlement [15]. In addition to the differences mentioned above, F/M steels and austenitic steels exhibit distinct corrosion mechanisms when exposed to LBE.

Yuji [10] compared the corrosion behaviours of F/M and austenitic steels in LBE under varying temperatures in a saturated oxygen environment. The results indicate that F/M steels primarily experience grain boundary corrosion, corrosion node formation, and internal oxidation. In contrast, austenitic steels undergo severe selective dissolution of Ni and Cr, leading to ferritization of the corroded layer, a process that becomes more pronounced at higher temperatures. Konstantina [22] researched on the LBE corroded 316L steels. The EBSD analysis verified the ferritization within the dissolution-affected zone, demonstrating grain refinement in this region compared to the grain size of the unaffected steel as shown in Fig. 2.3.

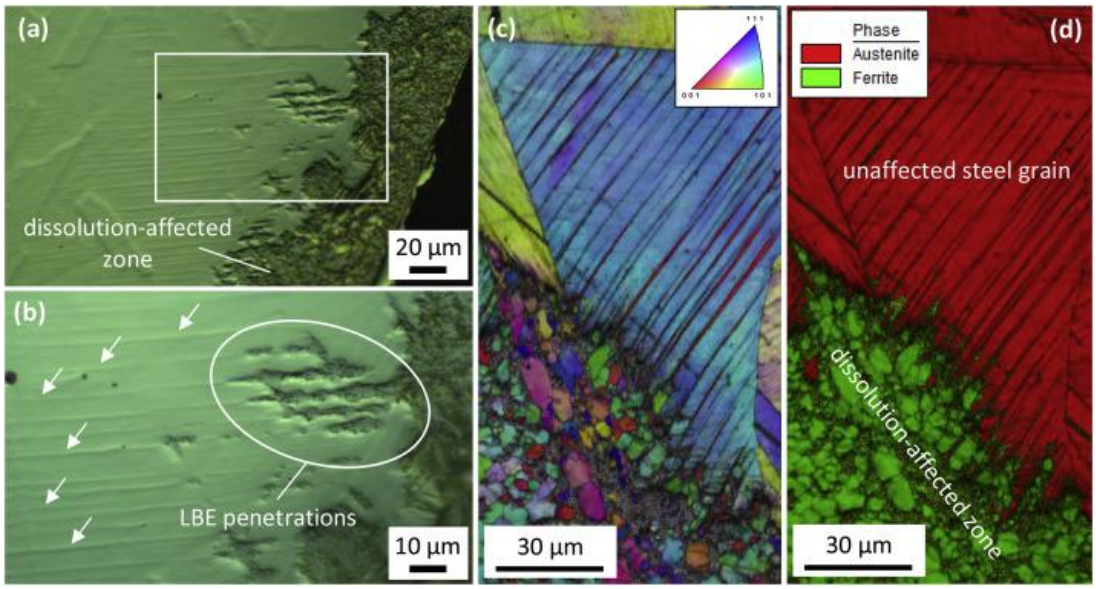

Fig. 2.3 Light optical microscopy images of a polished cross-section of a 316LH2 sample (1000 h) are shown. (a) An overview and (b) a detailed view highlights parallel steel grain striations (arrows) that locally guide LBE penetration. (c–d) EBSD data from a 316LH1 sample (3282 h): (c) an orientation map illustrating LBE penetration along closely-spaced grain striations, and (d) a phase map revealing ferritization in the dissolution-affected zone, while the unaffected steel grains remain austenitic [22]. Reprinted with permission from Elsevier.

Evangelia [48] also confirmed the prefer dissolution of Ni and Cr happens in the corrosion of austenitic stainless steels in LBE and the ferritization happened in the same region, as shown in Fig. 2.4.

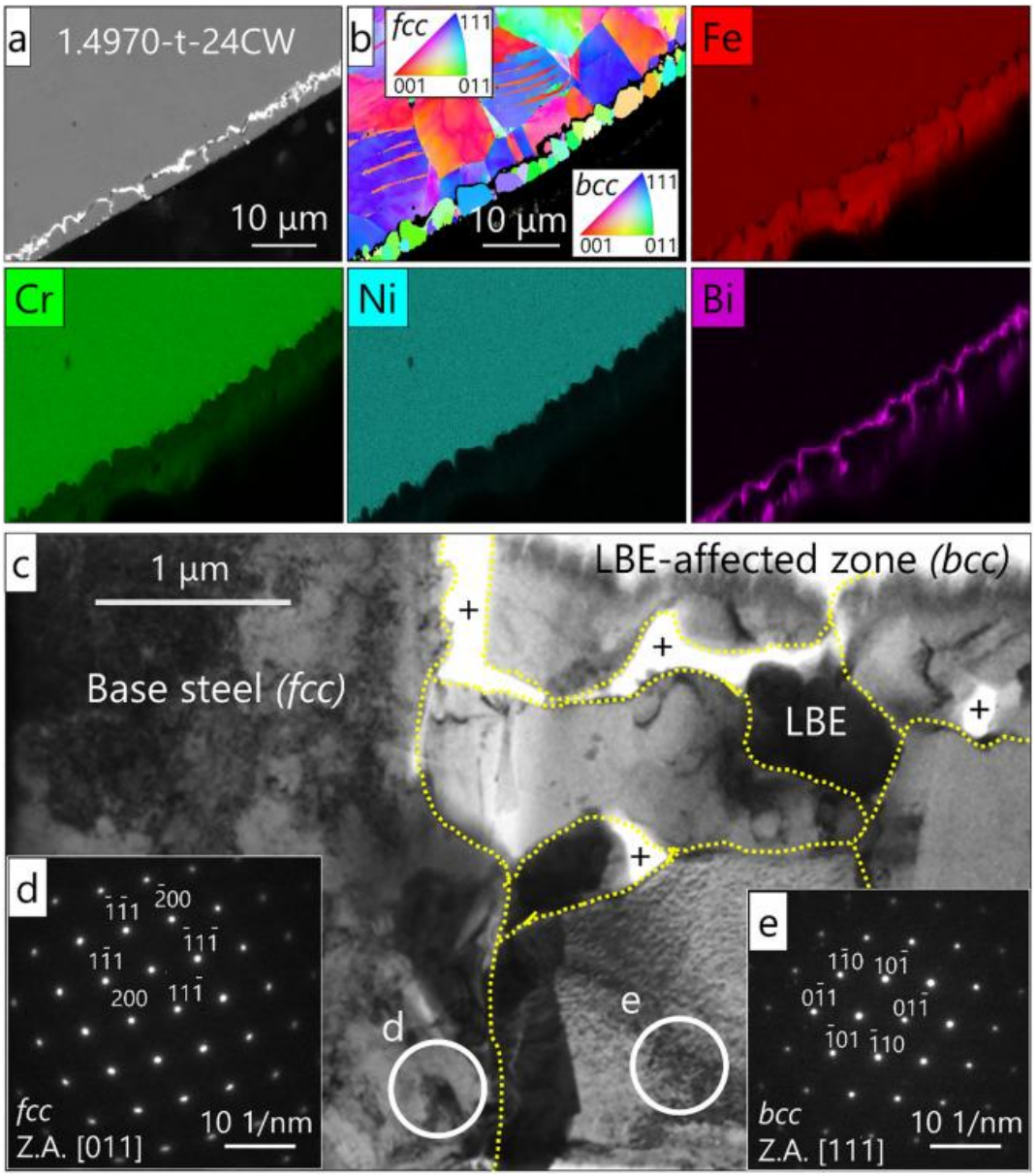

Fig.2.4 Early-stage dissolution-induced ferritization in 1.4970-t-24CW is illustrated. (a) BSE image and (b) EBSD orientation map combined with EDS elemental maps highlight ferritization in the dissolution-affected zone, confined to a layer of grains immediately beneath the steel surface. (c) TEM BF image displays the ferrite/austenite interface, while (d,e) SADPs from the circled regions

in (c) confirm the ferritization (area e) of the austenitic steel (area d). The "+" symbol indicates voids in the thin foil caused by LBE removal [48]. Reprinted with permission from Elsevier.

Fig. 2.5 shows transmission electron backscatter diffraction (t-EBSD) which is also known as transmission Kikuchi diffraction (TKD) phase maps and a schematic representation of the ferritization of austenitic stainless steel in LBE [18]. Zhaoguang [49] researched on the corrosion behaviour of T91 (F/M) steel in LBE at 550 °C and found the oxidation penetrating along GBs as shown in Fig. 2.6.

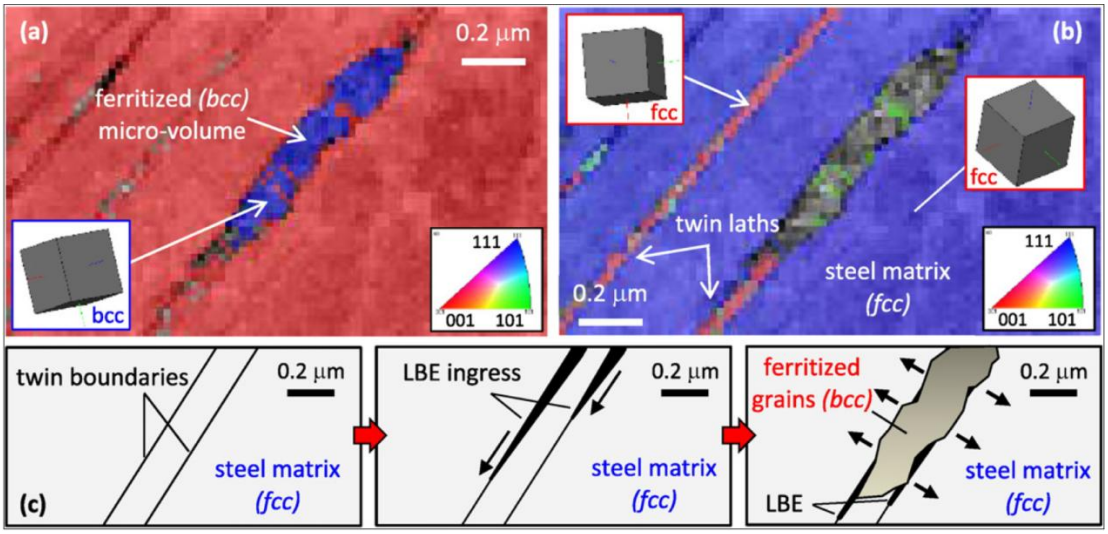

Fig. 2.5 T-EBSD phase maps of (a) a ferritized micro-volume in austenite SS316; (b) twin crystals oriented 60° relative to the steel matrix; (c) Schematic representation of twin boundary-accelerated ferritization of austenitic stainless steels in LBE [18]. Reprinted with permission from Elsevier.

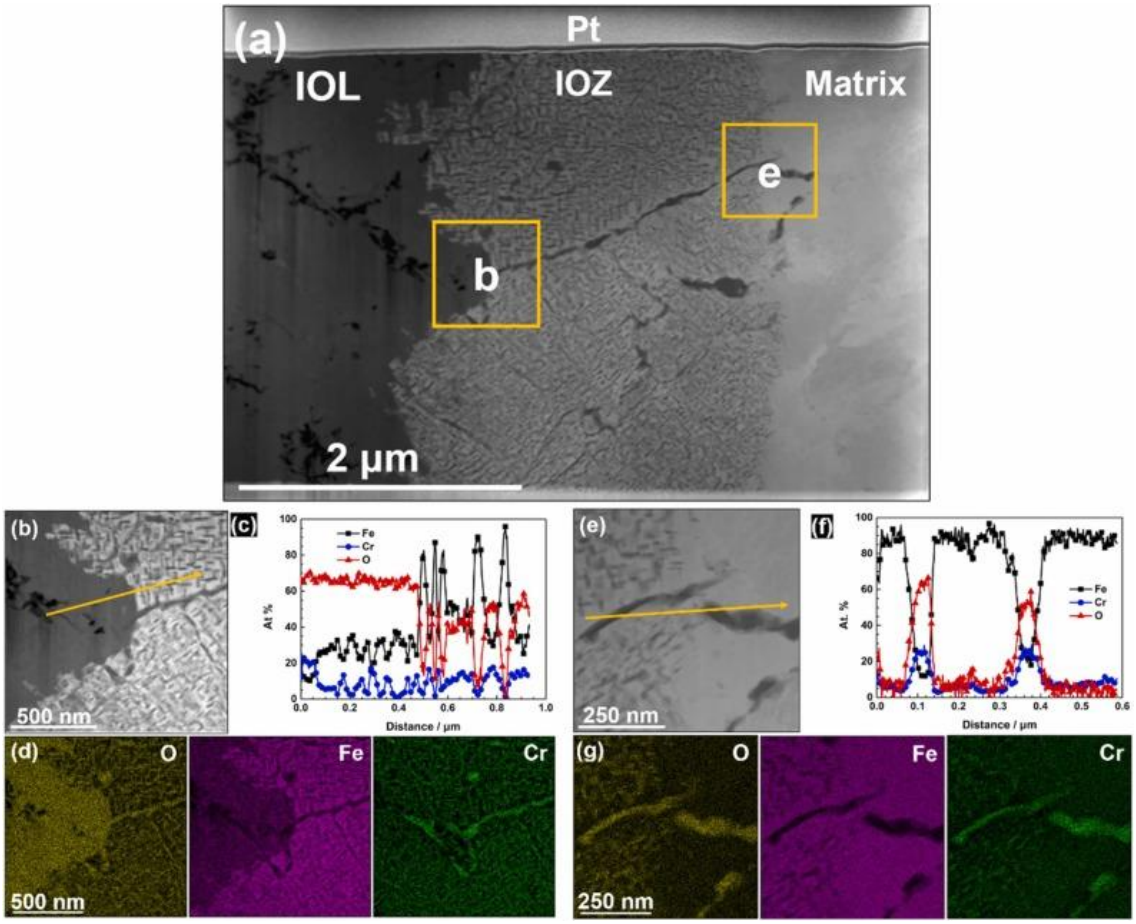

Fig. 2.6 TEM observation and analysis of the oxide film formed on T91 steel after 200 h exposure in liquid LBE: (a) TEM cross-sectional morphology of the oxide film, (b) magnified pattern of the square area in (a), (c) EDS line analysis collected along the line shown in (b), (d) mappings for O, Fe and Cr corresponding to (b), (e) magnified image of the square area in (a), (f) EDS line analysis collected along the line shown in (e), (g) mappings for O, Fe and Cr corresponding to (e) [49]. Reprinted with permission from Elsevier.

2.2.1.3 Oxygen content influence on corrosion

Liquid metal corrosion arises from one or a combination of several physical mechanisms: dissolution, diffusion, and alloying [50]. The presence of impurities can further complicate these processes. For liquid LBE, oxygen has been identified as the most significant impurity. Its

concentration dictates whether dissolution or oxidation becomes the dominant step in the corrosion process [51]. he Ellingham diagram is commonly used to estimate the prevailing corrosion mechanism, as varying oxygen levels influence the formation of oxides, as illustrated in Fig. 2.7 [52].

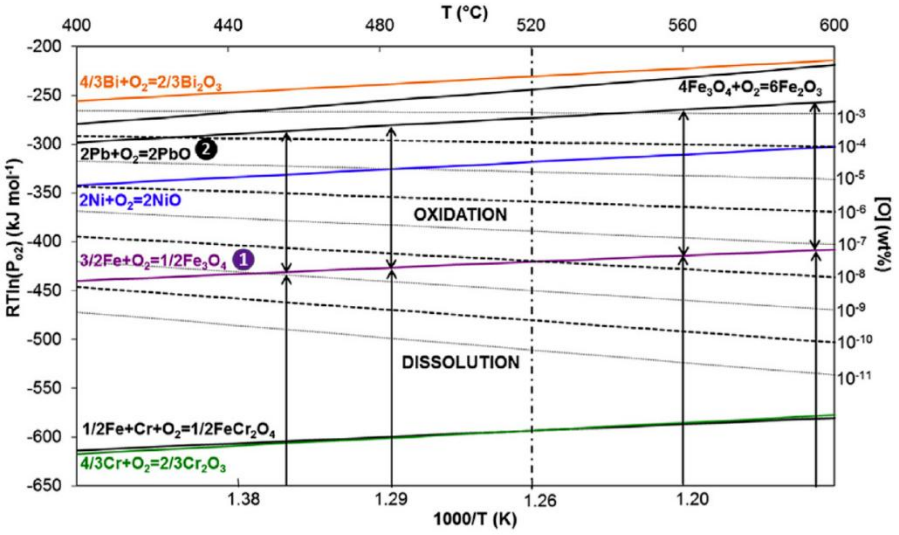

Fig. 2.7 Ellingham diagram for the 316L alloy (i.e. element activities are equal to the molar fractions of the elements in the 316L alloy) [52]. Reprinted with permission from Elsevier.

In oxygen-deficient environments, liquid metal corrosion primarily involves two processes: the physical dissolution of solid metal and the diffusion or penetration of liquid metals. The rates of these processes depend on temperature [53, 54], as illustrated in Fig. 2.2. For instance, Fig. 2.8 demonstrates a corrosion process dominated by dissolution, occurring in T91 steel when exposed to liquid LBE [50].

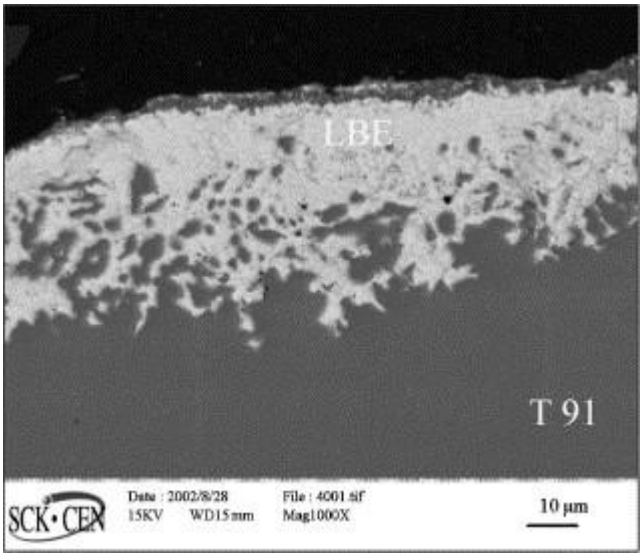

Fig. 2.8 T91-dissolution corrosion mode. Specimen tested at 575 ℃ for 2300 h [50]. Reprinted with permission from Elsevier.

In the oxygen-sufficient environment, oxidisation happens before lead/LBE diffuses into the steel, forming a protective layer against LBE corrosion [50]. Following the discussion in section 2.2.1.2, corrosion experiments reveal that martensitic and austenitic steels are affected in distinct ways. When exposed to liquid metal, austenitic steel develops a characteristic sponge-like surface layer, depleted of alloying elements with high solubility [55, 56]. In contrast, martensitic steel exhibits uniform penetration and forms a complex oxide surface structure, which often leads to significant variability in the observed corrosion rates [55]. Studies have shown the development of columnar double-layer oxide films below 500 ℃ [57]. Under oxygen-saturated and oxygen-controlled conditions, this oxide layer typically consists of an outer magnetite layer and an inner chromium-rich sublayer infiltrated by lead and LBE [57-59]. This structure is attributed to the preferential dissolution and diffusion of certain species [56]. Most researchers describe this penetration as intergranular.

Kurata [10] reported the oxide film formed on steels consists of an external Fe_3O_4 layer and an internal Fe-Cr spinel layer. Intergranular LBE initially penetrates the near-surface grains and

subsequently diffuses into the steel along preferential ingress paths. Depending on the operating conditions, this can result in grain boundary corrosion, internal oxidation, LBE penetration, and ferritization. In liquid LBE, since grain boundaries always contain disordered atoms and defects, they are generally the most critical path. Lambrinou found that oxide/steel interfaces also behave as a preferential path [22]. Fig. 2.8 shows a scanning electron microscope (SEM) image of a cross-section of a ferritic/martensitic (2.25Cr-1Mo) steel after corrosion in LBE at 550 ℃ for 3000 h, which has grain boundary corrosion inside [60].

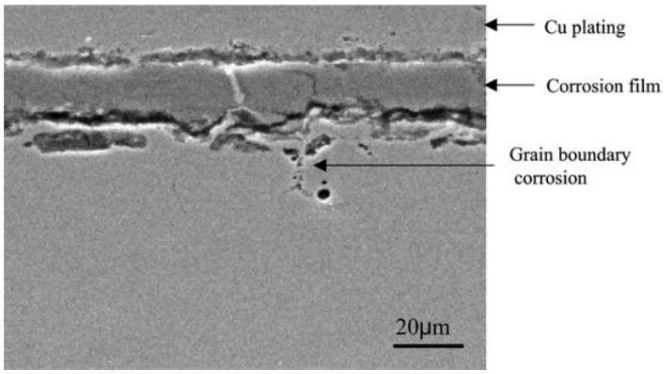

Fig. 2.9 SEM image of the cross-section of 2.25Cr-1Mo l after corrosion in LBE at 550 ℃ for 3000 h [60]. Reprinted with permission from Elsevier.

2.2.1.4 Temperature influence on corrosion

Kutateladze [53, 61] observed that the kinematic viscosities of LBE decrease with increasing temperature, resulting in a higher Reynolds number. Consequently, corrosion is exacerbated in the mass diffusion-limited situation. In addition to the more severe corrosion caused by the lower kinematic viscosities of liquid lead and LBE at elevated temperatures, the material properties also pose challenges to the use of LFRs and LBEFRs at higher operating temperatures.

Research by Marié and Wolski [22], indicates that the intergranular penetration of liquid metal into solid metal depends on the wetting transition temperature T_w [20, 21, 62]. Above this

temperature, the liquid metal wets the grain boundary, while below T_w, it diffuses into the grain boundary. Kurata [10] studied the behaviour of austenitic stainless steels and ferritic/martensitic steels in 450 ℃ to 600 ℃ LBE and found that Cr, Ni, and Si play important roles in the corrosion behaviour. At lower temperatures (450℃), the oxide film thickness on both steel types decreases with increasing Cr content. At 500℃, the oxide films thicken, and grain boundary corrosion begins to appear in some steels. At 550℃, severe grain boundary corrosion and internal oxidation are observed in F/M steels, while austenitic steels experience more severe corrosion, including ferritization and LBE penetration.

In austenitic steels, selective leaching of Ni, Cr, and Mn into LBE drives ferritization [63]. Since the solubility of Ni and Cr is significantly higher than that of Mn, these two elements are the dominant factors in ferritization. Ni and Cr are also primary austenite stabilizers [64]. Their removal by LBE leads to the transformation of the dissolution-affected zone from austenite to ferrite.

Kurata also reported LBE penetration at 600℃ for F/M steels. After 550℃, material corrosion increases significantly. The addition of Si to austenitic steels was found to improve corrosion resistance. A Si oxide film helps reduce Ni and Cr dissolution [60]. However, excessive Si and Cr content can negatively impact the material. High Si content compromises welding and creep properties and may reduce irradiation resistance due to swelling, radiation-induced segregation, and embrittlement. Elevated bulk Cr levels can also lower low-temperature toughness under irradiation conditions [19].

Fig. 2.10 summarizes the corrosion depth of F/M steels (2.25Cr-1Mo steel, F82H, and 410SS) and austenitic stainless steels (JPCA, 316SS, SX, and ZeCor, notably, SX and ZeCor contain a high Si content of approximately 5 wt.%) at different temperatures [10].

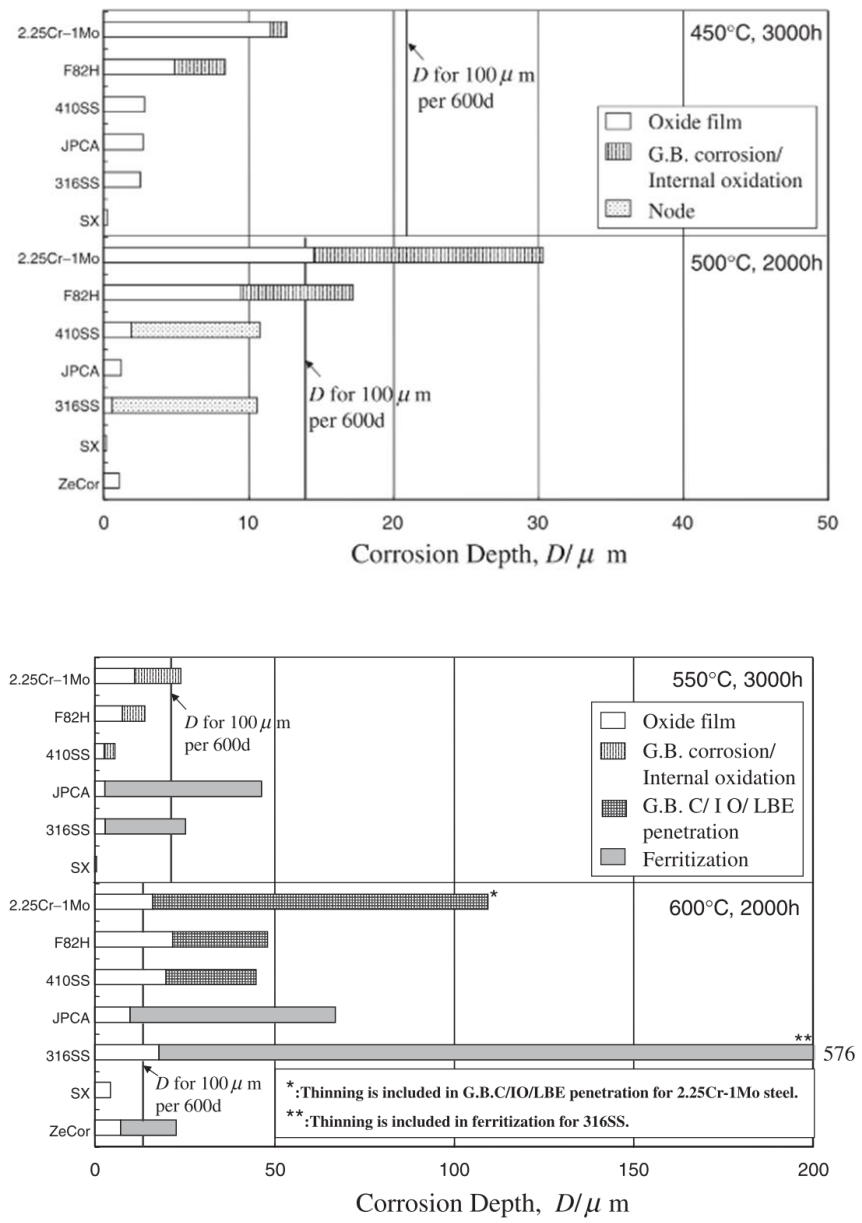

Fig. 2.10 Corrosion depths of austenite and ferritic/martensitic steels in oxygen-saturated LBE at 450, 500, 550, and 600℃ (2.25Cr-1Mo steel, F82H and 410SS are ferritic/martensitic steels. JPCA, 316SS, SX, and ZeCor are austenitic stainless steels. SX and ZeCor with high Si content of about 5%) [10]. Reprinted with permission from Elsevier.

Liquid lead and LBE contain small amounts of dissolved oxygen, which can induce the formation of metastable wüstite during the reduction process of iron oxide formation at temperatures

below 570℃ [65]. This compromises the protective function of the Fe oxide film and accelerates corrosion.

Corrosion progresses over time, with longer exposure accelerating the process. Fig. 2.11 [22] presents backscattered electron (BSE) images of 316 austenitic stainless steel subjected to dissolution attack in 500°C LBE for different durations. More severe corrosion is evident with increased exposure time.

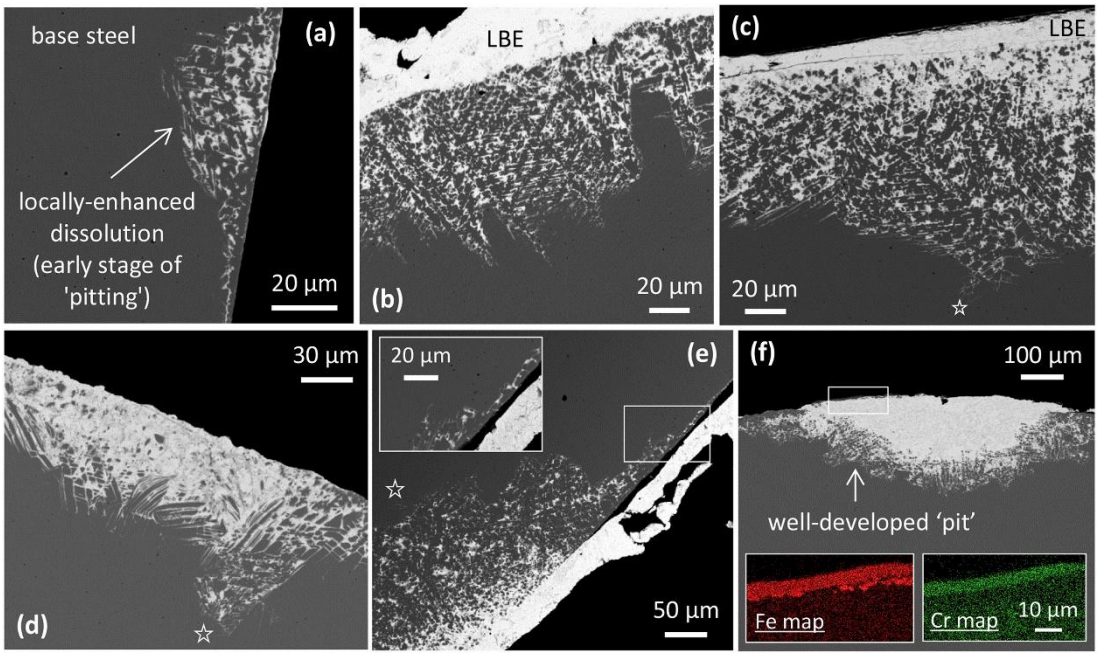

Fig. 2.11 Backscattered electron (BSE) images of 316 austenite stainless steel for different time with 500℃ LBE dissolution attack (a) 253 h (b) 501 h (c) 1003 h (d) 1000 h (e) 2055 h (f) 3282 h [22]. Reprinted with permission from Elsevier.

2.2.2 Liquid metal embrittlement

In addition to corrosion, liquid metal embrittlement (LME) is another critical issue limiting the use of F/M steels in LFRs and LBEFRs. For failure to occur, both a minimum strain and intimate contact between the solid and liquid metals must be present simultaneously. In many

susceptible systems, embrittlement is confined to a sharply defined temperature range. The onset of LME typically occurs near the melting point of the embrittler [66]. The lower temperature for the onset of LME is generally independent of strain rate, which alters the width of the embrittlement range. Fig. 2.12 [67] shows a typical quasi-brittle fracture surface of steel tested after exposure to LBE corrosion. LBE corrosion increases the steel's susceptibility to LME, leading to brittle fracture.

Several models and mechanisms have been proposed to explain liquid metal embrittlement, including surface energy effects [68], interatomic cohesion [69], grain boundary penetration [13], the injection of dislocations from crack tips [70], dissolution-condensation, and work hardening [71, 72].

However, austenitic steels do not experience LME to the same extent due to their superior ductility. In austenitic steels, the ferritization zone transforms from austenite to ferrite, leaving the surrounding area as unaffected austenite. This transformation is accompanied by an increase in atomic volume, which generates local stress. As a result, dissolution-induced ferritization may trigger liquid metal embrittlement. Nevertheless, any associated cracks are typically arrested within the ductile austenitic matrix of the unaffected steel. In contrast, F/M steels are more prone to LME because they lack the underlying ductile austenite matrix that could mitigate crack propagation [22].

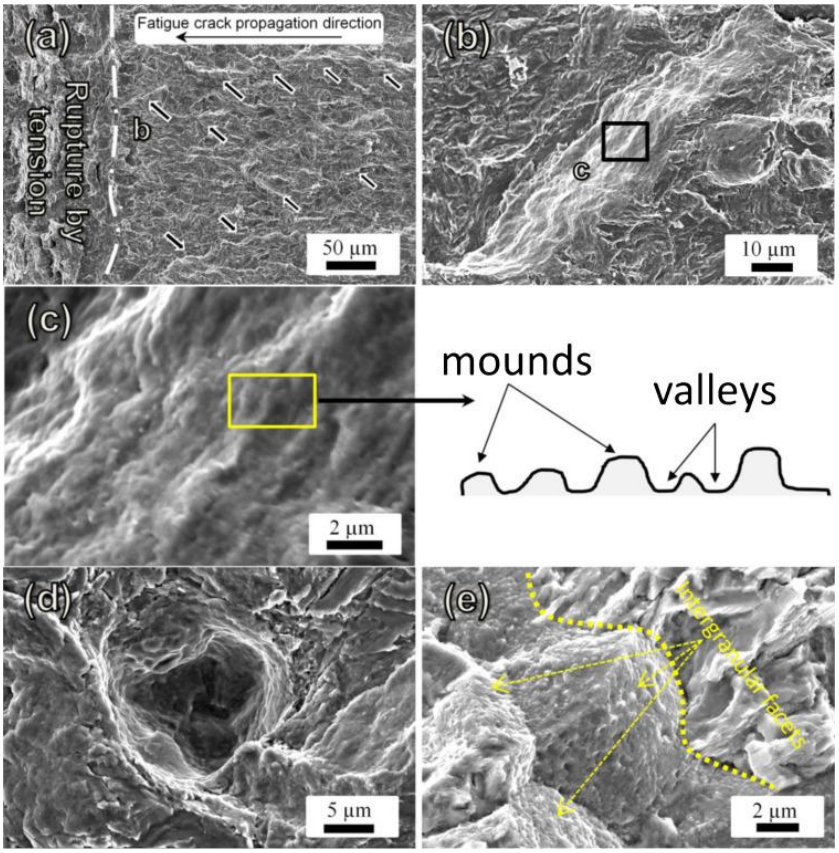

Fig. 2.12 SEM fractographic micrographs show a typical quasi-brittle fracture surface after testing in LBE [67]. Reprinted with permission from Elsevier.

Gorse [5] reviewed the effects of liquid lead and LBE exposure on the tensile, fatigue, and creep properties of F/M steels and austenitic steels. The study found that the fatigue resistance of F/M steels, particularly T91, decreases in LBE compared to air, whereas austenitic steels exhibit almost identical behaviour in both environments. Additionally, the density of short cracks in F/M steels exposed to LBE is much lower than in air. However, once a short crack initiates in LBE, it propagates rapidly into the bulk, in contrast to the slower propagation observed in air.

LEM is also temperature dependent. Gorse's review [5] highlights that the susceptibility of F/M steels to LME increases between 200°C and 300°C. However, the formation of an oxide layer on the steel surface has been shown to suppress surface wetting, thereby reducing the susceptibility of F/M steels to LME [3, 31, 73].

2.2.3 Creep in steel

LME primarily occurs at lower temperatures, while creep is more prominent at higher temperatures. As temperature increases, more slip systems become active, leading to easier cross-slip and climb, which facilitate dislocation rearrangement into sub-boundaries through polygonization [74]. Austenitic steels generally experience minimal mechanical changes when exposed to liquid lead or LBE. However, a significant acceleration of creep was observed in F/M steels at 550℃ in LBE and 525℃ in liquid lead with high stress (>180 Mpa), which limits the operation temperature [5, 75]. As shown in Fig. 2.13 Weisenburger [76] compared the creep properties of the same material under different stress conditions in both LBE and air. The results show that LBE accelerates creep compared to air. They also suggest that thin oxide layers formed on surface-modified steel samples are less prone to crack formation and, therefore, less susceptible to lead-alloy enhanced creep.

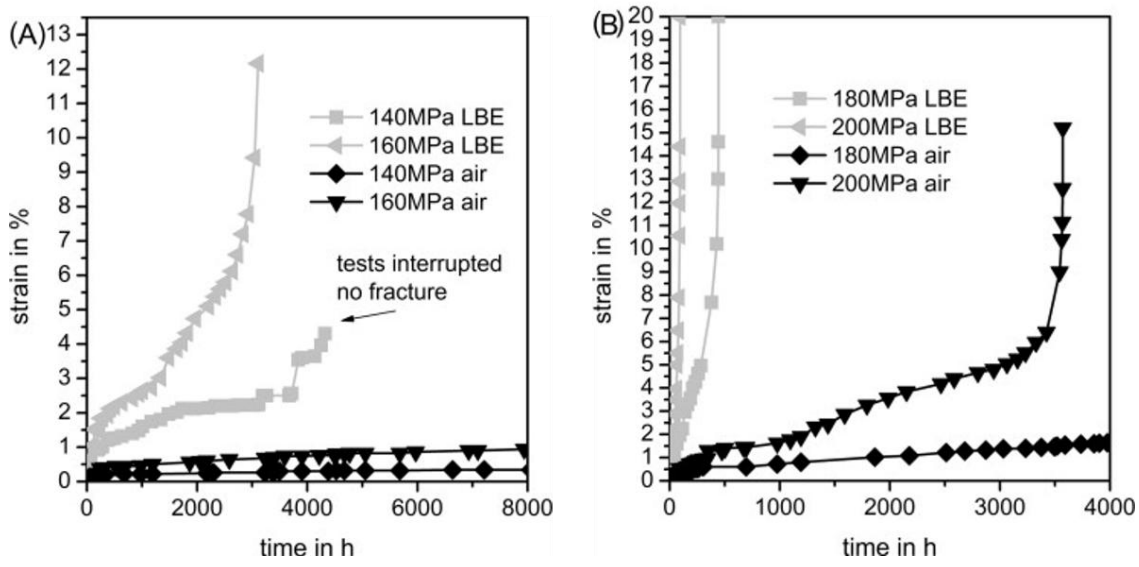

Fig. 2.13 Comparison of creep to rupture diagrams of T91 in LBE and in air at 550 ℃, (a) 140 and 160 MPa, (b) 180 and 200 MPa [75]. Reprinted with permission from Elsevier.

2.2.4 Radiation effect

Though the radiation effects on steels are beyond the scope of this thesis, it is important to note that the material discussed here is a candidate structural steel for LFRs and LBEFRs, which will be exposed not only to liquid metal but also to radiation. Therefore, the radiation effects on the material are also a critical consideration. A brief overview of the radiation effects on steels is provided below.

Radiation damage is known to significantly alter materials, affecting both their mechanical properties (e.g., increased hardness and yield strength, and decreased ductility and toughness) and their chemical composition.

Radiation increases the mobility of atoms within the metal [77], by generating more point defects and dislocations, which provide easy diffusion channels. The higher concentration of point defects directly leads to radiation-enhanced diffusion, which varies for different atomic species depending on the defect-mediated diffusion mechanism (vacancy or interstitial).

In the radiation-damaged area, excess point defects and accelerated diffusion cause vacancies and self-interstitials to eliminate each other at surfaces, dislocations, and grain boundaries, or recombine in the bulk through recombination, clustering, and annihilation. These radiation-induced precipitates, point defects, dislocation loops, and element redistribution result in glide dislocations that cannot move as easily as in unirradiated materials. As a result, the hardness, yield strength, and ultimate tensile strength of the material increase, while ductility and work-hardening rates decrease.

The increased hardness and embrittlement also directly raise the ductile-to-brittle transition temperature. In addition to mechanical properties, radiation can degrade thermal diffusivity [78-80]. The voids and cavities caused by irradiation can trap more hydrogen, and combined with the increased hardness, this can promote embrittlement [81].

2.2.4.1 Radiation-induced segregation (RIS)

RIS is one of the most widely discussed effects of radiation. It occurs due to the clustering of small irradiation-induced defects, such as dislocation loops, clusters, and cavities, in steels. This process can lead to the local redistribution of elements, which is known as RIS [82, 83]. RIS is influenced by the inverse Kirkendall effect and interstitial association [84, 85].

The inverse Kirkendall effect involves the exchange of elements that diffuse rapidly with vacancies, causing them to move away from point defect sinks like grain boundaries and surfaces. In contrast, elements with lower diffusion rates accumulate at these sinks. Interstitial association occurs when undersized solute atoms preferentially interact with self-interstitials and accumulate at sinks.

Allen [86] investigated the mechanisms of RIS in seven different Fe-Cr-Ni alloys. His findings showed that RIS, for both proton and neutron irradiation, is driven by the interaction of solutes with vacancies. RIS was first observed in austenitic steels, where the depletion of Cr and the enrichment of Ni at grain boundaries are the dominant phenomena [87]. The changes in Cr and Ni content are linked to corrosion cracking rates and the stabilization of austenite near the sinks [88]. The depletion of Cr and radiation-induced material hardening are considered primary factors contributing to irradiation-assisted stress corrosion cracking [89]. As temperature increases, enhanced vacancy diffusion may reduce RIS through back diffusion [90].

2.2.4.2 Temperature influence of radiation effects

Both the formation of point defects and the diffusion process are significantly influenced by temperature. The typical irradiation-induced microstructure of austenitic stainless steels includes dislocation loops, cavities, precipitates, and network dislocations, all of which are affected by both temperature and dose [91].

At temperatures below 350℃ , irradiation leads to the formation of fine 'black-spot' loops and larger Frank loops, which are dominated by dislocations. At higher temperatures, cavities—such as gas bubbles and voids—become the dominant feature. Under high-dose and high-temperature conditions, structural materials lose their effectiveness quickly due to radiation-induced void swelling, creep, and the formation of new phases (e.g., the G phase in steel). Fig. 2.14 illustrates the G phase formed [92] in irradiated stainless steel and the resulting changes in its mechanical properties [93, 94].

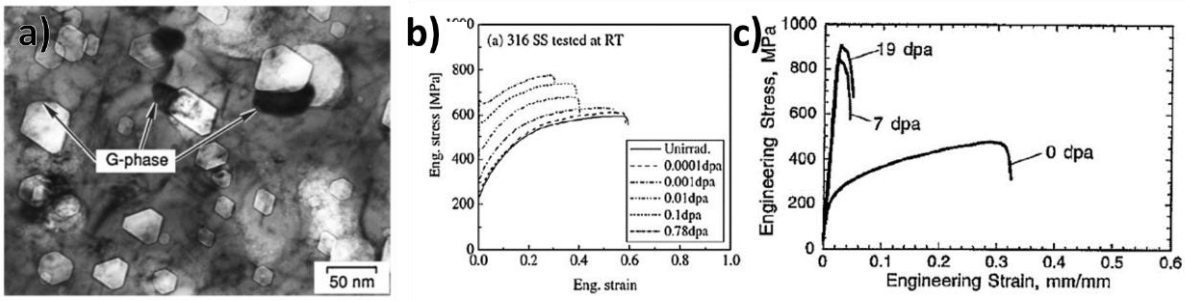

Fig. 2.14 (a) Formation of Ni-enriched G phase silicide at voids in a USPCA stainless steel irradiated in ORR to 11 dpa at 500 °C [92]. Stress–strain curves for (b) A solution-annealed 316 stainless steel irradiated to several doses <1 dpa in the mixed spectrum HFIR test reactor at 60 °C and tested at room temperature [93]. (c) A solution-annealed J316 both irradiated in HFIR and tested at 330 °C [94]. Reprinted with permission from Elsevier.

2.2.5 Simultaneous irradiation and corrosion

An important aspect of the future work in this thesis is examining the combined effects of irradiation and corrosion on steels, which is critical for further development. Radiation not only alters the mechanical properties of materials but also significantly impacts their corrosion behaviour. The corrosion rate is primarily controlled by three factors: (1) solid-state diffusion, (2) surface reaction or dissolution rates, and (3) the transport of corrosion products within the reactor coolant [95]. As discussed in section 2.2.4 radiation will increase diffusion, which means

that radiation will exacerbate corrosion. There are several research shows that corrosion gets more serious with the radiation involved.

Wang [96] investigated the corrosion of Zircaloy under proton irradiation in PWR and found that the proton irradiation increases the ion current by increasing interstitial and vacancy concentrations. Furthermore, radiation leads to lots of defects at the metal-oxide interface, which induces the uneven nucleation and growth process of crystallites. As a result, the porosity increased and the cohesion between grains reduced.

Iltis [97] reported in his paper that irradiation in Zr will induce extra grain growth and pore formation throughout the oxide layer. This will help the micro-cracks form an easy migration crack network. As a result, radiation leads to more severe corrosion of the material.

Other than cracks, the dissolution of intermetallic precipitates, known as secondary particle precipitates (SPPs) caused by radiation also accelerates the corrosion. Filippov investigated Zr-0.76Fe-1.6Sn which is irradiated and corroded in the reactor. The result shows that the corrosion rate is largely accelerated with irradiation due to the faster tin dissolution in the coolant and the changing oxidation state of the tin [98].

Raiman [99, 100] researched the properties of austenitic stainless steel under simultaneous irradiation and corrosion in high-temperature water, and found irradiation creates radiolysis products in the water and accelerates the corrosion. H_2O_2 is the dominant radiolysis product responsible for elevating corrosion potential. At the same time, the irradiated samples have a layer of hematite and are deficient in Cr while the unirradiated samples do not. The author suggests that water radiolysis is the determining factor for how the radiation accelerates the corrosion by comparing the samples both under radiation and one contact with irradiated water the other is not. It is also proved that higher temperatures will further speed up the corrosion.

Chao studied the impact of He irradiation on the corrosion behaviour of T91 steel in high-temperature steam. The results showed that irradiation accelerates corrosion by inducing pore

formation in the inner oxide layer of T91 steel, as shown in Fig. 2.15. As the irradiation dose increases, pore density also rises. These pores create diffusion short-circuits for oxygen, facilitating faster oxidation. Additionally, the displacement damage caused by helium ions thickens the oxide layer, further promoting corrosion. The combined effects of these processes significantly degrade the corrosion resistance of the material [101].

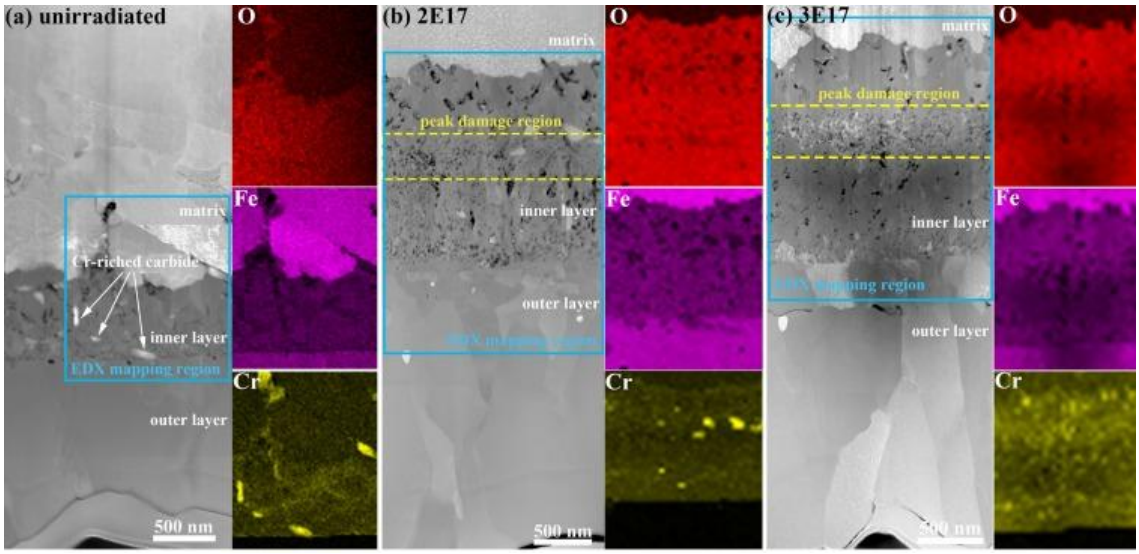

Fig. 2.15 The STEM images and corresponding EDS mapping of the oxide film formed on T91 subjected to different irradiation doses following 100-h exposure to high-temperature steam at 450 °C. (a) unirradiated. He^{2+} ions at fluences of: (b) 2.0×10^{17}; (c) 3.0×10^{17} ions/cm^2 [101]. Reprinted with permission from Elsevier.

2.3 Corrosion inhibitor

A key challenge in structural material performance within liquid lead and LBE environments is the combined effect of corrosion and radiation. While radiation accelerates damage mechanisms like void swelling and embrittlement, corrosion can compromise material integrity. The interplay between these factors necessitates effective strategies to mitigate material degradation in harsh reactor environments.

A widely used method for mitigating the corrosion of structural materials in liquid lead and LBE is the addition of corrosion inhibitors at controlled concentrations. Corrosion inhibitors are chemical substances that, when introduced in small amounts, reduce the corrosion rate by forming protective films on the material's surface, thereby providing a degree of protection.

For liquid lead and its alloy LBE, corrosion inhibitors can be broadly categorized into metallic and non-metallic types. Research conducted prior to the 1980s predominantly focused on metallic inhibitors, with zirconium (Zr) and titanium (Ti) identified as the most effective options. More recently, oxygen has been recognized as an effective non-metallic inhibitor for mitigating corrosion in liquid lead and LBE systems. Current studies primarily explore methods for controlling oxygen levels and understanding the behaviours of protective oxide layers in these environments [30, 40]. However, the oxygen content must be carefully controlled; excessive oxygen can lead to the formation of lead or bismuth oxides, which may block the reactor cooling system. Fig. 2.16 shows a comparison of corrosion rates between materials with and without inhibitors [46].

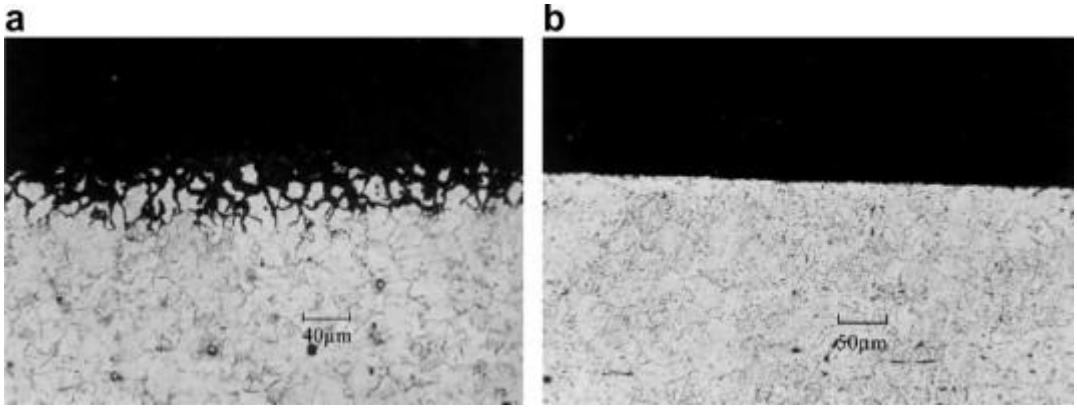

Fig. 2.16 Microphotographs show (a) the degradation of 2CrSiMoV steel after 300 hours in LBE without an inhibitor, and (b) the protection of CrMoV steel after 6000 hours in LBE with 10–40 ppm Ti added. The experiments were conducted at 873 K, with 300–500 ppm Mg used as an oxygen getter [46]. Reprinted with permission from Elsevier.

2.4 Conclusion

As energy shortages and environmental pollution continue to rise, nuclear power generation has garnered increasing attention. It is expected to play a key role in achieving zero-carbon emission goals. Fast reactor designs aim to improve fuel usage, and LBEFR, a candidate design for Gen IV reactors, offers high power density and enhanced safety. However, LBE corrosion of safety-critical components has been a major bottleneck for LBEFR deployment and has limited operational temperatures. A thorough understanding of LBE corrosion characteristics is crucial for the proper design and safe operation of liquid lead/LBE heat transfer circuits.

Although some research on LBE corrosion of structural materials has been conducted, a clear corrosion mechanism remains elusive, and much of the research focuses on micro-scale investigations. Furthermore, many studies have not considered the combined effects of corrosion and irradiation, which have led reactor designers to set low operating temperatures, hindering the advancement of LFR and LBEFR. For instance, the only upcoming commercial LBEFR, the SVBR in Russia, is limited to 390℃.

To improve reactor efficiency, future designs will require higher operating temperatures. Therefore, a better understanding of LBE corrosion mechanisms in steel at these extreme conditions is urgently needed, including characterization at the nano and atomic scales. Additionally, most corrosion studies of steels in LBE have been conducted under a fixed oxygen level. There is little literature that clearly explains the difference in corrosion mechanisms under reducing (oxygen-deficient) and oxidizing (oxygen-rich) environments.

Chapter III

Materials and methods

3.1 Introduction

3.1.1 F/M steels

Steel microstructures consist of various phases, including ferrite, martensite, austenite, and pearlite, which significantly influence mechanical properties. These phases exhibit distinct crystallographic structures and mechanical behaviours, each contributing uniquely to the performance of steel in a wide range of applications. As described in section 3.1.2.1, the elemental composition and cooling rate during heat treatment are the key factors determining the final phases.

3.1.1.1 Ferrite (α-iron)

Ferrite is the body-centred cubic (BCC) phase of Fe and represents the primary phase in low-carbon steels. Its crystal structure and atomic configuration are critical in defining its mechanical characteristics [102].

Crystal Structure and Lattice Parameters: Ferrite adopts a body-centred cubic (BCC) structure. The BCC lattice is stable at ambient temperatures and remains the dominant structure in pure Fe and low-carbon steel [103].

Carbon Solubility and Lattice Distortion: Ferrite can dissolve only a limited amount of C, with a maximum solubility of approximately 0.02 wt.% at at 727°C according to the Fe-FeC phase diagram [104]. This low solubility arises from the small size of the interstitial sites within the BCC lattice, which restricts the incorporation of more C atoms. When carbon atoms occupy these

interstitial positions, the lattice undergoes slight distortion, although this is insufficient to significantly alter the mechanical properties of ferrite [105].

Formation Mechanism: Ferrite forms from austenite upon cooling below the A3 transformation temperature (~910°C for pure Fe). In low-carbon steels, ferrite is the predominant phase at room temperature and is often found in conjunction with other phases, such as pearlite. Ferrite nucleation and growth occur during slow cooling, allowing C to diffuse out of the austenitic structure [106].

Mechanical Properties: Ferrite is characterised by its high ductility, and relatively low tensile strength. The ease of dislocation movement in the BCC lattice allows for substantial deformation under stress [106].

3.1.1.2 Martensite

Unlike ferrite or pearlite, martensite forms through a deformation of the austenite lattice without any diffusion of atoms. This deformation results in a striking change in the shape of the transformed region, involving a large shear and unidirectional volume expansion [106]. When the formation of martensite is constrained by its surroundings, it develops as thin plates or laths to minimise the strain energy caused by the deformation.

Formation Mechanism: Martensite forms via a diffusionless shear transformation when austenite is rapidly cooled below the martensite start temperature, as shown in Fig. 3.1 (b). During this process, atomic rearrangement occurs rapidly, trapping C atoms in the interstitial sites of the body-centred tetragonal (BCT) lattice. The transformation involves a change in crystal structure without atomic diffusion [106].

Martensite is a metastable phase and can decompose upon tempering. The tempering process involves heating martensite to temperatures below the eutectoid temperature (~727°C), which allows C to precipitate as fine carbides. This process relieves internal stresses and increases ductility [64].

Crystal Structure and Lattice Distortion: Martensite is a supersaturated solid solution of C in ferritic iron. It adopts a BCT structure, a distorted variant of the BCC lattice [64]. The distortion arises from the interstitial positioning of C atoms during rapid cooling. Since C atoms are significantly larger than the available interstitial sites in iron, their entrapment induces strain in the crystal lattice. This results in a tetragonal unit cell where the c-axis is elongated relative to the a-axes.

The degree of distortion in the BCT structure increases with C content, as shown in Formula 3-1. At higher C concentrations, the c/a ratio increases, leading to more pronounced tetragonal distortion. This distortion plays a key role in the mechanical behaviour of martensite, particularly its hardness and strength [106].

$$\frac{c'_\alpha}{a'_\alpha} = 1 + 0.0445\, w_C \qquad \text{[Formula 3-1]}$$

Carbon Solubility and Lattice Strain: Martensite can accommodate up to 1.2 wt% C, significantly more than ferrite. However, the C is not in equilibrium solid solution but is instead trapped within the lattice due to the diffusionless nature of the transformation. The supersaturation of carbon generates internal stresses, contributing to martensite's characteristic high hardness and brittleness [107]. The lattice distortion also introduces internal stresses that increase the likelihood of cracking, particularly in high-carbon martensite [64].

Mechanical Properties: Martensite exhibits extremely high hardness, typically ranging from 500–700 HV depending on the C content. Its high strength and wear resistance make it ideal for applications requiring superior hardness, such as cutting tools and wear-resistant surfaces [64].

However, the high hardness is accompanied by a significant reduction of ductility, making martensite prone to brittle fracture under stress. In its untempered state, martensite is highly susceptible to cracking, particularly under impact loading or cyclic stresses. The brittleness of martensite can be mitigated through tempering, a heat treatment process that allows partial

decomposition into more ductile phases such as ferrite and cementite, while reducing internal stresses [64, 108, 109].

3.1.2 Main alloying elements of T91 and their effects

3.1.2.1 Carbon (C)

The influence of C on the properties of steel is a fundamental aspect of this alloy system. A key starting point for understanding the composition and microstructure of all steel grades is the Fe-C equilibrium phase diagram, illustrated in Fig. 3.1 [104]. The Fe–C phase diagram, also referred to as the Fe–Fe_3C phase diagram, delineates the relationships between phases in iron-carbon alloys, comprising four solid phases (α-Fe, γ-Fe, δ-Fe, and Fe_3C) and a liquid phase.

Pure iron exists in three allotropic forms: α (ferrite), γ (austenite), and δ (ferrite). Allotropy refers to the ability of elements to exist in multiple crystalline forms under varying temperature or pressure. α-Fe, stable up to 912°C, has a BCC structure. γ-Fe, stable between 912°C and 1394°C, exhibits a FCC structure. δ-Fe, stable from 1394°C to iron's melting point (1538°C), also has a BCC structure but with a slightly larger lattice parameter due to its higher-temperature stability. The interstitial carbon solubility of α-Fe reaches a maximum of 0.021 wt% C at 740°C (the eutectoid temperature). γ-Fe, with its FCC structure, has a higher carbon solubility, up to 2.1 wt% C at 1153°C (the eutectic temperature). δ-Fe has a maximum solubility of 0.09 wt% C at 1493°C (the peritectic temperature) [110].

Cementite (Fe_3C), with its orthorhombic structure and 6.67 wt% C, defines the diagram's carbon limit. Although Fe_3C is metastable and can decompose into Fe and C over time, it is treated as stable in practical applications. The diagram is unique in spanning up to only 6.67 wt% C, reflecting the industrial irrelevance of higher C contents. This approach simplifies the study and application of commercially viable iron-carbon alloys [104].

The Fe–C phase diagram highlights critical temperatures, including the eutectoid temperature (A1), the lower critical temperature (A3), and the upper critical temperature (Acm). These define the boundaries for austenite transformations. Below the A3 temperature, hypoeutectoid steels transform as austenite forms ferrite. Below Acm, hypereutectoid steels experience austenite transforming into cementite. Understanding these transformations is essential for controlling the microstructure and mechanical properties of steel [106].

The Time-Temperature-Transformation (TTT) diagram is crucial for practical applications as it depicts how austenite transforms into other phases—such as pearlite, bainite, or martensite—under different cooling rates. Unlike the equilibrium Fe–C phase diagram, which assumes infinite time for phase stability, the TTT diagram reflects real-world cooling scenarios, enabling engineers to predict and dynamically manipulate phase transformations [104, 111].

For example, quenching steel rapidly through the martensitic transformation zone of the TTT diagram produces a hard, brittle microstructure, whereas slower cooling through the pearlite or bainite regions results in softer, more ductile phases. This ability to tailor properties is essential across industries, from automotive to construction, where steels with specific combinations of strength, toughness, and wear resistance are required [110].

In summary, while the Fe–C phase diagram provides a theoretical framework for phase stability at equilibrium, the TTT diagram serves as a practical tool for optimising heat treatment processes and achieving desired material performance.

Meanwhile, C is a γ-stabilising element, stabilising the FCC austenite (γ-Fe) phase in iron. Its stabilising effect alters critical transformation temperatures:

- **Raising the Upper Transformation Temperature (A_3):** In the presence of C and other γ-stabilising elements, the α-Fe (BCC) to γ-Fe (FCC) transformation occurs at higher temperatures, above 1394°C. Increasing the concentration of these elements in solid solution raises the A_3 temperature further.

- **Lowering the Lower Transformation Temperature (A_1):** γ-stabilising elements reduce the temperature at which austenite (γ-Fe) transforms into ferrite (α-Fe). This transformation, which begins below 912°C, occurs at even lower temperatures with higher carbon content in the austenite.

Carbon's ability to shift these transformation temperatures enhances the stability of austenite over a broader temperature range, making it critical for steels requiring high ductility and toughness [111].

The T91 steel analysed in this study has a C content of 0.09 wt.%, which is expected to result in the formation of ferrite and pearlite phases under conditions of very slow cooling. To further elucidate the phases that form as a function of cooling rate, we also need to refer to TTT diagram as shown in Fig. 3.2. Under sufficiently high rapid cooling rates, martensite may form, resulting in the production of ferrite/martensite (F/M) steel.

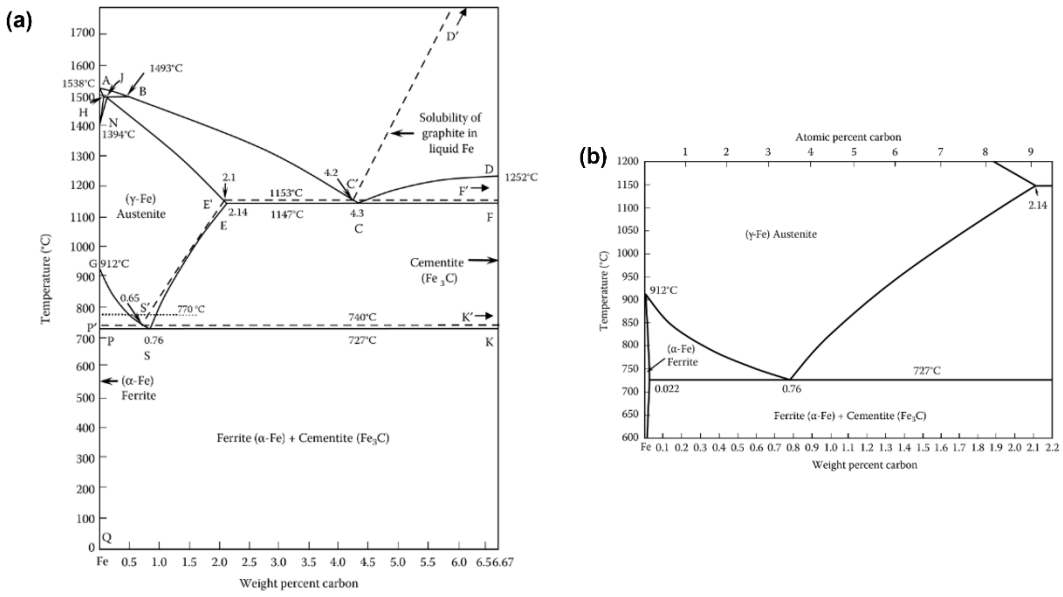

Fig. 3.1 Fe-C equilibrium diagram [104]. Reprinted with permission from Taylor and Francis.

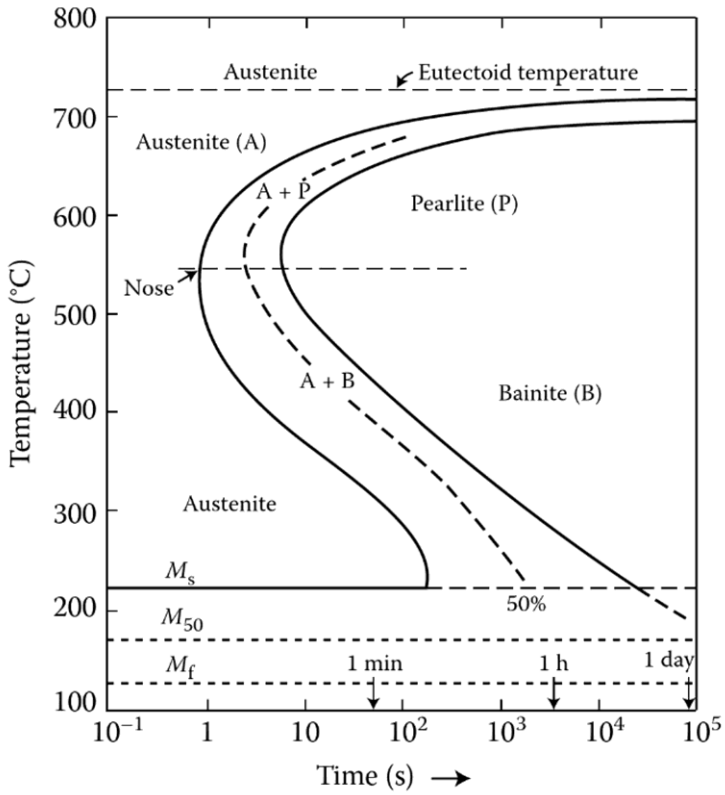

Fig. 3.2. TTT diagram for eutectoid steels. [104]. Reprinted with permission from Taylor and Francis.

3.1.2.2 Chromium (Cr)

Cr is a common alloying element used in steels to enhance corrosion and oxidation resistance [64]. This section will discuss the influence of Cr in steels from the following three perspectives:

Martensite Stabiliser: Cr is an α-stabilising element that stabilises iron's BCC form (α-Fe). However, its behaviour differs from other α -stabilisers in significant ways [111]:

1. Stabilising Role in Transformations: Cr stabilises the α-phase during the δ-Fe to austenite (γ-Fe) transformation, as illustrated in the Fe-Cr phase diagram (Fig. 3.3). At lower concentrations (<5%), Cr acts as a γ-stabiliser, promoting austenite formation. At higher concentrations (>7%), Cr consistently acts as an α -stabiliser.

2. Carbide-Stabilising Nature: Cr is part of a group of α -stabilising elements (e.g., Cr, Ti, V, Mo) that promote carbide formation. This contrasts with elements such as Si and Al, which inhibit carbide formation and instead favour graphite formation.

3. Impact on Properties: In solid solution, Cr marginally hardens ferrite but can also soften it by removing interstitial solutes. Unlike elements such as nitrogen (N) or phosphorus (P), Cr has minimal impact on the ductile-to-brittle transition temperature (DBTT), thereby preserving toughness in ferrite.

In summary, Cr's dual stabilising roles, suppression of phase transformations, and carbide-stabilising properties are critical for high-temperature ferritic stainless steels and specialised applications. It balances hardness and toughness without significantly reducing ductility [112].

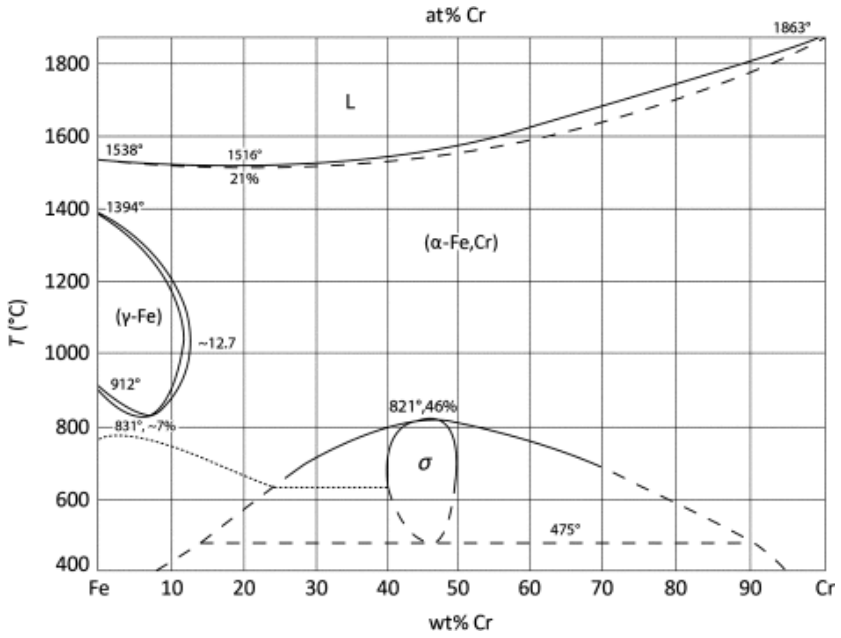

Fig. 3.3 Fe-Cr phase diagram [111]. Reprinted with permission from Elsevier.

Corrosion resistance: Cr is an essential element in stainless steels, imparting excellent corrosion resistance by facilitating the formation of a protective oxide layer on the surface. Depending on the environment, various Cr-enriched oxides can form. The primary types include $Fe_xCr_{3-x}O_4$

spinel and Cr_2O_3. Zhao investigated the structure of oxides formed on Fe-9Cr steel in high-temperature steam and found that Cr-enriched oxide primarily exists as spinel [113]. Additionally, Cr_2O_3 has been shown to enhance the corrosion resistance of steel in humid CO_2 atmospheres in Fe-Cr steels[114, 115]. This protective layer shields steel from aggressive environmental conditions, making it suitable for applications in chemical processing, marine environments, and medical devices [106].

The Cr content significantly influences which oxides form and their anti-corrosion properties. Diawara [116] developed a model to study the oxide layer on Fe-Cr steels, cross-verifying it with experiments. The findings showed:

1. At low Cr concentrations (<14%), oxide nuclei do not fully cover the alloy surface, resulting in metal corrosion.
2. At high Cr concentrations (>16%), the oxide layer grows uniformly, covers the entire surface, and reaches a stationary thickness of approximately 9 Å.
3. In the intermediate range (14−16%), a continuous transition occurs from incomplete passivation to complete passivation, where the passive film becomes enriched with higher Cr content.

For alloys with low Cr content, extensive iron dissolution is required to obtain passivation, leading to increased surface roughness. Oxidation creates vacancies in the alloy, which may form cavities at the oxide-metal interface or within the bulk of the alloy. In low-Cr alloys, these cavities coalesce, leading to passivity breakdown and pit initiation [116]. Further research on this topic supports these findings [117-119].

Temperature also has a significant influence on the mechanism of passivation, the chemical composition, and the structure of the passive layer. At lower temperatures (below 50 °C), the growth of the passive layer is governed by the high-field mechanism (high electric field) [120]. At higher temperatures, the oxide layer's initial growth is limited by a high electric field. Over

time, oxide layer growth is controlled by diffusion through the layer, as the electric field in the inner part decreases due to the increasing oxide thickness [121, 122].

Oxidation resistance: In high-temperature applications, Cr also enhances oxidation resistance by inhibiting the growth of surface oxides, thereby extending the operational lifespan of components exposed to elevated temperatures [123]. The selective consumption of Cr during oxidation leads to the formation of Cr_2O_3, which has a slow growth rate and acts as a barrier against further oxidation. This is due to the very low diffusion coefficient of oxygen and metals through chromia, providing excellent oxidation resistance[124, 125].

The formation of a protective Cr-rich oxide scale, Cr_2O_3, depends on the Cr concentration at the alloy/oxide interface and the Cr diffusion coefficient in the metallic substrate from [124]. To form an effective protective layer, a sufficiently high Cr content is required. However, this depends on operational temperatures and alloy properties, such as grain size and other alloying elements [126-128].

Adding appropriate amounts of Si and Mn can reduce the Cr content required for effective protection, thereby assisting with cost management [129-131]. At higher temperature (above 850 °C), "breakaway oxidation" may occur, characterised by the formation of other Cr-enriched oxides, such as $FeCr_2O_4$ spinel. This happens when Cr concentration and diffusivity are insufficient to sustain the continued growth of Cr_2O_3 [124].

3.1.2.3 Molybdenum (Mo)

Mo is incorporated into T91 steel for several key benefits:

High-Temperature Strength: Mo decreases the growth and coarsening of $Cr_{23}C_6$ particles, with its impact becoming more pronounced as the Mo content increases. As a reslut, a higher number of smaller $Cr_{23}C_6$ particles are present in the microstructure of 9Cr-Mo steels compared to 9Cr steels [132]. Chengru [133] observed that in TiC microparticle-reinforced steel, Mo enhances the contributions of dislocation strengthening, precipitation strengthening, and solution

strengthening by reducing dislocation annihilation and carbide coarsening. This improvement in microstructure directly enhances the steel's strength.

Enhanced Toughness: Mo segregates at grain boundaries, which reduces the concentrations of harmful elements like phosphorus (P) and sulphur (S). This improves grain boundary strength and enhances hot ductility. Han [134] noted that in the Mo-free steels, a lower ductility point occurs at 850℃, whereas this issue is eliminated in Mo-containing steels. The inclusion of Mo significantly improves the toughness of T91 steel, increasing its ability to withstand impact and dynamic loading. This toughness is critical for maintaining mechanical integrity in demanding operational environments [135].

Oxidation Resistance: The addition of Mo improves oxidation resistance by reducing the inward diffusion of oxygen and the outward diffusion of iron, thus accelerating the formation of a protective Cr oxide layer. Furthermore, Mo oxides can contribute directly to the formation of the protective oxide film, enhancing its resistance to oxidation [136, 137].

Corrosion Resistance: Mo is a commonly used alloying element to enhance the pitting resistance of steels in chloride or bromide solutions. It helps stabilize the passive protective layer formed on the steel surface [138, 139]. Heon [140] also reported that the addition of Mo reduces susceptibility to stress corrosion cracking by improving pitting corrosion resistance.

3.1.2.4 Silicon (Si)

Si plays an important role in steel, influencing both its microstructure and mechanical properties. Typically added in concentrations between 0.1% to 2%, its main effects are summarised below:

Influence on Mechanical Properties: Si affects the precipitation of secondary phases such as $M_{23}C_6$, MX, and Laves phases, which, in turn, impact the mechanical properties of steel [141]. It strengthens steel through two main mechanisms:

1. **Solid Solution Strengthening**: Si dissolves into ferrite, increasing the steel's strength and hardness[142].
2. **Grain Refinement**: Higher Si content refines the martensite in the steel, making it finer and more evenly distributed. This increases the grain boundary area between ferrite and martensite, raising resistance to dislocation movement and the stress required for deformation[143].

While Si enhances strength, higher concentrations (>1.5%) can reduce toughness. Therefore, careful optimisation of Si content is essential to maintain a balance between strength and ductility [102, 103].

Oxidation Resistance: Si improves the steel's resistance to high-temperature oxidation by forming a stable surface layer of SiO_2. This layer acts as a barrier, slowing the diffusion of oxygen and metal ions. This property makes Si-containing steels ideal for high-temperature applications such as boilers, heat exchangers, and furnace components [144, 145].

Enhanced Corrosion Resistance: Si also improves general corrosion resistance, especially in aggressive environments. Shaowu [146] compared the corrosion resistance of T91 steel with and without added Si. The results showed that Si slowed the diffusion of Fe while promoting the diffusion of Cr during oxidation, thereby enhancing the protective oxide film.

In stainless steels, Si contributes to improved resistance against acids and corrosive chemicals, making it valuable for producing durable materials for industrial applications [144].

Improved Creep Resistance: Si enhances the high-temperature performance of steel by improving creep resistance. Chengxu [147] found that at 550℃, Si additions promoted the formation of a small, dense, and discontinuous σ phase (Fe and Cr enriched phase) along grain boundaries. This inhibited intergranular cracking and extended the material's creep life. Additionally, Si increased the number of deformation twins in the alloy, improving its strength while maintaining plasticity.

Brittleness: Excessive Si can cause brittleness, particularly at higher concentrations [148]. Hu [143] reported that steels with 6.5 wt% Si had a significantly higher cracking sensitivity in the mushy zone compared to steels with 1.5 wt% Si. This was attributed to a wider high-temperature brittle region and a lower critical strain threshold for crack initiation.

3.1.2.5 LFR and LBEFR requirement for materials

Radiation and corrosion in LFR and LBEFR require materials that have adequate mechanical properties, dimensional stability, and corrosion/crack resistance over the operation temperature, dose, and stress range [149]. As we mentioned in section 2.2.1.2, LFR/LBEFR brings high requests for the structure materials due to its high corrosive property and potentially liquid metal embrittlement. As a fast reactor, the irradiation damage also needs to be considered. Austenite steels can be used for lower-radiation-dose ones while ferrite-martensite (F/M) steels will be used in high-dose situations due to their good resistance to void swelling under radiation [150].

3.1.3 T91

T-91, commonly known as 9Cr-1Mo, is a candidate steel for sodium and lead/LBE-cooled fast reactors. As a F/M alloy, it has excellent resistance to void swelling with radiation. T-91 has low thermal expansion, high thermal conductivity and a mature supply chain with ASME nuclear qualification [8]. Compared to martensitic steels with higher Cr contents, the ductile-brittle transition temperature shift of T-91 is lower, roughly -25 ℃ [9, 151]. The risk of brittle failure is reduced by lowering the ductile-brittle transition temperature [152].

T91 is proven to have a lath martensite structure with fine MX [M: Nb, V; X: C, N] carbonitrides and $M_{23}C_6$ [M: Cr, Fe, Mn, and Mo] carbides and high density of dislocation [153]. Large numbers of coarse precipitates were found along prior austenite grain boundaries (PAGBs) and fine precipitates within subgrain boundaries or matrix regions as shown in Fig. 3.4 [151]. Moreover,

the MX number decreasing can cause creep cavity formation and reduced rupture life. $M_{23}C_6$ coarsen and dislocation sub-structure boundaries are the main cause of creep damage [153].

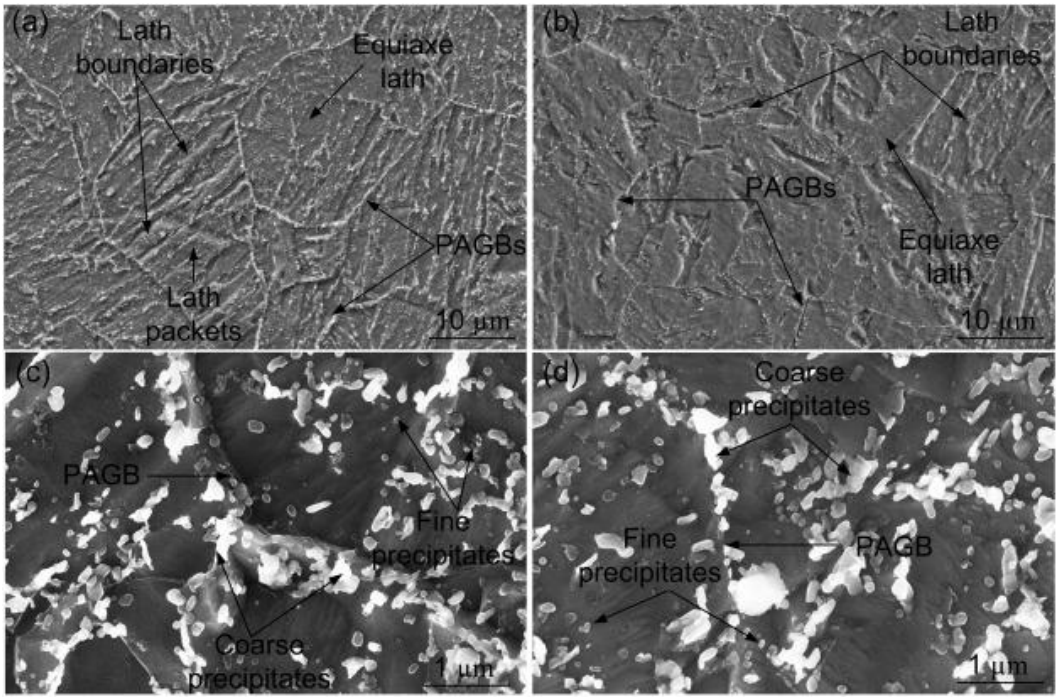

Fig. 3.4. Secondary electron micrograph of (a) and (c): T91 steel, (b) and (d): T92 steel [151]. Reprinted with permission from Elsevier.

3.1.4 Improvement of T91

3.1.4.1 HT-9

HT-9 is a ferritic/martensitic steel developed by the Sandvik Steel Corporation in Sweden. It has similar composition to T91 only the Cr is 3 wt. % higher than T91. HT-9 has been chosen as the cladding material for more than half of the major LFR and LBEFR concepts around the world and has been used in sodium-cooled US test reactors. It can withstand up to 200 dpa while retaining acceptable material properties [154]. HT-9 will form an oxide layer in liquid lead and LBE coolant which has two layers. The outer layer always consists of magnetite (Fe_3O_4) which is weak and

easily spalls off while the inner spinel iron-chromium layer ($(Fe_xCr_{1-x})_3O_4$) provides the main protective function [155].

3.1.4.2 Fe-Cr-Si alloys and Fe-Cr-Al alloys

Steel EP823 was designed in Russia specifically for usage in lead-bismuth. It is a 12 Cr ferritic/martensitic steel with elevated silicon levels (1–1.3 wt%) [149]. It has been found that Si can reduce the oxide growth rate at 500℃ [156]. Barbier compared different steels and found that in liquid LBE Si improves the oxidation resistance of steels. For example, EP823 has a thinner oxide layer than T91 in liquid LBE at 743 K [24]. Kurata [32] analysed the corrosion behaviours of 316 stainless steel, Si-enriched 316 stainless steel, T91, and Si-enriched T91 in oxygen-controlled LBE. The results show that the added Si can reduce the oxidation of 316 stainless steel under both low and high oxygen levels. And the ferritization of 316 stainless steel is also reduced. For T91, Si addition can reduce the corrosion when the oxygen content is higher but makes little difference with low oxygen content. Prince also presented, that with lower Si content (~4 wt. %), the strength and ductility of steel will be improved as long as the microstructure keeps the same [157].

Fe-Cr-Al alloys also show good anti-corrosion properties with the formation of a thin layer of Al_2O_3 on the surface [158]. However, Al adding may cause difficulty for welding. Fe-Al weld cladding is susceptible to cracking due to hydrogen embrittlement at elevated Al concentration [159].

3.2 Materials used in this thesis

T91 is a F/M steel purchased in the quenched and tempered condition (provided by Edelstahl Witten-Krefeld GmbH). The T91 material was sectioned by wire electrical discharge machining (EDM) to dimensions of 25 mm x 25 mm x 3-4 mm. All samples were produced from the same bar. One surface of each sample was polished to a mirror finish with the last step using 50 nm

alumina suspensions, while the opposite face was ground with 120 grit SiC paper. The composition specified by the manufacturer is listed in Table 3.1. APT analysis was conducted on the as-received T91. The average measured composition is reported in Table 3.1. For the most part, the measured composition agrees well with the nominal values. Deviations in the measured values are observed for V, C, N, P, and Nb. V exists in the steel incorporated into precipitates, mostly combined with nitrogen. In the nanoscale volumes inspected by the APT analyses only a few precipitates were sampled. However, in other APT analyses of the same or similar (with different heat treatment) material, large VN precipitates were observed as seen in Fig. 3.5. Similarly, Nb, P, and C are all predominantly associated with carbides as shown in Fig. 3.6.

Ultra-pure (99.999 wt %) lead and bismuth were purchased from Surepure Chemetals, Inc. and mixed according to a eutectic composition of lead (44.5 *at* %) and bismuth (55.5 *at* %).

Table 3.1: Composition from the certificate of the T91 material and APT-measured composition (wt %).

	Fe	**Cr**	**Mo**	**Si**	**Mn**	**Ni**	**V**	**Cu**
Nominal	88.01	9.44	0.96	0.35	0.51	0.28	0.20	0.14
APT	89.7	7.91	0.88	0.39	0.48	0.30	0.11	0.11
	C	**N**	**P**	**S**	**Al**	**Nb**	**Ga**	
Nominal	0.091	0.052	0.017	0.003	0.008	0.070	0	
APT	0.002	0.013	0.009	-	0.001	0.001	0.04	

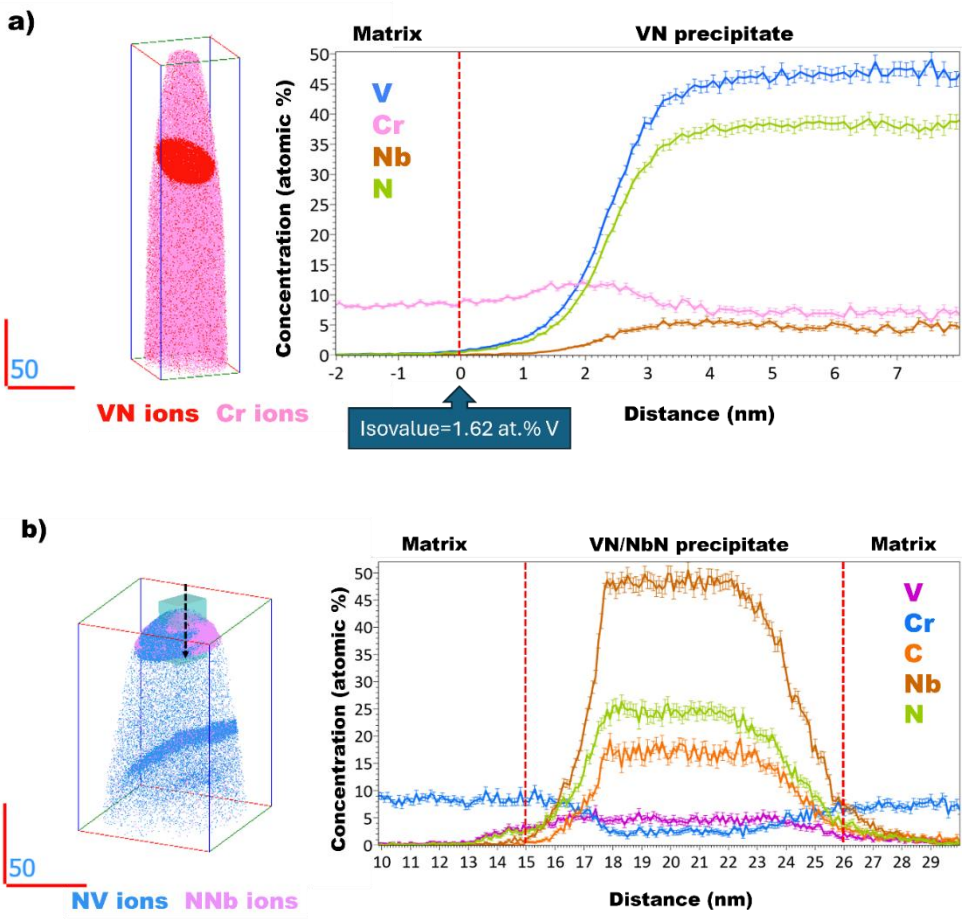

Fig. 3.5. Precipitates observed in as-received T91.

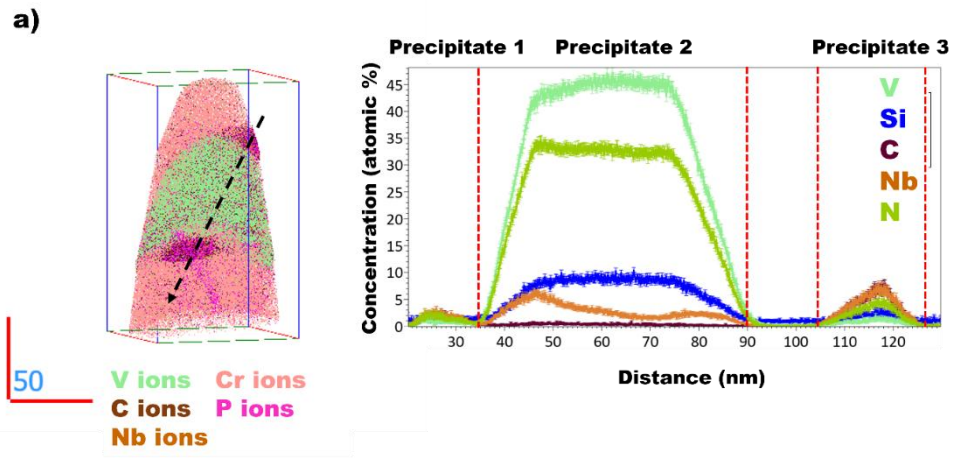

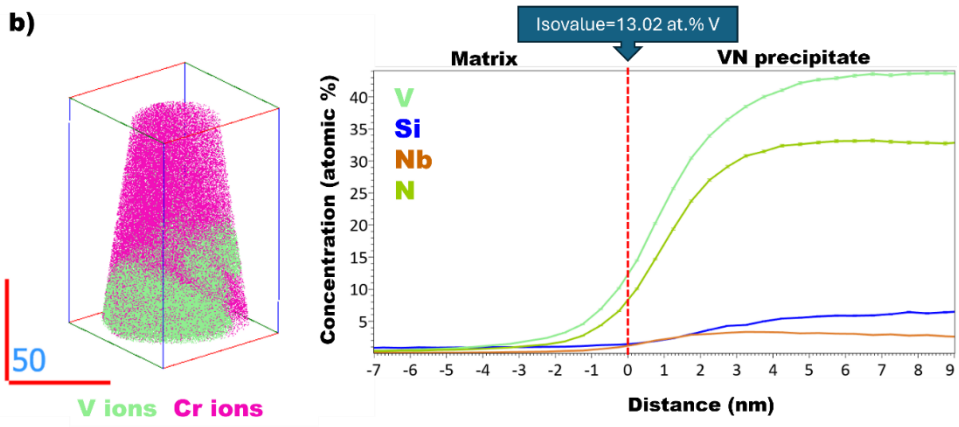

Fig. 3.6. Precipitates observed in as-received T91 with similar heat treatment.

3.3 Static corrosion test

T91 samples were lowered into liquid LBE for static corrosion using a Ti rod, to which they were attached with Mo wires. Two holes near the top edges of the samples were used to fix their orientation and ensure submersion in the LBE. The LBE was contained in 56 mm I.D. alumina crucibles from McDanel Advanced Ceramics Technologies. The crucibles were enclosed in a stainless steel autoclave, sealed by copper gaskets with knife edges, as shown in Fig. 3.7 (a). The autoclave defined the experimental volume with the controlled atmosphere. Details of the experimental configuration are provided elsewhere [160]. For researching the oxygen level influence on the corrosion, two environments were designed for the test: “oxidising” and “reducing” atmospheres. These terms are defined with respect to the potential for forming iron oxides.

For the reducing environment, argon and hydrogen used to control the oxygen content were purified and mixed to a hydrogen concentration of 0.25 % or 2500 ppm. The gas mixture was delivered to the autoclave to lower the oxygen potential during the corrosion testing. Moisture leaving the autoclave was measured and used to calculate the oxygen potential, using the known hydrogen concentration in the gas stream, since the oxygen potential was below the

measuring range of oxygen sensors. During the static corrosion testing, the moisture level in the outlet stream was around 2.5 ppm, and thus the hydrogen to moisture ratio around 1000. The corresponding oxygen potential was smaller than 10^{-26} atm, and falls between the equilibrium oxygen potential of Fe_3O_4 and $FeCr_2O_4$ at the testing temperature [160]. For the oxidising environment, the mixed gas stream was pumped through a water bath at a controlled temperature of 12 ℃ ± 0.1 ℃,providing a nominal inlet moisture concentration of 13,150 ppm for the oxidising atmosphere. The Ellingham diagram in Fig. 3.7 (b) shows the Ellingham diagram for experiments performed in this thesis, showing the temperatures and oxygen potentials for the oxidising and reducing atmospheres.

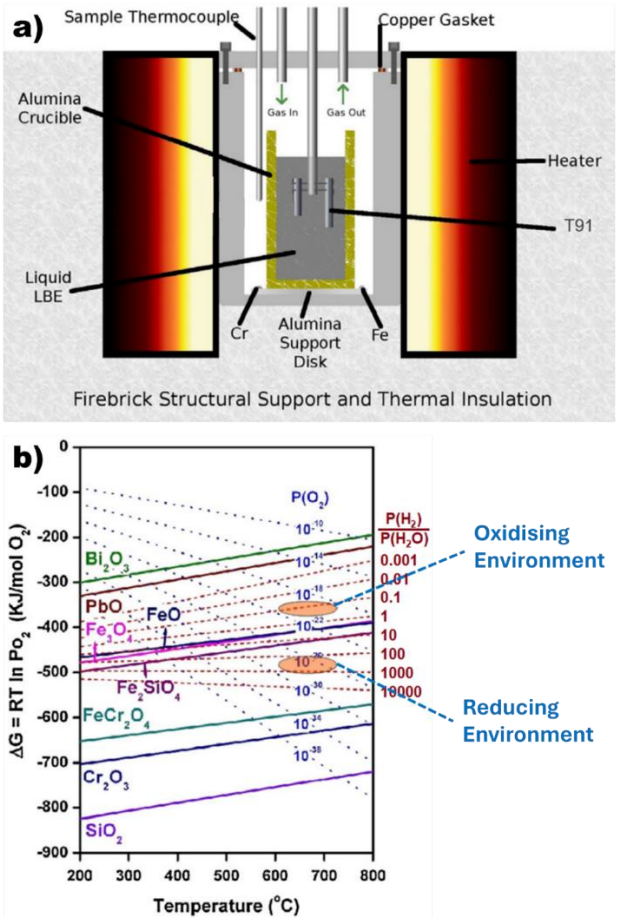

Fig. 3.7. Ellingham diagram for experiments performed in this thesis, showing the temperatures and oxygen potentials for the oxidising and reducing atmospheres. [160]. Reprinted with permission from Elsevier.

The temperature of the LBE was monitored with a K-type thermocouple positioned immediately outside the alumina crucible. The autoclave was heated by a cylindrical furnace (Mellen Company, Inc.) The autoclave was first heated up to around 400°C for around 12 hours to ensure the mixing of LBE and to allow the gas atmosphere to reach a stable state. Next, the autoclave was heated up to 715 °C, and the samples were inserted for different durations of 70, 245, and 506 hours, respectively. At the end of the exposure the samples were retracted and cooled down inside the furnace. The furnace was then shut down to allow the system to cool. It took around 18 hours to reach 40 °C. Samples were cleaned using acetone to remove organic impurities but were not cleaned to remove adhered LBE. They were then mounted in Bakelite in cross-section at 90 degrees to the original, LBE-exposed surface facing outside. The cross-section samples were then ground with SiC grinding paper to 2500 grit and polished with diamond polishing liquid to 1 μm. Colloidal 50nm silica polishing was the final preparation step.

3.4 Characterisation techniques

3.4.1 Methods introduction

3.4.1.1 Scanning Electron Microscopy (SEM)

How does SEM work: Electrons are emitted from the cathode and accelerated by a voltage ranging from 0.5 to 30 kV between the cathode and anode. This creates a small beam cross-section, called the crossover, near the anode, with a diameter of about 10-50 µm. However, this spot size is too large to produce a sharp image. To address this, the crossover is demagnified by a lens system, typically consisting of one or two condenser lenses and an objective lens, and focused on the specimen surface. Most SEMs can produce an electron beam with a spot size as small as 5-10 nm and an electron probe current ranging from 10^{-12}-10^{-10} A, This is sufficient to generate an image with a reasonable signal-to-noise ratio [161, 162].

Signals generated: When the beam electrons interact with the atoms of the specimen, they either elastically or inelastically scatter. The energy spectrum of the electrons emitted from the specimen includes secondary electrons (SE), backscattered electrons (BSE), and Auger electrons. SEs are produced by inelastic scattering of the beam electrons as they travel through the specimen, with most of them having energies between 2-5 eV. BSEs, on the other hand, primarily result from multiple scattering of the beam electrons within the specimen. The majority of BSE is due to multiple scattering of the beam electrons within the specimen. The energy spectrum of BSEs typically ranges from 50 eV to the accelerating voltage (E_o) [161]. In SEM images, areas with a high atomic number appear bright due to stronger backscatter, while areas with a low atomic number appear dark. Figure 3.8 illustrates the difference in signals that can be acquired using SEM.

As shown in Fig. 3.8 (b), for bulk samples, there is an interaction volume, which is the region within the specimen where the beam electrons travel and deposit energy [163]. One important aspect of the interaction volume is that increasing the accelerating voltage results in a deeper penetration depth and a larger primary excitation region, which can cause a loss of surface detail in the image [162]. The interaction volume increases with higher acceleration voltage and decreases with higher atomic number.

Applications: The widespread success of SEM over several decades can be attributed to its exceptional depth of focus, excellent image contrast, and relatively simple sample preparation for surface imaging. Additionally, when combined with x-ray microanalytical equipment, SEM enables local quantitative element analysis of specimens [161].

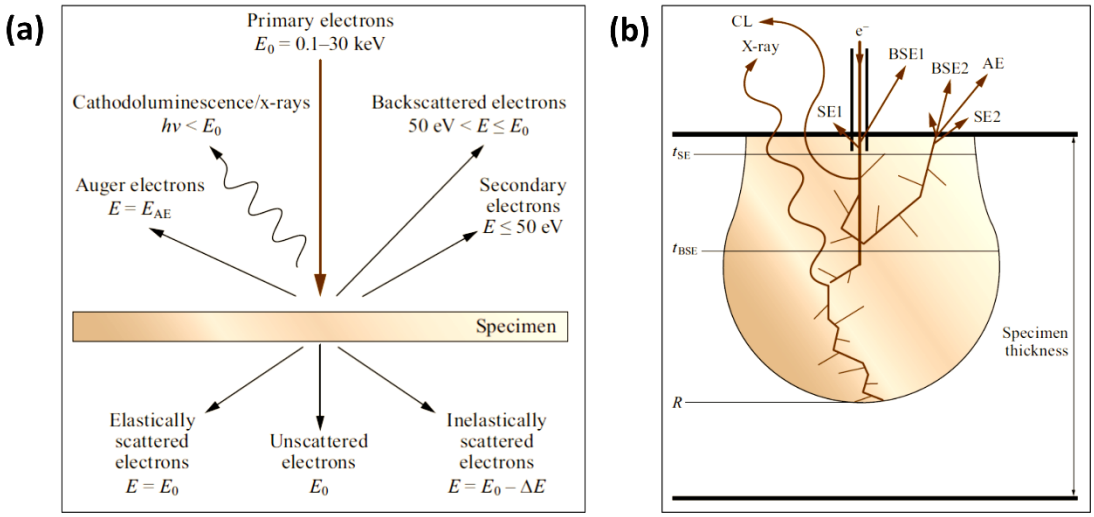

Fig. 3.8. (a) Schematic drawing of signals for a thin sample generated by the impinging electrons. (b) Schematic illustration of the generation of signals in a bulky specimen. t_{SE} and t_{BSE} indicate the escape depth for SE and BSE, respectively. R is the electron range [161]. Reprinted with permission from Springer International Publishing.

3.4.1.2 Energy Dispersive X-ray Spectroscopy (EDX)

How does EDX work: X-rays are generated either by the deceleration of electrons (resulting in x-ray continuum or Bremsstrahlung) or by an electron transition from a higher energy state to fill a vacancy in a lower electron shell, producing characteristic x-ray lines. These characteristic x-rays provide a "fingerprint" of the elemental composition of the sample [161]. The x-ray spectrum consists of peaks at discrete energies, which are superimposed on the continuous x-ray spectrum. The positions of these peaks are independent of the energy of the incident electrons. When a high-energy electron ejects an electron from an inner shell, it is replaced by an electron from an outer shell, creating a characteristic x-ray (or Auger electron). The intensity of the x-rays increases with the atomic number of the element and depends on which inner electron shell is involved. X-ray lines are classified by the shell where the ionization occurred, such as K-shell, L-shell, M-shell, etc. The quantum energies of these lines follow Moseley's law

[161, 164]. Figure 3.9 shows an example of EDS spectra excited at both 5 kV and 20 kV beam voltage on SiO_2 spherical nanoparticles on a titanium substrate [165].

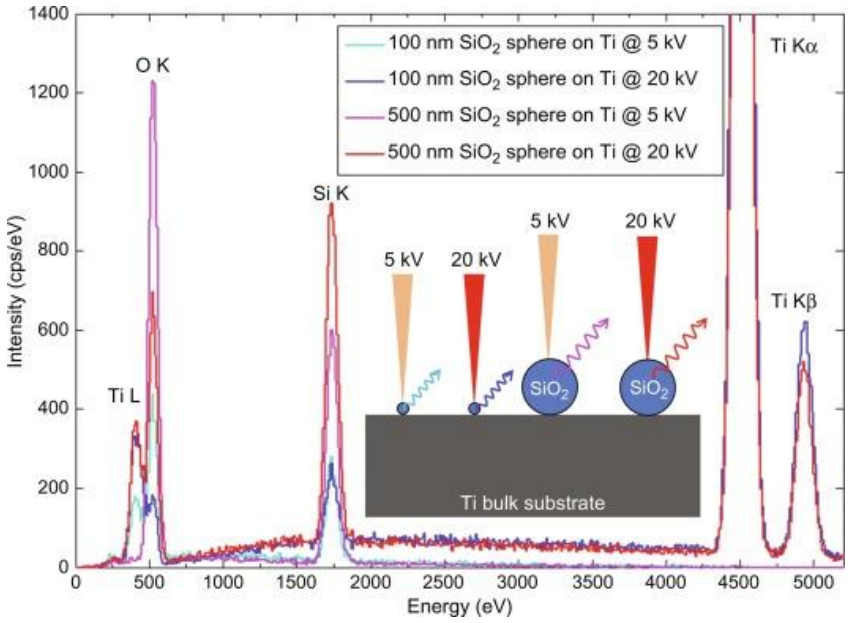

Fig. 3.9 EDS spectra excited at both 5- and 20-kV beam voltage on SiO_2 spherical nanoparticle on a titanium substrate [165]. Reprinted with permission from Elsevier.

How to use EDX for chemical analysis: The peak energies in an EDX spectrum provide qualitative information about the elements present in the sample. The intensity (height) of these peaks offers quantitative data regarding the elemental composition. Spectra can also be used to track changes in the concentration of specific elements. With proper corrections and calibration standards, EDX spectra can be used to calculate the weight percentage (wt. %) or atomic percentage (at. %) of compositional elements [166].

Benefits: EDX offers fast and straightforward elemental analysis. It can be used alongside imaging techniques such as SEM and TEM, providing spatially resolved composition data [167].

Drawbacks: EDX has limited sensitivity for light elements (e.g., hydrogen, lithium) and lower resolution compared to the primary imaging technique (SEM or TEM). Additionally, EDX spectra can suffer from peak overlaps, which may complicate the analysis [168].

3.4.1.3 Electron Backscatter Diffraction (EBSD)

How the EBSD works: EBSD patterns capture the angular variation of BSE intensity [169]. As described in section 3.4.2.1, beam electrons interact with the specimen and scatter both elastically and inelastically. These scattered electrons travel in all directions within the excitation volume, and this scattering process can be treated as a small electron source within the crystalline specimen, emitting electrons in all directions. Some of these electrons may be diffracted by parallel lattice planes, following Bragg's law. The resulting EBSD pattern, which includes Kikuchi lines, provides local information about the crystalline structure within the excitation volume [161, 169, 170].

The EBSD patterns are recorded on a scintillator screen placed near the specimen in the SEM chamber. A large capture angle (>70°) is required to collect sufficient data. Specimens are typically tilted at a high angle (around 70°) to increase the BSE yield and reduce energy loss [171]. Figure 3.10 shows the EBSD setup and an example of a Kikuchi pattern [161].

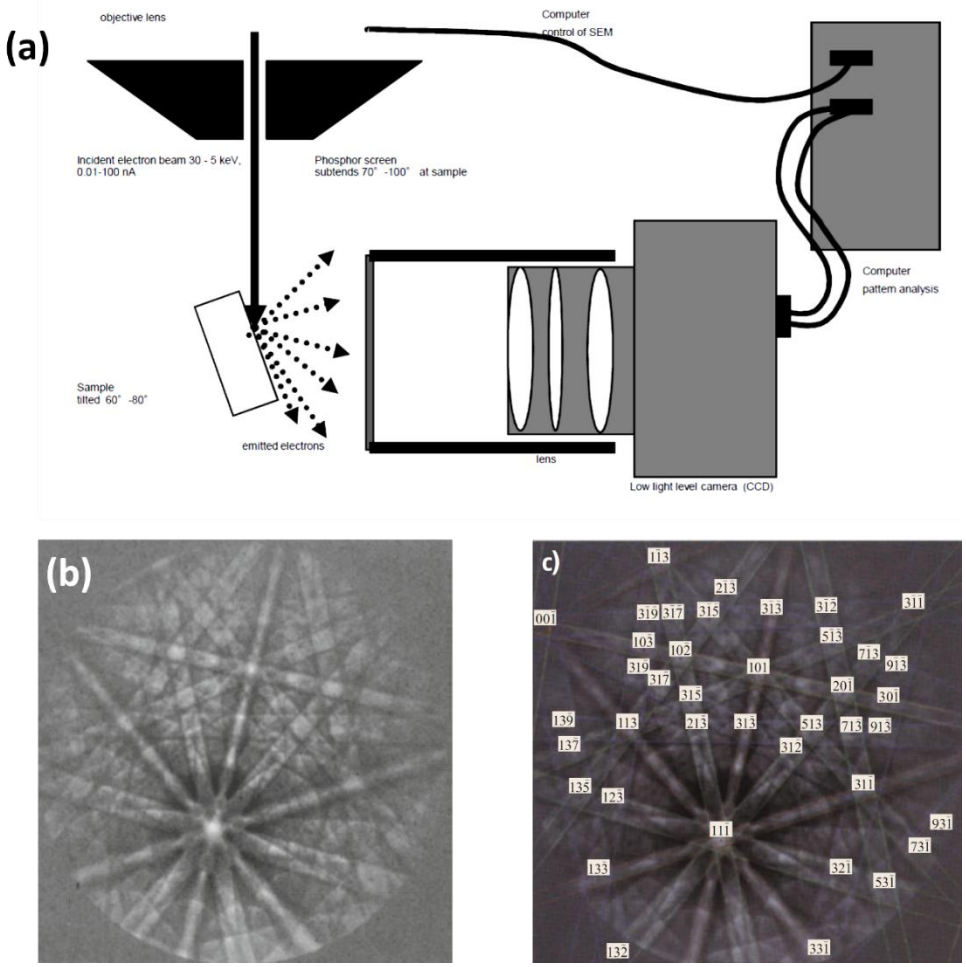

Fig. 3.10. (a) Schematic drawing of EBSD equipment set up. ESBD patterns from an as-cast niobium specimen: (b) High-resolution EBSD pattern with background subtraction. (c) EBSD pattern from (a) with pairs of Kikuchi lines generated by automatic indexing [161]. Reprinted with permission from Springer International Publishing.

Information provided: EBSD has become a powerful tool for crystallographic analysis, including the determination of individual crystallite orientations in polycrystalline materials within the SEM, phase identification, and the characterization of grain boundaries [172]. Figure 3.11 demonstrates the use of EBSD to analyse the austenite-to-ferrite transformation in austenitic stainless steels caused by dissolution corrosion when in contact with liquid Pb-Bi eutectic [173].

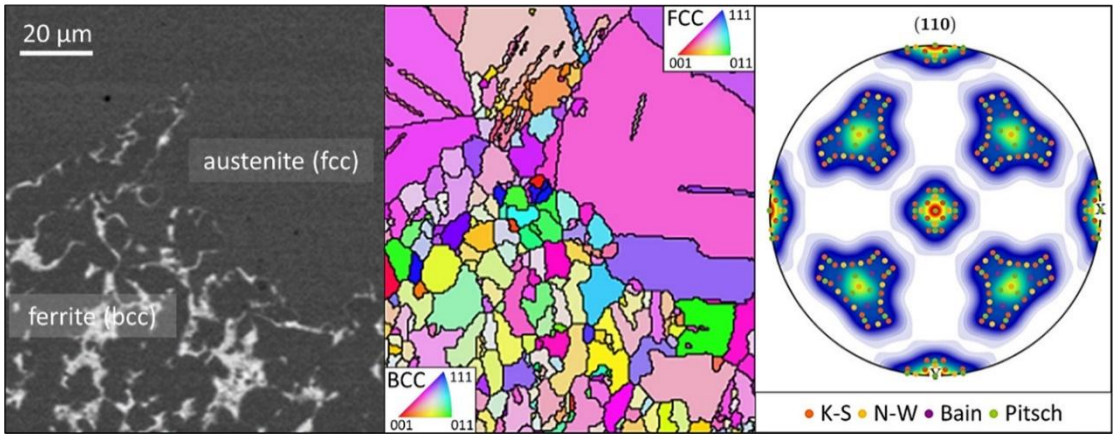

Fig. 3.11. EBSD in analysing the austenite-to-ferrite transformation in austenitic stainless steels due to dissolution corrosion in contact with liquid Pb-Bi eutectic [173]. Reprinted with permission from Elsevier.

Benefits: EBSD provides the ability to select specific features of the microstructure for orientation analysis, and it can be used to investigate grain boundary misorientations and boundary plane types. These types of analysis cannot be performed using macroscopic X-ray or neutron diffraction techniques. Compared to TEM-based methods, EBSD is advantageous because it allows measurements to be made on bulk specimens that are easier to prepare, handle, and orient relative to external reference axes, such as extrusion or rolling directions [171].

Drawbacks: The standard metallographic processes of sectioning, grinding, and polishing are required as initial steps. However, extra care must be taken during the final polishing to ensure that the sample surface is free of any sectioning damage. This is crucial because the EBSD pattern is generated from a very thin surface layer (~40 nm) of material [174]. Therefore, EBSD is sensitive to the surface finish.

3.4.1.4 Transmission Kikuchi Diffraction (TKD)

The link between TKD and EBSD: TKD is a recent and innovative advancement in EBSD. It uses ultrathin, TEM-like specimens to achieve much higher spatial resolution, allowing crystallographic analysis at resolutions as fine as 10–20 nm within a SEM [161].

In contrast to conventional EBSD, which is commonly used to analyse ultrafine-grained metals and alloys with grain sizes down to the sub-micron scale, TKD addresses key limitations, particularly in spatial resolution. EBSD typically provides a resolution of about 20 nm for dense materials and 50 nm for lighter materials like magnesium and aluminium. However, these resolutions apply only along the sample tilt axis. The technique requires samples to be tilted at a high angle (usually 70°), which reduces spatial resolution by about three times along the tilted surface. This limitation makes EBSD less suitable for routine analysis of nanostructured materials [161].

TKD overcomes these issues by using transmitted electrons for diffraction instead of backscattered electrons. The technique involves a special holder for ultrathin samples, enabling precise study of nanoscale structures in a SEM. This capability allows for routine crystallographic characterization of materials with nanoscale grains, surpassing the limitations of conventional EBSD [175].

There are two main types of TKD: Off-Axis TKD and On-Axis TKD. Both use thin specimens and produce Kikuchi diffraction patterns, but they differ in their setup, the orientation of the electron beam, and the resolution they can achieve [176].

Why on-axis:

In EBSD, the sample is tilted approximately 70° away from the incident beam to capture the maximum intensity of backscattered electrons that form Kikuchi patterns. In TKD, however, Kikuchi patterns are generated by forward-scattered electrons, which have their highest intensity near the incident beam, below the electron-transparent sample. Using EBSD hardware

for TKD results in Kikuchi pattern acquisition far from the pattern center, leading to limited diffracted intensity and significant gnomonic distortion [176].

Advantages of On-Axis TKD Over Off-Axis TKD [176]:

On-axis TKD provides several key advantages over off-axis TKD due to its improved sensitivity to beam and geometric parameters and its ability to capture Kikuchi patterns with higher intensity. These advantages make it a better choice for various applications:

1. Enhanced Sensitivity and Pattern Intensity

Higher Pattern Intensity: On-axis TKD captures Kikuchi patterns with much greater intensity compared to off-axis TKD. This is because forward-scattered electrons produce their strongest patterns near the incident beam, directly beneath the electron-transparent sample.

Beam Parameter Optimization: The higher pattern intensity allows for lower beam currents or faster acquisition rates without sacrificing pattern quality. This improves throughput and reduces sample damage during analysis.

2. Improved Spatial Consistency

On-axis TKD is less affected by variations in working distance or detector distance, resulting in stable performance across different experimental setups. Unlike off-axis TKD, which is prone to beam alignment and drift issues, on-axis TKD provides reliable resolution for extended mapping tasks. While the spatial resolution of on-axis TKD is comparable to off-axis TKD under similar conditions, on-axis TKD maintains consistent resolution over large areas, even during longer acquisition times or minor beam fluctuations.

3. Reduced Distortion

In off-axis TKD, patterns are captured far from the centre due to the oblique detector alignment, resulting in lower diffracted intensity and severe gnomonic distortion in the Kikuchi patterns. In

contrast, on-axis TKD aligns the detector to the region of highest electron intensity, enhancing the quality and interpretability of the Kikuchi patterns, as illustrated in Figure 3.12.[176].

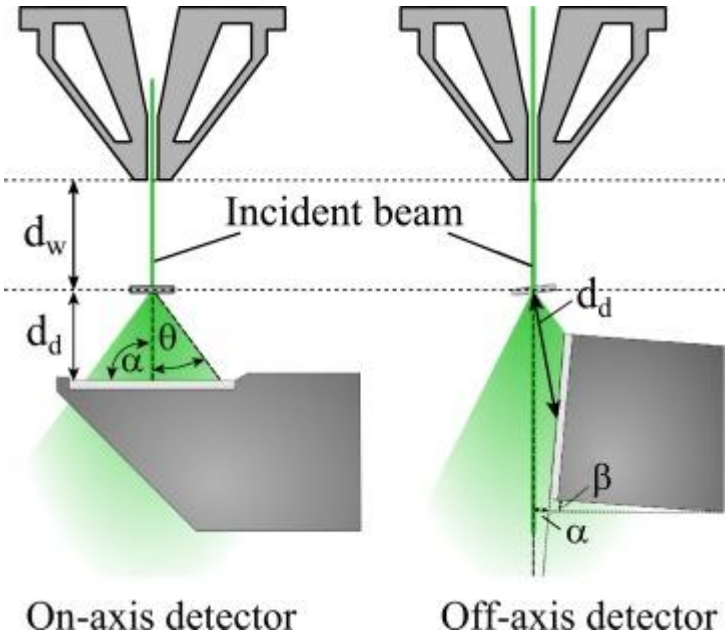

Fig. 3.12. Schematic of beam–specimen interaction and chamber geometry for On-axis TKD and Off-axis TKD [176]. Reprinted with permission from Elsevier.

4. Suitability for Large-Area Analysis

On-axis TKD is highly suitable for large-area analysis due to its robustness against beam drift and its ability to consistently achieve high resolution across extensive areas, making it ideal for comprehensive material characterization. In contrast, off-axis TKD, while functional, struggles to maintain stability and resolution over similar scales. Figure 3.13 illustrates an application of on-axis TKD in studying oxide formation on steel corroded in high-temperature steam, a critical area of research for future reactor designs [113].

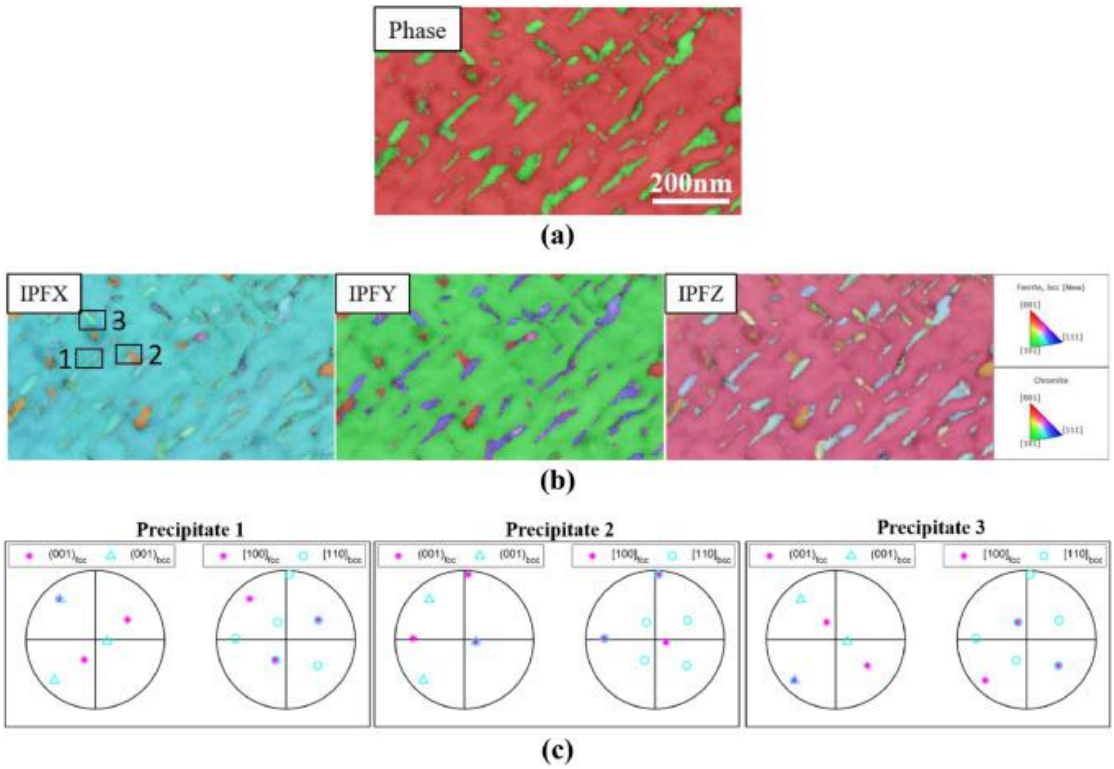

Fig. 3.13. TKD analysis on the internal oxide layer (step size=5 nm) (a) Phase map (red and green pixels represent metal matrix and oxide precipitates, respectively); (b) IPF maps with orientation triangle legends; (c) pole figures of the three selected oxide precipitates with their surrounding metal matrix. [113]. Reprinted with permission from Elsevier.

In conclusion, on-axis TKD surpasses off-axis TKD in several key aspects, including pattern quality, intensity, spatial consistency, and resilience to experimental variability. These advantages make on-axis TKD a more effective and versatile tool for high-resolution crystallographic analysis, especially in demanding applications such as large-area mapping and nanoscale material characterization.

3.4.1.5 Geometrically Necessary Dislocation (GND) Calculation

How GND works: The lattice curvatures obtained from EBSD can be linked to a continuous distribution of GNDs, through the dislocation tensor, as described by the geometrical

constructions developed by Nye [177] and Kroner [178]. GNDs are dislocations that accommodate strain gradients in crystalline materials, arising from factors such as deformation, grain boundaries, or local heterogeneities. EBSD provides high-resolution crystallographic orientation maps, which resolve the orientation of each grain or sub-grain within a material. Since GNDs accommodate local variations in crystal orientation, their density can be inferred by calculating orientation gradients within the material. Using EBSD data, local lattice curvature and strain gradients can be quantified, allowing for the estimation of GND density [169, 174, 179].

Conventional Hough-based EBSD analysis has relatively low sensitivity, often leading to issues such as high noise levels that obscure important features in the dislocation structure or requiring larger step sizes to reduce noise. In contrast, higher-angular-sensitivity cross-correlation-based analysis of EBSD patterns significantly reduces noise while maintaining high spatial resolution. With this method, GND densities can be determined with much higher accuracy, achieving $\pm 10^{12}\ m^{-2}$ at 200 nm step size [179].

Applications: GND analysis is widely used to investigate material strain properties, with many applications in material science. Two notable examples include:

Creep behaviour of metals: Creep is a critical property to consider when selecting structural materials for reactor plants. GND analysis plays an essential role in understanding this behaviour. For instance, Soran [180] studied dislocation behaviour and GND development in a nickel-based superalloy during creep. The study highlighted variations in GND density between soft and hard grains and the impact of neighbouring grain orientation on local dislocation density. Figure 3.14 illustrates an example of these findings [180].

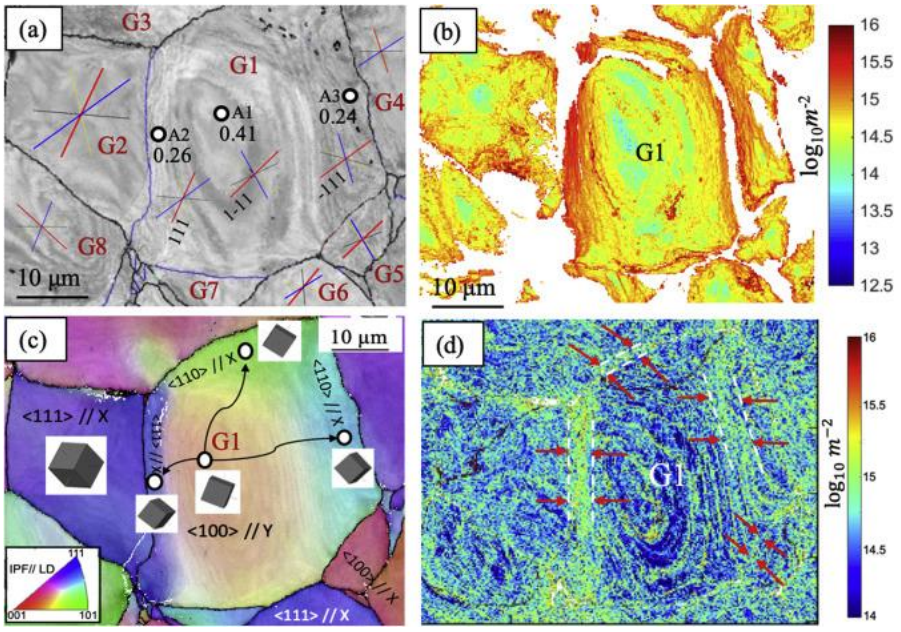

Fig. 3.14. HR-EBSD map for the indicated area. Cross correlation method for GND calculation is applied the sample after creep test at 800 MPa/700 °C. (a) Bruker images qualify (IQ) map. (b) GND map using cross correlation method for the same area in (a). (c) Magnified area of EBSD-HKL derived IPF//LD map. (d) Magnified GND map [180]. Reprinted with permission from Elsevier.

Recrystallization: Recrystallization is a common metallurgical phenomenon that occurs during heat treatment or operational cycles involving temperature changes. GND analysis is a valuable tool for characterizing strain changes across different phases [179]. For example, Shubo [181] studied the influence of strain states on the recrystallization of 316L stainless steel and explored the relationship between GND density and strain. The research determined the threshold of GND density required to trigger recrystallization, as illustrated in Figure 3.15 [181].

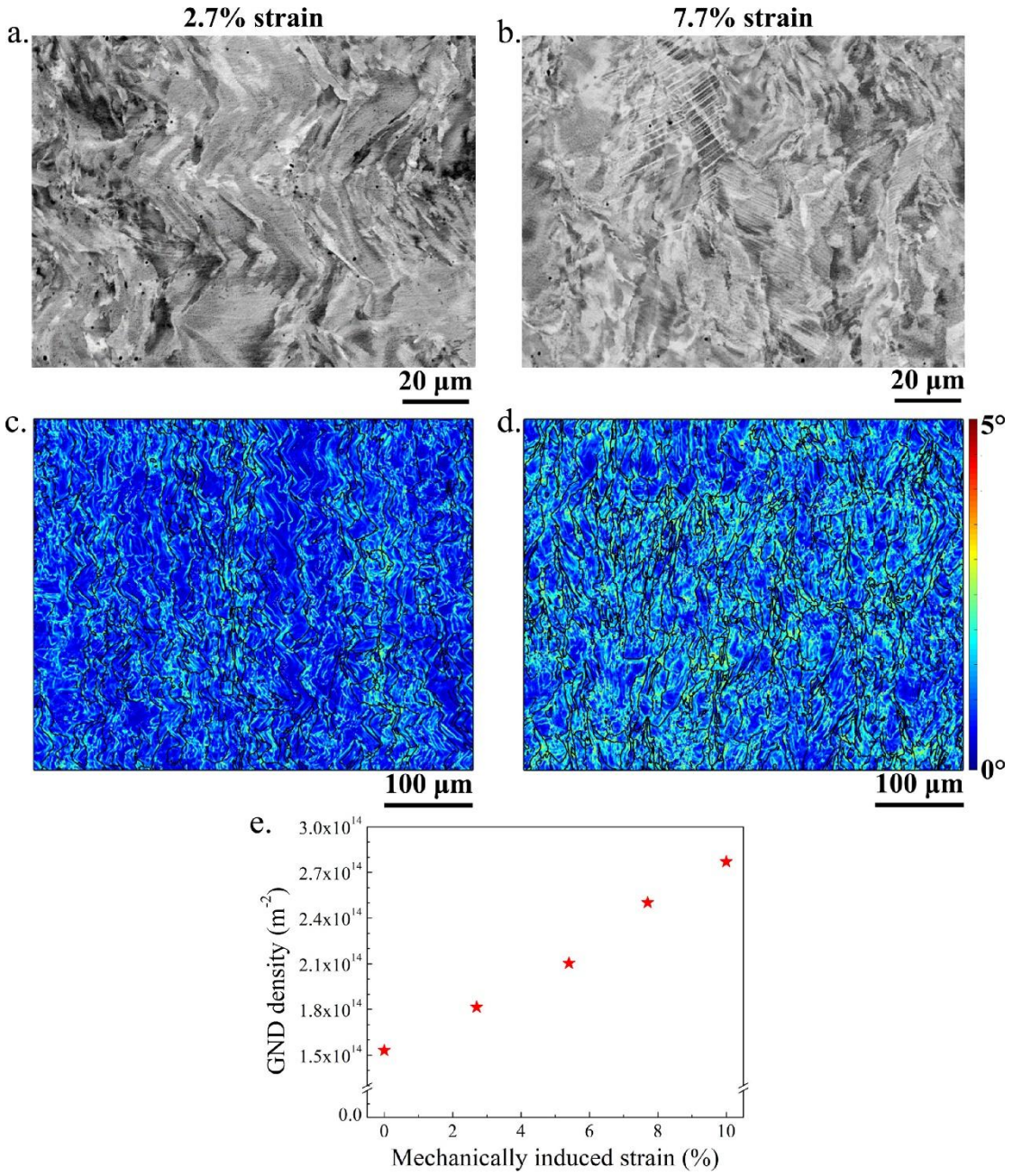

Fig. 3.15. Deformed 316L SS microstructures: (a) and (b) BSE micrographs and (c) and (d) corresponding Kernel Average Misorientation maps of samples deformed up to 2.7% and 7.7% strains, respectively. (e) Estimated average GND density as a function of plastic strain [181]. Reprinted with permission from Elsevier.

3.4.1.6 Scanning Transmission Electron Microscopy (STEM)

How STEM works:

In transmission electron microscopy, the two primary imaging modes are TEM (Transmission Electron Microscopy) and STEM. Beyond these, several advanced techniques have been developed, including Electron Holography [182], Differential Phase Contrast (DPC) [183, 184], and the rapidly evolving 4D-STEM technology [185]. Routine aberration-corrected TEM generally achieves a resolution of 1 Å, while non-corrected TEM typically provides resolutions of 2 Å or higher. SEMs, by comparison, usually operate at resolutions ranging from a few nanometres to about 1 nm [161].

In TEM mode, electrons emitted from the electron gun pass through the condenser lens system and the upper pole piece of the objective lens, forming parallel or nearly parallel beams that interact with the sample. After passing through the sample, the exit wave is magnified by the objective lens, projector lenses, and other magnetic lenses, creating an image on a fluorescent screen or electron detector [161].

STEM, however, operates differently. In STEM mode, the electron beam from the gun is accelerated and passed through the condenser lens system, forming a convergent beam that illuminates the sample. The beam is scanned across the sample using deflection coils. As the convergent beam interacts with the sample during scanning, electrons scatter, and detectors positioned in the diffraction plane collect the scattered electrons [186, 187]. Fig. 3.16 illustrates the differences in how STEM and TEM focus on the specimen.

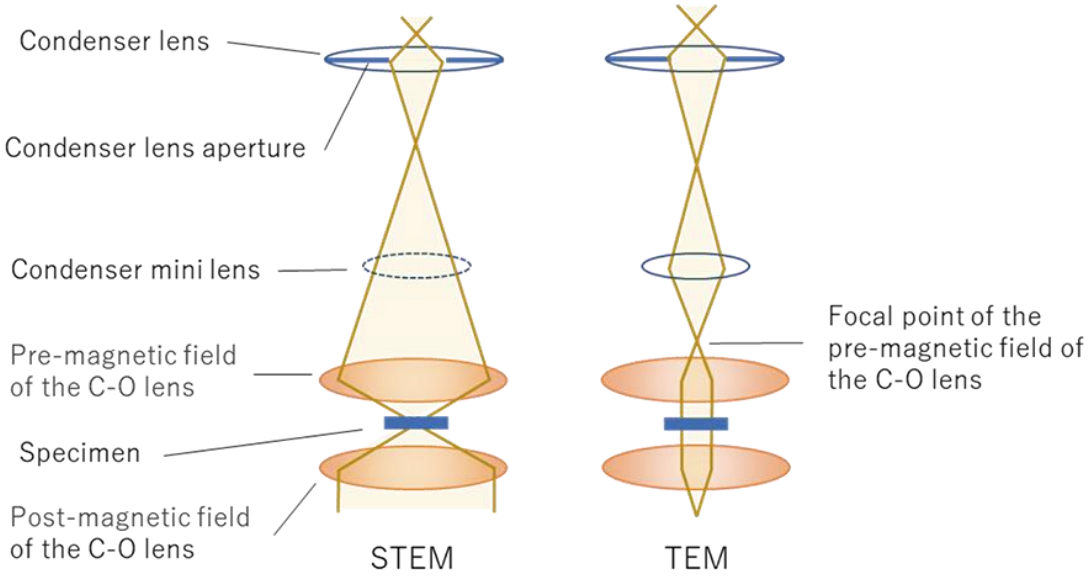

Fig. 3.16. Left: Ray path of the STEM mode using the C-O lens. Right: Ray path of the TEM mode, where the parallel beam is produced on the specimen using the condenser-mini lens [188]. Reprinted with permission from JEOL.

Image methods:

In STEM mode, the contrast of the sample is determined by the collection angle of the detector. STEM imaging is categorized based on the angular range of the collected electron signals and their relationship to the convergence angle. Based on this classification, STEM imaging is divided into Bright Field (BF), Annular Bright Field (ABF), Annular Dark Field (ADF), and High-Angle Annular Dark Field (HAADF) modes [161, 187].

Bright Field (BF) and Annular Bright Field (ABF):

In BF and ABF modes, images are formed by collecting signals at angles no greater than the convergence angle of the electron beam. Most transmitted electrons fall within this angular

range, resulting in strong signals. These modes are particularly effective for resolving lighter elements, as they scatter electrons more weakly compared to higher-angle signals.

Annular Dark Field (ADF):

Annular Dark Field (ADF) images are formed by collecting signals within an angular range of approximately 15 mrad (lower bound) to 50 mrad (upper bound). The contrast in ADF images is primarily based on medium-angle scattering, providing a different perspective of the sample's structure compared to BF and ABF modes.

High-Angle Annular Dark Field (HAADF):

HAADF images are formed using signals collected at angles with a lower bound around 50 mrad and an upper bound extending beyond 200 mrad. These images typically offer better spatial resolution but weaker signals. HAADF is particularly sensitive to heavy elements, as heavier atoms scatter electrons to higher angles more effectively, leading to enhanced contrast for these elements.

Electron Energy Loss Spectroscopy (EELS) and EDX in STEM:

STEM's capabilities extend beyond imaging elastic and quasi-elastic scattering phenomena. One of its key strengths is its ability to perform detailed analytical characterization, allowing researchers to gain valuable insights into a sample's chemistry, electronic structure, and elemental composition. Two highly effective analytical techniques commonly used in STEM are EELS and EDX [161].

EELS [189, 190]:

Principle: EELS examines electrons that have undergone inelastic scattering within the sample. These electrons lose energy due to interactions with the sample's atoms, such as the excitation of electrons to higher energy states or lattice vibrations.

Output: The result is a spectrum of scattered electrons, displaying the number of electrons as a function of their energy loss.

Key Features: EELS is sensitive to light elements (e.g., elements with atomic number Z < 11) and provides information on transitions and bonding states of transition metals and rare earth elements. It offers high energy resolution (better than 1 eV) and can achieve collection efficiencies up to 50% due to the focused trajectory of electrons. EELS is ideal for local compositional analysis because of its small probe size and thin sample requirements. However, it has a limited spectral range (~2 keV energy loss).

EDX [161]:

Principle: EDX detects x-ray photons emitted when an electron from a core shell is excited by the STEM's electron beam and is subsequently replaced by an electron from a higher shell. The energy of these emitted photons is characteristic of the elements present.

Output: The result is an x-ray emission spectrum, which identifies elements by their characteristic photon energies.

Key Features: EDX has a wider spectral range, detecting elements with excitations up to 20 keV, and is effective for a broader range of elements, including heavier ones. It offers lower energy resolution (100–150 eV compared to EELS) and has relatively lower collection efficiency (~1%) due to isotropic x-ray emission. To compensate for this reduced efficiency, EDX requires a high probe current (~1 nA) and a larger probe size. The concluded difference between EELS and EDX is listed in Table 3.2.

Table 3.2. The key differences between EELS and EDX in STEM.

Feature	EELS	EDX
Analysed Signal	Inelastically scattered electrons	X-ray photons emitted after core excitation
Sensitivity	High for light elements (Z < 11)	High for heavier elements
Energy Resolution	Better than 1 eV	100–150 eV
Spectral Range	Up to ~2 keV	Up to ~20 keV
Collection Efficiency	Up to 50%	Around 1%
Spatial Resolution	Higher due to small interaction volume	Lower due to isotropic x-ray emission
Probe Current	Lower (smaller beam size)	Higher (~1 nA required)

Applications:

EELS is preferred for analyzing chemical bonding, oxidation states, and light elements (e.g., H, Li, B).

EDX is better suited for detecting a wide range of elements across the periodic table, particularly heavier elements, and for general compositional analysis.

By combining EELS and EDX in STEM, researchers can achieve comprehensive elemental and chemical characterization with complementary strengths. Fig. 3.17 shows an example of using EELS and EDX to study the interface of corroded T91 in liquid lead-bismuth eutectic (LBE) [191].

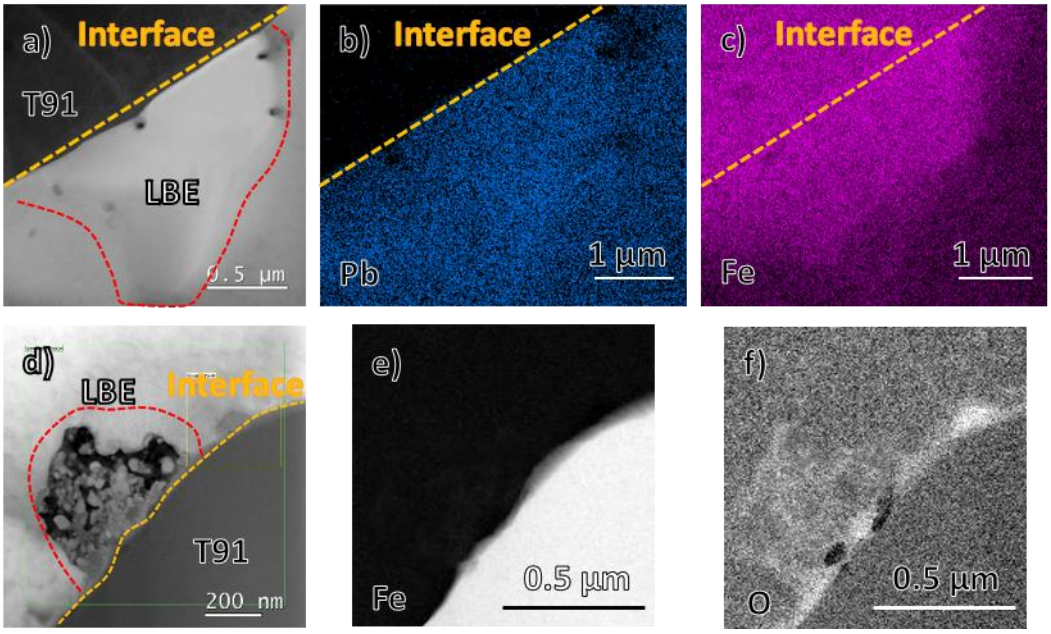

Fig. 3.17. STEM investigation of two regions with interface of T91 and LBE included. (a) STEM HAADF image. (b) and (c) show the EDX maps of Pb and Fe respectively. (d) STEM HAADF image. (e) and (f) show the EELS maps of Fe and O respectively [191]. *Reprinted with permission from Elsevier.*

3.4.1.7 Atom Probe Tomography (APT)

How APT works: APT involves the field evaporation of atoms from a sharp, needle-shaped sample under an electric field. Field evaporation is a process where surface atoms are polarized by a high electric field and are pulled away from the surface, with one of their electrons drained into the surface. The ion, now created, is accelerated toward the detector screen due to the high surrounding voltage. By calculating the mass-to-charge ratio using the detected time of flight and the known flight path, the chemical identity of each detected ion can be determined [192].

Using the identified atoms, the recorded sequence of evaporation, the voltage used to evaporate each atom, and the position of each atom on the detector, researchers can

reconstruct the sample [193]. The process assumes a uniform atom-by-atom, layer-by-layer evaporation of ions across the sample's surface.

What can be measured: APT provides 3D chemical mapping of materials at the atomic scale, offering precise insights into small-scale chemical composition and structure [193]. It can detect very low concentrations of additions or impurities [194], such as radiation-induced atomic-scale solute clustering, precipitate interface chemistry, and precipitates formed after aging [195]. Meanwhile, APT is helpful to research on the element segregation either in phases or grain boundaries [196], and it can map chemical species in nanostructures, like those found in semiconductors [197].

Just like TEM samples, specific features in a sample can be extracted for APT analysis with the help of FIB and SEM. For instance, using a FIB/SEM equipped with EBSD and TKD detectors, grain boundaries can be selected and converted into samples for analysis [198]. Fig. 3.18 illustrates the process of using TKD to position a grain boundary inside a sample [198]. Fig. 3.19 shows how APT works and the information it provides [193]. Additionally, combining APT with TEM to investigate radiation and corrosion is a powerful method for studying fine structures such as defects and grains [113].

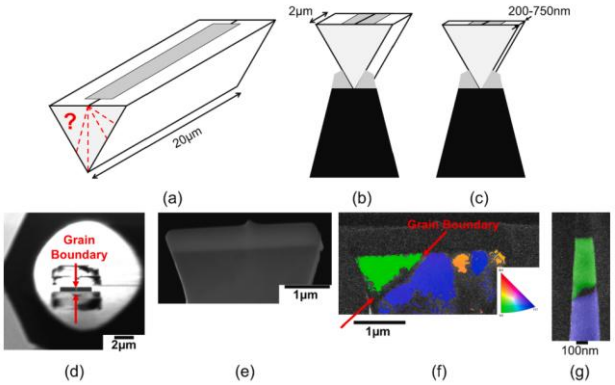

Fig. 3.18. Schematic diagram of (a) lift-out bar with grain boundary (b) lift-out section on a micro tip (c) thinned to 200-750 nm in thickness (d) (e) SEM view of the top and side lift-out section (f) TKD of the section (g) the final needle [198]. Reprinted with permission from Elsevier.

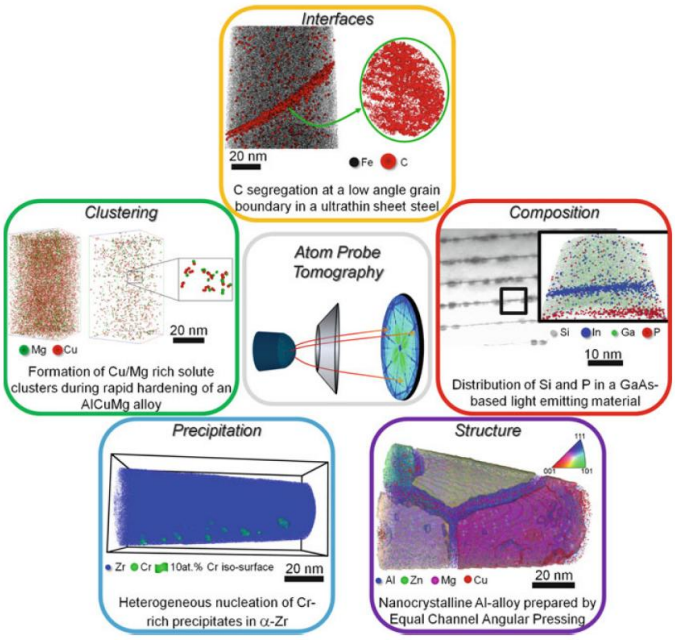

Fig. 3.19. Typical applications of APT in materials science and engineering [193]. Reprinted with permission from Springer New York.

3.4.1.9 Differential Aperture X-ray Microscopy (DAXM)

How DAMX works: The experimental setup for sub-micrometre resolution, three-dimensional X-ray microscopy using DAXM technique on the UNI-CAT Sector-34 undulator beamline at the APS is shown in Fig. 3.20 [199-201]. A polychromatic (white) X-ray beam enters from the right. The monochromator system is designed to either pass the white beam directly or reflect a monochromatic beam from the lower part of the undulator beam (with double (111) Si crystals) onto the Kirkpatric–Baez (K–B) focusing mirrors. These K–B mirrors are differentially coated to create an elliptical focusing figure, producing X-ray microbeams with a diameter of $\sim$0.5 μm and an approximate 0.5 mm depth of field at the sample position [202]. The CCD detector, positioned at 90° to the incident beam, collects diffraction patterns in this microdiffraction technique. Since the X-ray beam has penetration depth on the order of 10s to 100s of um. Given that the X-ray

beam has a penetration depth on the order of tens to hundreds of micrometres, the detector records the cumulative diffraction patterns along the entire path of the X-ray beam. To achieve micron spatial resolution along the penetration direction, it is necessary to depth resolve the diffraction patterns for each micron [200].

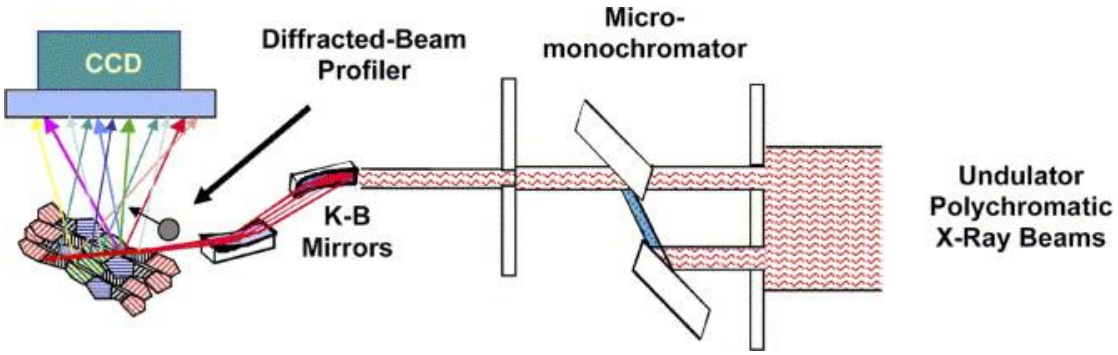

Fig. 3.20. Schematic depiction of a 3D X-ray structural microscope layout [200]. Reprinted with permission from Elsevier.

Since the diffraction patterns contain an angular cross-fire of approximately 45° or larger, profiling the diffraction patterns requires a micron-resolution aperture with an angular acceptance of 45° or more. Hard X-ray slits with a one-micron opening and approximately 10 μm thickness for attenuation would only pass about a 6° angular range. To overcome this limitation, a 50 µm diameter Pt wire is used as a differential-aperture, or knife-edge absorption profiler, to depth resolve the Bragg-diffracted intensity from the sample [200]. As it is shown in Fig. 3.21 [203].

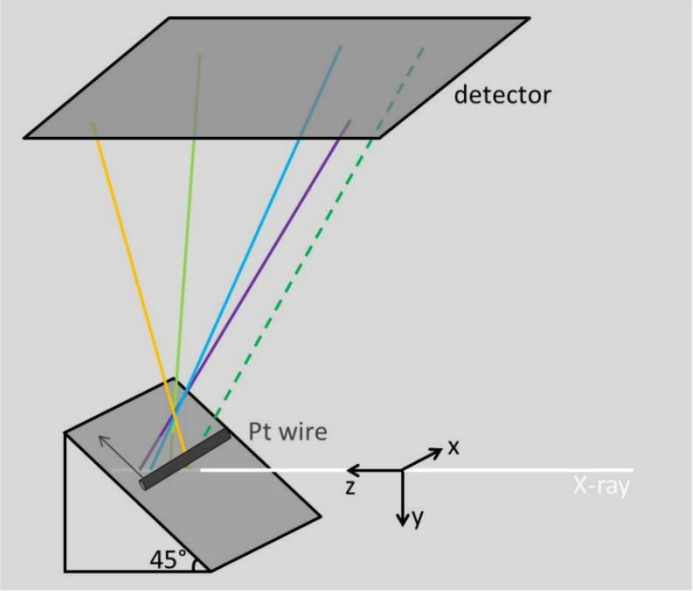

Fig. 3.21. A sketch showing the experimental set-up of the differential aperture DAXM. The Pt wire is used as a differential aperture to resolve where different diffracted signal (represented as coloured lines) recorded by the 2D panel detector is originating from within the sample volume illuminated by the focused microbeam [203]. Reprinted with permission from MDPI.

Applications:

(1) Intra- and inter-granular structure of polycrystalline materials:

Grain boundaries, grain orientations, grain sizes, and their thermal evolution are crucial factors in materials research. DAXM now enables in-situ, non-destructive 3D grain growth measurements by providing detailed mapping of the polycrystalline structure during sequential thermal annealing [200].

(2) Spatially resolved strain tensor measurements:

Understanding the impact of externally applied stress distributions, as well as processing or deformation-induced residual stresses, is critical for evaluating the performance and microstructural evolution of structural materials. Both local crystal orientation and local elastic

strain tensors can be measured with 3D submicron resolution using white and monochromatic DAXM [200]. Fig. 3.22 demonstrates an example of DAXM orientation and strain measurements in cylindrically bent Si [199].

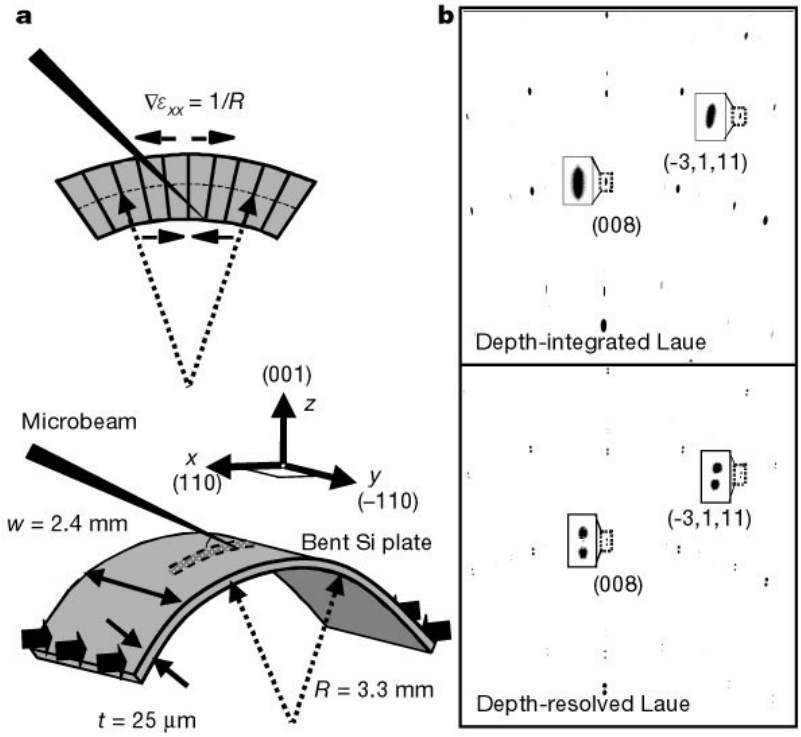

Fig. 3.22. DAXM orientation and strain measurements in cylindrically bent Si [199]. Reprinted with permission from Springer Nature.

(3) GND density measurements:

The DAXM capability to determine local lattice orientations with submicron, point-to-point spatial resolution offers direct insight into the local lattice curvature in three dimensions. This capability allows for quantitative measurement of GND densities in plastically deformed regions, with a spatial resolution of one micron used as the length scale for curvature measurement [200]. Fig. 3.23 illustrates the use of DAXM to calculate the average GND density changes in the region 0–5 μm from the graphite nodule and the metal matrix interface [203].

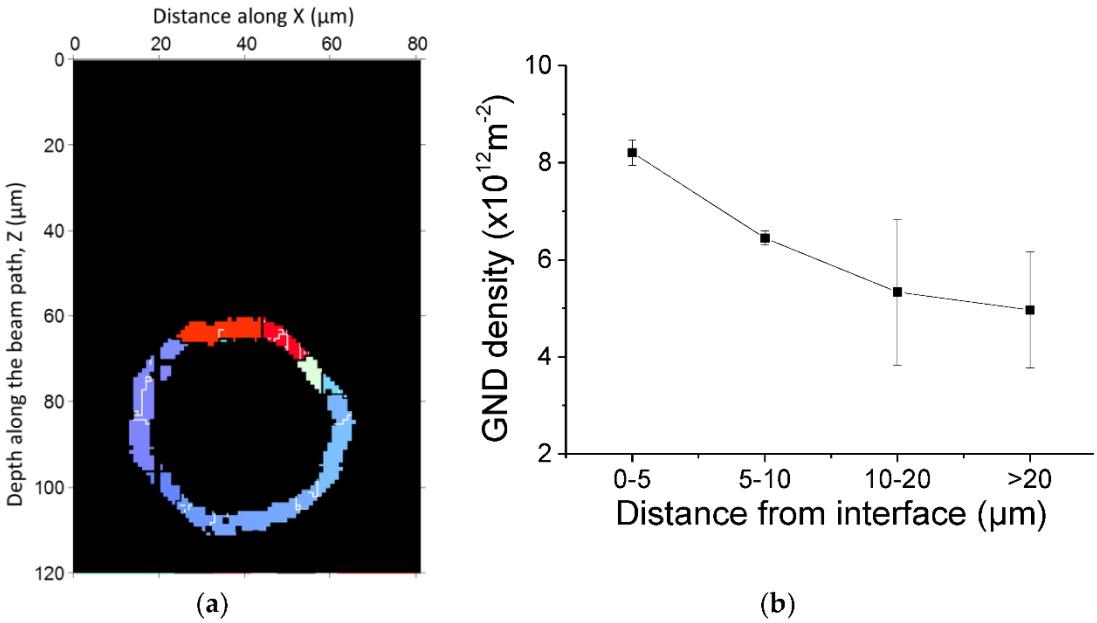

Fig. 3.23. The calculation of average GND density with DAXM [203]. Reprinted with permission from MDPI.

Benefits: DAXM offers superior angular resolution compared to EBSD. The shape of the diffraction peaks provides valuable insights into the distribution of misorientation within each probed volume. Additionally, the indexing of Laue patterns in DAXM is much more sensitive to small misorientations, ensuring that only regions with near-cubic symmetry are indexed as cubic. Furthermore, X-rays can penetrate well below the polished surface, allowing for the detection of subsurface features and minimizing artefacts often introduced by polishing, to which EBSD is particularly susceptible [204, 205].

3.4.2 Equipment and parameter used in this thesis

3.4.2.1 SEM equipped with EDX and EBSD

Three SEM instruments were used to characterise cross-sections of the corroded samples at the micro-scale depending on the information needed.

Firstly, a Zeiss NVision 40 FIB-SEM is used for morphology analyses, TEM samples, and APT sample preparation. For the imaging, 5KV and 500 pA was used.

Secondly, a Zeiss Merlin FEG-SEM equipped with a Bruker XFlash FlatQUAD 5060F EDX detector and Bruker e-flash high-resolution EBSD detector is mainly used for EDX and EBSD analyses. For the EDX analyses, a working distance of 15-18 mm, normally 15-20 KV, 500 pA was used to excite the K lines, overcoming the overlap problem of Cr-L (0.573) and O-K (0.525) and providing much higher counts. However, the high voltage means a higher electron beam energy which will induce a larger interaction volume. The net spatial resolution decreases with increasing electron energy [206]. Thus, 5 KV, 400 pA was also used to analyse the finer structures, as shown to improve the spatial resolution [167]. However, due to the existence of Pb and Bi from the LBE and Mo from T91, there is still a peak overlap issue between Mo-L (2.293), Pb-M (2.342), and Bi-M (2.419). EBSD maps were obtained at a working distance of 18 mm and a sample tilt of 70 degrees, with a beam voltage of 20 kV and 5-10nA probe current.

The last SEM-based equipment used is a Zeiss Crossbeam 540 FIB-SEM equipped with Oxford Instrument XmaxN 150 EDX and EBSD. EDX maps were obtained at a working distance of 5 mm and a beam voltage of 10-20 KV, probe current of 500 pA or 5 KV/1 nA considering the spatial resolution discussed above. EBSD maps were acquired with a working distance of 12 mm, beam voltage of 15-20 KV, and probe current of 10 nA.

3.4.2.2 TEM and STEM equipped with EDX and EELS

3 plan-view TEM samples and 1 normal TEM sample were prepared using a Zeiss NVision 40 FIB-SEM, following the approach presented by Lozano-Perez [207]. The TEM sample was lifted out onto a Cu grid, then thinned using 30kV Ga ions to under 100 nm with ion currents ranging from 700 pA to 40 pA. The final step uses 2 kV, 200 pA Ga ion polishing to remove surface defects induced by the 30 kV Ga ions. STEM images were recorded using a Jeol ARM 200F cold-FEG TEM operating at 200 kV, fitted with a 100 mm^2 Centurion EDX detector and Gatan GIF Quantum 965

ER, allowing for EDX and EELS map acquisition in regions of interest. The step size for the EDX and EELS maps was 5 nm.

3.4.2.3 On-axis TKD

On-axis Transmission Kikuchi Diffraction (TKD) analysis of the TEM sample used a Zeiss Merlin FEG-SEM equipped with a Brucker e-flash high-resolution EBSD detector with an Optimus TKD head. The sample was held normal to the electron beam at a working distance of 5.4 mm and Kikuchi patterns were captured beneath the sample with a horizontal phosphor screen. An electron beam accelerating voltage of 30 kV was used. The step size was 6 nm, and TKD data was processed using the Esprit 2.3 software.

3.4.2.4 APT

APT samples were prepared using a dual-beam Zeiss Crossbeam 540 FIB-SEM. The samples were first trenched and then lifted out and attached to standard silicon micro tip coupons purchased from Cameca. Next, annular FIB milling was used to mill the samples into sharp needles with tip diameters <100 nm. An acceleration voltage of 30 kV was used for FIB milling, followed by a final low-energy polishing step (2 kV, 200 pA) to remove FIB-induced surface damage. APT samples were analysed using a Cameca LEAP 5000XR atom probe. A laser energy of 60 pJ, stage temperature of 50 K, pulse frequency of 125 kHz, and detection rate of 0.4 was used for the samples corroded in a reducing environment. Much higher laser energies varying from 80-200 pJ, stage temperature 50 K, pulse frequency 200 kHz, and detection rate of 0.4 were used for the samples corroded in the oxidising environment. For Pb-containing samples we found that a pulse rate of 125 kHz or less should be used, as higher pulse rates caused excessive detection loss of Pb ions, as will be detailed in full in the following chapter. The APT data was analysed using AP Suite 6 with the needle shape estimated using the voltage reconstruction approach [193]. Mass spectrum peak overlap issues were resolved using AtomprobeLab [208, 209].

3.4.2.5 GND calculation

Total geometrically necessary dislocation (GND) density maps, similar to those produced by Britton and Wilkinson using the high-resolution EBSD (HR-EBSD) approach [210], were generated from the EBSD data using custom MATLAB codes. Further details of the HR-EBSD methodology to obtain GND densities are provided elsewhere [169].

3.4.2.6 DAMX

The crystal structure of different parts of the corroded sample was probed by X-ray micro-diffraction at the 34-ID-E beamline at the Advanced Photon Source (Argonne National Laboratory, IL, USA). The sample was mounted in 45° reflection geometry and 2D Laue diffraction patterns were collected on an area detector positioned above the sample. An incident polychromatic beam (7-30 keV) with a size of 185 x 360 nm^2 on the surface was used. A line scan was taken along the polished sample cross-section. Depth resolution was achieved using the Differential Aperture X-ray Microscopy (DAXM) technique [199, 211]. Briefly, a platinum wire is scanned along the surface of the sample, cutting through the diffracted beam. By triangulating using the positions of the incident beam, detector and wire, a profile of the intensity reaching each pixel on the detector as a function of depth in the sample (along the beam path) can be reconstructed. This allows depth-resolved measurements of grain orientation on a 2D slice at a 45° angle into the cross-section surface. Indexing of the diffraction patterns was performed using the LaueGo software package (J.Z. Tischler: tischler@anl.gov).

3.4.3 Methods conclusion

A rigorous approach to materials characterisation necessitates the use of multiple complementary techniques to enable cross-validation and confirmation at various length scales. By employing methods such as SEM, EDX, EBSD, TKD, TEM, STEM, APT, GND calculations, and DAXM, we can obtain a multi-scale dataset, providing a more holistic understanding of the material. Each technique contributes unique insights—ranging from chemical composition and

crystallography to atomic-scale resolution and strain field quantification—ensuring that results are corroborated and validated across different structural scales and levels of complexity.

Chapter IV

Atom Probe Tomography Conditions and Data Analysis Techniques

4.1 Sample preparation

There are two primary methods for preparing the needle-shaped samples required for APT. The first is electropolishing, which is relatively faster, more straightforward, and avoids the risk of material damage that can occur with ion beam-based approaches. However, electropolishing has several limitations.

Firstly, it requires the specimen to be cut into a matchstick-like shape with a squared cross-section and a length of approximately 25 mm, necessitating larger sample sizes. Secondly, if the material contains regions with phases exhibiting different dissolution rates, this may result in uneven polishing. Additionally, a major drawback of electropolishing is its lack of site specificity. This means that the prepared sample represents a randomly selected volume of the microstructure. Combined with the limited sampling volume typical of APT experiments, this significantly reduces the likelihood of capturing sparsely distributed microstructural features, such as grain boundaries and other interfaces [212].

In this study, the LBE-corroded samples measure approximately 5 mm × 5 mm × 3 mm and consist of two distinct phases, LBE and T91, which exhibit significantly different dissolution rates during electropolishing. Furthermore, obtaining APT results from specific positions is essential to understanding the corrosion mechanism. Therefore, a Ga FIB is employed for sample preparation in this study. The process is illustrated in Fig. 4.1.

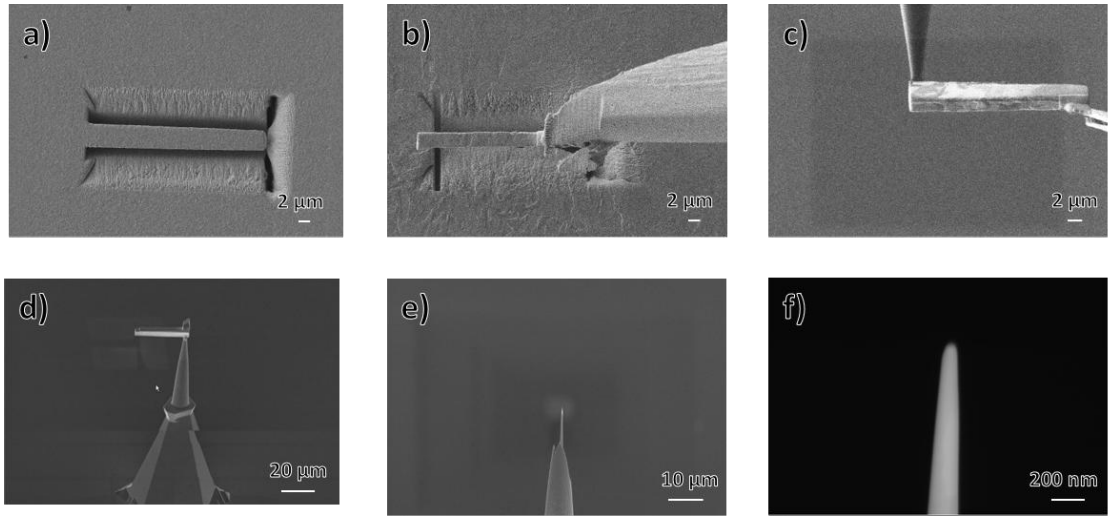

Fig. 4.1. Process of APT sample making with FIB. (a) Trenching. (b) Lift-out. (c) (d) Attaching the lift-out to the Si post. (e) Sharpening. (f) Final APT sample after 2 KV 200 pA polishing to remove the surface defects induced by 30 KV Ga ions.

4.2 TKD-assisted sample preparation

As introduced in the methods chapter, researchers have previously developed FIB-based sample preparation methods that incorporate TKD to locate grain boundaries within the sample [198]. A similar approach was adopted in this study to analyse the as-received T91 (normalized and tempered), as shown in Fig. 4.2.

First, EBSD mapping was performed to identify a region with a high density of grain boundaries, increasing the likelihood of incorporating grain boundaries into the prepared specimens, as shown in Fig. 4.2(a). The dashed orange box in Fig. 4.2(a) highlights such a region with a high density of grain boundaries. Subsequently, a higher magnification EBSD image was acquired from the region of interest (ROI) marked in Fig. 4.2(a) and is presented in Fig. 4.2(b). The final lift-out region is indicated with an orange dashed rectangle in Fig. 4.2(b).

The lift-out bar was then divided into six separate samples, which were thinned to <100 nm and analysed using TKD, as shown in Fig. 4.2(c). The TKD results enabled the confirmation of the APT

sample positions. Additionally, the final needle-shaped APT specimens could also be analysed by TKD, allowing for a direct comparison with the APT results. This comparison is demonstrated in the bottom-right corner of the first two samples in Fig. 4.2(c).

Fig. 4.3 presents the APT 3D reconstruction of the second APT sample, for which corresponding TKD results were obtained at both the lamella stage and the final specimen stage. By comparing the APT 3D reconstruction in Fig. 4.3 with the TKD data in Fig. 4.2(c), a strong correlation is observed. The reconstruction reveals carbon-rich precipitates.

Proxigram analysis using an isosurface defined by a carbon concentration of 1.67 at.% indicates that the precipitates are enriched with Cr and C. The atomic ratio of Cr to C is approximately 28:5, which is consistent with $M_{23}C_6$ carbide [153]. The lower carbon content measured in APT may be related to detector dead time, which preferentially affects carbon detection due to its tendency to evaporate as molecular ions [213].

According to Thuvander's research, the primary reason for underestimating carbon concentrations in laser-pulsing APT mode is the frequent evaporation of carbon as molecular ions. If these molecular ions decompose en route to the detector, they produce multiple smaller ions that may arrive within the detector's dead time, leading to ion loss [213]. Furthermore, during the APT measurement, although the applied voltage increases as the needle radius enlarges, the resulting field strength decreases, which may promote the generation of molecular ions.

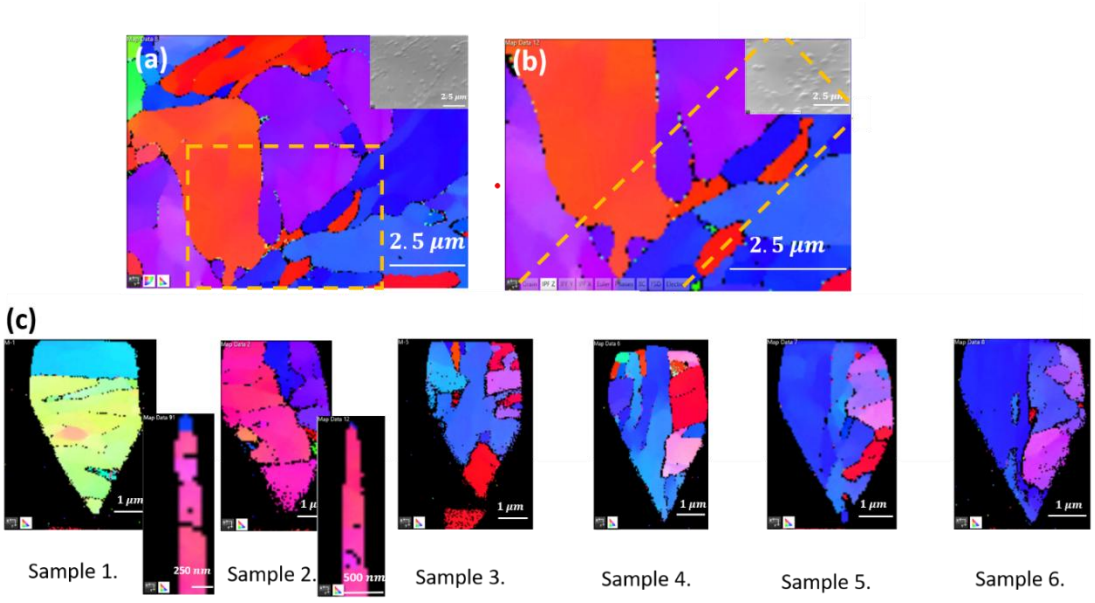

Fig. 4.2. (a) EBSD with lower magnification, SEM image shown on the top right, and high-density grain boundary region highlighted with orange rectangular. (b) EBSD with higher magnification, SEM image shown on the top right, and lift-out region highlighted with orange rectangular. (c) TKD of each laminar and two final APT samples.

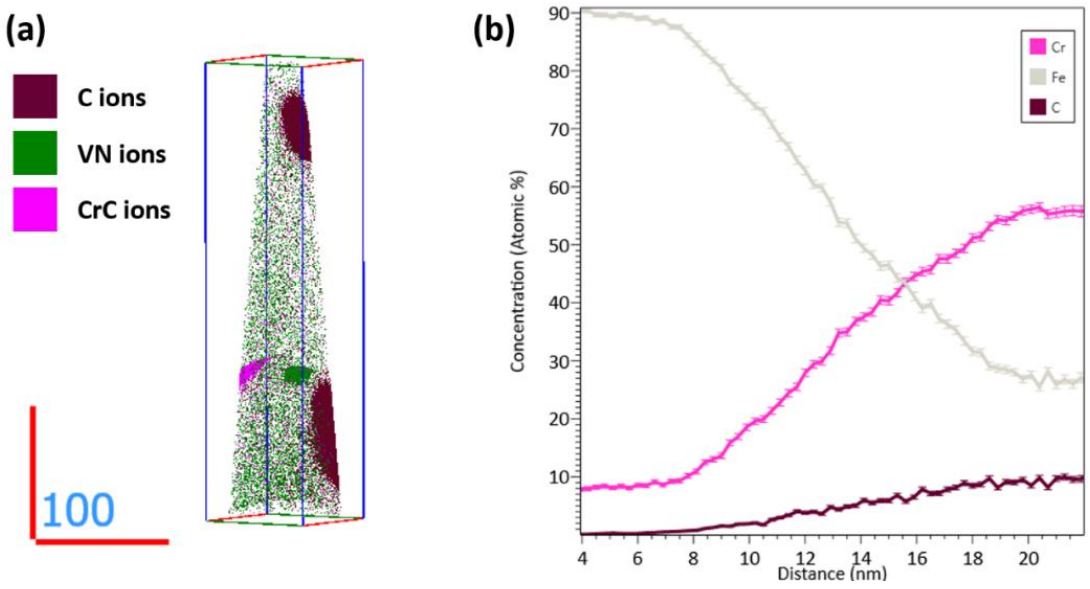

Fig. 4.3. (a) 3D APT reconstruction of sample 2. (b) Proxigram of C content=1.67 at.%.

4.3 Difficulties of FIB LBE corroded T91

During the sample preparation stage using a Ga FIB, it becomes readily apparent that LBE is highly sensitive to the Ga beam. Even imaging with low currents results in material loss, as shown in Fig. 4.4. In Fig. 4.4(b), it can be clearly observed that within the red dashed rectangle, the T91 region is slightly etched, while the LBE region is significantly more severely etched.

Due to this high sensitivity of LBE to the Ga beam, the final sharpening of APT samples poses challenges. To mitigate this, a substantial protective layer (W, Pt, or C, depending on the FIB instrument) must be retained on the sample surface during annular milling. A final low-energy polishing step is then used to just remove the protective layer without damaging the sample.

During the sharpening process, extended exposure to the ion beam can also cause bending or failure of the sample, as shown in Fig. 4.4(c). To minimize FIB imaging time during sharpening, fewer annular milling steps should be employed. The experimental parameters used in this study are as follows:

- **30 kV, 700 pA** to achieve a diameter of 1 μm,
- **30 kV, 300 pA** to reduce the diameter to 500 nm,
- **30 kV, 100 pA** to further reduce the diameter to 200 nm, and
- **30 kV, 100 pA** to achieve a final diameter of less than 100 nm.

Considering the beam tail effect, a larger diameter for annular milling must be configured for the system, depending on the current of the FIB probe [214].

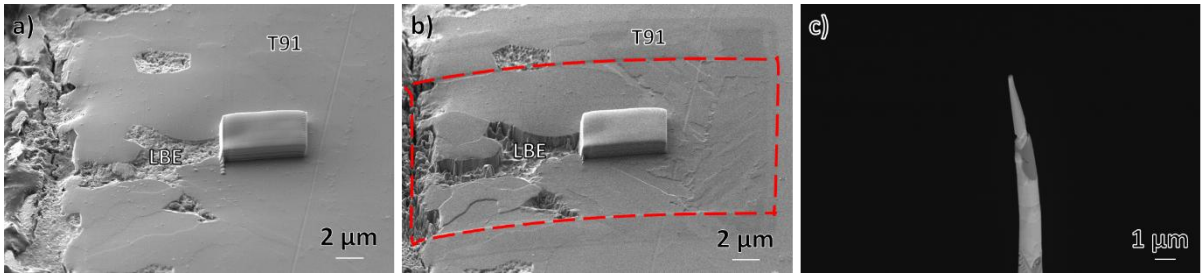

Fig. 4.4. (a) SEM image of the sample with left side not exposed to FIB. (b) SEM image after the red dashed rectangular exposed to FIB. (c) Bending and failure of the sample due to extended exposure.

4.4 APT parameters to analyse the sample with LBE and T91

APT uses an electric field to polarise the surface atoms and when it gets sufficiently intense, the atom can be pulled away from the surface while one of its electrons is drained into the surface which is also known as ionisation [193]. Within the APT experiment, there is another term, evaporation field, also known as zero-barrier evaporation field is the value of the electric field (F_{evap}) at which the energy barrier is reduced to zero. F_{evap} varies from different species atoms and charge states. Normally, the lowest value is the dominant value. Evaporation rate means the number of atoms that evaporate per second. Atoms with huge F_{evap} differences can cause the sudden change of required voltage to evaporate the different atoms at the same evaporation rate. For the sample used in this study which contains T91 and LBE, the sudden big change in voltage creates a higher possibility of sample fracture. T91 is mainly composited with Fe, the evaporation field for Fe is 42 V/nm. For LBE, the evaporation field for Pb is 20 V/nm and for Bi is 18 V/nm [193]. The voltage sudden changes were observed during the tests as shown in Fig. 4.5 (e) which are partly highlighted in red dashed circles.

There are multiple parameters can be adjusted for APT analyses and they are related to the composition measurement accuracy along with optimal spatial resolution. For laser-pulsing

mode, the main parameters are specimen temperature, voltage, detection rate, pulse energy, and pulse rate (also known as pulse frequency). Lower Specimen temperature can reduce the atom migration and improve the special resolution. However, lower temperature will also cause the embrittlement of materials which introduces more fractures. The detection rate is set as the target value which unit is a few atoms per 100 or 1000 pulse. A higher detection rate means a higher electric field which normally provides lower background noise and higher accuracy of composition measurements but more fracture. Pulse energy sets the laser energy used for pulsing. The higher energy will reduce the fracture but will bring more thermal effects like atom migration and degrade spatial resolution. Pulse rate controls the time of detection window. Normally higher pulsing rate is desirable. However, for the heavy ions, a lower pulse rate has to be chosen or they won't have enough time to reach the detector within one of the detection windows which will cause a specific loss of ions. This effect was observed in the test and shown in Fig. 4.5 (a) and (b) which was carried out with temperature 50 K, laser energy 60 pJ, detection rate 0.3, pulse rate 200-260 kHz. Due to Pb and Bi ions being much heavier, with the higher pulse rate, s specific loss of ions was detected. To improve the situation, (c) (d) was undertaken with specimen temperature 50 K, laser energy 60 pJ, detection rate 0.4, and pulse rate 125 kHz. Comparing the detector ion hit map (histogram) in Fig. 4.5 (a) and Fig. 4.5 (c), a less severe loss of ion detection is observed in Fig. 4.5 (c) corresponding to the LBE region which may imply better pulse rate. After lowering the pulse rate, a more homogeneous hit map is acquired as shown in Fig. 4.5 (c). Similar results are also seen in the 3D reconstruction in Fig. 4.5 (b) and Fig. 4.5 (d). For the LBE-contained samples, the pulse rate should not be set higher than 125 kHz or it will induce a severe loss of ions. Other than the pulse rate effect discussed above, the evaporation field difference may also play a role in the ion loss. As it is stated in the literature, preferential evaporation will lead to specific loss of the atoms with the lower evaporation field [193]. As the samples in this chapter use laser-pulsing mode, a lower pulse rate is also good for

the heat to transfer from the sample surface which benefits the mass resolution and background level [193].

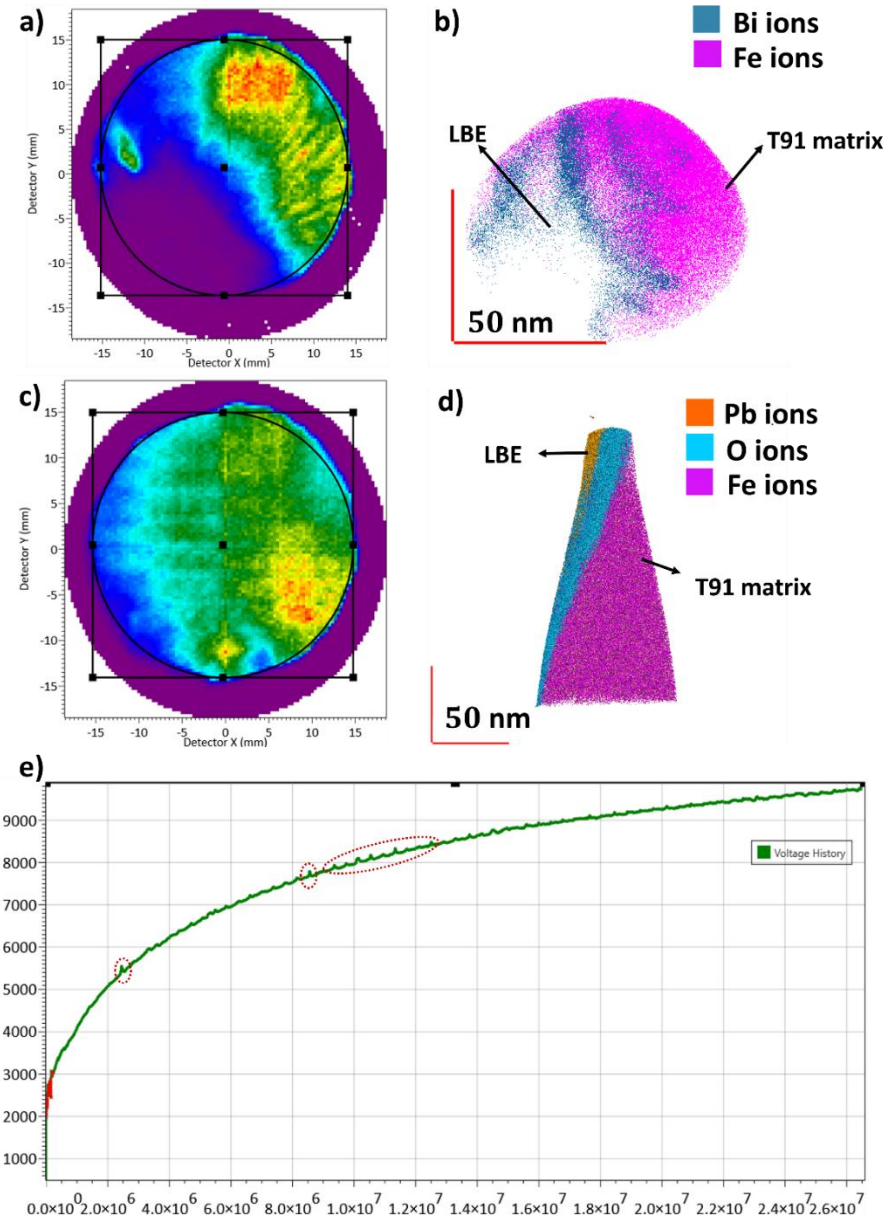

Fig. 4.5. APT detector hit map and 3D reconstruction of the LBE contained samples analysed with different experimental parameters [Sample: 506 h, reducing environment, 715 ℃, LBE]. (a) (b) analysed with temperature 50 K, laser energy 60 pJ, detection rate 0.3, pulse rate200-260 kHz. (c) (d) analysed with temperature 50 K, laser energy 60 pJ, detection rate 0.4, pulse rate125 kHz. (e) The voltage curve for results shown in Fig. 4.3 (c) and (d) with the representative voltage sudden changes highlighted with dashed red circles.

4.5 Si movements due to laser pulse

During the APT data analyses, an aberrant uneven distribution of Si was observed. To study the reason that induced this artefact, a series of systematic experiments were undertaken varying the parameters for the APT experiment, as listed in Table 4.1 of the as-received T91. The 3D reconstructions for these tests are shown in Fig. 4.6-4.12. The X and Y plane orientation images cannot clearly show the Si unevenly distribution for some tests. So, the Z plane orientation images are provided for each test. For the laser-assisted APT, the temperature systematically varied from 40 K-55 K, the laser energy varied from 40 Pj -70 pJ, and the detection rate varied from 0.25-0.5 ions per pulse. A low temperature, 30 K, was also tested. However, this temperature resulted in severe fracture of samples before providing any useful data. By comparing the first 6 groups of tests (laser-assisted APT), it is apparent that despite how the parameters temperature, detection rate, and laser energy were varied, the cause for the observed uneven distribution of Si remained unexplained. However, for experiments in the voltage-pulsing mode, although the temperature is 50 K, a homogeneous Si distribution is observed. Together, these results suggest that the aberrant distribution of Si introduced in APT 3D reconstruction is a result of laser heating which increases the surface migration and that the best way to avoid this issue is to use voltage-pulsing mode. The effects of Si surface migration during the experiment are considered in subsequent research. However, as discussed in Section 4.4, the LBE-containing samples are not compatible to be analysed with voltage pulsing. Thus, there may be some spurious Si migration in the results presented in this thesis, though all possible steps have taken to minimise this effect.

Table 4.1. APT parameters used for the comparative tests.

	Operation mode	Temperature (K)	Detection rate	Laser energy (pJ) Pulse fraction (%)	Pulse rate (kHz)
1	Laser mode	40	0.25	40	200
2		40	0.3	50	200
3		45	0.3	50	200
4		50	0.35	50	200
5		50	0.5	50	200
6		55	0.5	70	125
7	Voltage mode	50	0.3	15	200

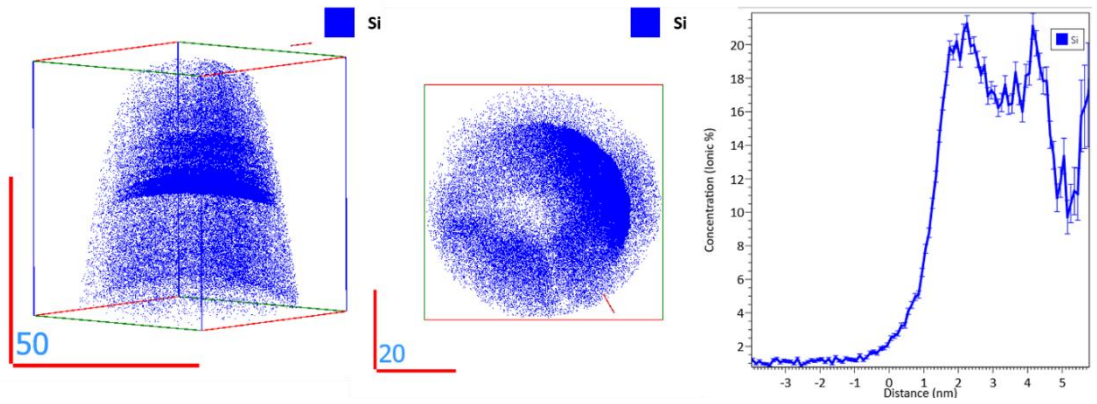

Fig. 4.6. X and Z plane orientation image of test 1 and the proxigram of Si=1.58% (laser-assisted APT measurement with temperature 40 K, detection rate 0.25, laser energy 40 pJ, and pulse rate 200 kHz) [Sample: as-received T91].

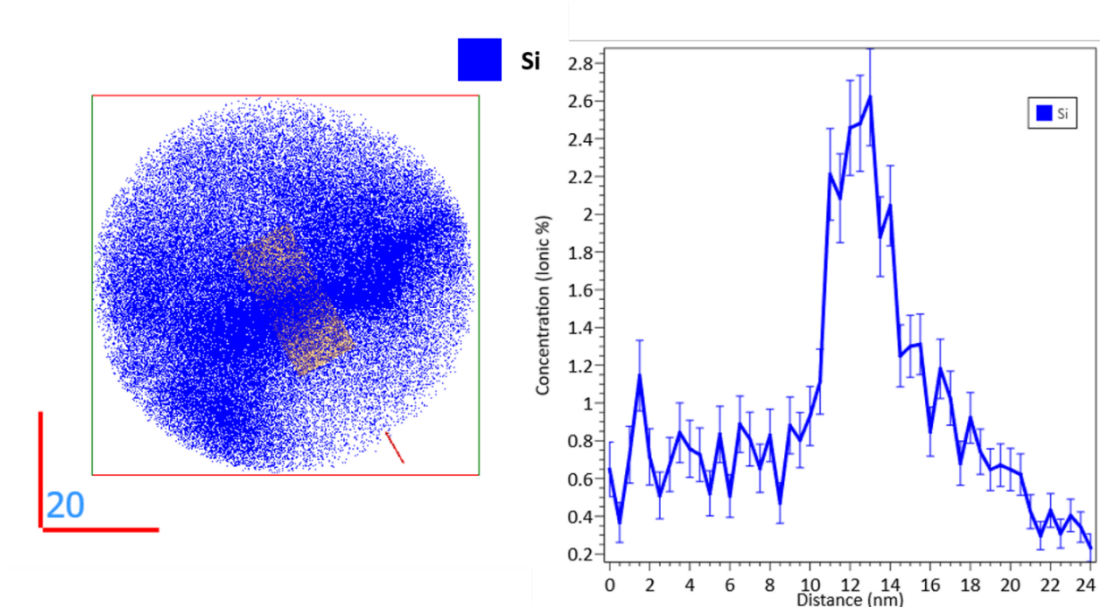

Fig. 4.7. Z image plane orientation of test 2 and the 1-D concentration of Si along the ROI in left image (laser-assisted APT measurement with temperature 40 K, detection rate 0.3, laser energy 50 pJ, and pulse rate 200 kHz) [Sample: as-received T91].

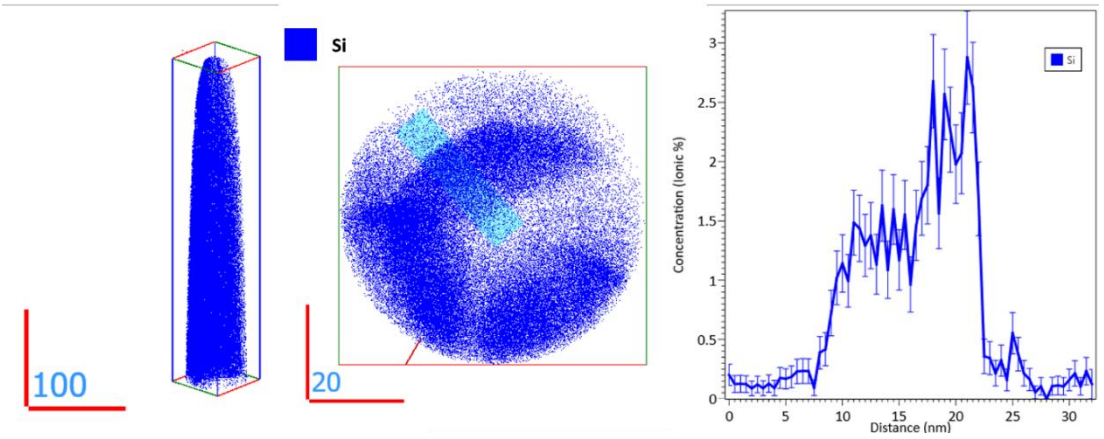

Fig. 4.8. X and Z plane orientation images of test 3 and the 1-D concentration of Si along the ROI in the middle image (laser-assisted APT measurement with temperature 45 K, detection rate 0.3, laser energy 50 pJ, and pulse rate 200 kHz) [Sample: as-received T91].

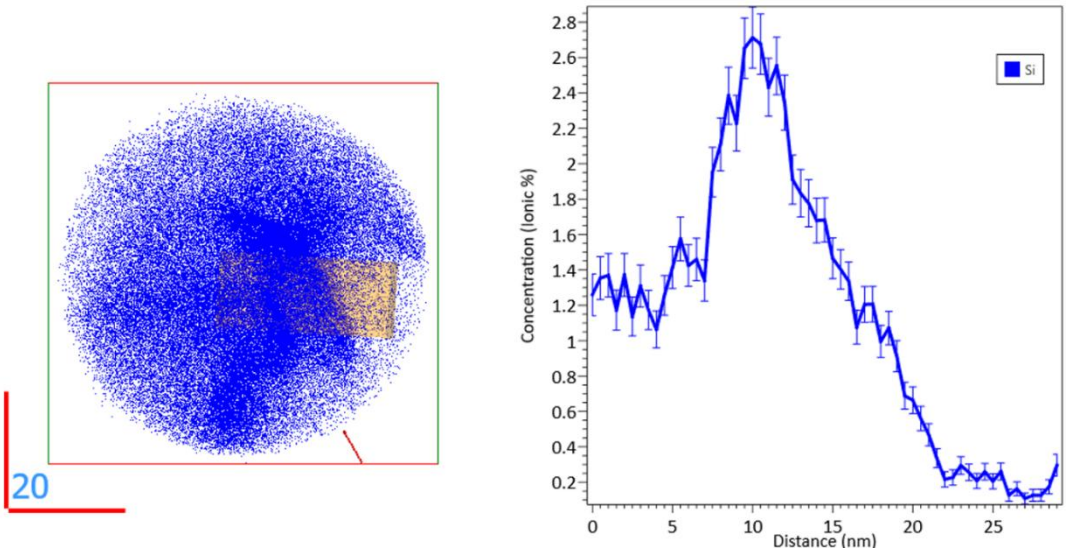

Fig. 4.9. Z plane orientation image of test 4 and the 1-D concentration of Si along the ROI in left image (laser-assisted APT measurement with temperature 50 K, detection rate 0.35, laser energy 50 pJ, and pulse rate 200 kHz) [Sample: as-received T91].

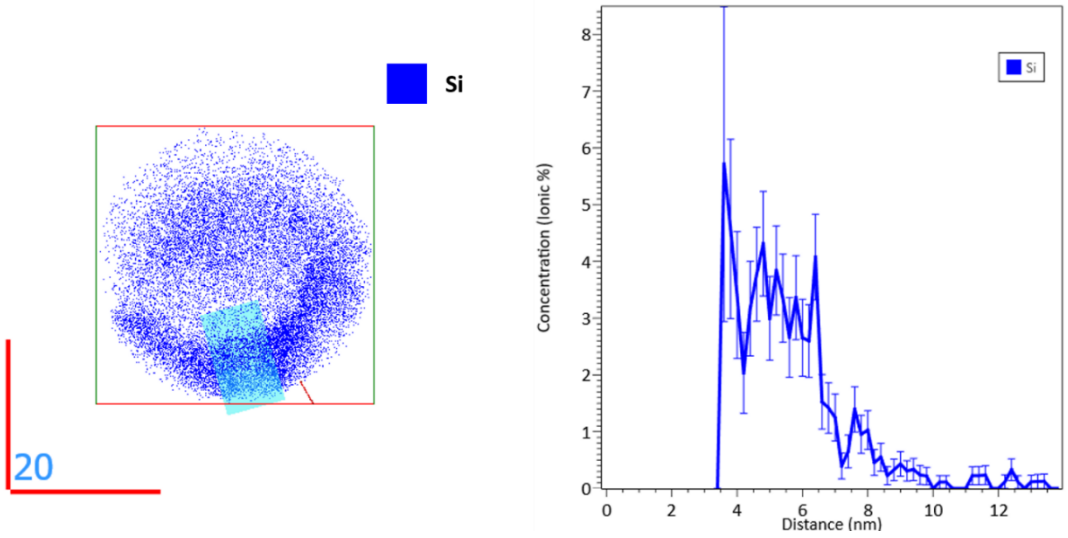

Fig. 4.10. Z plane orientation image of test 5 and the 1-D concentration of Si along the ROI in the left image (laser-assisted APT measurement with temperature 50 K, detection rate 0.5, laser energy 50 pJ, and pulse rate 200 kHz) [Sample: as-received T91].

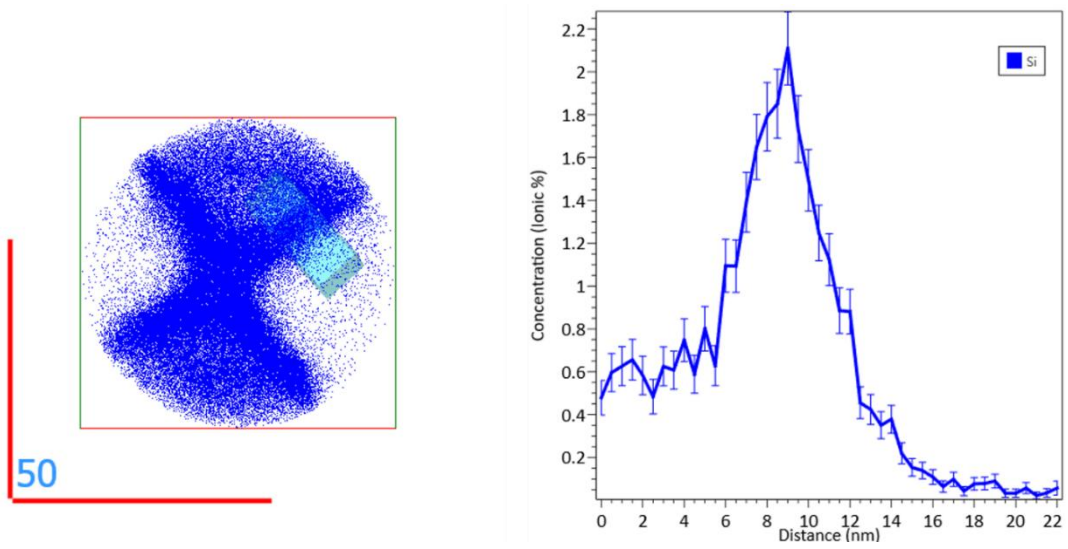

Fig. 4.11. Z plane orientation image of test 6 and the 1-D concentration of Si along the ROI in the left image (laser-assisted APT measurement with temperature 55 K, detection rate 0.5, laser energy 70 pJ, and pulse rate 125 kHz) [Sample: as-received T91].

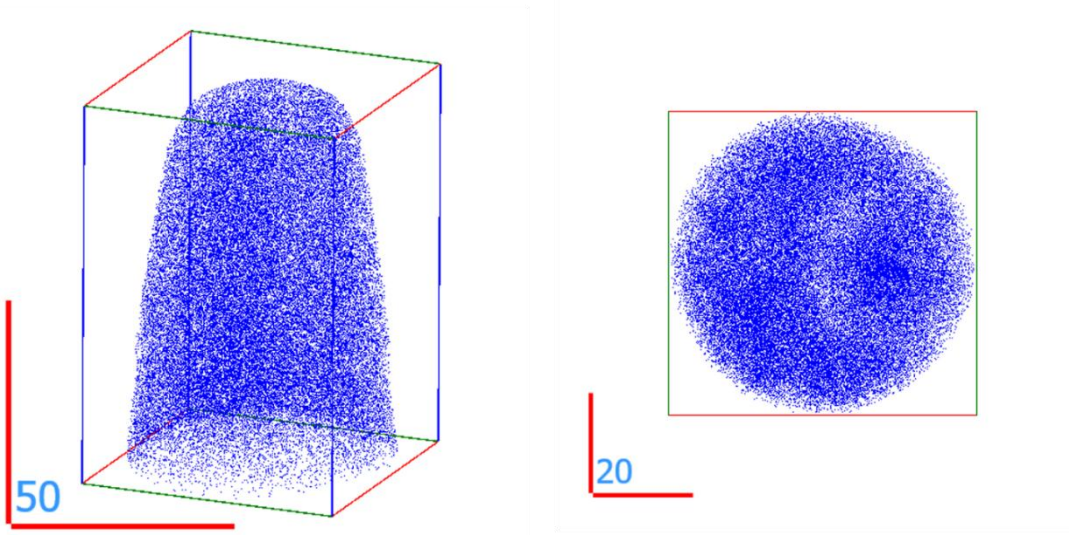

Fig. 4.12. APT parameter of test 5: voltage-pulsing APT measurement with temperature 50 K, detection rate 0.3, pulse fraction 15%, and pulse rate 200 kHz [Sample: as-received T91].

4.6 Interpretation of the Mass Spectra

In APT, the mass spectrum refers to the histogram of the mass-to-charge-state ratio generated during the experiment, as shown in Fig.4.13 (a). This histogram must then be "ranged," meaning that the user assigns a chemical identity to each peak (Fig. 4.13 (b)-(f)). The bars above the mass spectrum in Fig. 4.13 (b)-(f) represent the mass-to-charge-state ratios of different isotopes, with the thickness of each bar corresponding to the natural isotopic abundance (thicker bars indicating higher abundance). The ranging shown in Fig. 4.13 (b)-(f) is a how the peaks were labelled for the LBE corroded T91 in this thesis.

As the boundaries of the peaks are defined by the user, there is often variation in the ranged data between different users [215]. This variation poses a challenge, as the accuracy of the ranging process directly influences the determination of the number and concentration of ions in the analysis. Hudson et al. conducted an investigation into different ranging techniques, showing that the variance in concentration estimates increases when data is manually ranged and as the actual solute concentration decreases [215]. Assessing the accuracy of these techniques is difficult, as the "true" composition of a real dataset is unknown. Therefore, it is essential to apply a consistent ranging method across all datasets to ensure comparability.

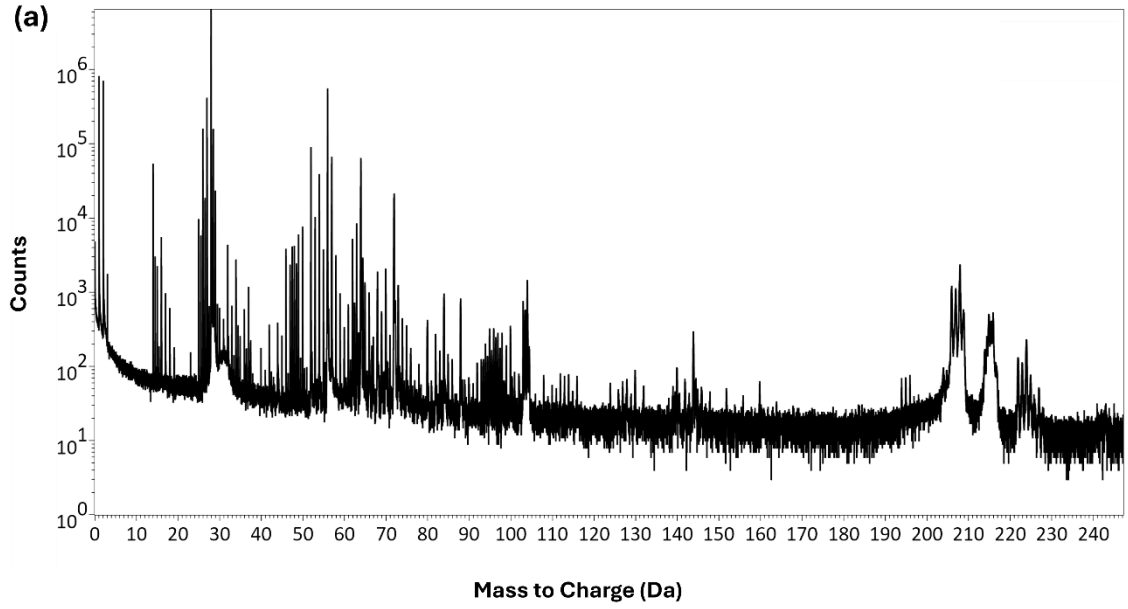

(b)

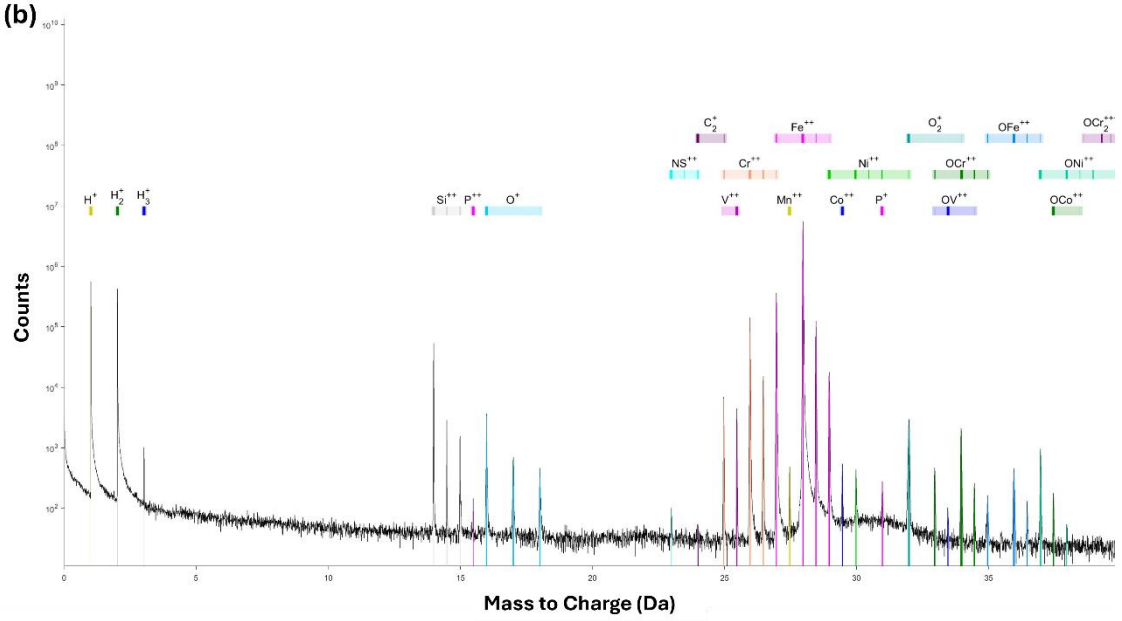

(c)

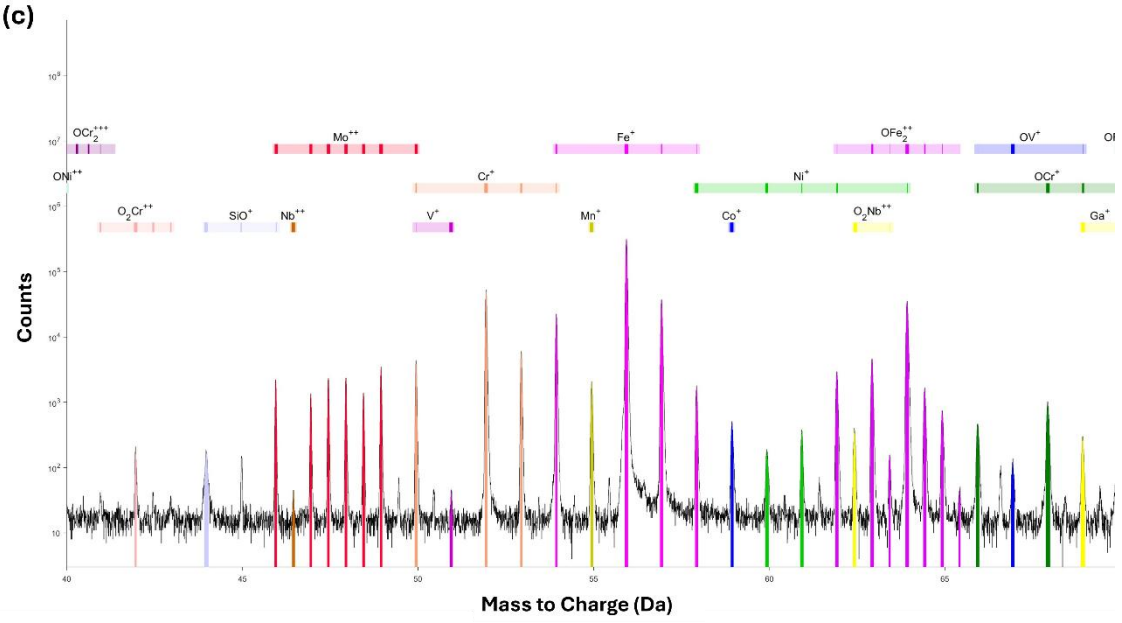

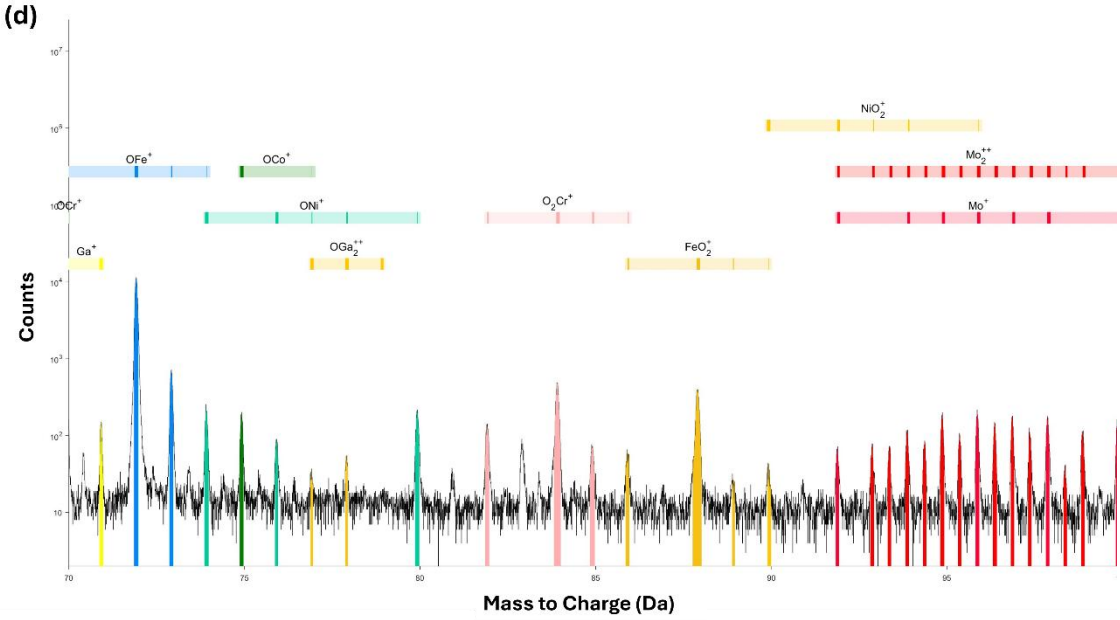
(d)
Counts
Mass to Charge (Da)
OFe+
OCo+
OCr+
ONi+
O2Cr+
Ga+
OGa2++
FeO2+
NiO2+
Mo2++
Mo+

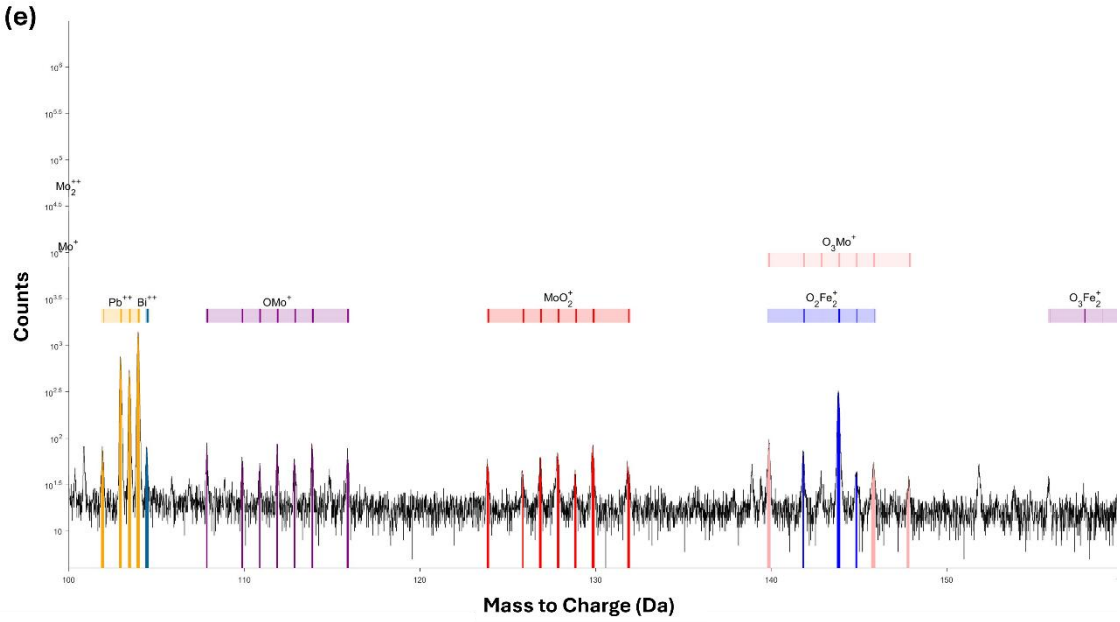
(e)
Counts
Mass to Charge (Da)
Mo2++
Mo+
Pb++
Bi++
OMo+
MoO2+
O3Mo+
O2Fe2+
O3Fe2+

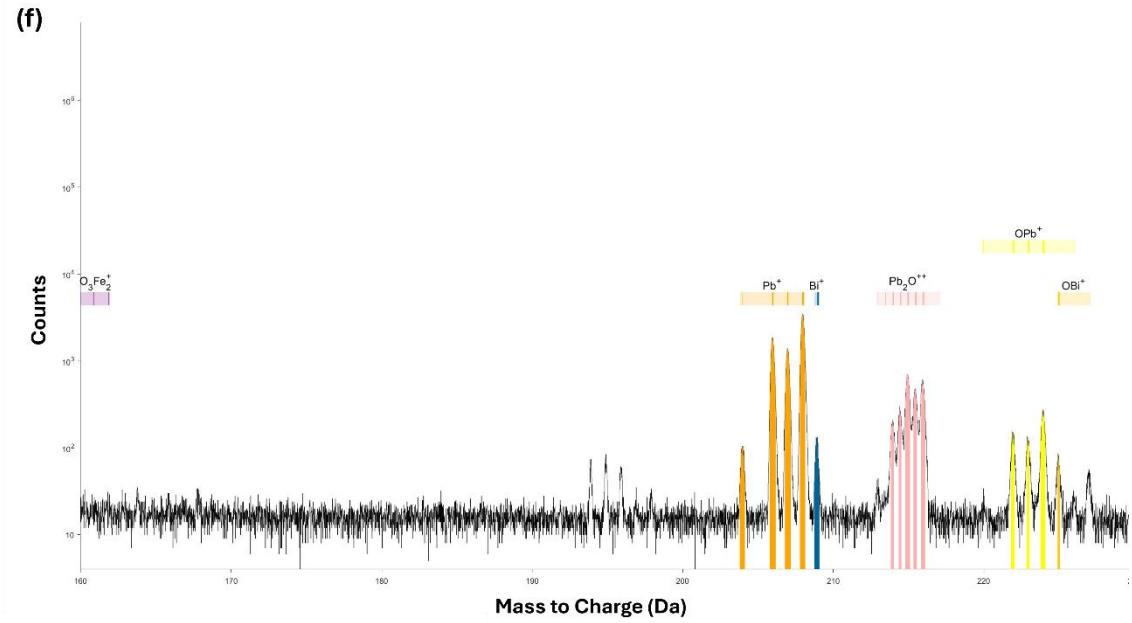

Fig. 4.13. Typical mass spectrum generated during APT analysis of LBE corroded T91. (a) before ranging. (b)-(f) after ranging. The plot is created using AtomProbeLab-v0.2.4.

Due to the fact that detected ions can possess multiple charge states (typically from 1+ to 4+), two ions with different masses can exhibit the same mass-to-charge ratio (e.g., both $^{28}Si^{1+}$ and $^{56}Fe^{2+}$ have a mass-to-charge ratio of 28 Da). This leads to overlapping peaks in the mass spectrum, which cannot be resolved individually. A summary of the common overlaps encountered in the steels analysed in this thesis is provided in Fig. 4.14 (a)-(c). The thickness of the overlap lines represents how difficult it is to resolve the overlap. Thicker lines indicate greater difficulty in distinguishing between overlapping peaks. Mass spectrum peak overlap issues were resolved using AtomprobeLab [208, 209].

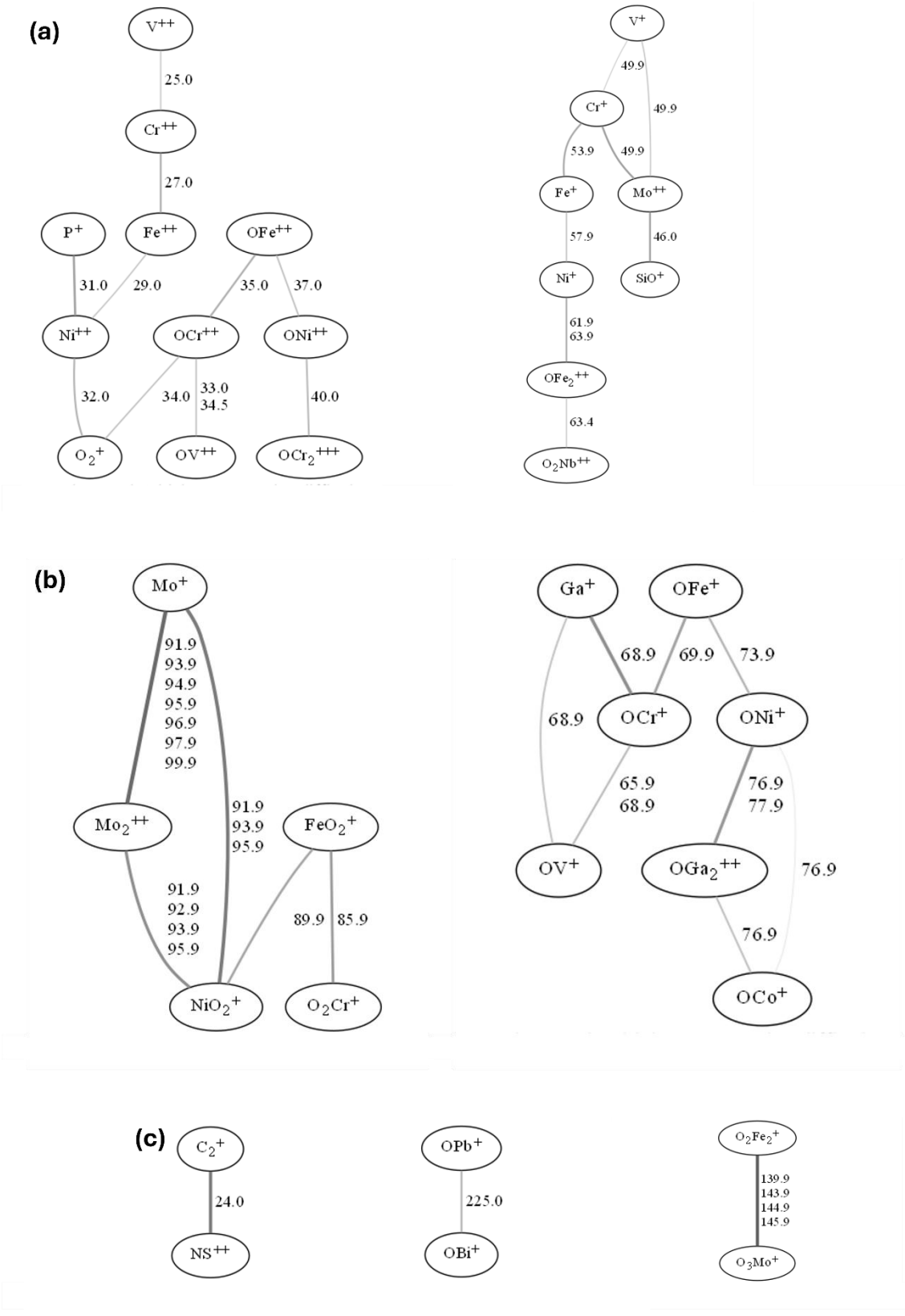

Fig. 4.14. Potential sources of peak overlaps from APT analysis of T91.

4.7 Reconstruction Method

The reconstructions for the APT data in this thesis followed this sequence:

1. Range the main peaks and perform a simple voltage-based reconstruction.

2. In IVAS, range all the peaks and save the result as a new range file.

3. Redo the reconstruction using the newly saved range file. This is necessary because each atom occupies a volume, and if an atom is not ranged during reconstruction, no volume will be allocated for it.

4.8 Conclusion

In conclusion, the sample preparation methods discussed in this chapter were used to prepare all the APT samples analysed in this thesis. Although the issue of Si movement could not be fully resolved with the laser settings employed, this is not a significant concern as the focus of the thesis is not on Si. Additionally, the APT analysis techniques outlined in this chapter—such as reconstruction, ranging, and resolving peak overlaps—were consistently applied throughout the entire thesis. These foundational methods are critical to the analyses and interpretations presented in the following chapters.

Chapter V

Corrosion mechanism of T91 steel in static lead-bismuth eutectic in reducing environment

5.1 Introduction

T91 steel is a candidate material for structural components in lead-bismuth-eutectic (LBE) cooled systems, for example, fast reactors and solar power plants [216]. However, the corrosion mechanisms of T91 in LBE remain poorly understood. In this chapter, the static corrosion of T91 in liquid LBE in reducing environment is investigated using a range of characterisation techniques at increasingly smaller scales. A unique pattern of liquid metal intrusion was observed that does not appear to correlate with the grain boundary network. Upon closer inspection, EBSD reveals a change in the morphology of grains at the LBE-exposed surface, suggesting a local phase transition. EDX maps show that Cr is depleted in the T91 material near the LBE interface. Furthermore, the dissolution of all Cr-enriched precipitates is observed in this region. Although the corrosion is conducted in an oxygen-deficient environment, both STEM and APT reveal a thin surface oxide layer (presumably wüstite) at the LBE-steel interface. Using EELS in the STEM, as well as APT, the atomic scale elemental redistribution and 3D morphology of the corrosion interface is investigated. By combining results from these different techniques, several types of oxide phases and structures can be identified. Based on this detailed nano-scale information, potential mechanisms of T91 corrosion in LBE are proposed.

5.2. Results

5.2.1 Microstructure and chemical composition analysis of cross-section samples

5.2.1.1 Morphology of corroded T91

The respective corrosion microstructures of samples associated with different LBE exposure times are presented in Fig. 5.1 (a), (d), and (g). The micrographs show a cross-section, with the LBE-exposed surface on the right-hand side, as indicated in Fig. 5.1 (a). The 506-hour exposed sample shown in Fig. 5.1 (g) was directly polished from the cross-section at 90 degrees to the original without being mounted in Bakelite. However, this resulted in a slightly curved edge after grinding and polishing, as can be seen on the right side of Fig. 5.1 (g). Thus, all subsequent samples were mounted in Bakelite to maintain sharp edges. The corrosion penetration depth was measured as the distance from the original face of the sample to the feature exhibiting maximum LBE penetration. The liquid metal attack channels are similar in shape and protrude deeper into the material with longer corrosion time. This is consistent with the observations reported by Short et al. [26].

Micro-scale elemental re-distribution due to LBE corrosion is revealed by SEM EDX. Fig. 5.1 (b) shows significant Cr depletion ahead of the LBE corroded regions in the sample exposed for 70 hours. In contrast, Fe in Fig. 5.1 (c) surrounding the LBE channels exhibits no apparent depletion. Cr depletion alone cannot account for the volume taken up by LBE in the channel, suggesting that Fe is also removed by LBE attack. Furthermore, in Fig. 5.1 (b), the Cr-enriched precipitates that are visible in the non-corroded matrix, on the left side of the image, all appear to have dissociated in the Cr-depleted region. As a point of comparison, Fig. 5.1 (j) shows the Cr distribution in the as-received T91 sample, indicating that the subsurface depletion of Cr is an effect caused by LBE exposure. The EDX for 245 h and 506 h exposed samples shows similar results as presented in Fig. 5.1 (e), (f), (h), and (i).

The separation of Pb and Bi at room temperature is detected as shown in Fig. 5.1 (b), (c), (e), (f), (h), and (i). This is expected, as a result of the formation of a Bi-rich phase (γ) and an intermetallic phase (β) below 123.5℃ (the solidus) for Pb-Bi mixtures with eutectic composition [36]. This is indicated in Fig. 5.1 (c) and (l). Local quantitative EDX analyses were undertaken for different phases marked by the dashed blue circles in Fig. 5.1 (c). The measured EDX composition of Bi rich phase (phase γ) is 91.2 wt.% Bi and 8.8 wt.% O. For intermetallic phase (phase β), it has 56.9 wt.% Pb, 35.1 wt.% Bi, and 8.0 wt.% O. A similar two-phase microstructure in the LBE region is also found at higher magnification using TEM, shown in Fig. 5.1 (k) and (l). Since the morphology appears the same aside from the depth of the corrosion paths, the sample corroded at 506℃ in a reducing environment will be analysed in detail in the following sections to illustrate the corrosion mechanism.

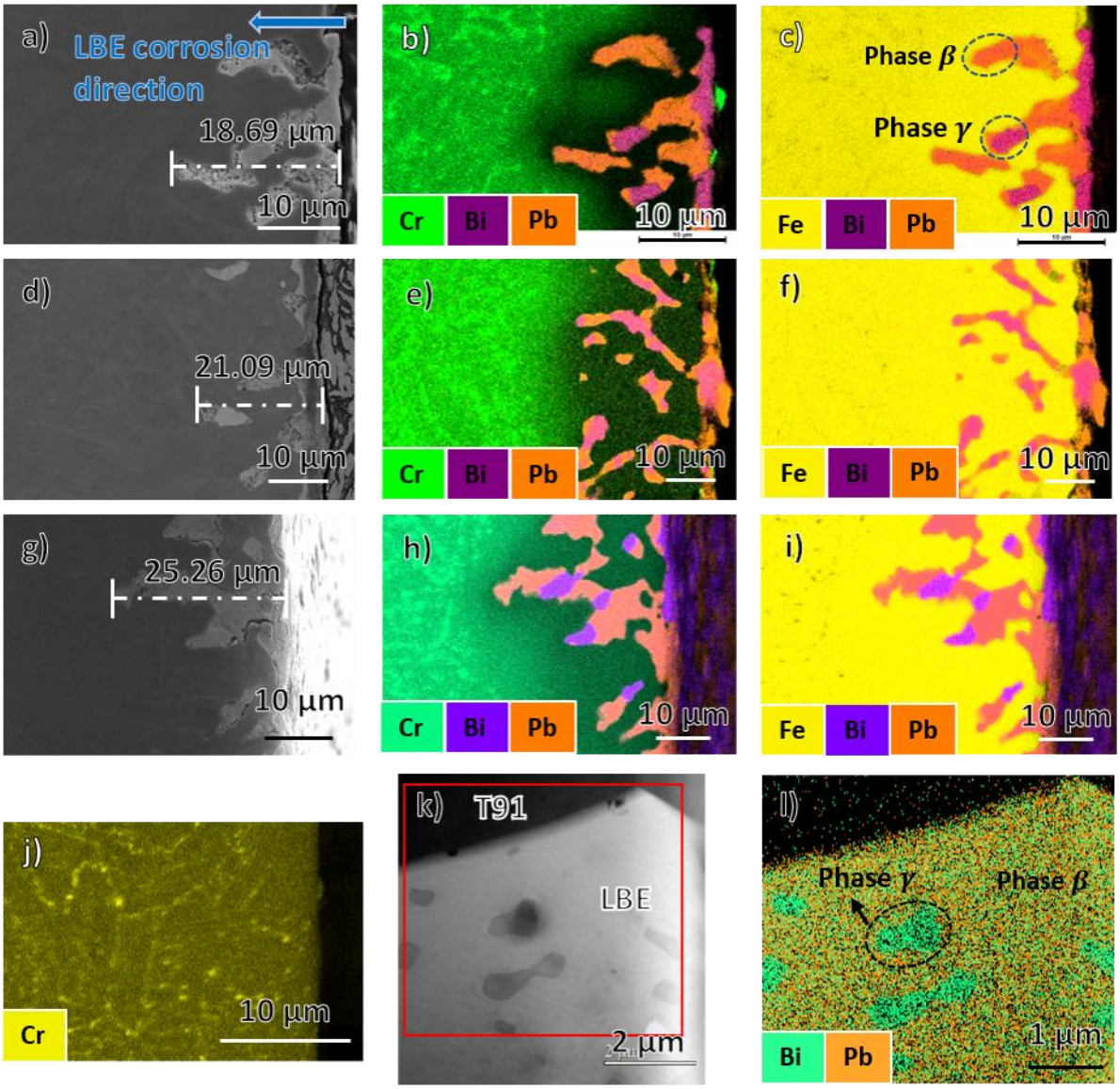

Fig. 5.1. Cross-section SEM micrographs for samples exposed to LBE corrosion in reducing environment for (a) 70h at 715℃, (d) 245h at 715℃, and (g) 506h at 715℃. SEM-EDX micrograph shows Cr, Bi, and Pb for samples exposed to LBE corrosion for (b) 70h at 715℃, (e) 245h at 715℃, and (h) 506h at 715℃. SEM-EDX micrograph shows Fe, Bi, and Pb for samples exposed to LBE corrosion for (c) 70h at 715℃ (highlighting the Bi-rich phase (γ) and an intermetallic phase (β) in LBE), (f) 245h at 715℃, and (i) 506h at 715℃. (j) SEM-EDX map of as-received T91 with Cr shown. (k) STEM HAADF showing features in the LBE region from the sample corroded at 715℃ for 506h. (l) STEM-EDX showing Pb and Bi in the red box region of (k) highlighting the Bi-rich phase (γ) and an intermetallic phase (β).

5.2.1.2 Depletion of Cr and Fe in the corroded region

The different depletion behaviour of Cr and Fe is characterised using SEM EDX. Fig. 5.2 (a) shows an SEM EDX map for the liquid metal attack channels with Cr depletion at a larger scale. The white box corresponds to the region of interest that is shown enlarged in Fig. 5.2 (b). For quantitative analysis, an SEM EDX line scan was applied as indicated by the white line in Fig. 5.2 (b). Based on the Cr content, the area in Fig. 5.2 (b) can be roughly divided into three regions: (1) the T91 matrix, which is yet to be influenced by the LBE; (2) the depletion region, where the depletion of Fe and Cr takes place, and (3) the LBE region, where all Fe and Cr are depleted and only LBE can be found. The original surface of the T91 sample is set to be the 0 µm reference point. The boundary between the uninfluenced T91 matrix and the original surface is at an approximate depth of 35 μm in the 506h corroded sample. According to the EDX line scan profile in Fig. 5.2 (b), if only considering the concentration along this line, the Cr content gradually decreases from ~ 9% in the steel matrix to ~0% at the LBE-steel interface across the 35 µm depth range. In comparison, the Fe content drops sharply from ~ 90% to almost 0% over the much smaller distance of ~1 µm from the LBE-steel interface. Interestingly the EDX map in Fig. 5.2 (b) shows that Cr depletion occurs to a roughly constant distance into the T91 steel, even though the LBE has penetrated to varying depths at different positions along the surface which is likely because there are LBE corrosion channels just outside the plane of this cross section (either deeper in the metal or the region which is polished away).

The gradual depletion of Cr was also measured by APT. In total 8 APT specimens were lifted out from the positions shown in Fig. 5.2 (c), with 5 of these successfully providing data in the subsequent analyses. All of the sampled regions were found to be homogenous, with the exception of APT specimen 3, which contained 2 small VN precipitates (APT reconstructions for these samples are provided in Fig. 5.3). The Cr content measured by APT at each of the respective depths below the surface is plotted in Fig. 5.2 (d), superimposed upon the SEM EDX

line scan that was conducted on the same region. The linear interpolation of the APT results matches well with the EDX measurements, providing some cross-validation for the Cr concentrations determined by SEM EDX.

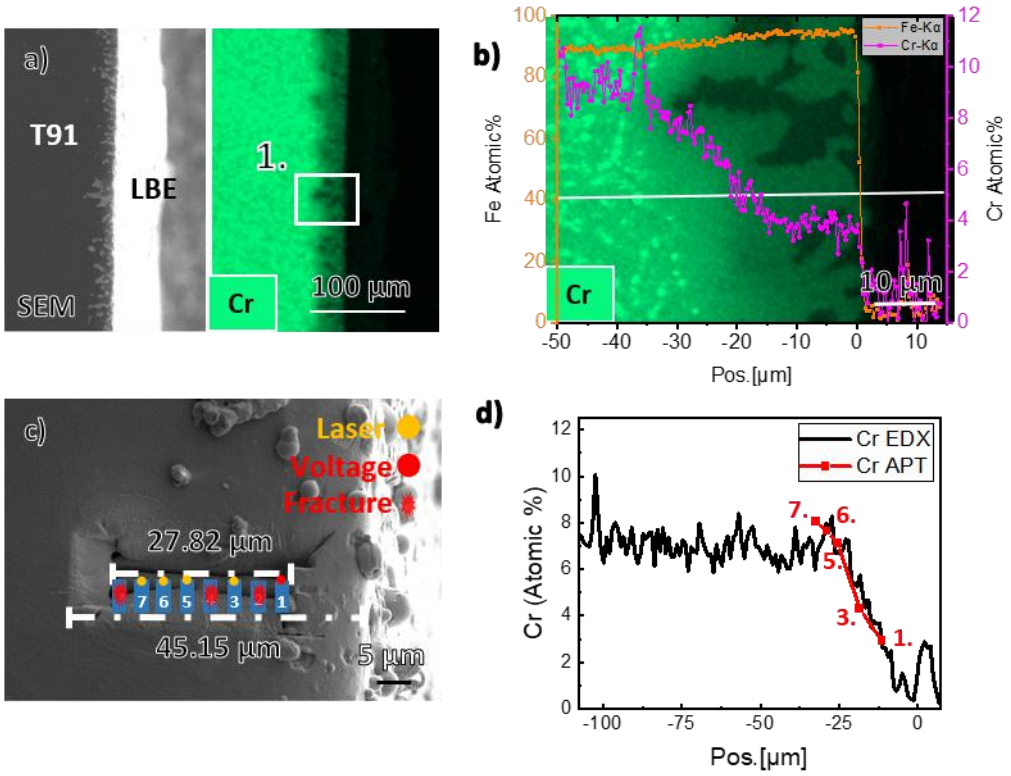

Fig. 5.2. EDX and APT analysis [Sample: 506 h, reducing environment, 715 °C, LBE] (a) SEM image and Cr - EDX map for a large cross-section area. (b) EDX map for the white box in part (a). The superimposed white line shows the position of the EDX line scan measurement. Plots of Fe and Cr content along the line scan are superimposed. (c) The APT lift-out bar and the sample positions. The samples that provided data are numbered. (d) Cr content for the same areas of APT lift-out bar from EDX line scan and APT samples in (c).

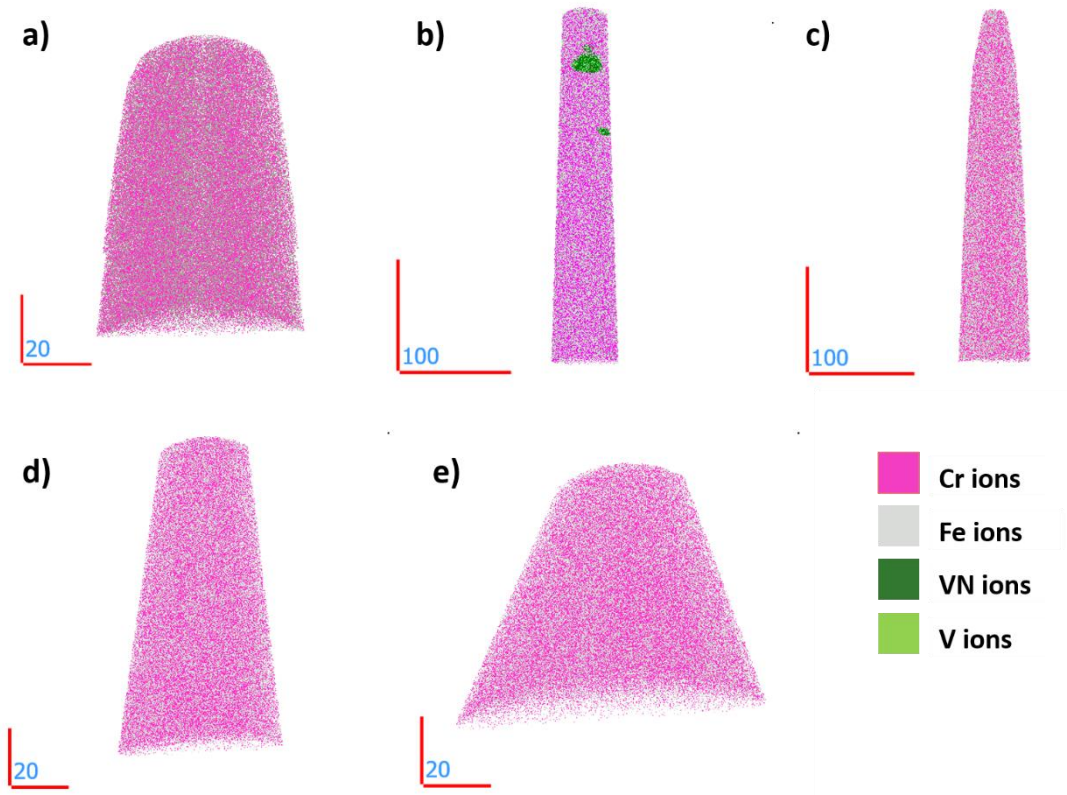

Fig. 5.3. APT results of samples exposed to LBE corrosion [Sample: 506 h, reducing environment, 715 ℃, LBE]. Only one sample contained a VN precipitate. (a) sample 1. (b) sample 3. (c) sample 5. (d) sample 6. (e) sample 7. The corresponding positions are shown in Fig. 5.2 of the main text.

5.2.1.3 Grain morphology change near LBE-exposed surface

EBSD was carried out for as-received T91 and corroded samples, respectively. The IPFZMap of as-received T91 (Fig. 5.4 (a)) shows that the matrix is mainly composed of martensite with a lath structure [217]. After the liquid LBE corrosion (Fig. 5.4 (b)), the grains near LBE intrusions exhibit a somewhat rounder shape, rather than a lath structure. However, the grain morphology on the left side of Fig. 5.4 (b) closely matches that of a sample of the as-received material which has experienced the same heat treatment but without exposure to the corrosive environment. This suggests that a restructuring or a phase change occurs in T91 near the corrosion region that is the result of high temperature LBE corrosion.

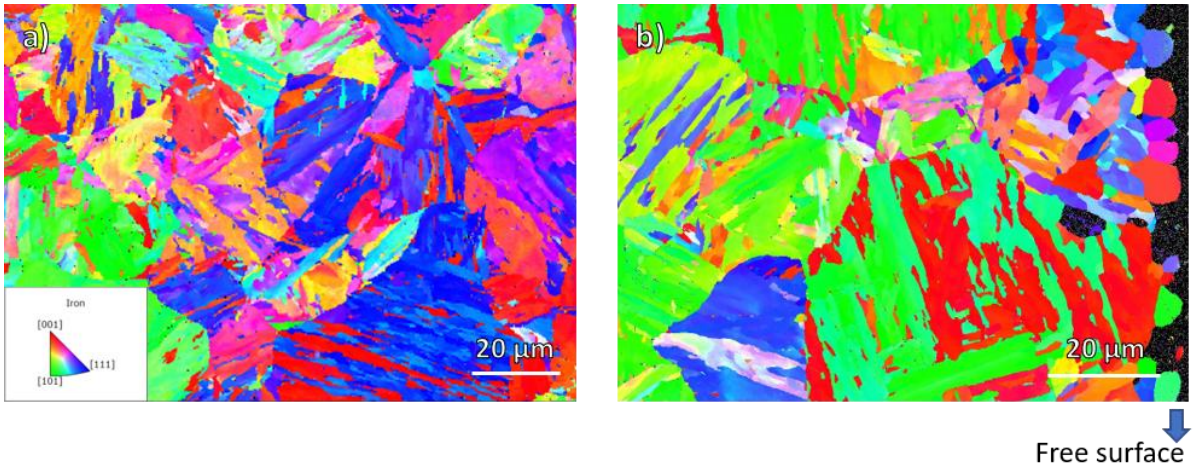

Fig. 5.4. EBSD examination of sample cross-sections: (a) EBSD IPFZ map for as-received T91. (b) EBSD IPFZ map for 506h, 715°C, reducing environment, LBE corrosion sample.

Further data analysis was conducted on the results presented in Fig. 5.5 to explore the potential relationship between grain orientation and corrosion tendency. The MTEX toolbox [218] was employed to process the data. The results are illustrated in Fig. 5.5.

The EBSD map for the sample corroded for 506 hours was divided into two sections, highlighted with red and blue rectangles, as shown in Fig. 5.5(a). The left section represents the uncorroded region, which corresponds to the as-received T91 material that underwent the same heat treatment as the corroded region. This approach helps mitigate any discrepancies due to heat treatment differences between samples. Fig. 5.5(b) displays the cropped EBSD map of the uncorroded region, while Fig. 5.5(c) shows the corroded region.

Figs. 5.5(d) and 5.5(e) present the MTEX analysis results for the uncorroded and corroded regions, respectively. These results detail the statistical distribution of grain orientations [111], [001], and [011] for IPFX, IPFY, and IPFZ. For illustrative purposes, the focus here is on IPFZ. In the uncorroded region, the grain orientation ratios are [011] > [001] > [111], whereas in the

corroded region, the ratios shift to [001] > [011] > [111]. This shift suggests that [011] grains in IPFZ may be more susceptible to corrosion in T91 exposed to LBE under a reducing environment.

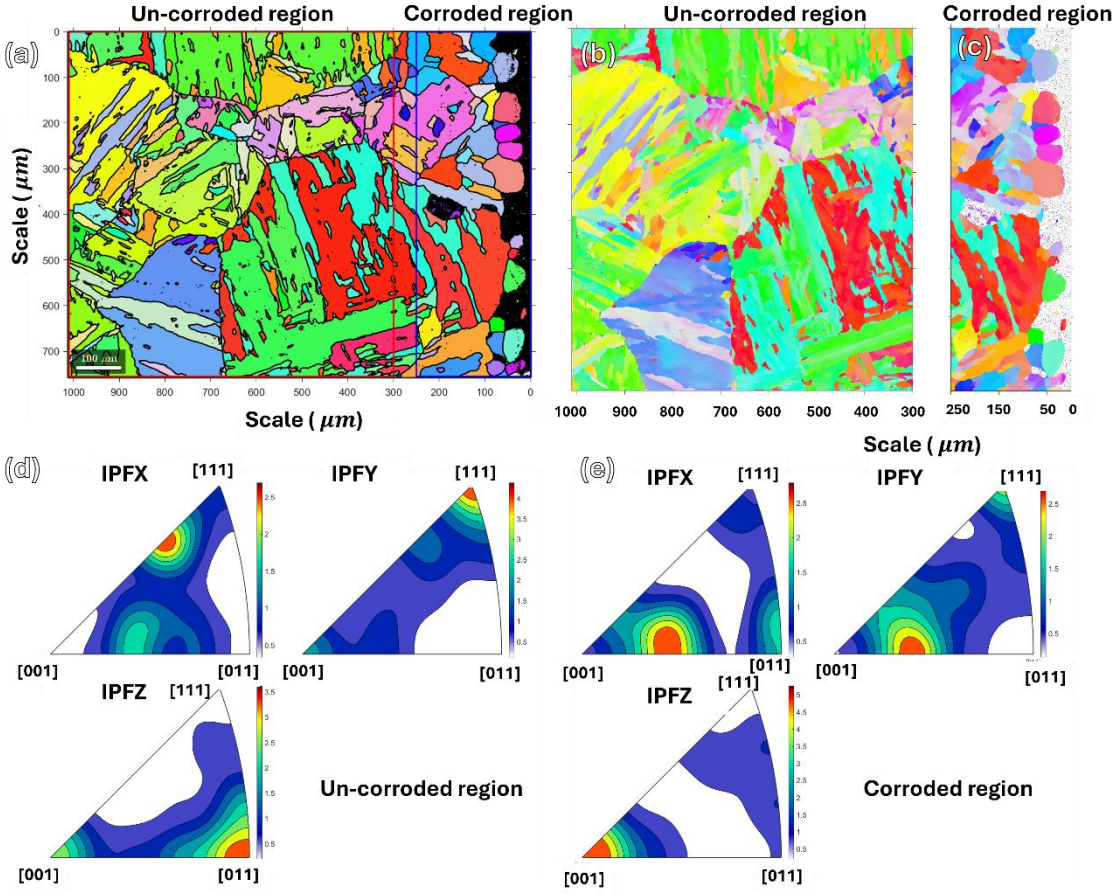

Fig. 5.5 (a) EBSD examination of sample shown in Fig. 5.4 (b) with red rectangle highlighting the un-corroded region and blue rectangle highlighting the corroded region [Sample: 506 h, reducing environment, 715 ℃, LBE]. (b) (c) EBSD result of the un-corroded region and corroded region shown in Fig. 5.5 (a), respectively. (d) (e) MTEX analysis results showing the ration of [111], [001], and [011] of IPFX, IPFY, and IPFZ for un-corroded region and corroded region respectively.

5.2.2 Nano-to-atomic scale characterisation of the LBE and T91 interface

To further examine the structure and chemical composition of the interface between the LBE and T91 matrix, two sets of APT samples and a plan view TEM sample were prepared. Nano-to-atomic scale analytical TEM (STEM), APT, and on-axis TKD were carried out.

5.2.2.1 Grain scale LBE corrosion of T91 steel

Fig. 5.6 (a) presents a cross-section SEM view of the 506h corroded sample. The porous areas are LBE, the progression of which appears to have been halted by particular grain boundaries. The same morphology can also be seen in Fig. 5.4 (b). A TEM sample was extracted from the area protected by carbon deposition in Fig. 5.6 (a). Fig. 5.6 (b) shows a STEM overview of the TEM sample. The bright area is LBE, while the darker region corresponds to the T91 matrix. From the contrast between different phases, there is no visible LBE penetration into surrounding grain boundaries. This is surprising since several previous corrosion studies observed grain boundaries to corrode preferentially. Their higher density of defects and less ordered atomic arrangement, compared to the material matrix, promote faster dissolution of elements into the coolant [219]. As a result, grain boundaries have been previously observed to be preferentially attacked by the coolant, manifested through the formation of thin, elongated corrosion patterns [220]. To further confirm that the LBE attack in T91 does not preferentially progress via infiltration of grain boundaries, STEM-EDX was carried out on the area marked by red box 1 in Fig. 5.6 (b). The results are shown in Fig. 5.6 (c), (d), and (e). The EDX results for other elements are shown in Fig. 5.7. While there are several grain boundaries surrounding the LBE region, neither Pb nor Bi penetrate along any of these. At the same time, Fe remains evenly distributed in the T91 matrix without depletion. These observations lead us to hypothesise that LBE corrodes the T91 matrix in a grain-by-grain fashion, resulting in thick channels of liquid metal attack, rather than nano-scale infiltration along grain boundaries. The rationale for, and proposed mechanism of, Fe

dissolution into the LBE following Cr dissolution in the LBE will be reviewed thoroughly in the Discussion section below.

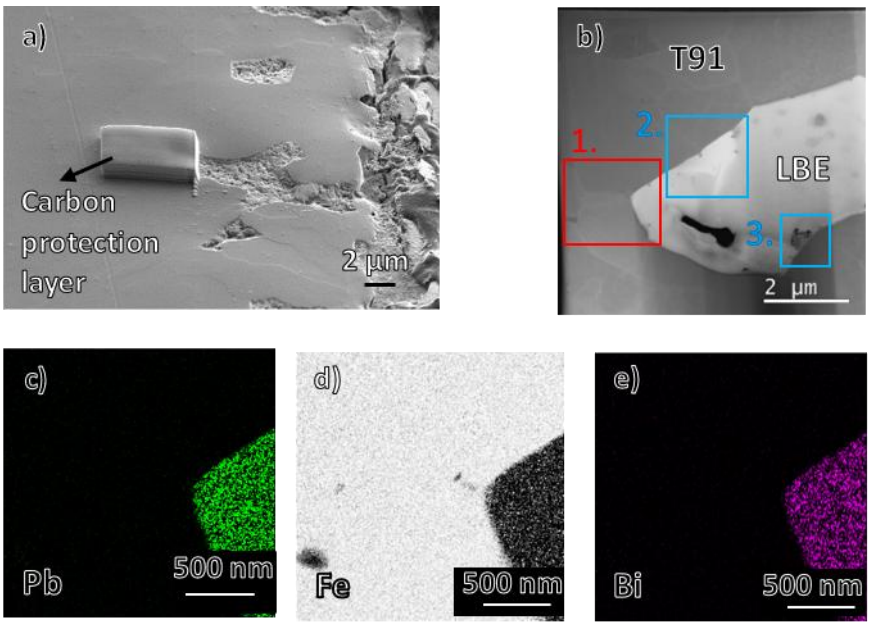

Fig. 5.6. TEM imaging [Sample: 506 h, reducing environment, 715 ℃, LBE]: (a) SEM view showing the location from where the TEM lift-out sample was taken (underneath the carbon protection layer) relative to the bulk sample. (b) STEM HAADF view of the TEM lifts out the foil. The bright region is LBE, while the dark region is the T91 matrix. EDX mapping was carried out in the red box and the corresponding maps of certain elements are shown in (c) Pb, (d) Fe, and (e) Bi.

Two corroded regions of particular interest can be identified in the TEM sample which are marked with blue boxes in Fig. 5.6 (b). Fig. 5.7 (a), a detailed view of blue box 2 in Fig. 5.6 (b), shows a Fe-rich region, highlighted by the red dashed curve, in the LBE. The interface between T91 steel and LBE is marked by a straight dashed yellow line. According to the EDX results in Fig. 5.2, the LBE region is expected to have no Fe and high levels of Pb, respectively. However, the EDX maps in Fig. 5.7 (b) and (c) clearly indicate a substantial Fe content still in the LBE-rich region. This suggests a partly corroded grain, before the Fe content (and therefore the entire grain) is fully removed by the LBE.

Fig. 5.7 (d) shows a detailed view of the region highlighted by blue box 3 in Fig. 5.6 (b). Here a multi-phase structure can be seen. The corresponding EELS results, in Fig. 5.7 (e), show that this structure contains negligible Fe. Instead, EELS analysis in Fig. 5.7 (f) reveals the presence of a thin oxygen-enriched layer at the interface of LBE and T91 matrix. The EDX results from the same area further corroborate the EELS results and are included in Fig. 5.7.

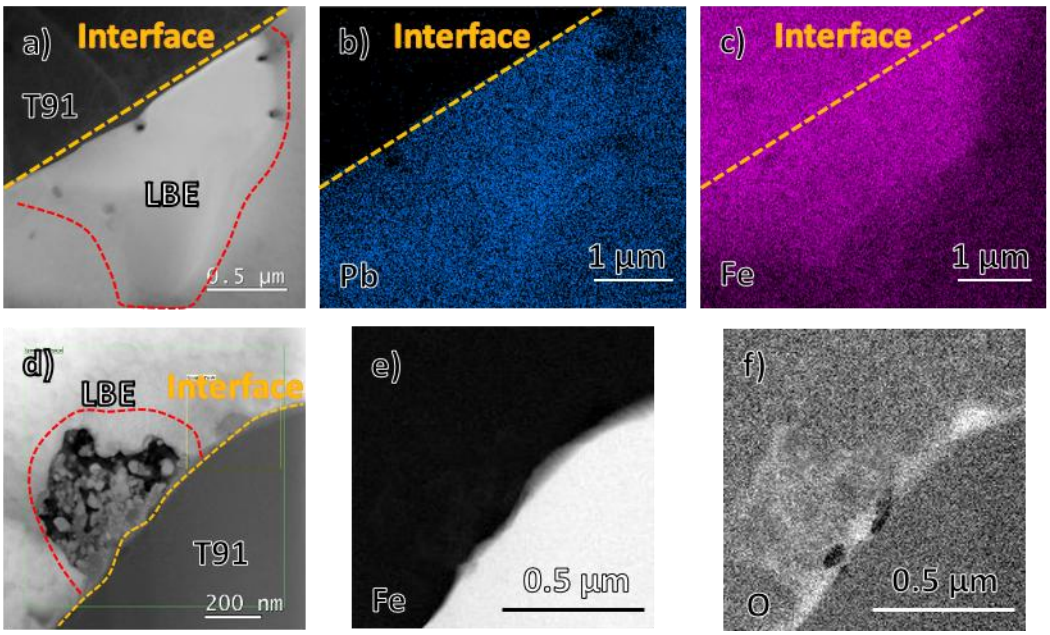

Fig. 5.7. STEM investigation of two regions of interest in Fig. 4 (b) [Sample: 506 h, reducing environment, 715 ℃, LBE]. (a) shows a STEM HAADF image corresponding to blue box 2 in Fig. 5.6, (b) and (c) show the EDX maps of Pb and Fe respectively. (d) shows a STEM HAADF image corresponding to blue box 3 in Fig. 5.6, (e) and (f) show the EELS maps of Fe and O respectively.

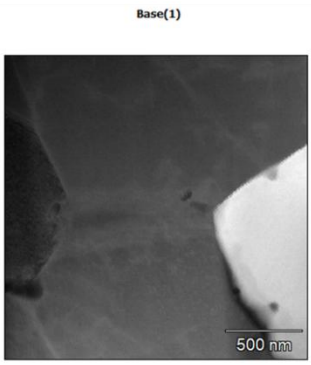

TEM-EDX

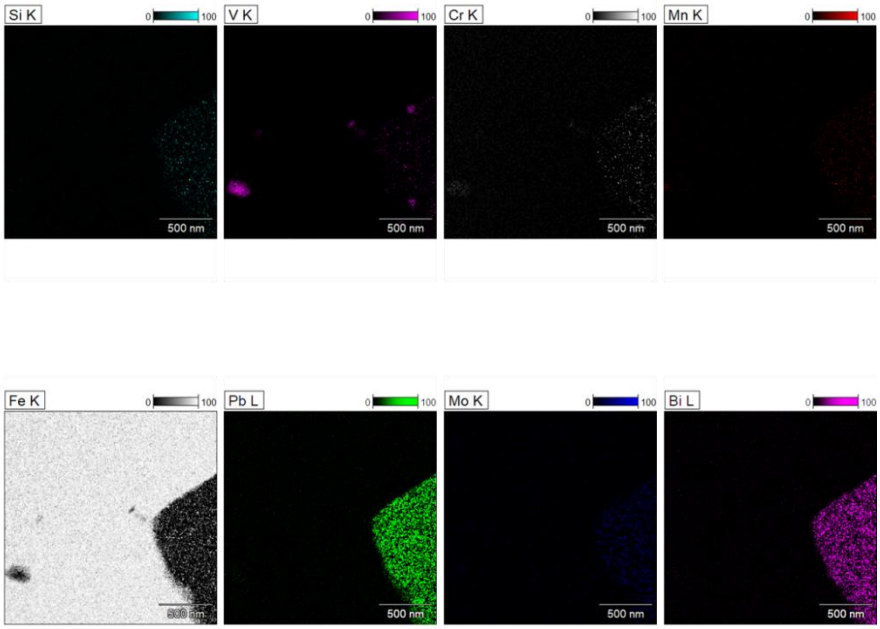

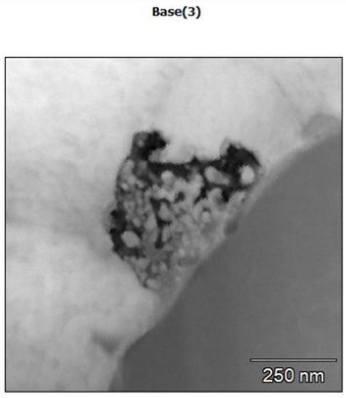

TEM-EDX

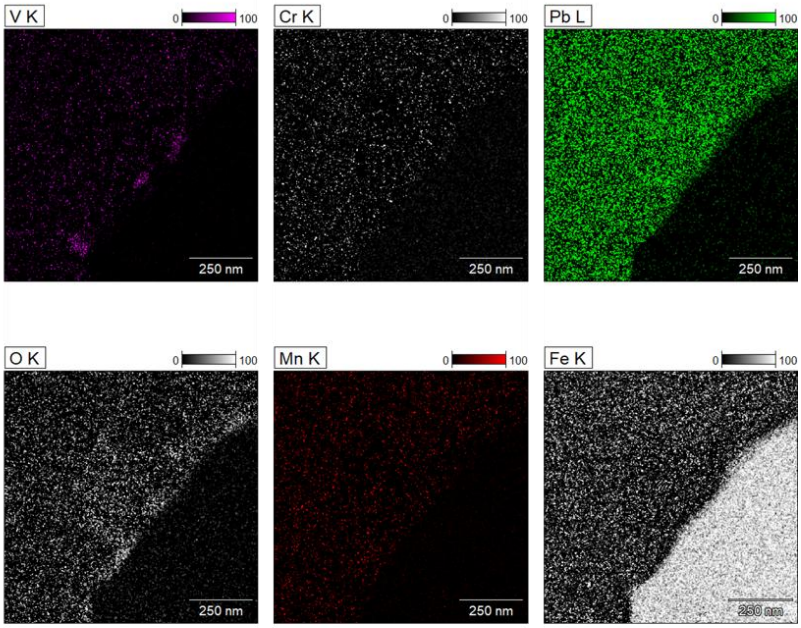

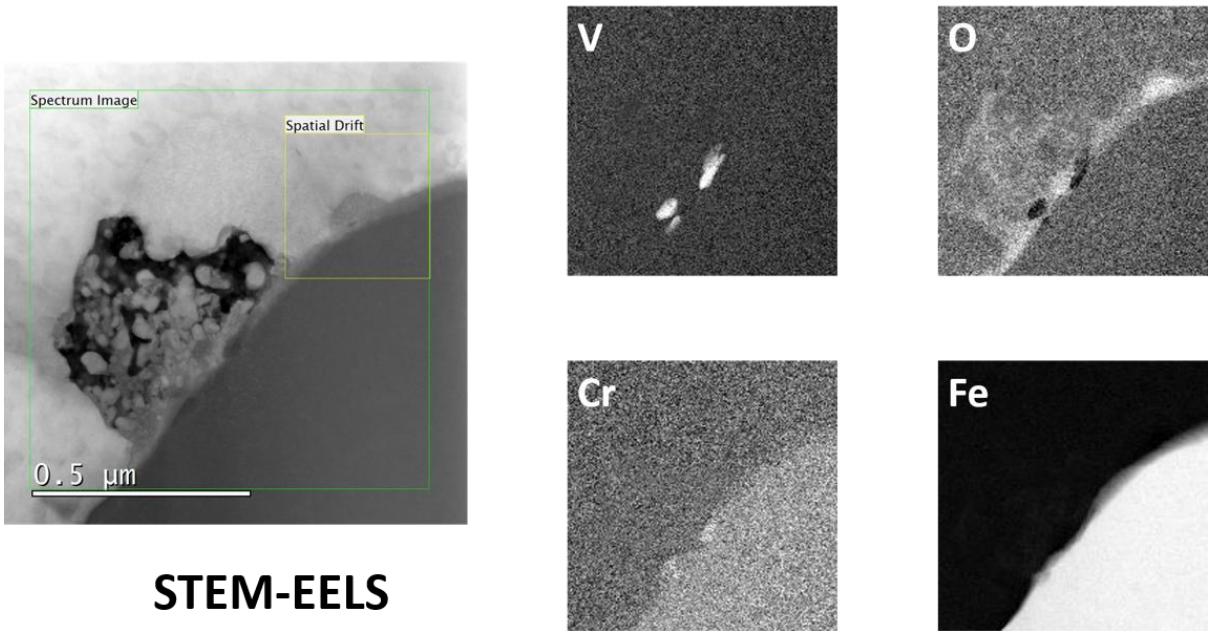

Fig. 5.7. EDX and EELS maps for other elements in Fig. 5.6 and Fig. 5.7 [Sample: 506 h, reducing environment, 715 ℃, LBE].

5.2.2.2 Oxide layer at the corrosion interface

Fig. 5.7 (f) shows an oxygen-rich layer at the interface of LBE and T91 matrix. Detailed analysis is carried out using STEM imaging, EDX, EELS and APT, respectively. A representative STEM low-angle annular dark field (LAADF) image is presented in Fig. 5.8 (a), with several further examples included in Fig. 5.10. Fig. 5.8 (a) shows an interface thickness of ~50 nm. The thickness varies depending on position but is generally on the order of tens of nanometres.

Spectroscopic analysis of the interface is reported in Fig. 5.8 (b), (c) and (d). Fig. 5.8 (b) shows a STEM high-angle annular dark field (HAADF) image taken close to the interface, where the dark region corresponds to the uncorroded T91 grain and the bright region corresponds to the LBE-rich area. An EDX line scan was carried out across the interface along the arrow in Fig. 5.8 (b). The results, shown in Fig. 5.8 (c), suggest that a layer of Fe oxide has been formed at the interface. This is further confirmed by the comparison of EELS core loss spectra, shown in Fig.

5.8 (d), recorded in the two locations marked in Fig. 5.8 (b). The core loss spectrum comes from the energy loss due to interaction between the incident electrons and the inner shell electrons of the elements in the specimen [190]. The excitation of the specimen electrons depends on two states, the initial state that is characteristic to specific elements, and the final state that depends on the local bonding environment. Therefore, a shift of several eV of the core loss edge will be identified for atoms of the same elements but of different valence states [190]. The energy shift of the Fe L3 edge in Fig. 5.8 (d) indicates that the Fe found in region 2 has been oxidised to a higher valence state than the unoxidised Fe found in region 1 [221].

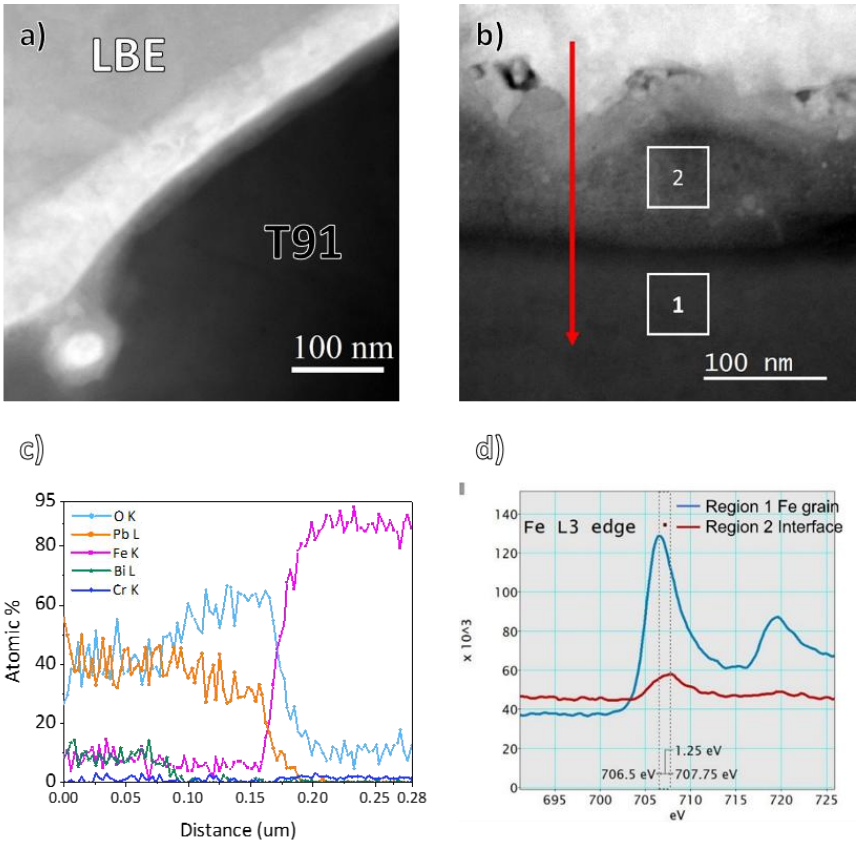

Fig. 5.8. Oxide layers at the interface between LBE and T91 of 506h, 715℃, reducing environment, LBE corrosion sample. (a) (b) STEM micrographs of interfacial oxide layers in two different sample regions. (c) EDX line scan along the red arrow in (b). (d) Comparison of EELS spectra extracted from regions 1 and 2 in (b).

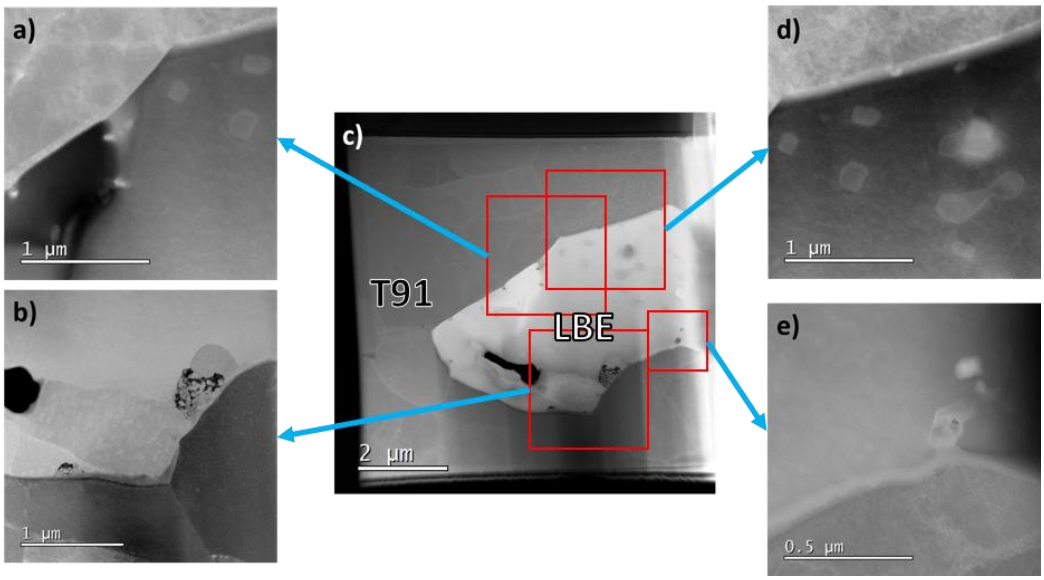

Fig. 5.10. STEM images of several positions around the LBE ingress of 506h, 715℃, reducing environment, LBE corrosion sample. All images show the presence of a thin oxide layer.

However, from the STEM and EELS results, it is difficult to determine the nature of the oxide and oxide distribution at the interface. Thus, APT was used to further analyse the LBE T91 interface in the 506h, 715℃ corrosion sample. An interfacial oxide layer, consistent with the observations in Fig. 5.8, is also present in the APT data. Fig. 5.11 (a) shows the distribution of Fe, Pb, O, and Cr ions in the 3D APT reconstruction. The reconstructed sample exhibits a three-layer structure with LBE as the top layer, a thin oxygen-enriched layer in the middle, and the T91 steel matrix at the bottom. Fig. 5.11 (b) and (c) show the distribution of detected complex Fe oxide ions and Cr oxide ions. Note that APT reconstructions in Fig. 5.11 (b) and (c) have been rotated anticlockwise by 90° compared to Fig. 5.11 (a). The detection of complex ions is an artefact of the APT experiment and the form of ions observed does not necessarily imply information about the material phase from which they were evaporated [193]. By comparing Fig. 5.11 (b) and (c), several conclusions can be reached: Firstly, Fe oxide ions are distributed relatively uniformly throughout the interface, while Cr oxide ions tend to accumulate in specific areas. Secondly, locations with an increased presence of Cr oxide have less Fe oxide. Inspection of the

distribution of other metal oxide ions, such as Ni and V, show higher concentrations at the same locations as Cr oxide ions. This data can be viewed in Fig. 5.12. Fig. 5.11 (d) is a proximity histogram (proxigram) analysis showing how elemental concentrations change across the oxide from LBE to T91 matrix. In this proxigram analysis, a Pb iso-concentration value of 60 at. % is chosen to define the position of the LBE-oxide interface (i.e. 0 nm on the proxigram) with a 1 nm bin size for each step in the histogram. The thickness of the Fe depleted region is ~26 nm, which agrees with the rapid drop in Fe content as measured by SEM-EDX (Fig. 5.2 (b)), and confirms the much shorter depletion distance of Fe compared to Cr. The thickness of the oxide layer measured by APT (~32 nm) is in good agreement with the thicknesses determined by STEM in Fig. 5.8 (a) and (b).

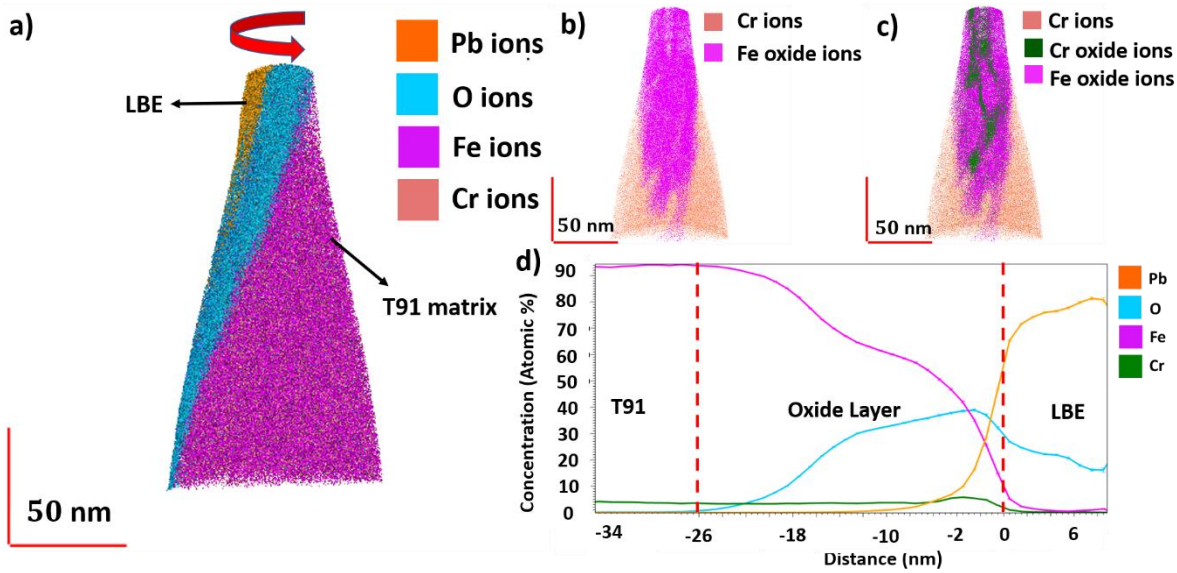

Fig. 5.11. APT characterisation of the LBE – T91 interface [Sample: 506 h, reducing environment, 715 °C, LBE]. (a) 3D APT reconstruction showing Pb, Cr, Fe, and O ions. (b) 3D APT reconstruction showing iron oxide and Cr ions. (c) 3D APT reconstruction showing iron oxide, chromium oxide, and Cr ions (d) Proxigram showing elemental concentration changes normal to the T91 – LBE interface (Pb isoconcentration value = 60 at. %).

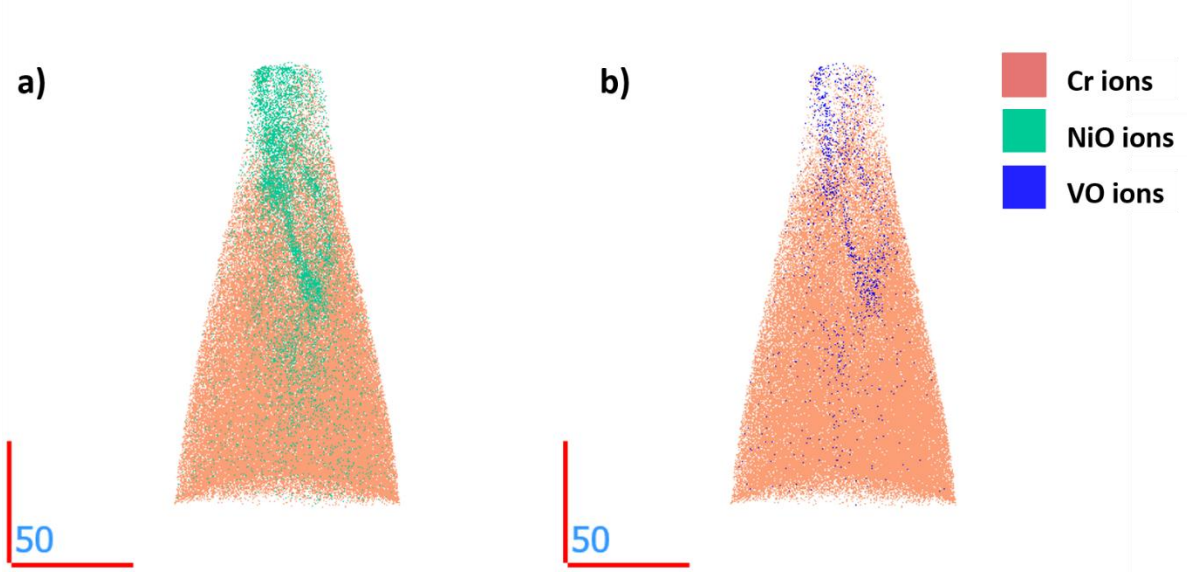

Fig. 5.12. 3D APT reconstruction showing Ni oxide, V oxide, and Cr ions [Sample: 506 h, reducing environment, 715 ℃, LBE].

APT enables further nanoscale analysis of the microstructure within the oxide layer [222]. Fig. 5.13 (a) highlights the region where Cr oxide ion concentration is higher than 5.5 at. % within the APT sample. We observe Cr oxide ions in two distinct types of structures that appear to correspond to distinct, newly formed small oxide phases or segregation at grain boundaries. Different Cr-oxide-ion-enriched structures, marked by the pink circles in Fig. 5.13 (a), are investigated in detail by comparing the local composition. Compositions were measured in three blue, cuboidal ROIs created within different structures marked by pink circles (see Fig. 5.13 (a)). The measured compositions are listed in Table 5.1 and plotted in Fig. 5.13 (d) with the as-received T91 measured by APT (Table 3.1) also presented. Region 1 in Fig. 5.13 (a), represents a possible Cr oxide phase formed during corrosion; Region 2 corresponds to a grain boundary segregation; Region 3 measures the composition of the surrounding oxide material as a reference. The composition results in Fig. 5.13 (d) show that region 1 is mainly composed of Cr and O with relatively low Fe content and high Mn content compared to regions 2 and 3. The Pb content is also very low in this region. For region 2 the main constituents are O and Fe. The Cr

content is lower than in region 1, but still significantly higher than in the surrounding oxide measured in region 3. Region 2 also contains more Pb than the other two areas. In region 3, i.e. the surrounding oxide phase, there is a very limited amount of Cr and Mn. The Pb content is less than in region 2 but still significant. Comparison of the chemical composition in the three regions, suggests that they correspond to different types of structures. Region 1 most likely represents the Cr oxide phase formed on the surface. However, due to the low oxygen content and lack of Cr, it forms a discontinuous structure, rather than a layer of chromium oxide across the surface. Mn accumulation in the Cr oxide phase is shown in Fig. 5.13 (b). Fig. 5.13 (c) provides the Bi distribution within the sample. Interestingly, more Bi ions are incorporated in the Cr oxide phase than in the surrounding areas. This can be stated with some certainty since there are no overlap issues between Bi and Cr oxide ions in the APT mass spectrum.

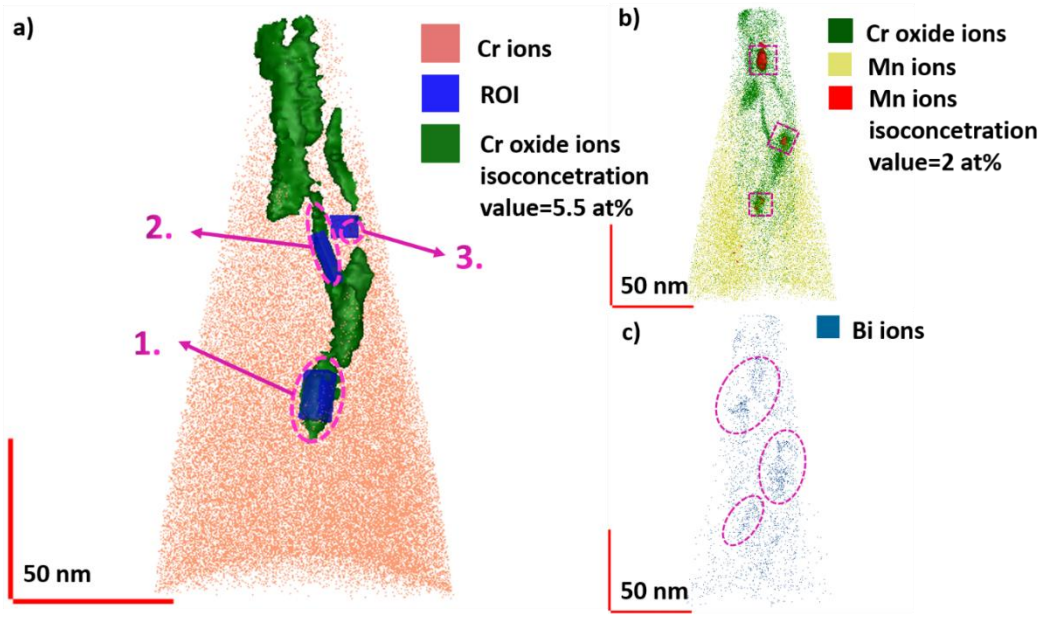

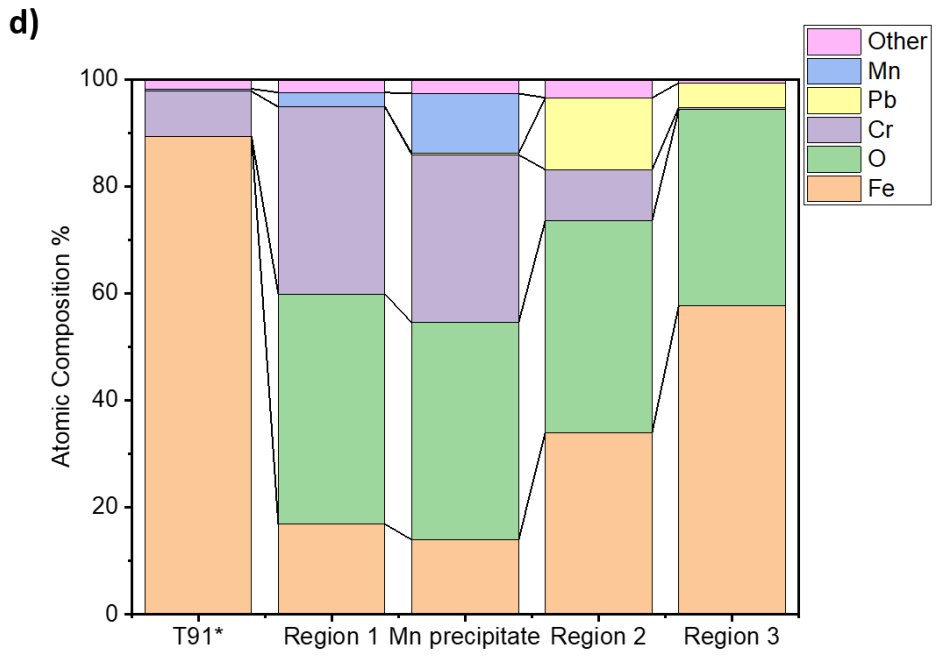

Fig. 5.13. Detailed analysis of Cr oxide structures in the APT reconstruction [Sample: 506 h, reducing environment, 715 ℃, LBE]. (a) APT 3D reconstruction with different chromium oxides highlighted. (b) APT 3D reconstruction with Mn-enriched precipitates. (c) APT 3D reconstruction showing Bi. (d) the concentration of 3 ROI highlighted in Fig. 8 (a), Mn precipitates, and as-received T91 listed in Table 3.1.

Table 5.1. Compositions of different regions of the APT sample shown in Fig. 7 and 8 [Sample: 506 h, reducing environment, 715 ℃, LBE].

Atomic Percent (%)	Region 1	Region 2	Region 3	Mn precipitate
O	43.01	39.65	36.61	40.56
Cr	34.96	9.52	0.42	31.41
Fe	16.86	33.96	57.69	13.94

Mn	2.66	0.02	0	11.20
Ni	1.40	1.72	0.31	1.18
V	0.33	0.63	0	0.35
Co	0.27	0.10	0.06	0.49
Mo	0.06	0.82	0.18	0.10
Pb	0.04	13.41	4.60	0.24

5.2.2.3 V-enriched precipitates at the corrosion interface.

EDX mapping was applied to the opposite side of the entire TEM sample in Fig. 5.6 (b). The results in Fig. 5.14 (a) show a population of V-enriched precipitates. Compared to the Cr-enriched precipitates in Fig. 5.1 (b), Fig. 5.1 (e), Fig. 5.1 (h) and Fig. 5.2 (b) that disappear from the Cr-depletion region, it is apparent that the V-enriched precipitates are more resistant to LBE corrosion. The Observations suggest that the density of V-enriched precipitates is higher at the T91 and LBE interface than in other areas. On-axis TKD was used on the area marked with a red rectangle in Fig. 5.14 (a) to identify different phases based on their crystal structure. In Fig. 5.14 (b) V-precipitates appear as yellow, which corresponds to a cubic, rock-salt crystal structure. VC and VN have the same space group and very similar lattice parameters, which makes it challenging to distinguish them using TKD. Fig. 5.14 (c) and (d) show EELS analysis corresponding to Fig. 5.7 (d). They confirm that the precipitates are vanadium-rich nitrides. In the set of APT samples lifted out near the corroded interface (Fig. 5.2 (c)), one sample contained V-enriched precipitates that were found to be V nitride based on the APT mass spectrum analysis. Fig. 5.14 (e) shows the APT analysis of this sample, and Fig. 5.14 (f) provides a proxigram analysis, with the interface defined by a VN iso-concentration of 0.83 at% of VN with 0.1 nm bin size for the histogram. The proxigram analysis suggests that these V nitrides contain higher Nb content than

in the surrounding matrix, i.e. the right side of the profile represents the composition of the VN precipitate, with a concentration of Nb ~ 5 at. %, whereas left side is T91 matrix, with Nb content ~ 0 at. %.

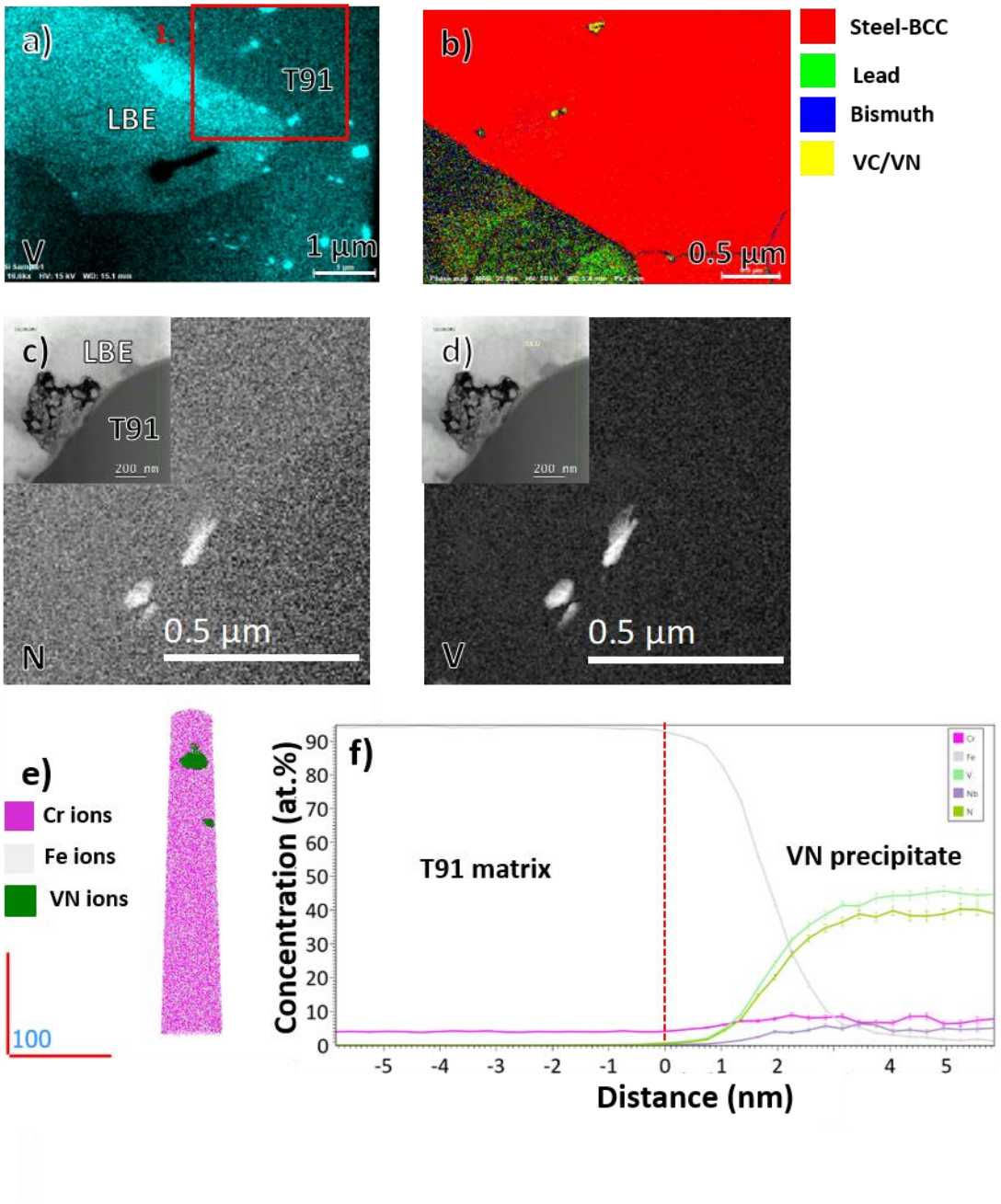

Fig. 5.14. Detailed analysis of V-rich precipitates near the LBE T91 interface [Sample: 506 h, reducing environment, 715 ℃, LBE]. (a) TEM-EDX for V on the sample examined in Fig. 5.6 (b). (b) on-axis TKD phase map for the red box 1 in Fig. 5.14 (a). (c), (d) STEM-EELS for N and V on the sample examined in Fig. 5.7 (d), also shown inset. (e) 3D APT reconstruction of a liftout sample

containing a V-enriched precipitate (also can be found in Fig. 5.3 (b)). (f) Proxigram centred on the interface between the T91 matrix and the V-enriched precipitate in (e).

5.3. Discussion

5.3.1 The control mechanisms for the dissolution of Cr and Fe in LBE

In the static corrosion system discussed in this chapter, the dissolution of T91 elements in LBE is the main part of the corrosion mechanism investigation. Thus, it is necessary to work out the control mechanisms which decide how much Fe and Cr can dissolve in the LBE. To make it clearer, we can discuss it by dividing the controlling mechanisms to 3 parts by the positions where it dominates. For the restrictions work in LBE, we classify it as outer factor; For the restrictions dominate at the LBE and T91 interface, we classify it as inner factor; For the restrictions control in T91, we classify it as internal factor.

For the mechanism works in LBE, we refer it as the outer mechanism. It is mainly influenced by the diffusion rate of Fe and Cr in LBE which decides the corrosion product transport rate in LBE [4].

For the mechanism that works at the interface of LBE and T91, we refer to it as an interfacial mechanism. It mainly refers to the solubility of Fe and Cr in LBE which can also indicate as saturation content of Fe and Cr in LBE.

For the mechanism that works in T91, we refer to it as an internal mechanism. It is mainly dominated by the diffusion rate of Fe and Cr in T91. After the Fe and Cr at the interface of T91 and LBE are dissolved, a concentration gradient will be built up between the interface of T91 and LBE and the unaffected T91 matrix. Thus, the Fe and Cr from unaffected T91 matrix will diffuse to the interface which allows more Fe and Cr dissolve into the LBE. However, with the

diffusion scale getting larger, the concentration gradient decreases which will slow down this process according to Fick's diffusion law.

These 3 mechanisms are the main ones which effect how much Fe and Cr can dissolve into the LBE. The firstly reached one will be the decisive mechanism. The following phenomenon will happen with different dominant mechanisms:

- When the dissolution is controlled by the outer mechanism: the concentration at the interface is always at saturation and the corrosion rate is determined by the diffusion rate of corroded product in LBE. This will be observed in a gradually deeper corrosion zone with a longer corrosion duration time which allows the corroded products to have a longer time to diffuse.
- When the dissolution is controlled by the interfacial mechanism: the diffusion rate in LBE is fast enough to take all the dissolved species and the Fe and Cr from the unaffected T91 matrix can supply enough elements. The corrosion rate is determined by the solubility. However, with the volume of LBE provided in this test, the interfacial mechanism shouldn't be a control factor here.
- When the dissolution is controlled by the internal mechanism, the corrosion process is limited by the supply of Fe and Cr from the unaffected T91 matrix. All the Fe and Cr diffuse to the interface can be dissolved into LBE. As a result, a constant distant depletion zone will be developed.

From our results in Fig. 5.1, we can observe deeper LBE intrusions with longer test time (from 70h to 245h and then to 506h) and Fe does not show obvious depletion across the samples. However, for depletion depth of Cr measured from the deepest LBE intrusion (~0 at. % Cr) to the position where the Cr concentration returns to the bulk value of 9 at. % shows a similar Cr depletion depth of ~5 μm for both 506 h and 70 h corroded samples as shown in Fig. 5.1 (d), (e), (h) and Fig. 5.2 (b). Thus, it is reasonable to suggest that Fe dissolution in LBE is controlled by

the outer mechanism and Cr dissolution in LBE is controlled by the internal mechanism. At the same time, considering the Fe and Cr depletion depth difference, the Cr should diffuse faster into the LBE than Fe at the beginning of the corrosion.

5.3.2 Cr removal from the T91 matrix

To explore the mechanisms underpinning the observations presented in this study, the behaviour of Cr in the corroded T91 was then focused on. According to the dissolution speed of elements in T91, as observed in previous studies and verified here, Cr diffuses from a further distance within the T91 to dissolve into liquid LBE in comparison to Fe [26]. When the steel is in contact with liquid LBE, Cr starts to dissolve into the LBE from both grain boundaries and matrix. Grain boundaries can act as fast diffusion paths according to literature [219], though no preferential Cr removal from grain boundaries was observed in this chapter. The Cr depletion in the surrounding matrix induces the dissociation of local Cr-enriched precipitates both at prior-austenite grain boundaries and martensite block boundaries. This process can be observed in Fig. 5.1 (b) , (e), (h) and Fig. 5.2 (a), (b) which show the Cr depletion and precipitate dissociation, consistent with previous observations [223]. From the line scan in Fig. 5.2 (b), the start of Cr precipitates dissolution corresponds to only a slight drop in the surrounding Cr matrix content below approximately 8 at. %. In future it would be interesting to investigate the stability of Cr-containing precipitates as a function of the matrix Cr content from a theoretical perspective. After the Cr precipitates dissociate, residual Cr in the matrix further diffuses to and dissolves into the LBE, leading to the Cr concentration gradient near the T91-LBE interface seen in Fig. 5.2 (b).

In the present geometry, the Cr concentration difference is fixed (from 9 at. % in the matrix to ~0 at. % at the LBE-T91 interface as per EDX linescan). The depletion depth is measured from the deepest LBE intrusion (~0 at. % Cr) to the position where the Cr concentration returns to the bulk value of 9 at. %. Fig. 5.1 (d), (e), (h) and Fig. 5.2 (b) show a similar Cr depletion depth of ~5

µm for both 506 h and 70 h corroded samples. This suggests that the Cr depletion depth from the furthest LBE ingress is roughly constant as a function of time. This is further confirmed by systematic EDX scans that all show similar depletion depths across a range of different positions on the sample surface and for different exposure times, respectively (see Fig. 5.15). The concentration gradient can be approximated by the concentration difference across the depletion depth. Thus, samples exposed for different lengths of time have similar Cr concentration gradients. This could be qualitatively explained by the following mechanism: The Cr dissolution speed is expected to decrease as the concentration gradient decreases, i.e. as the depletion depth increases. As more and more Cr is dissolved, the Cr dissolution rate will eventually reduce to a level at which the ratio of dissolution of Cr and Fe remains approximately constant. Fe dissolves into the liquid LBE resulting in the very steep concentration gradient seen in Fig. 5.2 (b). Thus, a steady state develops, with an approximately constant Cr depletion distance from the moving interface associated with LBE intrusions.

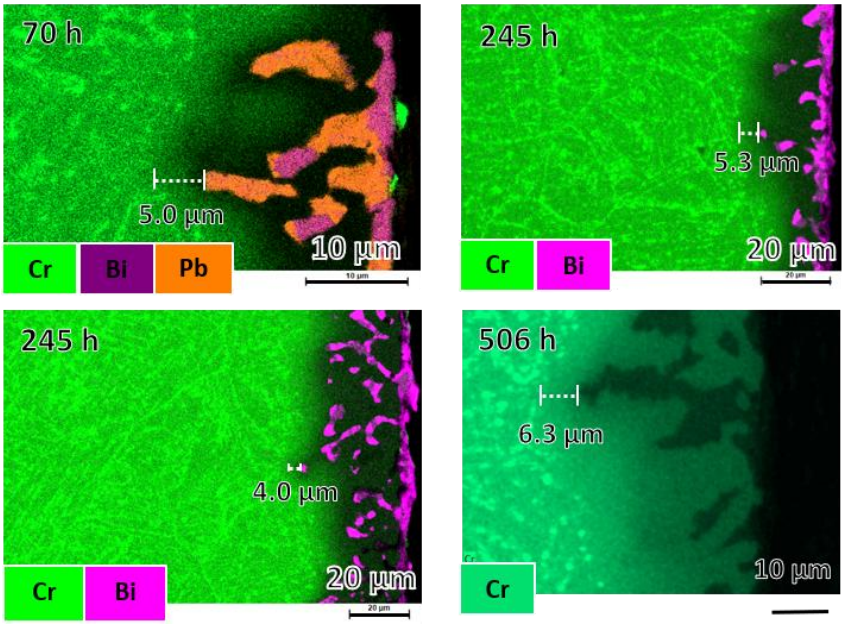

Fig. 5.15. SEM-EDX maps for different exposure time LBE corroded T91. We note that the Cr depletion depth is similar for all exposure durations [Sample: reducing environment, 715 °C, LBE].

5.3.3 Preferential path for LBE corrosion

Our characterisation shows that LBE corrosion advances through attack patterns of thick liquid intrusions (e.g. Fig. 5.2 and Fig. 5.6). This corrosion mechanism is different to that observed in previous studies of molten salt corrosion [224-226] and even some previous studies of LBE corroded austenite [18, 22, 227] and ferrite/martensite [25, 228]. The corrosion of molten salt has been previously observed as a preferential attack on grain boundaries. The underlying mechanism is the de-alloying of Cr from the steel matrix, with a preferential intrusion of molten salt as a thin layer following grain boundaries. Austenite was observed corroded with large area ferritization. LBE corrosion results show no clear correlation of LBE intrusions with grain boundaries. The width of the liquid LBE intrusions is around 2 µm, which is similar to the typical width of martensite lath blocks or packets in T91 [229]. The surprisingly consistent width of corrosion channels suggests a characteristic length scale. Furthermore, from the STEM HAADF image in Fig. 5.6 (b), the LBE liquid attack channel does not show any local penetration along grain boundaries. This is very different to the wetting of grain boundaries observed e.g. in the molten salt attack [230]. Instead, in the case of LBE, where grain boundaries meet the LBE interface, a blunt corrosion front is seen. Fig. 5.6 (c) also shows that there is no lead or bismuth detected in the surrounding grain boundaries meeting the LBE. This is potentially related to the fact that Pb and Bi atoms are much larger than oxygen or other atoms that can use grain boundaries (GBs) as fast diffusion paths. Their larger size creates a higher barrier for Pb and Bi atoms to utilise GBs as rapid diffusion pathways.

In addition to the lack of a clear correlation with grain boundaries, LBE corrosion also exhibits uneven corrosion across the sample surface, as shown in Fig. 5.1. Varying levels of grain recrystallisation are observed, as shown in Fig. 5.4. This may be related to differences in grain orientation, grain strain, and surface roughness of the sample.

Interestingly, larger-scale characterisation showed that there is some correlation of corrosion channels with prior austenite grain boundaries [28]. Overall, a picture emerges where there is no wetting of grain boundaries by the LBE, but where LBE corrosion progresses more quickly in regions of high disorder is observed, e.g. triple junctions and prior austenite grain boundaries.

5.3.4 Oxide layer at corrosion interface

Both the STEM results in Fig. 5.7, Fig. 5.8, and the APT analysis in Fig. 5.11, independently confirm the formation of a thin oxide layer (10s of nm) at the interface of LBE and T91 matrix in the 506 h corroded samples. According to literature, an oxygen content above 10^{-6} wt. % and temperatures below 600℃ [231, 232] are required for the formation of a passivating oxide layer. Thus, passivation is not expected in the present case because the oxygen content in the LBE in this experiment is 1.8×10^{-9} wt.% and the temperature is 715 ℃. Rather we observe the formation of discontinuous Cr oxide islands within the thin layer of Fe-rich oxide (see Fig. 8). In addition, because of the Cr dissolution in LBE, the Cr content at the interface is low, which may further contribute to the discontinuous Cr oxide growth.

The corrosion experiment took place in reducing conditions, as indicated by the Ellingham diagram [26, 233], which predicts that the environment lacks oxygen to spontaneously form iron oxides. Instead, Fe-Cr-O is predicted as the only Fe-containing oxide to form. However, according to the TEM-EDX line scan result in Fig. 5.8 (c) and APT results in Fig. 5.11 (d), the interface contains approximately equal amounts of Fe and O with only a low Cr content. High Cr content structures are only detected in some parts of the oxide layer, as shown in Fig. 8. According to the literature when the temperature is higher than 570℃, magnetite (Fe_3O_4) will transform to wüstite (FeO) [65]. Thus, we propose that the oxide layer is likely wüstite rather than Fe-Cr-O. For the static corrosion conditions of T91 investigated in this study, the combination of low Cr content and limited reaction time may promote the formation of wüstite. Because wüstite is porous [234], Fe and Cr can diffuse through it into the LBE. Similarly, the LBE

can still penetrate through the wüstite, contact the T91 matrix and thus continue to further corrode the steel. As a result, some grains will simultaneously incorporate high levels of both Pb and Fe during the corrosion process, as seen in the partly corroded grain in Fig. 5.7 (a). In addition, Fig. 5.7 (d) shows an oxide region surrounded by LBE. This suggests that, as the corrosion front moves forward, the oxide layer may become detached, rather than moving with the steel/LBE interface.

5.4 Conclusion

In this chapter, the static corrosion of T91 in high-temperature, low-oxygen liquid LBE was investigated. Using APT, TEM, EELS, EDX, EBSD and SEM, the micro- and nano-scale morphology and composition of the LBE ingress and the LBE-T91 interface have been characterised. From this, the following mechanistic insights and conclusions can be reached:

For the LBE attack pattern: In the process of liquid LBE corrosion, the intrusion of the corrosion front does not appear to correlate preferentially with the grain boundary network. The Cr depletion adjacent to the corrosion interface is much larger in scale than that observed for Fe. At the same time, in the Cr depletion region, Cr-enriched precipitates are dissolved. Furthermore, markedly different grain morphology is observed in the near-LBE region. This suggests that there may be a LBE-induced phase change of T91, though this requires further investigation.

At the interface formed between LBE and T91: The corrosion of T91 in liquid LBE in reducing environment is a combination of oxidation and elemental dissolution. The thin oxide layer formed is likely FeO (wüstite), with other phases also appearing in a variety of structures. VN precipitates possess much higher resistance in liquid LBE than Cr precipitates.

Based on our observations, we propose the following corrosion sequence (as shown in Fig. 5.16):

- Cr initially preferentially dissolves from T91 into liquid LBE creating a depilation zone adjacent to the corrosion interface.
- Cr precipitates dissociate in the region adjacent to the interface corresponding to the drop in Cr content.
- The rate of Cr dissolution eventually slows, relative to that of Fe, with a decreasing concentration gradient.
- Constant Fe and Cr dissolution rates are reached which promotes the development of a stable Cr depletion distance.
- Fe dissolution into LBE progresses in a grain-by-grain fashion.

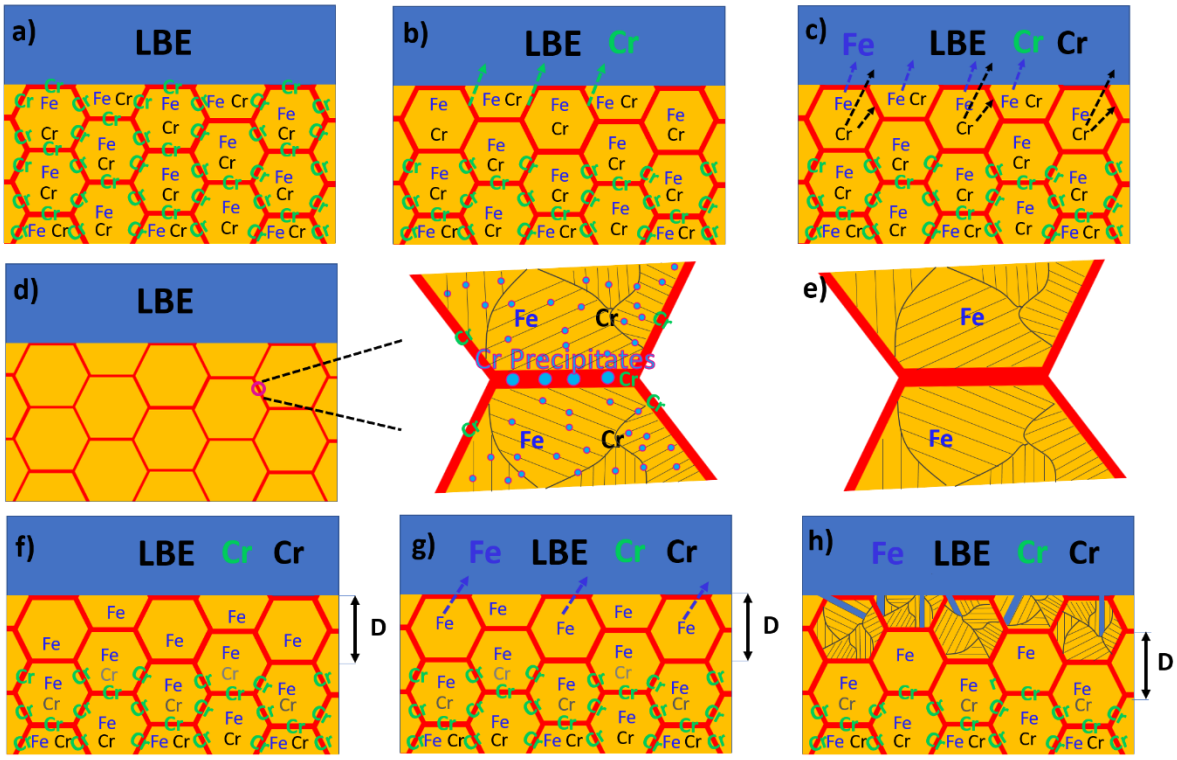

Fig. 5.16. The hypothesis of the mechanism of LBE. (a)-(h) the process of corrosion [Condition: reducing environment, 715 ℃, LBE]. (a) the T91 before corrosion. (b) Free Cr in grain boundaries dissolute into the LBE. (c) Free Cr in grains dissolute into grain boundaries and LBE. (d) The Cr-enriched precipitates along pre-austenite grain boundaries and martensite block boundaries before corrosion. (e) The Cr-enriched precipitates dissociated after the surrounding Cr content decreased. (f) Cr depleted to the lowest level from the LBE and T91 interface, the depletion

distance is D in (g). (g) The dissolution of Fe becomes the main part of corrosion. (h) the dissolution of T91 following martensite blocks makes the diffusion scale of Cr (from D in (g) to D′ in (h)) which allows more Cr to diffuse into LBE.

Chapter VI

The correlation of Cr carbides dissociation and phase change observed in liquid lead-bismuth eutectic corroded T91

6.1 Introduction

In chapter 5, a systematic analysis of T91 steel samples corroded in static LBE under reducing environment has been undertaken, proposing a possible mechanism by which the corrosion proceeds [191]. The disappearance of Cr-rich precipitates and an apparent phase change in the Cr-depleted region adjacent to the corrosion front is observed. However, this was not investigated in detail, and it is unable to fully explain the dissociation of Cr precipitates and the observed phase change at the corrosion-affected surface. Cr precipitates have a major influence on the material strength and crack susceptibility of F/M steels [235]. There have been limited previous studies in which the dissolution of Cr-rich precipitates was observed in F/M steels exposed to LBE corrosion [236]. The dissociation of Cr-rich precipitates has also been observed in other alloy systems when exposed to different environments: For example, Was and Allen reported $Cr_{23}C_6$ dissociation in Ni-Cr alloys, for helium-cooled reactors, following exposure to CO and CO_2 atmosphere [237]. They proposed a dissolution mechanism that acts above a critical temperature and was driven by decarburization of the alloy through the formation of CO, resulting in a region depleted of carbon near the corroded surface [238]. Was et al. also suggested that Cr depletion, caused by the preferential dissolution of Cr, is the driving force for the dissociation of Cr carbides in molten salt-cooled reactors [150]. Durham et al. observed Cr carbide dissociation in oxidised Fe-Cr-C alloys, explaining this phenomenon as the result of carbon diffusion to the alloy surface, undergoing oxidation to form carbon monoxide, and then diffusing through the scale, along nano-scale defects, presumably as carbon monoxide

molecules [239]. They also reason that the carbide size will influence dissociation in austenitic steels, which have a lower diffusion rate, while this effect is small in F/M steels as these have a higher C diffusivity. There are few prior works in the literature [240, 241] that consider LBE corrosion induced phase change in F/M steels.

In the present chapter, the mechanisms leading to Cr precipitate dissociation and phase change by characterising the surface microstructure of LBE-corroded T91 steel across a range of different length scales is studied. Scanning electron microscopy (SEM) equipped with energy-dispersive X-ray spectroscopy (EDX) and electron backscatter diffraction (EBSD) detectors, and micro-beam Laue X-ray diffraction were used to study micro-scale material structure. Scanning transmission electron microscopy (STEM) equipped with EDX and electron energy loss spectroscopy (EELS) detectors provides nanoscale information. Atom probe tomography (APT) is used to provide complementary precise measurements of C contents in the matrix.

6.2 Results

6.2.1 Baseline of as-received T91

Electron microscopy results for as-received T91 are shown in Fig. 6.1. A high-magnification SEM micrograph is presented in Fig.6.1 (a) with precipitates visible along prior-austenite grain boundaries (GBs) and martensite lath boundaries. The compositions of these precipitates are analysed in detail below using TEM. Lower magnification EBSD and EDX results are shown in Fig. 6.1 (b) and Fig. 1 (c) to provide an overview of the microstructure across a larger area. The EBSD grain map in Fig. 6.1 (b) shows the expected martensite lath structure within the as-received T91. Fig. 6.1 (c) shows an EDX map for Cr. Cr is present in the matrix, in precipitates and at GBs. Neither Cr depletion nor precipitate dissociation are observed either at the sample surface or elsewhere.

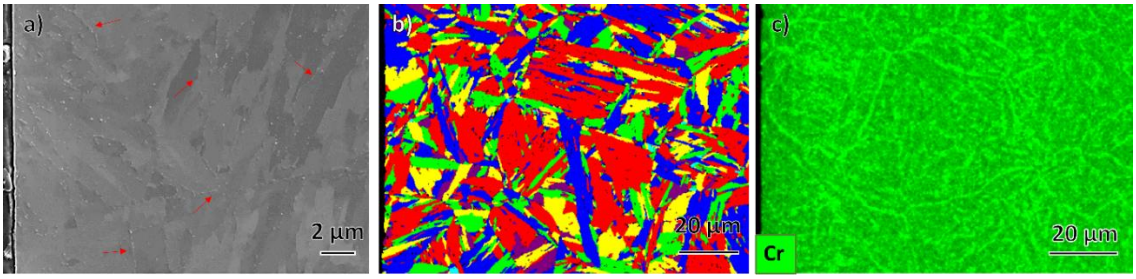

Fig. 6.1. Microstructure of the as-received T91 material. (a) SEM map with red arrows highlighting some of the visible precipitates. (b) EBSD-grain map showing the expected martensite lath structure. (c) EDX map of Cr showing Cr presents in the matrix, precipitates and GBs.

6.2.2 Phase change and carbide dissociation observed in corroded samples

Fig. 6.2 shows SEM-EBSD and SEM-EDX maps for T91 corroded in LBE for 245 hours in a reducing environment. Fig. 2 (a) is a larger scale map, while Fig. 6.2 (b)-(e) show a close-up of the region at the surface where changes are observed, as marked with a yellow dashed rectangle in Fig. 6.2 (a). In Fig. 6.2, the LBE penetrates T91 from the left side which is marked with an orange arrow in Fig. 6.2 (d).

Figure 6.2 (a) and (b) illustrate that the grain structure adjacent to the corroded region has transformed from martensite laths into more equiaxed grains with lower grain average misorientation, suggesting a phase transformation in this area. Figure 6.2 (c) presents the GND density of the same region, where a significantly lower GND density is observed in the transformed grain structure compared to the martensite lath region in Figure 6.2 (a) and (b). The higher GND density in the martensite lath region indicates a greater dislocation density, which may act as a driving force for phase transformation [179, 181]. Consequently, the notably lower GND density in the transformed region, compared to the original martensite laths, suggests that

a phase transformation has taken place. Compared to both the as-received sample in Fig. 6.1 (b) and the uncorroded sub-surface martensite lath structure on the right-hand side of Fig. 6.2 (a), it is apparent that the grain morphology change near the left surface is triggered by LBE static corrosion rather than a direct result of surface effects or temperature influence. EDX analysis of the same area in Fig. 6.2 (d) shows the Fe and Cr distributions. Fe is presented to give an approximate indication of the location of the T91 surface. From Fig. 6.2 (d), we can observe that the Cr depletion region extends over 10 μm from the LBE-exposed surface. This is most likely due to the higher solubility and diffusion speed of Cr compared to Fe in LBE [242]. Furthermore, there is an apparent dissociation of Cr-rich precipitates that were formerly within this Cr depletion region. Referring to Fig. 6.1 (c), it is reasonable to propose that the Cr depletion observed in Fig. 6.2 (d) is caused by LBE corrosion.

Next, 33 EDX line scans normal to the surface were acquired, distributed evenly across Fig. 6.2 (d). The mean profiles determined for both Cr and Fe, superimposed on the SEM image showing grains, are plotted Fig. 6.2 (e). Fe and Cr are the main elements in T91 and are assumed to play the most prominent roles. Thus, these two elements are considered here. The results show that the proposed phase change region at the surface closely correlates with the volume within which Cr was depleted and where Cr-rich precipitates have dissociated. This would appear to suggest that the two phenomena are linked. Corroded samples corresponding to exposure times of 70 hours and 506 hours show similar grain morphology changes, as presented in supplementary Fig. 6.3.

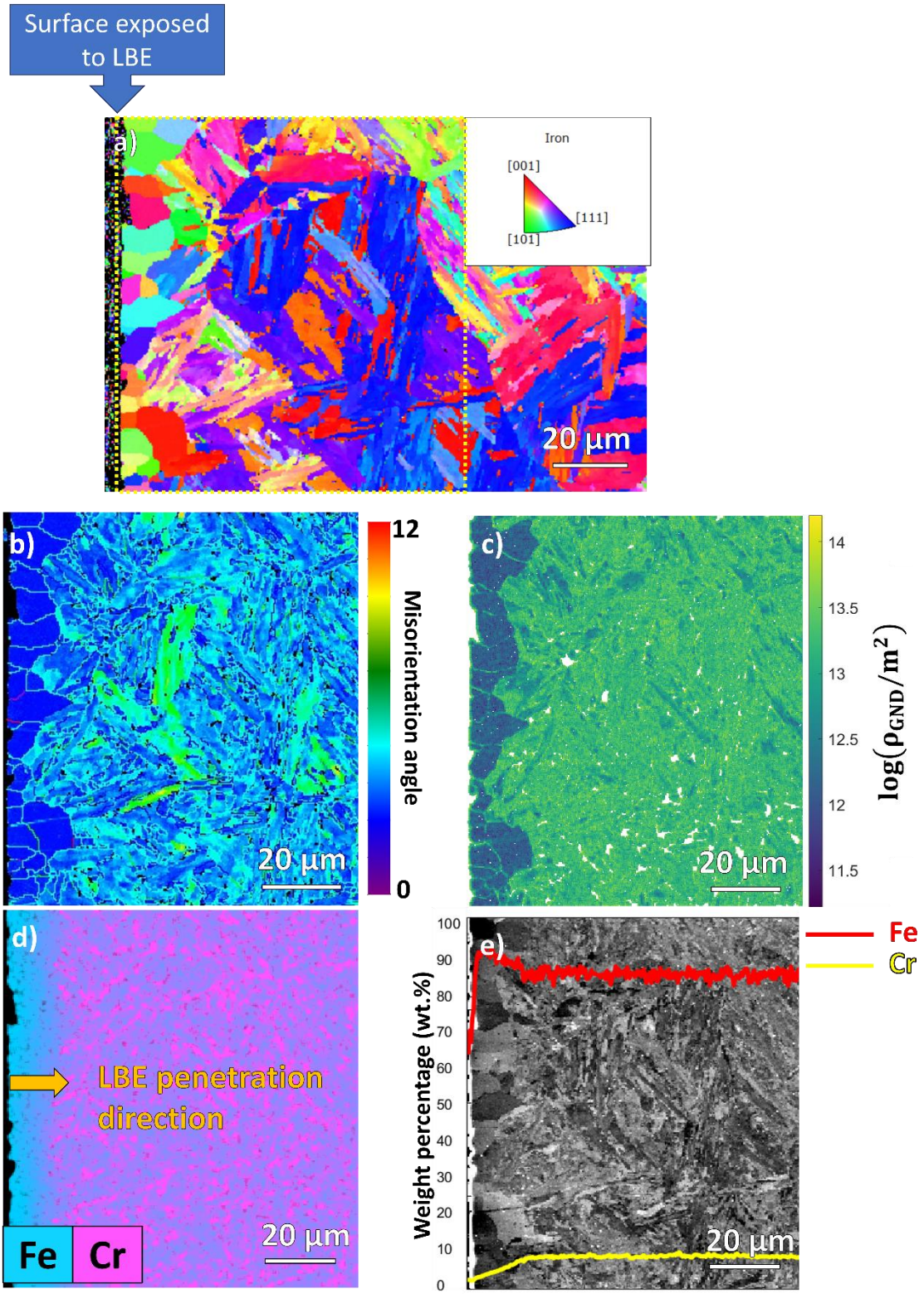

Fig. 6.2 Cross-section SEM-EBSD and EDX results for the sample exposed to LBE [Sample: 245 h, reducing environment, 715 ℃, LBE]. (a) EBSD IPFZ Map with the yellow dashed rectangle highlighting region for subsequent analysis in (b), (c), (d), & (e). (b) EBSD grain average

misorientation map with scale bar. (c) GND density map. (d) EDX map showing Cr and Fe. (e) Overlay of EDX line-scan results from Fe (red) and Cr (yellow) on SEM grain map.

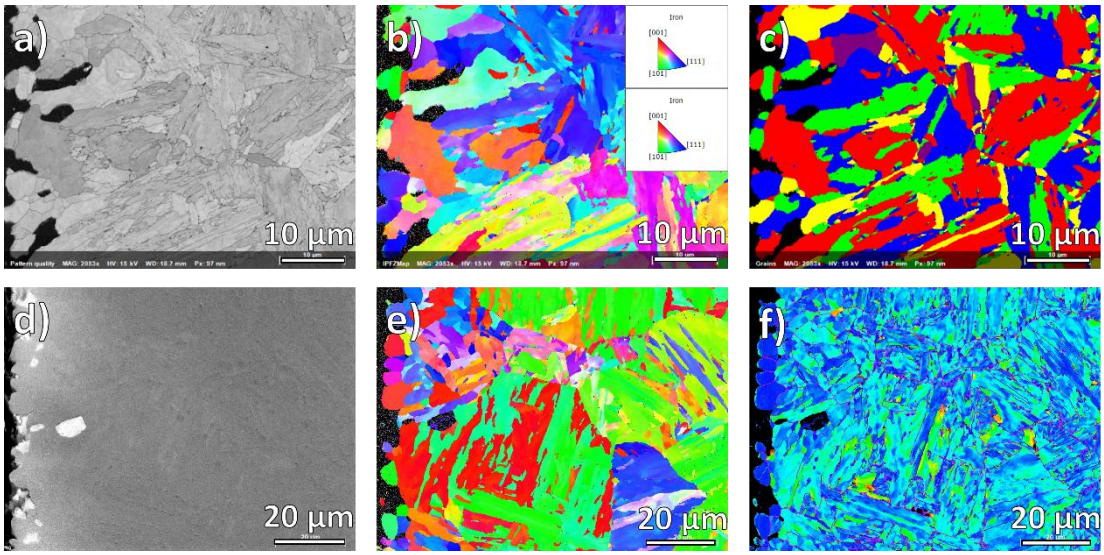

Fig. 6.3. Cross-section SEM-EBSD and EDX results for the sample exposed to LBE corrosion for 70 hours (Fig. 6.3 (a), (b) and (c)) and 506 hours (Fig. 6.3 (d), (e) and (f)) at 715 °C in reducing environment. (a) EBSD pattern quality. (b) EBSD IPFZ map. (c) EBSD grain map. (d) SEM map. (e) EBSD IPFZ map. (F) grain average misorientation map.

Several studies have reported an austenite-to-ferrite transformation at the surface of austenitic stainless steels that were exposed to liquid LBE at elevated temperatures (T>450℃) [18, 173]. Because of the dissolution of highly soluble austenite stabilizers (i.e., Ni and Mn) from austenite into the LBE, the material eventually transforms from face-centred cubic (fcc) austenite to body-centred cubic (bcc) ferrite. This change in crystal structure can be clearly identified in the EBSD analysis map, as the transition from fcc to bcc results in the classification of two distinct phases in the EBSD analysis. However, in the present study, the body-cantered tetragonal (bct) martensite exhibits a crystal structure very similar to that of bcc ferrite, making differentiation between the two phases more challenging. Due to this structural similarity, both phases become indistinguishable when using Hough-based indexing, leading to their classification as ferrite in

EBSD analysis. In the case of our T91 material, which has a relatively low carbon content of 0.09 wt.%, the c/a ratio is close to 1. As a result, the distinction between martensite and ferrite becomes even more difficult when analysing individual EBSD patterns [243]. Thus, X-ray diffraction, which offers higher angular resolution, is used as an additional method to determine the crystallography. DAXM provides superior angular resolution compared to EBSD, allowing for a more detailed assessment of misorientation variations within each investigated volume. Misorientation refers to the angular difference in crystallographic orientation between two adjoining grains or regions within a polycrystalline material. It describes how much one crystal lattice is rotated relative to another, and it is an important parameter in understanding the microstructure and mechanical properties of materials. The precise diffraction peak profiles captured through DAXM offer unique insights into the distribution of misorientation, making it particularly valuable for understanding local strain gradients. Additionally, Laue pattern indexation in DAXM is highly sensitive to small misorientations, ensuring that only regions with crystallographic orientations very close to cubic structures will be indexed as such. While this enhanced sensitivity does not enable a definitive distinction between phases like martensite and ferrite, the improved indexation observed near the surface of samples is indicative of a ferrite-like structure as shown in Fig. 6.4 (b).

Another key advantage of DAXM is its ability to probe deep beneath the polished surface, thereby avoiding artefacts introduced during sample preparation, such as polishing-induced strain, which can affect EBSD results. This makes DAXM particularly useful for bulk material analysis. However, EBSD, despite being more prone to surface-related artefacts, provides superior spatial resolution and is much more accessible in terms of ease of use and application [203].

The combination of DAXM and EBSD is therefore crucial for comprehensive material characterisation. DAXM's superior angular resolution complements EBSD's finer spatial resolution, enabling the cross-validation of crystallographic data. Using both techniques ensures

more reliable phase identification and a more complete understanding of misorientation distributions, strain gradients, and phase transformations within complex microstructures.

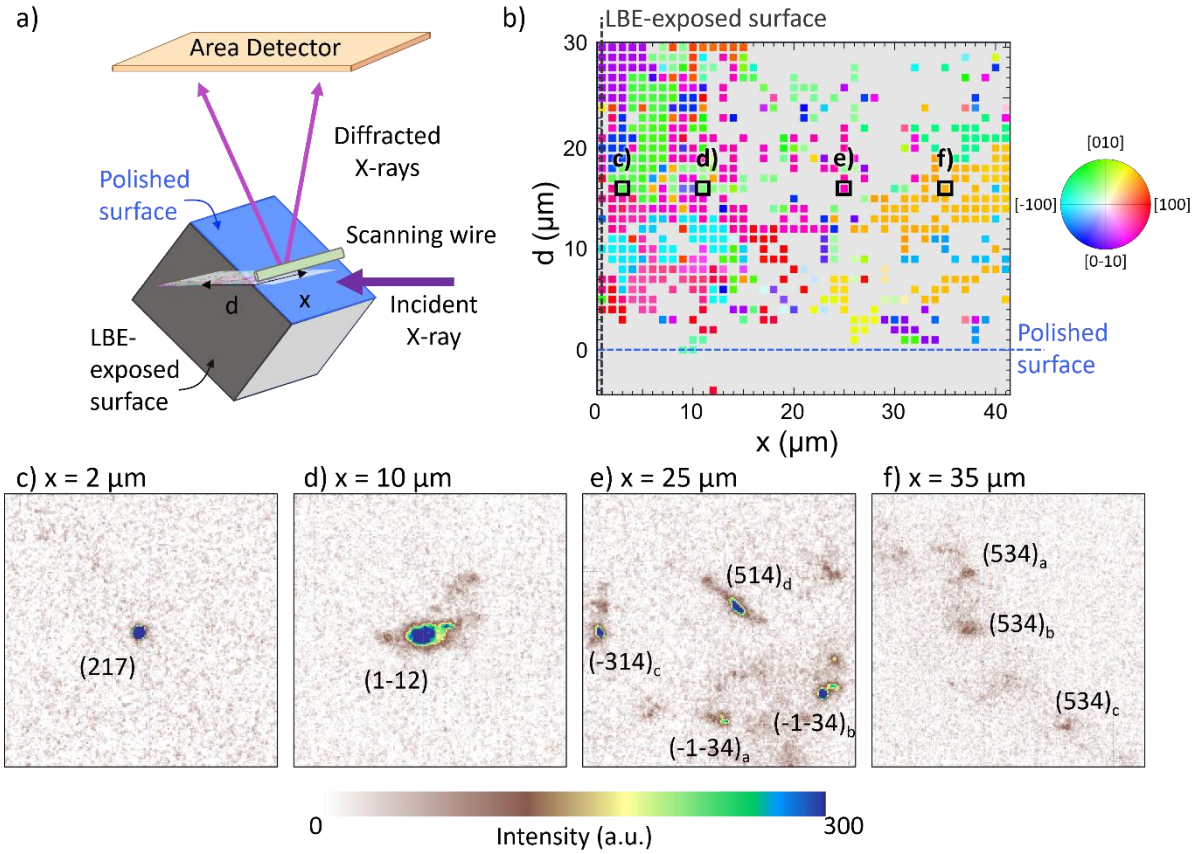

Fig. 6.4. (a) Schematic of the DAXM measurement setup and coordinates relative to the sample [Sample: 70 h, reducing environment, 715 °C, LBE] and the LBE-exposed surface (grey). (b) Indexation map (using ferrite crystal structure) measured along the polished surface (x-direction) and at 45° into the sample (d-direction). The LBE-exposed surface lies along x = 0 (grey dashed line) and the polished surface lies along d = 0 (blue dashed line). The pole figure legend is oriented with [001] at its centre along the surface normal of the polished surface. Non-indexed points are shown in white. (c)-(f) Indexed peaks at various depths in the sample. The area of the detector shown in each sub-figure is the same size. Note that for (e) and (f), up to 4 different grains were detected and denoted with subscripts a-d.

DAXM was used to determine the crystallography within a 2D slice oriented at 45° to the polished surface of the sample as illustrated in Fig. 6.4 (a). The depth-resolved patterns were indexed assuming a ferritic crystal structure (a_0 = 0.287 nm). The indexed results are shown in Fig. 6.4 (b), with the LBE-exposed surface on the left at x = 0, and the polished surface of the sample on the bottom at d = 0. The region within 15 µm of the LBE-exposed surface indexes to a ferritic structure to a much greater extent than the rest of the sample further away from the LBE-exposed surface. This suggests that this region has more ferritic character than the bulk.

Furthermore, there are significant qualitative differences in the diffraction patterns at different distances from the LBE-exposed surface as shown in Fig. 6.4 (c) to (f). Close to the LBE-exposed surface (x = 2 µm), the diffraction peak appears very circular with high intensity, suggesting a low-strain crystal structure. This is characteristic of a recrystallised ferritic microstructure. Moving further away from the LBE-exposed surface, the shape of the diffraction peak becomes less symmetric and more 'smeared', which is an indication of increasing strain heterogeneity [244-247]. Far away from the LBE-exposed surface (x = 25 – 35 µm), the peaks have much lower scattering intensity, indicating smaller grain size. Diffraction patterns of several grains can be identified at once and usually with very small amounts of misorientation (~1°) between them. This is consistent with diffraction from a martensitic lath structure [248].

Alongside the EBSD measurements in Fig. 6.2 (a), Fig. 6.2 (b), and GND calculation in Fig. 6.2(c), we can conclude that while the bulk of the T91 sample remains martensitic, regions closer to the LBE-exposed surface adopt a ferritic character. The length scale over which the ferritic microstructure is observed with DAXM (~15 µm) agrees closely with the length scale of low GND grains in Fig. 6.2 (b) and width of the Cr-depleted zone shown in Fig. 6.2 (e).

6.2.3 Influence of Cr depletion on phase change

To further investigate the correlation between Cr depletion and phase change, we identified three distinct near-surface regions significantly differing in the level of Cr depletion (as shown in

Fig. 6.5 (a) and divided by black horizontal dashed lines) and acquired EDX and EBSD data from these regions. The results are presented in Fig. 6.5. The sample surface is marked with the yellow dashed line and the location of the scans in Fig. 6.5 (b) and (c) is highlighted with a dark blue dashed rectangle in Fig. 6.5 (a). Comparing the averaged EDX line scans (each region acquired over 10 line scans evenly spaced over the area) of the three regions shown in Fig. 6.5 (a), it can be seen that the upper region has limited Cr depletion. Furthermore, the Cr-enriched precipitates in this region are visible even close to the LBE and T91 interface with some Cr accumulation at the interface which can be attributed to Cr-rich oxides. In comparison, the middle region in this figure exhibits significant levels of Cr depletion and Cr-enriched precipitate dissociation. Finally, the lowest region has most Cr depletion and the greatest reduction of Cr-enriched precipitates. Both the middle and lower regions have no observable Cr accumulation at the LBE-T91 interface. The EBSD grain map and grain average misorientation map in Fig. 6.5 (b) and (c), respectively, show that in comparison to the microstructure before LBE exposure, little change in grain morphology or misorientation can be observed in the upper region. However, the middle and lower regions now incorporate small, recrystallised grains, highlighted by the black dashed rectangle in Fig. 6.5 (b). This suggests the phase change occurring at the T91 and LBE interface is a result of Cr depletion, and that the dissociation of Cr precipitates is also influenced by the extent of Cr depletion.

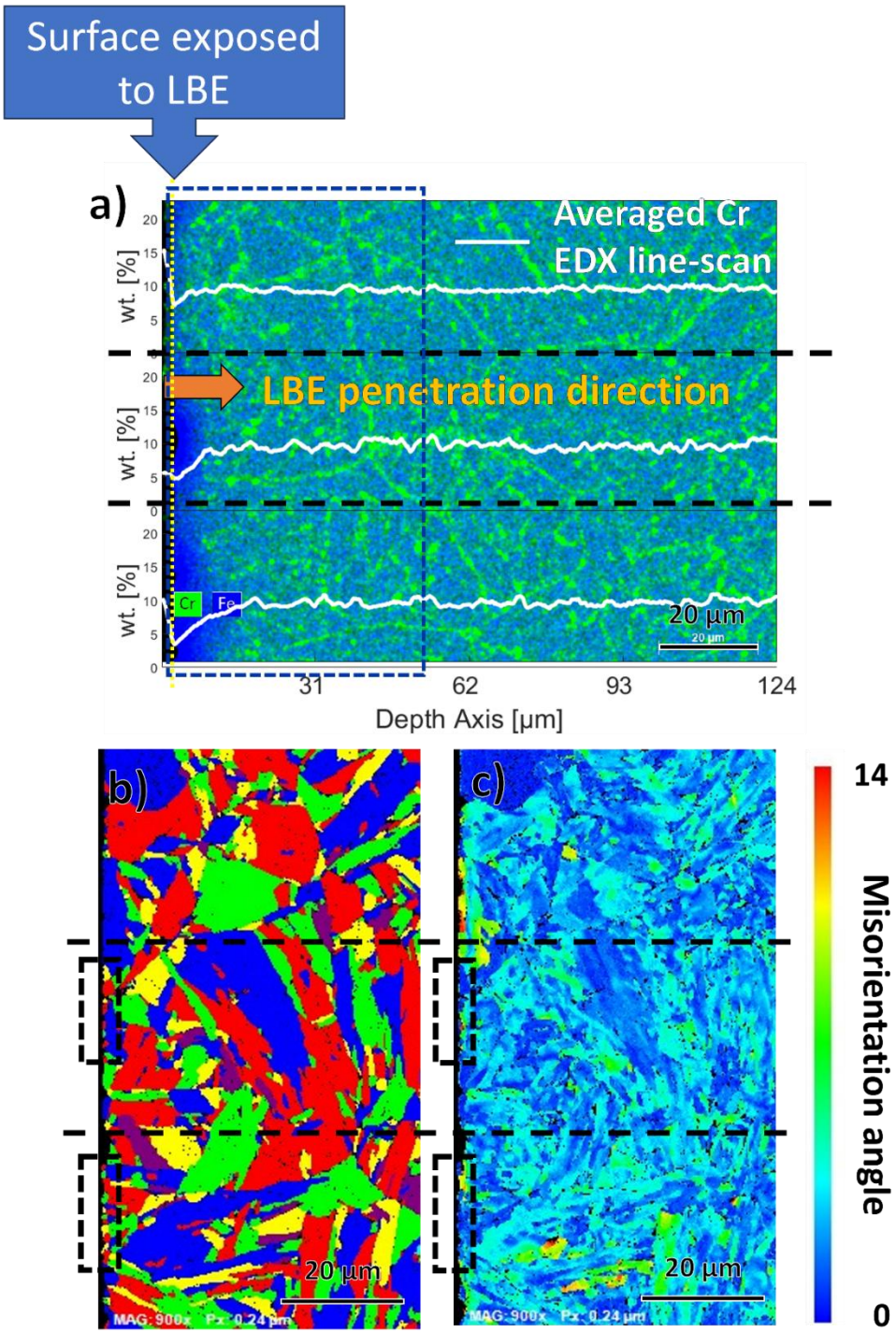

Fig. 6.5 Cross-section SEM-EBSD and EDX maps [Sample: 245 h, reducing environment, 715 °C, LBE]. (a) EDX map showing Cr and Fe and Cr EDX line-scans in different regions with the LBE penetration direction shown and sample surface marked with a yellow dashed line. The location where Fig. 6.5 (b) and (c) were recorded is marked by the dashed dark blue rectangle. (b) EBSD

grain map with small, recrystallized grains highlighted by black dashed rectangles. (c) EBSD grain average misorientation map with scale bar.

6.2.4 The Cr carbides dissociation process

To investigate the nature of the Cr precipitates seen in Fig. 6.1 (c), Fig. 6.2 (d), and Fig. 6.5 (a), and the mechanisms responsible for their dissociation, scanning transmission electron microscopy (STEM) equipped with EELS and EDX detectors was used. Two TEM sample were prepared with one from the LBE and T91 interface here referred to as TEM-1, and the other from the region just beside the interface which is referred to TEM-2. The relative positions of these 2 samples are shown schematically in Fig. 6.7 (a). Fig. 6.6 (a) shows a STEM image of TEM-2 from the 506 h corroded sample with the different types of precipitates identified. EELS was applied to the region indicated by the red box in Fig. 6.6 (a), with the results shown in Fig. 6.6 (b) - (e). These suggest that the Cr-rich precipitates are Cr carbides. The observed V-rich precipitates contain N, with only a small amount of C, and will be referred to as V nitride. To examine the morphological differences between Cr carbides and V nitrides, a lower magnification STEM image containing several precipitates is shown in Fig. 6.6 (f). Cr carbides have lower contrast and larger size (>100 nm) compared to V nitrides which give higher contrast and are smaller in size (<100 nm). Both Cr carbides and V nitrides are preferentially located at grain boundaries, in agreement with the literature [151, 153]. Cr carbides have a round morphology, whereas V nitrides vary from round to disc shaped. Atom probe tomography results that show similar shapes for V nitrides are provided in supplementary Fig. 6.8.

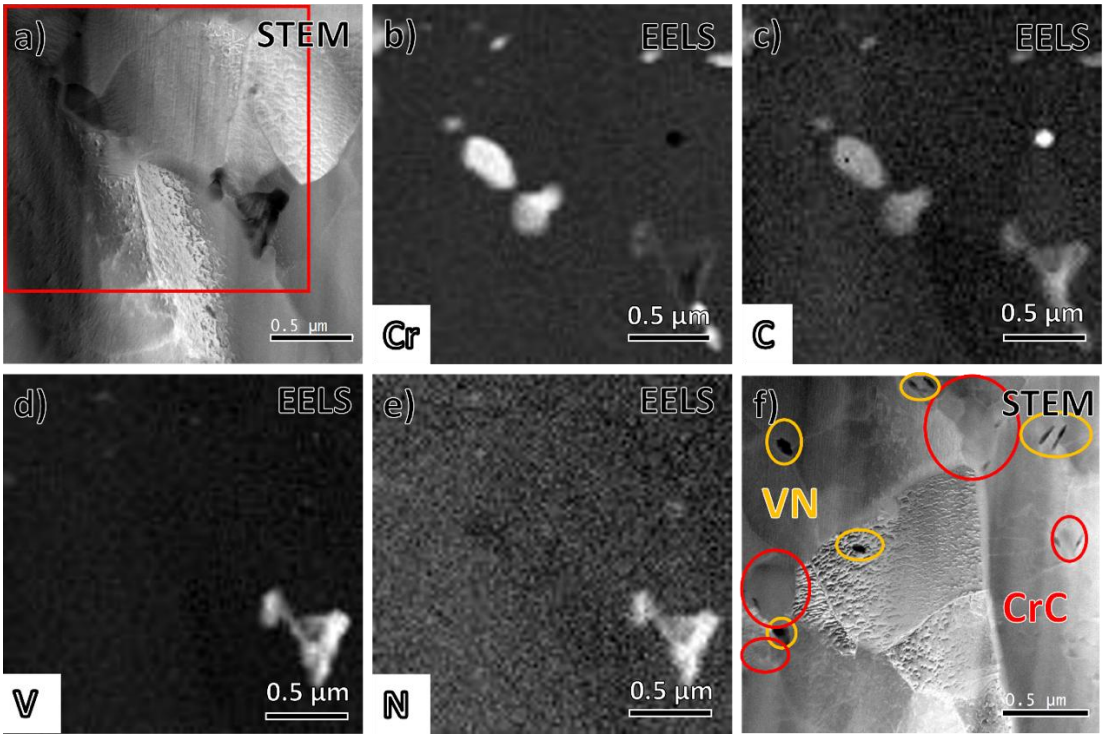

Fig. 6.6. TEM-2 liftout [Sample: 506 h, reducing environment, 715 ℃, LBE]: (a) STEM image with red box indicating the region for EELS analysis. This region is near the corroded surface of the sample exposed to LBE corrosion. Some Cr carbides are still present. (b)-(e) EELS maps corresponding to Cr, C, V, and N, respectively. The area corresponds to the red box shown in (a). (f) STEM image showing Cr carbides (circled in red) and V nitrides (circled in orange).

Long exposure (~1 hrs) STEM-EDX maps of the sample highlight the significant change in the distribution of Cr, starting at the LBE/T91 interface (sample TEM-1) to deeper locations in the T91 matrix (sample TEM-2). Fig. 6.7 (b) is from sample TEM-1 of the corrosion interface and Fig. 6.7(c) is from sample TEM-2 of the T91 matrix near the interface. Fig. 6.7 (c) shows 2 EDX maps, and the relative positions of maps TEM-1 and TEM-2 are shown in Fig. 6.7 (a). Fig. 6.7 (b) shows there are no Cr carbides close to the LBE. Cr carbides are only seen further from the LBE as shown in Fig. 6.7 (c). A comparison of the 2 EDX maps in Fig. 6.7 (c) suggests a change in the size of Cr carbides, with those closer to the LBE corroded region being larger than those further from the surface. The projected area of Cr carbides highlighted with red boxes in Fig. 6.7 (c) are

counted by applying the same threshold to the overall EDX maps. Carbide 1 is 1.47 times larger than carbide 3, and carbide 2 is 1.40 times larger than carbide 3 (see Fig. 6.9 for details). EDX point analysis for the 4 precipitates marked by dashed rectangles in Fig. 6.7 (c) was used to probe any compositional changes. The composition measurements are plotted in Fig. 6.7 (d) and listed in Table 2. In sample TEM-2, the precipitates closer to the LBE interface exhibit higher C content than those further from the surface. From previous studies of carbides in T91, they are expected to be of the form $M_{23}X_6$ (M=Cr, Fe, Mo, or Mn) [249, 250]. The Cr: C atomic ratio in the precipitates labelled 3 and 4 is ~ 23:5, whereas precipitates 1 and 2, closer to the corrosion surface, have a much higher C content with an average Cr: C ratio of ~ 23:13. However, we are cautious when interpreting these observations as are they are qualitative and do not represent a quantitative statistical analysis of the distribution of Cr carbides sizes and compositions.

Table 2. The atomic composition for precipitates measured with STEM-EDX marked in Fig. 6.7 (c).

	C (at %)	**Cr (at %)**	**Fe (at %)**
Precipitate 1	30.32	49.43	20.25
Precipitate 2	26.87	49.49	22.42
Precipitate 3	12.77	48.54	36.97
Precipitate 4	10.78	52.06	36.6

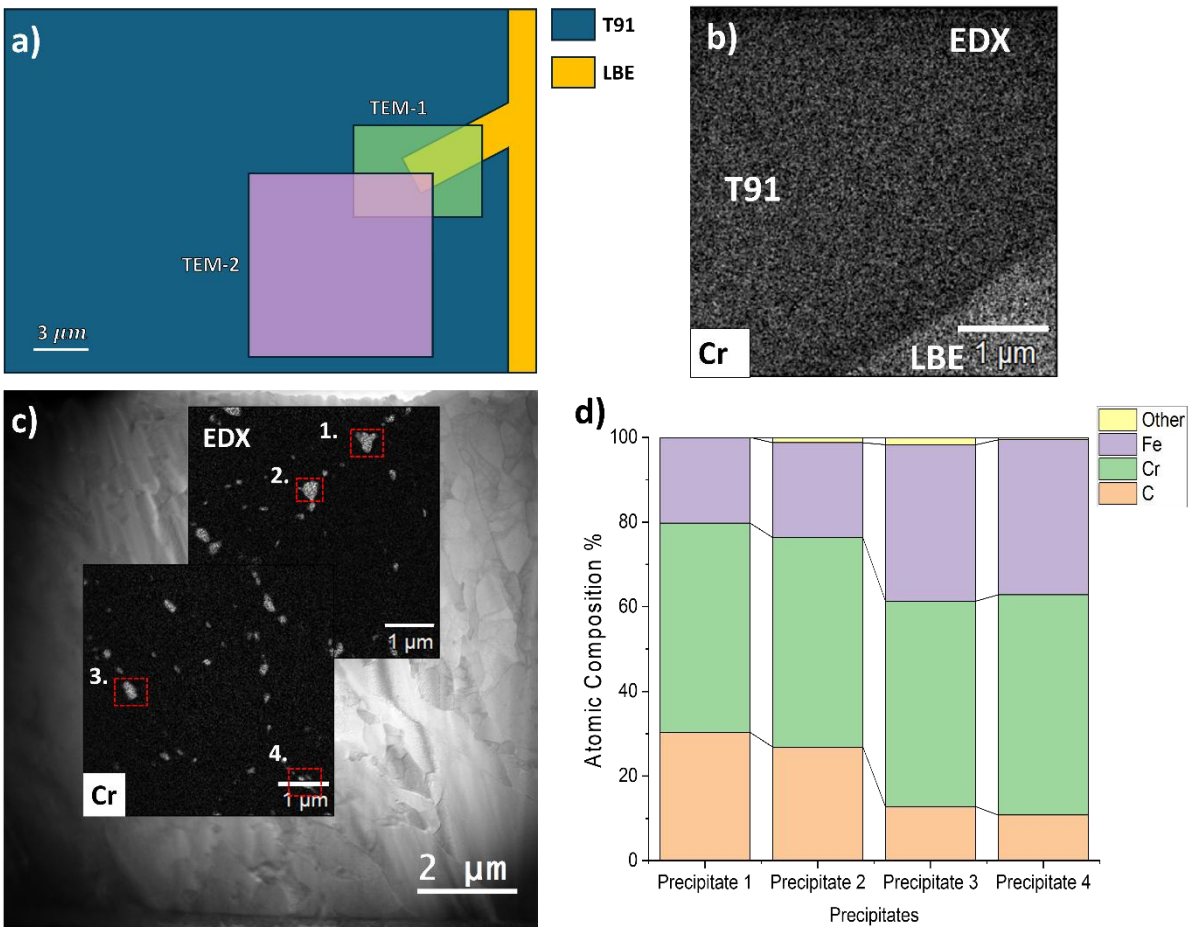

Fig. 6.7 (a) The relatively position of samples TEM-1 and TEM-2, both extracted from the same sample [Sample: 506 h, reducing environment, 715 ℃, LBE]. (b) STEM-EDX map of Cr from liftout TEM-1 at the T91-LBE interface. There are no Cr precipitates in the matrix adjacent to the LBE. (c) STEM-EDX map of Cr from liftout TEM-2, showing different sizes of Cr precipitates in the matrix at increased distances from the T91-LBE interface. (d) The EDX-derived atomic composition of precipitates 1-4 as highlighted with dashed red rectangles in Fig. 6.7 (c).

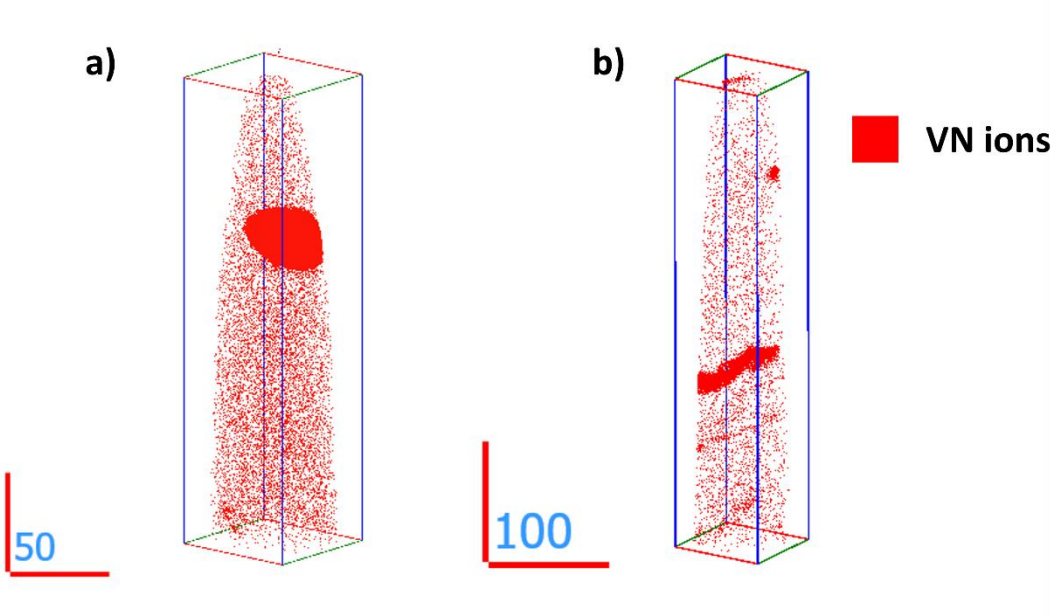

Fig. 6.8. APT reconstructions of VN.

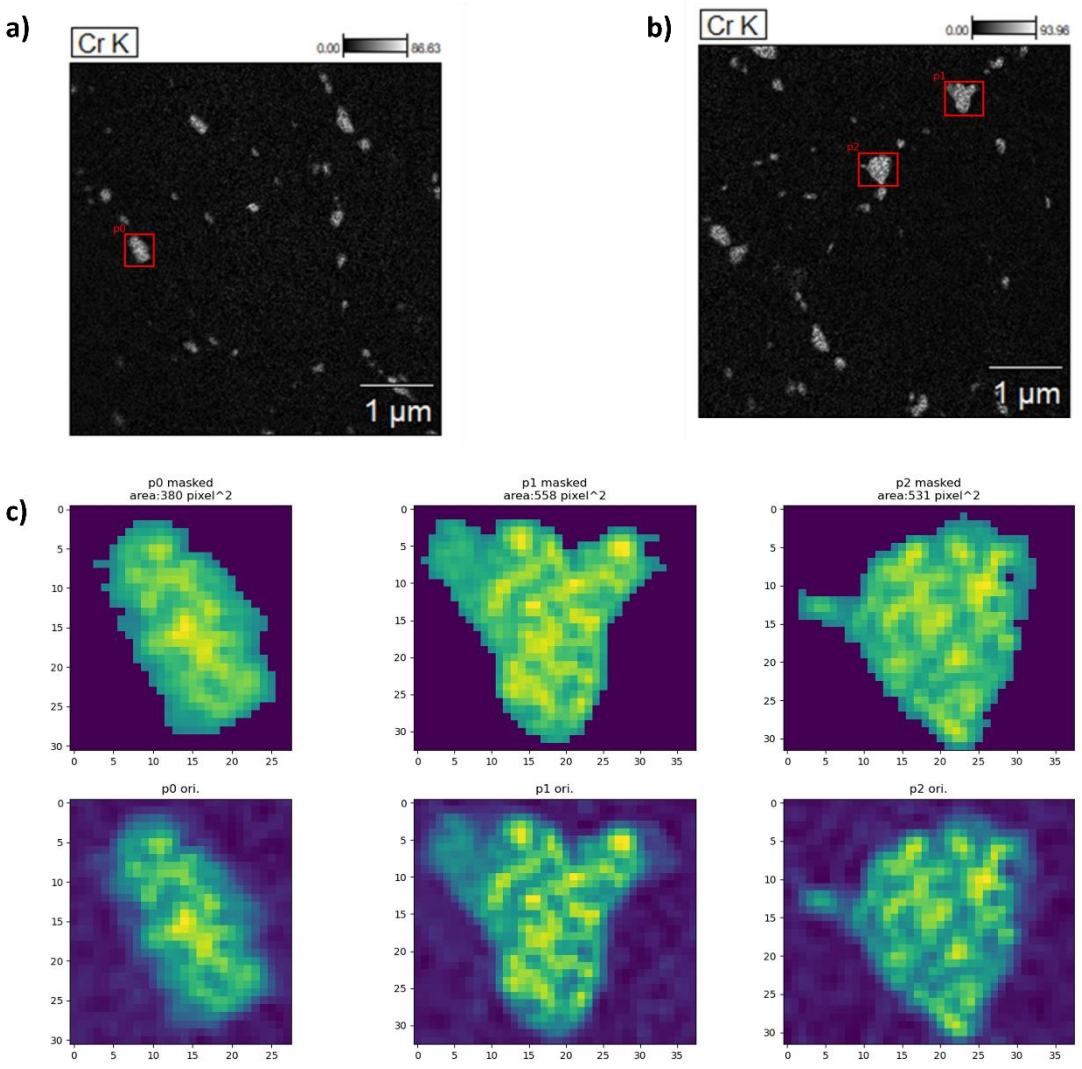

Fig. 6.9. (a) (b) Cr carbides showing different sizes as presented in Fig. 6 [Sample: 506 h, reducing environment, 715 ℃, LBE]. (c) Calculation of projected area of Cr carbides highlighted with red rectangular in (a) and (b). carbides are masked using a uniform threshold. After applying the mask, the number of pixels brighter than the threshold is counted and used to determine the relative area.

To further investigate the changes in local composition at different distances from the LBE-T91 interface, a systematic set of APT samples, shown in Fig. 6.10 (a), was prepared from the sample exposed to LBE corrosion for 506 hours at 715 °C. No Cr carbides were detected in these samples. The total C content per APT specimen at different depths beneath the surface was measured

and is presented in Fig. 6.10 (b). Except for sample 3 in Fig. 6.10 (a), carbon ions were detected at peaks at both 6 Da and 12 Da in the APT mass spectra. Fig. 6.10 (b) provides further confirmation that Cr is deplete near the surface and approaches the bulk concentration when moving deeper into the matrix. Simultaneously, the C content increases towards the surface, displaying a trend opposite to that of Cr. Complementary to the APT analysis, Fig. 6.10 (c) and (d) shows TEM images from sample TEM-1, just beside the LBE and T91 interface, where according to the APT results the C content should be higher and the Cr reduced compared to the matrix. According to the literature, the curved high contrast lines correspond to dislocations, while the dark dots may be interpreted as carbon-enriched phases [251].

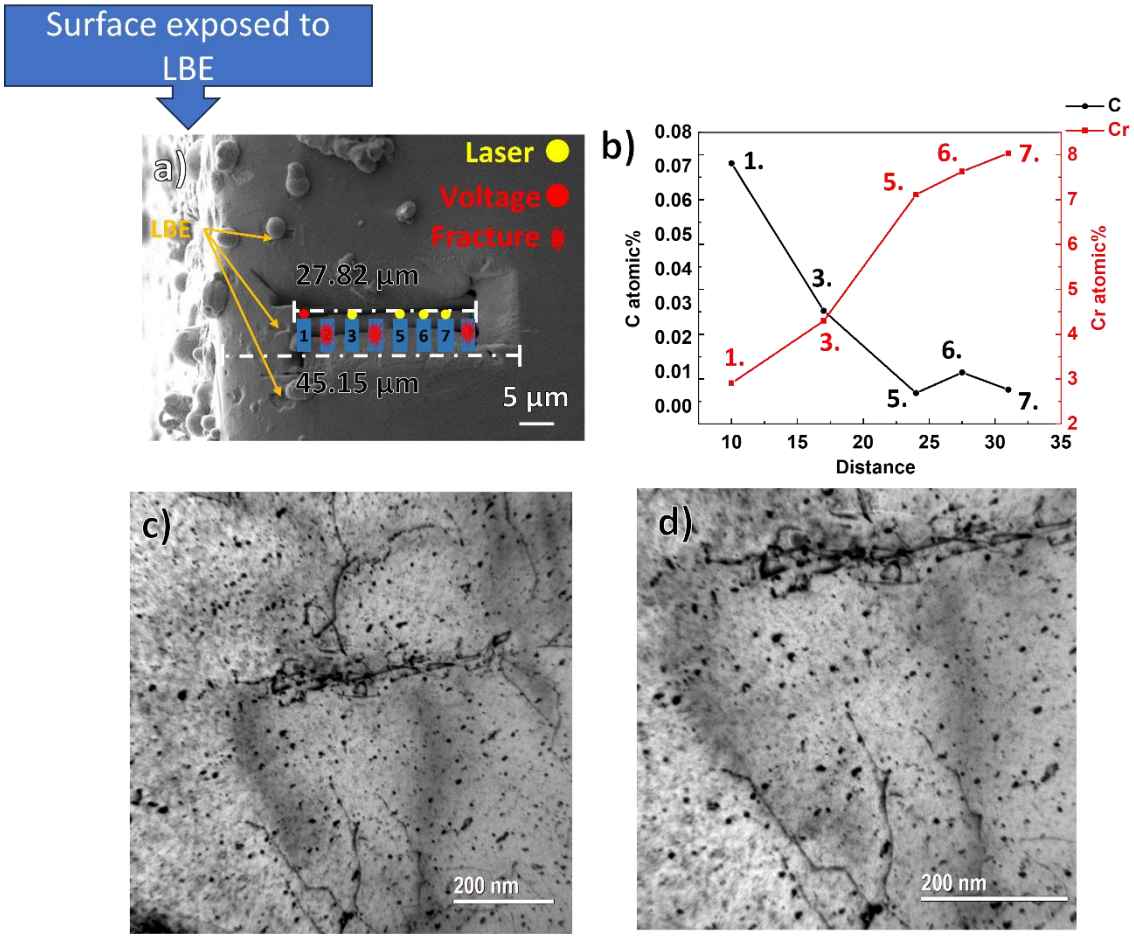

Fig. 6.10. (a) Indicates regions where APT samples were lifted out from the sample [Sample: 506 h, reducing environment, 715 ℃, LBE]. LBE is visible on the exposed sample surface. (b)

Concentration profile showing the bulk content of C and Cr determined by APT. (c), (d) TEM bright field images from the surface region of TEM-1 experiencing Cr depletion.

6.3 Discussion

6.3.1 Phase change at the interface of LBE and T91

A clear evolution of grain morphology is seen in Fig. 6.2 (a), which shows equiaxed grains at the interface of T91 and LBE, very distinct from the as-received martensitic T91 material. X-ray diffraction results in Fig. 6.4 (b) further add to this, indexing more readily as ferrite at the corrosion interface in comparison to grains sampled further into the unaffected matrix. Fig. 6.2 (b) and Fig. 6.2 (c), respectively, demonstrate that the new grains have much lower average misorientation and GND density, while Fig. 6.4 (c) indicates that these near-surface grains also have comparatively lower strain. Combined, these results strongly suggest a transformation of martensite grains to ferrite near the interface of T91 and LBE.

6.3.2 Cr carbides dissociation process

Our results show that LBE corrosion in a reducing environment induces Cr depletion of T91 near the T91-LBE interface. Within the Cr-depleted region, Cr carbides are also dissociated, which can be seen in Fig. 6.2 (d) and Fig. 6.5 (a). We hypothesise the following mechanism for this process: Cr dissolves into the LBE when T91 comes into contact with LBE, as is well documented in the literature [160]. This reduces the Cr content in the matrix surrounding the Cr carbide precipitates. The low Cr content environment destabilises Cr carbides, which start to dissolve. The released Cr also diffuses into the LBE. Due to the low solubility of C in LBE [252], the C lattice concentration in T91 near the LBE interface increases. From the (S)TEM-EDX results shown in Fig. 6.7, it is proposed that C then diffuses in the opposite direction, away from the surface and deeper into the matrix to form further Cr carbides, increasing the size of existing precipitates. This would

promote the formation of a region with a higher number density of Cr carbides or larger precipitates as observed in Fig. 6.7 (c). Considering the relatively low bulk C content in this material (0.09 wt%), the precipitate density and size changing region would be expected to be quite small. Indeed, our results show that this region is only on the order of a few micrometres deep away from the LBE.

Other than the C movement in the opposite direction to Cr, the APT and TEM results in Fig. 6.10 also suggest an alternative possibility: Some of the C dissociated from Cr carbides may remain in the Cr-depleted region and form other C-enriched phases. Evidence for this is the higher C content at the surface shown in Fig. 6.10 (b) and the apparent C-enriched phases in the TEM images in Fig. 6.10 (c) and (d). There are no carbides detected in this group of APT samples. Thus, the higher C content APT finds in the region corresponds to the bulk concentration. No C-enriched phase, as seen in Fig. 6.10 (c) and (d), were seen in the APT reconstructions, perhaps because they are too small to be detected. To summarise, the Cr carbides in the Cr depleted region dissociate with Cr dissolving into LBE and C partially diffusing in the opposite direction to the unaffected T91 matrix and partially remaining within the ferritized grains where it forms other C-enriched phases.

6.3.3 Correlation between Cr depletion/Cr carbide dissociation and phase change

Fig. 6.2 (e) shows that the phase change region closely correlates with the region of Cr depletion and Cr carbides dissociation, suggesting these features are related. Fig. 6.5 supports this hypothesis, by showing that an area at the corrosion surface with no apparent phase change also has significantly less Cr depletion and Cr carbide dissociation. Moreover, from Fig. 6.5, it is apparent that even a relatively small amount of Cr depletion and Cr carbide dissociation will induce small, recrystallised grains. Thus, the following mechanism for the phase change can be proposed: Firstly, LBE corrosion results in the Cr depletion at the T91-LBE interface. The lower Cr content leads to a reduced recrystallisation temperature [253, 254], meaning that grains with

lower Cr content start to recrystallise at the test temperature (715 ℃) while the grains with higher Cr content remain stable. The recrystallisation will initially form small grains, as seen in Fig. 6.5 (b), which then coarsen as shown in Fig. 6.2 (a). Before recrystallisation, there is normally a recovery stage that releases strain in the grains [255]. This may explain our observation of much lower grain average misorientation and GND density in the phase-changed grains as seen in Fig. 6.2 (b), Fig. 6.2 (c) and Fig. 6.4 (c). The recrystallised equiaxed grains are likely to be ferrite rather than martensite which forms either plates or laths [110]. Normally, ferrite has lower C content than martensite, however, the APT results in Fig. 6.10 show an increased C content in the ferritized region. This can be explained as follows: The highest C content detected in Fig. 6.10 (b) is 0.07 at. %, which corresponds to 0.0147 wt.%. The solubility of C in ferrite at 723 ℃ is 0.021 wt.% according to the Fe-C phase diagram. This is appreciably higher than the highest C content detected. Thus, the C dissociated from Cr carbides and left in this region will not influence the ferritization process. Finally, the upper region of Fig. 6.5 (a), where Cr has accumulated at the LBE and T91 interface, suggests that a continuous Cr oxide scale may act to reduce Cr depletion, which may impede the LBE corrosion of T91.

6.4 Conclusion

Cr depletion and Cr carbide dissociation has been examined in detail in T91 samples exposed to static LBE corrosion under reducing conditions. Based on EDX and STEM data, we propose the following mechanism:

- The Cr content decreases at the surface of the T91 after contact with LBE.
- The Cr carbides in this region become unstable due to the lower matrix Cr content and undergo dissociation.
- The Cr from dissociated Cr carbides diffuses into the LBE. The released C partially diffuses in the opposite direction, away from the surface, either forming new Cr carbides, or growing existing Cr precipitates in the region not yet depleted of Cr. Some

C is also retained near the T91-LBE interface, leading to a higher local C lattice concentration.

A transformation of the microstructure from the original martensitic laths to equiaxed grains with lower defect content is observed up to a similar depth as the Cr depletion. Considering the close correlation between Cr depletion and microstructural transformation, we propose that the Cr depletion is a key driving force for this phase change. Based on the experimental evidence, we formulate the following mechanism:

- Cr depletion reduces the recrystallisation temperature for the near-surface grains.
- At the corrosion temperature of 715 ℃ applied in this study, the Cr-depleted grains undergo recovery and recrystallisation from martensite laths to equiaxed ferrite grains, which then continue grow to into larger grains. The recovery stage releases the residual stresses the grains and lattice misorientation is greatly reduced. The retained C from dissociation of Cr carbides will not impede this ferritization process, as the amount of C is below the solubility limit of C in ferrite.

These observations of substantial LBE-induced compositional and morphological changes may have significant consequences for the structural integrity of components exposed to LBE corrosion. Our observations may also guide the design of materials with enhanced LBE corrosion resistance, optimised to mitigate the degradation mechanisms we have identified.

Chapter VII

Corrosion mechanism of T91 steel in static lead-bismuth eutectic in the oxidising environment

7.1 Introduction

Passivation is a common way to improve the anti-corrosion properties of structural materials [256]. For example, the Russian LBEFR, SVBR, is designed to form an oxide layer to protect the structure steel [257]. According to literature, an oxygen content above 10^{-6} wt. % and temperatures below 600℃ [231, 232] are required for the formation of a passivating oxide layer in LBE. Thus, passivation is not expected at the temperature we used in this test (700 ℃). This is why the research in Chapters 5 and 6 was conducted. However, determining the mechanism of how T91 is corroded in an oxidising environment is essential because oxygen is also one of the common impurities [258] in LBE and may offer opportunities to reduce the corrosion of structural materials at high temperatures.

According to the literature, under oxygen-saturated and oxygen-controlled conditions, the surface oxide consists of two parts: An outer layer of magnetite (Fe_3O_4) and an inner Cr-containing layer, mainly Fe-Cr-O spinel [24]. Variations in dissolution or corrosion rate often explain the formation of these complex surface oxide structures [55, 56]. The growth of these two layers requires the outward migration of Fe and inward diffusion of oxygen ions [259].

Cracks at the oxide/substrate interface have been observed in the literature. From Dionisio's research [259], these crakes may be caused by differences in the thermal expansion coefficient of the substrate and the oxide scale, especially at long oxidation times. Considering the operation cycles of the reactors, this can be a serious issue.

7.2 Results and Discussion

To investigate the corrosion mechanism of T91 in static LBE with oxygen, samples were corroded in an oxidising environment, at 700 ℃ for 70, 245, and 506 h respectively. Fig. 7.1 shows the SEM results, which reveal different corrosion patterns for the three exposure times.

Based on the SEM results, the observed corrosion patterns are categorized into four types, which are discussed in detail in this chapter.

i) **The first type is intergranular corrosion, occurring at the GBs.** The 245 h corroded sample shows a different pattern of GB corrosion compared to 70 h and 506 h corroded samples. In Fig. 7.1 (a) and (c), the 70 h and 506 h corroded samples exhibit oxidation at the martensite GBs, while the 245-hour sample, shown in Fig. 7.1 (b) shows extensive oxidation of prior austenite grain boundaries (PAGB).

ii) **The second type is corrosion occurring not only at the GBs but also within the grains, marked as area corrosion in Fig. 7.1 (d)-(f).** It is observed only in certain regions of each sample. From the SEM images, it is difficult to determine whether the corroded patterns are associated with LBE penetration or large oxide formations. To explain the formation of these structures, EDX analysis was conducted to investigate the element redistribution in these regions.

iii) **The third type consists of distinct corrosion patterns observed in specific locations.** In Fig. 7.1(g), cracks are visible at the ends of LBE intrusions, accompanied by different contrast phases nearby. Fig. 7.1(h) shows a region where the LBE intrusions resemble samples corroded in a reducing environment, as presented in Chapter 4, which may be due to a localized lack of oxygen. Fig. 7.1(i) shows the onset of intergranular oxidation, which may suggest that corrosion began with GB oxidation.

iv) **The fourth and final type corresponds to regions in all three exposure-time samples where no obvious corrosion is visible.**

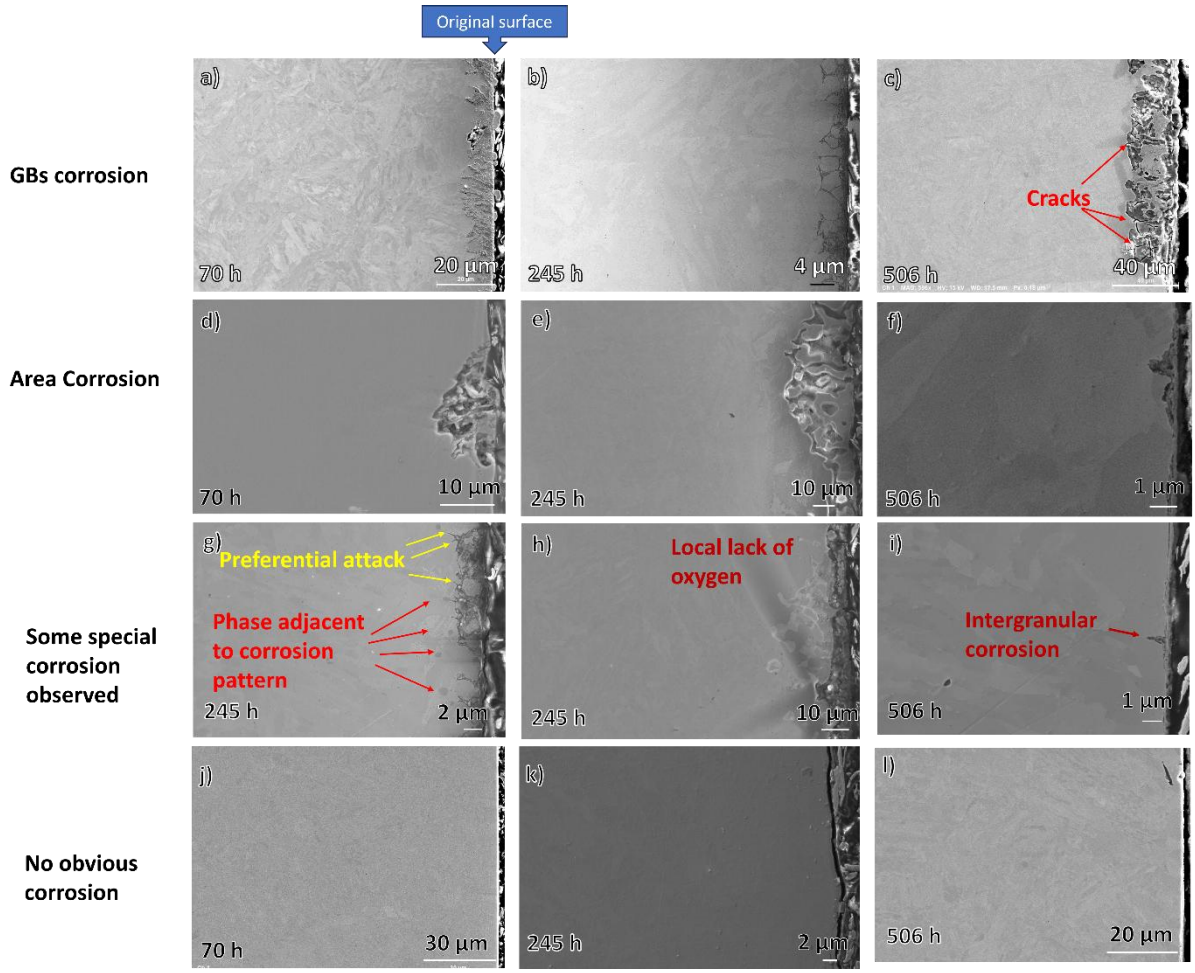

Fig. 7.1. Different kinds of corrosion patterns for 70 h, 245 h, and 506 h corroded samples in oxidising environment at 700℃, respectively. (a) (b) (c) the GBs homogenous oxidation. (d) (e) (f) local attack. (g) (h) (i) some specially corroded spots. (j) (k) (i) no obvious corrosion observed regions.

The four types of corrosion patterns mentioned above will be discussed individually in the following sections.

7.2.1 Intergranular corrosion, occurring at the GBs

7.2.1.1 Corrosion occurring at martensite GBs (70h and 506h)

This section will first focus on the initial corrosion pattern—intergranular corrosion occurring at the grain boundaries (GBs). Fig. 7.2 shows the SEM-EDX results for the 506-hour corroded sample, from a region similar to Fig. 7.1(c). As seen in Fig. 7.2(b) and (c), the corroded GBs are enriched with Cr and O, while Fe is absent. This indicates that the corrosion is oxidative, with the GBs oxidized, forming Cr oxides. Some Fe-enriched lumps, observed in Fig. 7.2(d), have formed outside the original sample surface. No enrichment of other elements is observed in the EDX results.

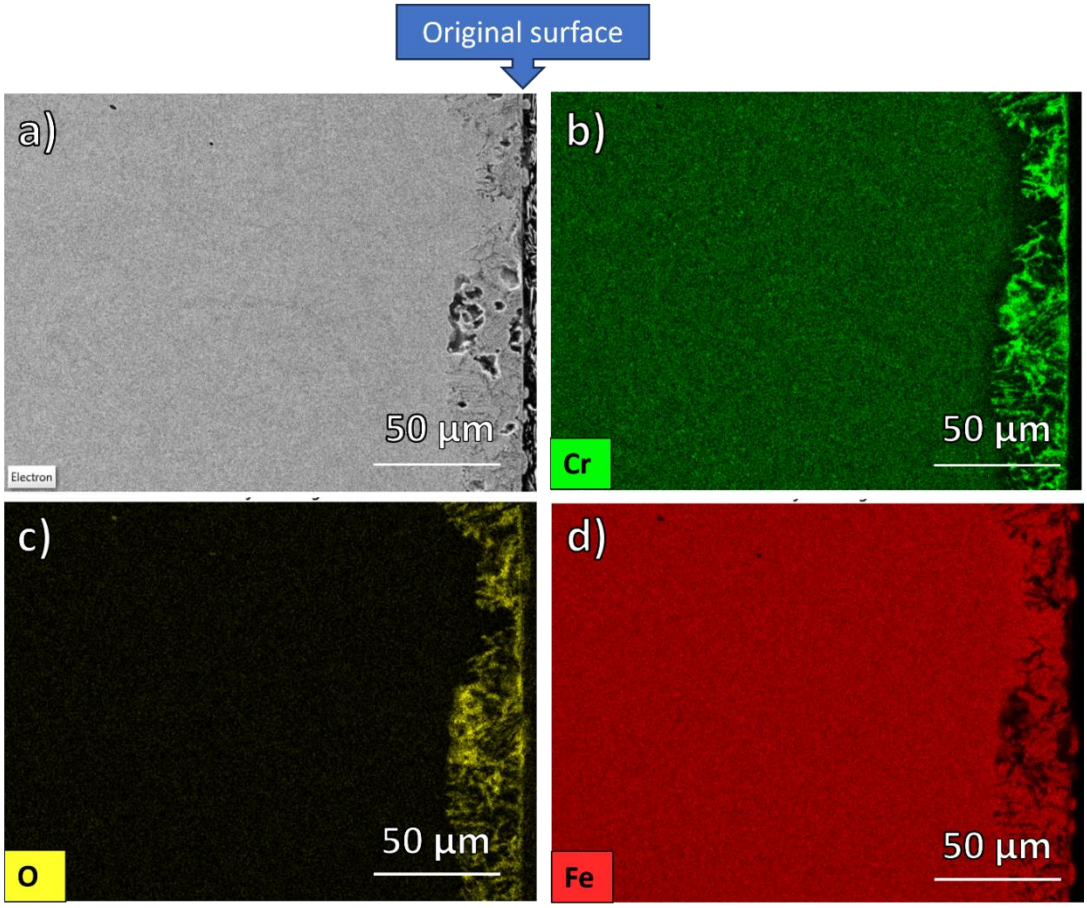

Fig. 7.2. SEM-EDX results [Sample: 506 h, oxidising environment, 700 °C, LBE]. (a) SEM image. (b) (c) (d) EDX results highlighting Cr, Si, and Fe.

Figs. 7.3 and 7.4 show the SEM-EDX and EBSD results, respectively, for the 70-hour corroded sample, corresponding to Fig. 7.1(a). From Figs. 7.3(b) and (c), it can be seen that Cr and Si are enriched in the corroded GBs, with no Fe remaining. Although the Si EDX map shows high contrast, this does not necessarily indicate a higher Si content. The contrast in the EDX maps is independent for each element, meaning the brightness for Si does not imply a higher concentration compared to other elements or environments. All EDX maps have been background noise corrected but not normalized (i.e., the brightness/contrast of the different elements has not been adjusted to sum to 100%). Combined with the EDX in Fig. 7.2 (c), it suggests that the GBs have both Cr and Si oxides. From Fig. 7.3 (b), a depletion of Cr is observed adjacent to the Cr-enriched places. This may be caused by the diffusion of surrounding Cr to the oxidised GBs.

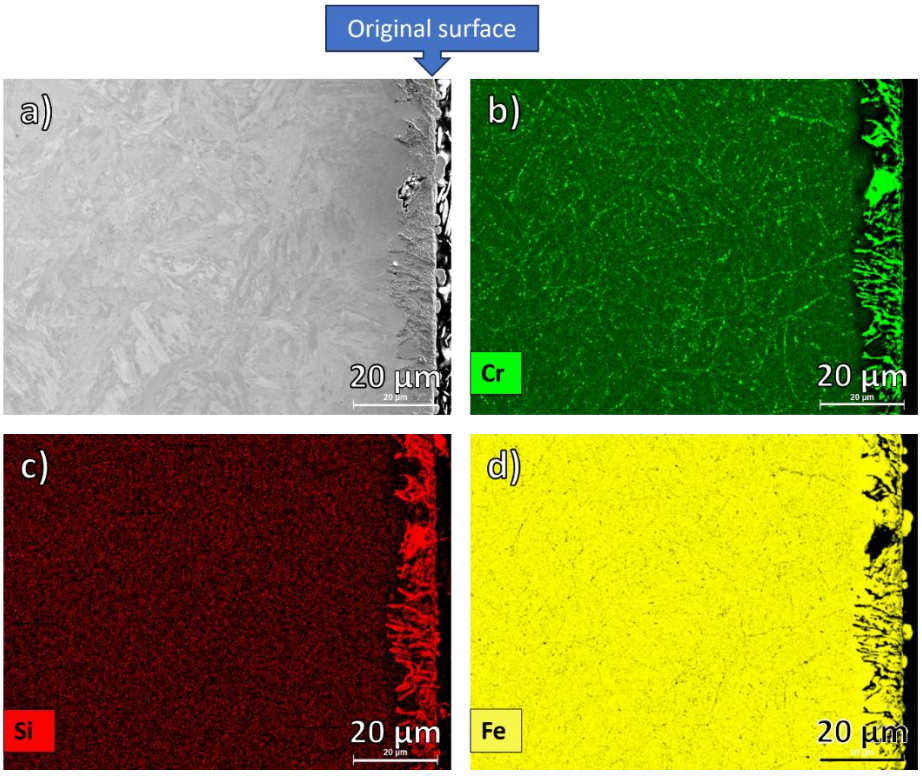

Fig. 7.3. SEM-EDX results [Sample: 70 h, oxidising environment, 700 °C, LBE]. (a) SEM image. (b) (c) (d) EDX results highlighting Cr, Si, and Fe.

From Fig. 7.4 (b) and (c), the low average misorientation grains highlighted by red dashed circles are observed in the Cr-depleted region. These grains are below the original sample surface, which can be the phase-changed grains as discussed in the chapter 5. Fig. 7.3 (d) shows the growth of the Fe-enriched layer outside the original T91 surface. Fig. 7.4 (a) shows a newly formed layer outside the original T91 surface. Combining the results from Fig. 7.3 (d) and Fig. 7.4 (b), the newly formed layer is enriched in Fe and shares the same crystal structure as the T91 matrix. To determine the phase of this layer, a higher magnification was applied and the SEM-EDX/EBSD results are shown in Fig. 7.5 and Fig. 7.6.

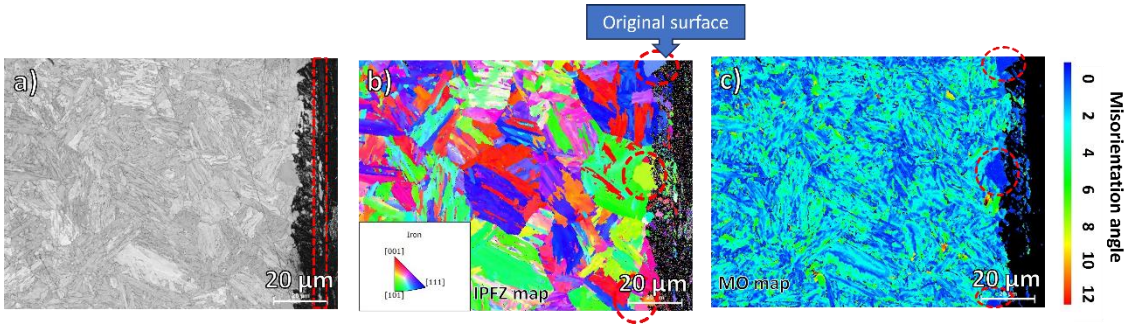

Fig. 7.4. SEM-EBSD correlated with SEM-EDX shown in Fig. 7.3 [Sample: 70 h, oxidising environment, 700 °C, LBE]. (a) EBSD pattern quality map with red dashed rectangular highlighting the layer formed outside the surface. (b) IPFZ map with black dashed circles highlighting the grains may have phase change happened. (c) Grain average misorientation map with a scale bar on the right. The red dashed circles highlight the same grains as the ones in (b).

Fig. 7.5(a) shows an area with corroded GBs and a dense layer formed on the surface of T91. To achieve better EDX resolution, a setting of 5 kV and 2 nA was used. The EDX results in Figs. 7.5(b)–(d) show that the corroded GBs consist of Cr- and Si-enriched oxides. The dense layer formed on the T91 surface is primarily composed of Fe, with no observable Cr, Si, or O. Fig. 7.5(f) confirms the absence of Pb in this area. To quantitatively analyse the results, an EDX line scan was conducted along the white line shown in Fig. 7.5(a), and the results are presented in Fig.

7.5(g). Three regions are highlighted in the line scan: Region 1, where a layer of Fe-enriched phase has formed; Region 2, where the GBs are oxidised; and Region 3, deeper within the T91 matrix.

From Fig. 7.5(g), Region 1 consists mainly of Fe (over 80 wt.%) with small amounts of other elements. Region 2 shows that the oxidised GBs are primarily composed of Cr and O, with some Si detected. To further confirm the compositional differences between the regions, spectra from four areas highlighted by red rectangles in Fig. 7.5 (a) were extracted, with the results shown in Fig. 7.5(h). The presence of C may be due to contamination from prolonged EDX exposure. However, it can still be confirmed that the spectrum of the Fe-enriched surface layer is similar to that of the Cr-depleted region (rectangles 2 and 3), except that more O is detected.

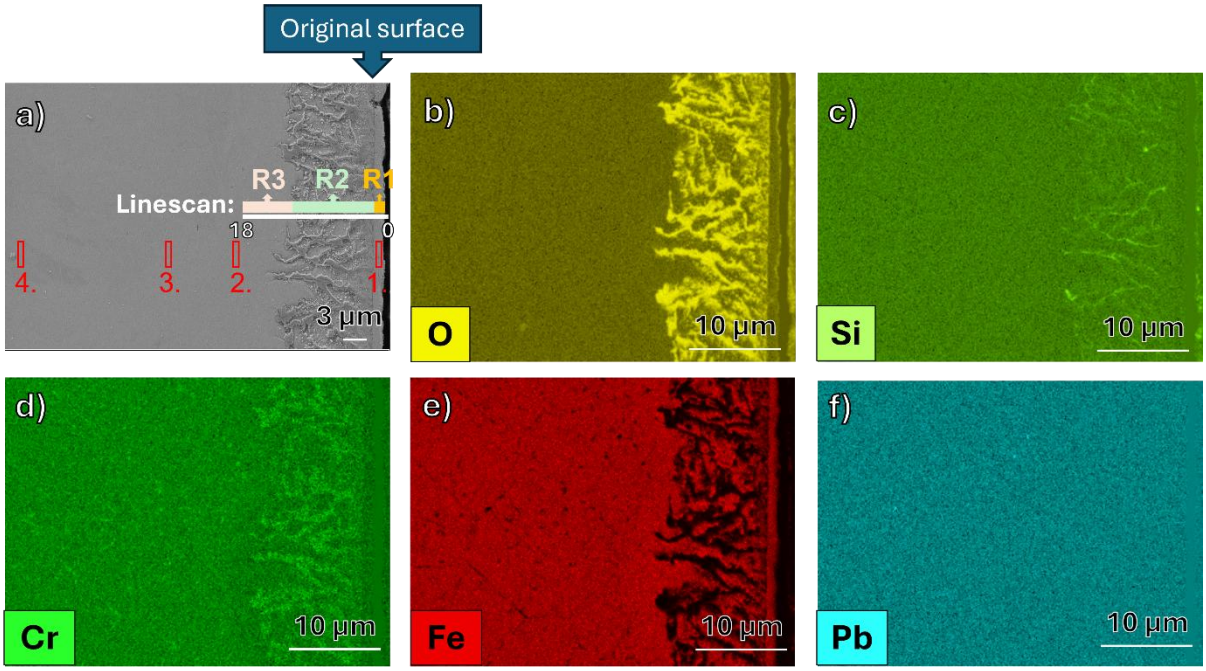

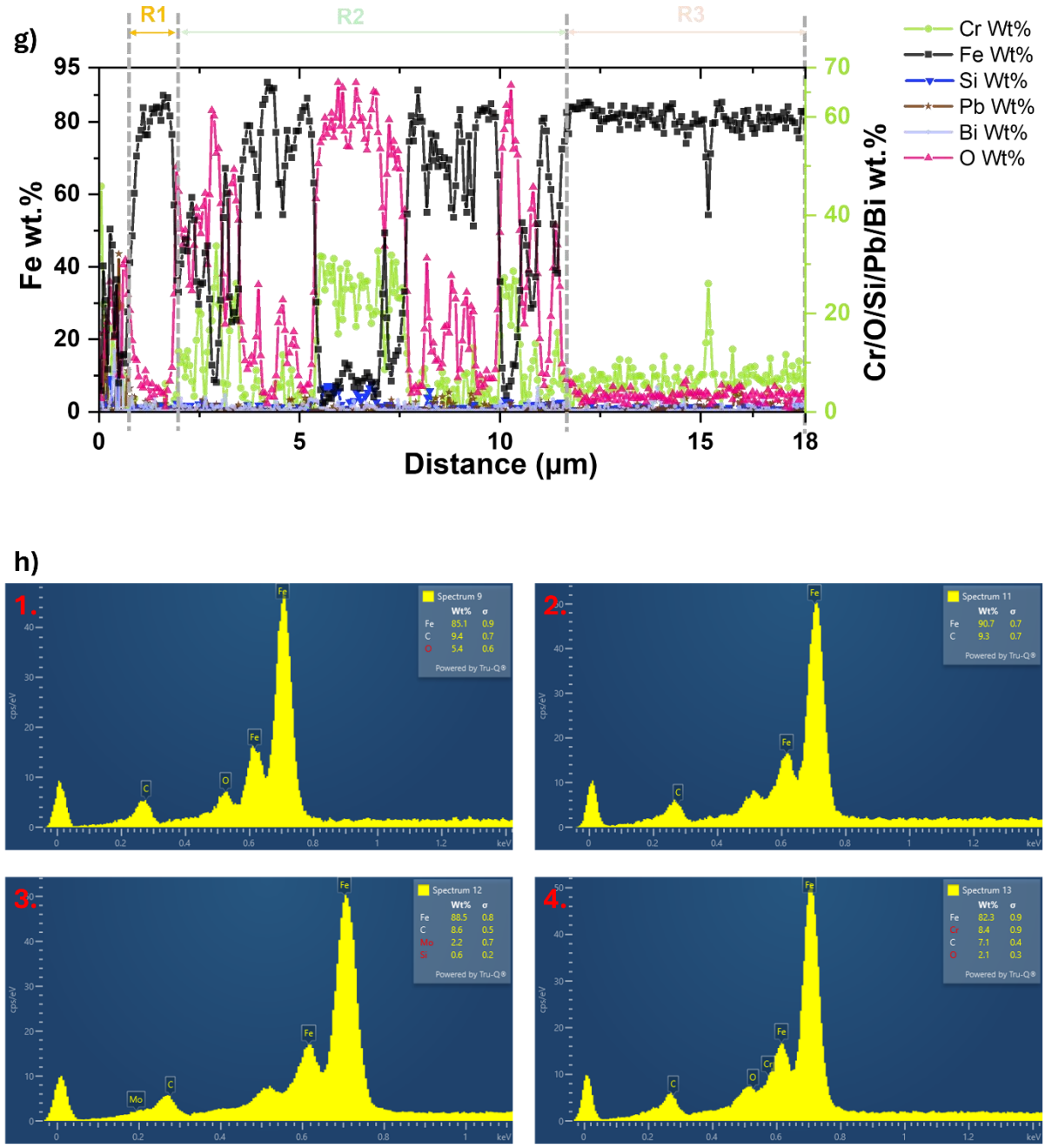

Fig. 7.5. SEM-EDX [Sample: 70 h, oxidising environment, 700 ℃, LBE]. (a) SEM image with the linescan position highlighted with the white line. The different regions of the linescan are highlighted with R1 in orange, R2 in green, and R3 in pink. The positions of where the spectrums of Fig. 7.5 (h) are acquired is highlighted with 4 red rectangular. (b)-(f) EDX results highlight O, Si, Cr, Fe, and Pb. (g) EDX linescan follows the position of Fig. 7.5 (a) with R1, R2, and R3 marked. (h) Spectrums from the positions highlighted in Fig. 7.5 (a) with red rectangular.

The EDX analysis provides only compositional information. To determine the phase, the lattice structure can be useful. Thus, the EBSD results from a similar region were acquired and are shown in Fig. 7.6. The surface Fe-enriched layer is highlighted with a dashed rectangle. Fig. 7.6(b) further shows that the lattice structure is BCC, similar to the T91 matrix. At first glance, one might assume it is a Fe-enriched oxide. However, FeO is a cubic phase with an Fm-3m space group, 225 international number similar to α-Fe, while Fe_3O_4 has Fd-$\bar{3}$m space group, 227 international number. Both of these phases are FCC. Combining the EDX composition information, it can be concluded that this layer is likely just Fe rather than an oxide. This differs from those recorded in the literature, which often report Fe_3O_4 [113, 260]. Fig. 7.6 (c) shows that the average grain misorientation of the oxidised GBs and the surface Fe-enriched layer is smaller than that of the T91 matrix.

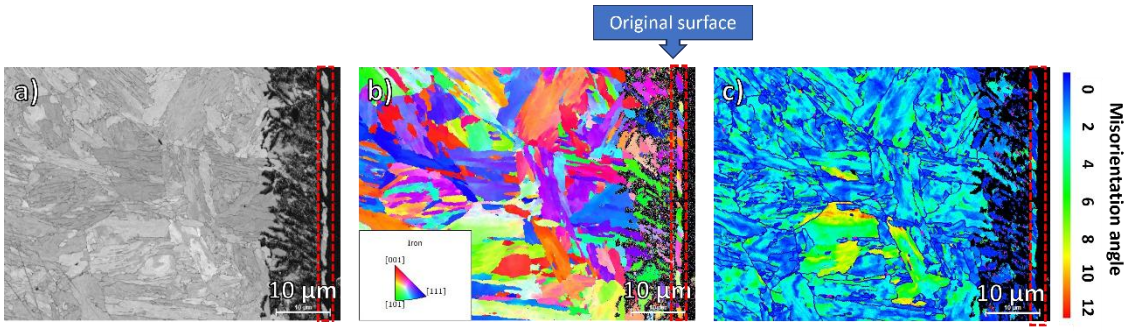

Fig. 7.6. The SEM- EBSD highlighting the surface formed Fe-enriched layer with dashed rectangular [Sample: 70 h, oxidising environment, 700 °C, LBE]. (a) EBSD pattern quality. (b) EBSD-IPFZ map. (c) EBSD grain average misorientation map.

7.2.1.2 Corrosion occurring at martensite GBs with crakes (506h)

Besides the martensite GBs corrosion shown above, cracks are observed in the oxide layers. Fig. 7.7 (a) shows a region of the 506 h corroded sample where cracks are observed in the oxide. EDX is acquired from this region and the results are shown in Fig. 7.7 (b)-(f). According to the literature, the cracks are formed because of the difference in the thermal expansion coefficient

[261]. The EDX overlayed with SEM in Fig. 7.7 (d) shows the oxides decorate the cracks. The Cr-enriched region is also enriched with O. Fig. 7.7 (f)shows the lack of Pb in this region.

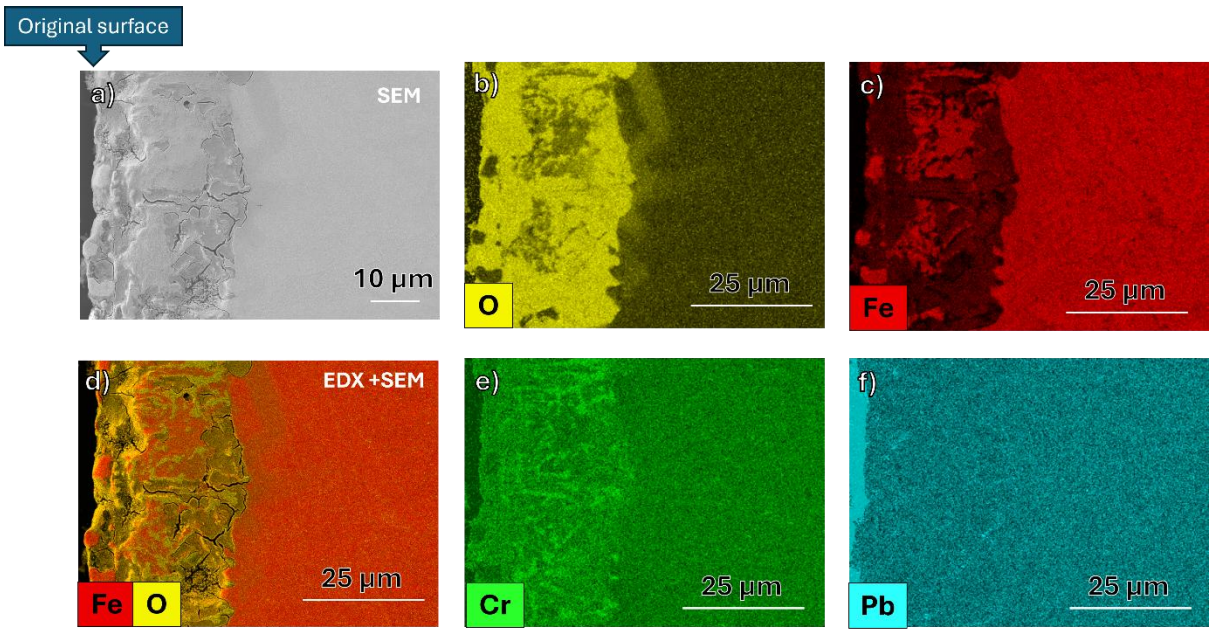

Fig. 7.7. SEM-EDX with cracks observed in the oxide layer [Sample: 506 h, oxidising environment, 700 ℃, LBE]. (a) SEM image. (b)(c)(e)(f) EDX results highlight O, Fe, Cr, and Pb, respectively. (d) EDX results highlight Fe and Cr overlay with the SEM image.

GB oxidised and cracks are observed also in Fig. 7.1 (c), Fig 7.8 presents the EDX and EBSD results for it. From the results shown in Fig. 7.8 (b) and (c), the Cr and Si are distributed in different places which indicates the oxides may have different compositions depending on the position. This is further confirmed by the line scan result shown in Fig. 7.8 (e), which suggests that the oxide may have a layered structure consisting of Cr and Si oxide. Fig. 7.8 (d) shows no phase changes happened in this area.

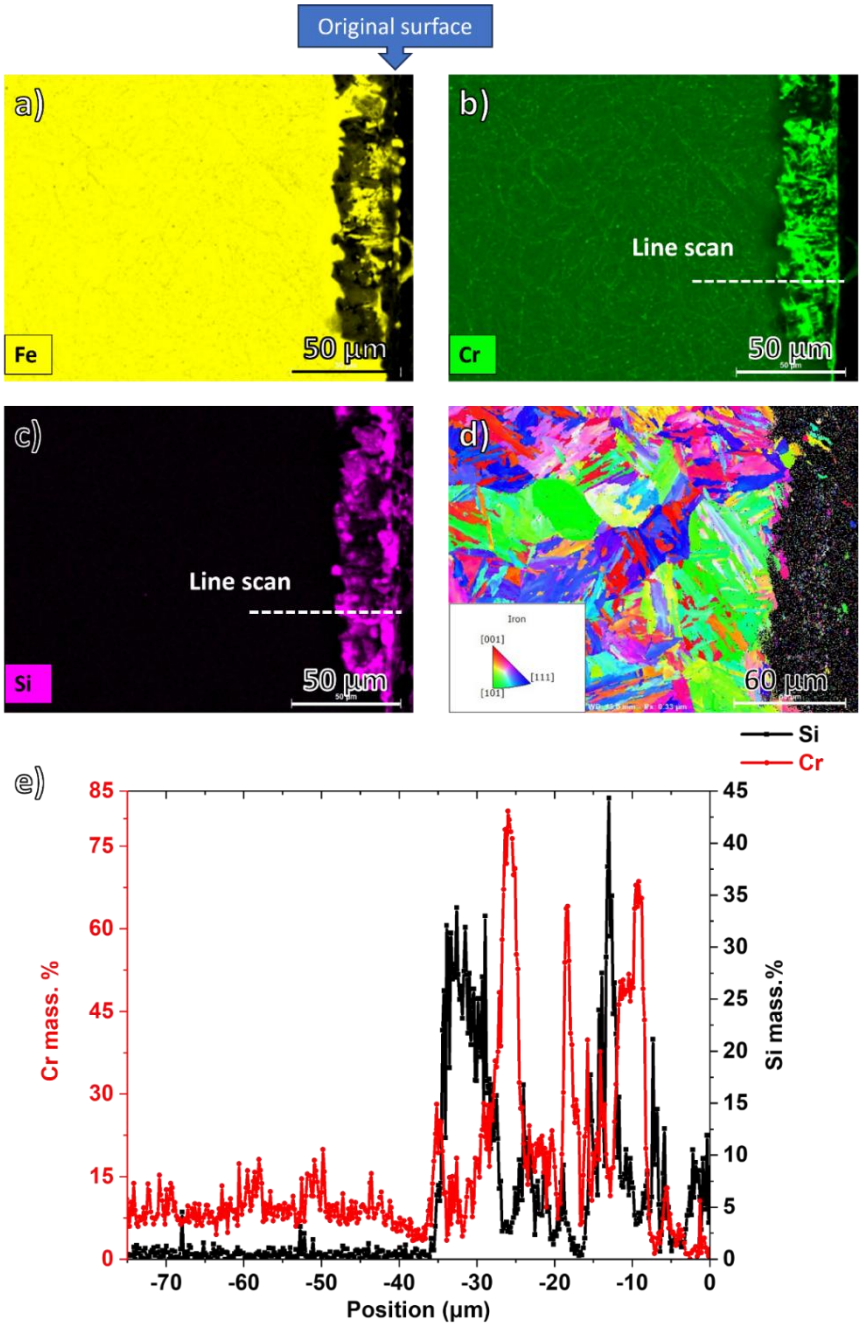

Fig. 7.8. The SEM-EDX and EBSD with GB oxidised [Sample: 506 h, oxidising environment, 700 ℃, LBE]. (a) EDX map highlighting Fe. (b) EDX map highlighting Cr. (c) EDX map highlighting Si. (d) EBSD-IPFZ map. (e) EDX line scan result following the line shown in Fig. 7.8 (b) and (c)with the original sample surface as position 0 µm.

7.2.1.3 Corrosion occurring at PAGBs – part I: SEM based (245h)

For the 245 h corroded sample shown in Fig. 7.1 (b), an oxidation at PAGBs is observed which is different from the 70 h and 506 h samples discussed in section 7.2.1.1. Low energy (5 KV) was used to acquire the O signal and get a better resolution to reveal more detail [167]. SEM-EDX data is shown in Fig. 7.9. Cr and Si form oxides located in the GBs. A Cr-depleted zone is observed in Fig. 7.9 (b) highlighted by a yellow dash box. The Cr-enriched precipitates observed deeper in the material dissociated in the Cr-depleted region. This is probably formed because the Cr diffused to form Cr-enriched oxide in GBs in the red dash box shown in Fig. 7.9 (a).

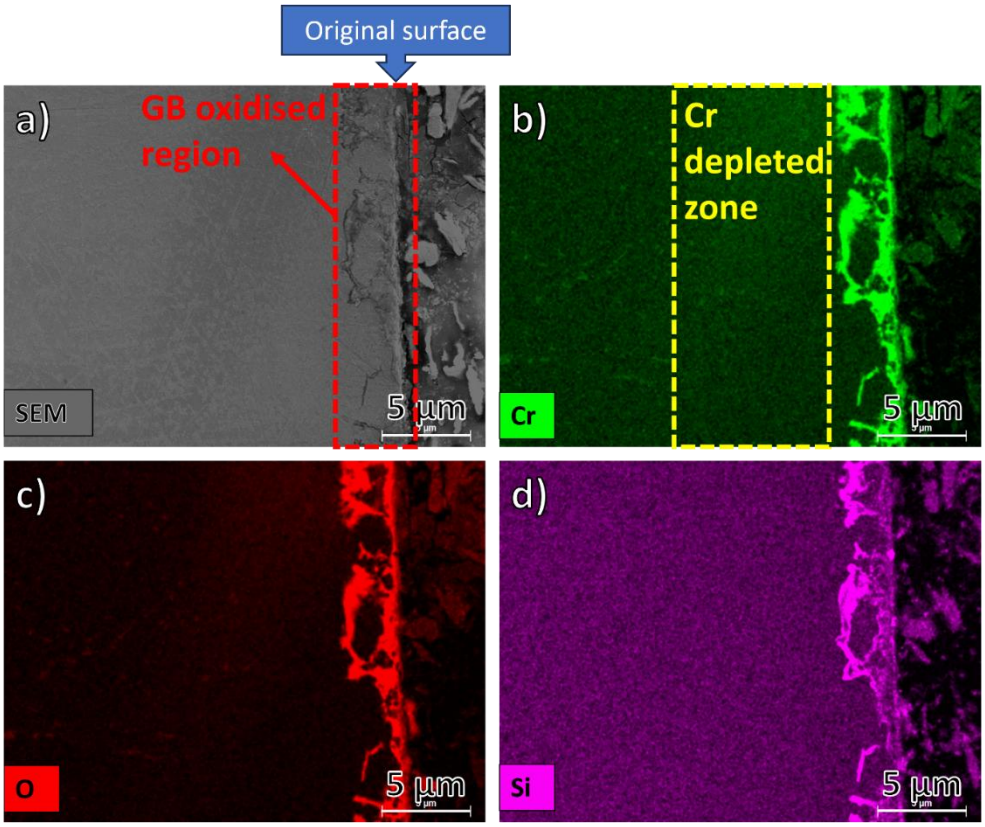

Fig. 7.9. The low energy SEM-EDX results [Sample: 245 h, oxidising environment, 700 ℃, LBE]. (a) SEM image with a red dashed box highlighting the GB oxidised region. (b) EDX result highlighting the Cr with the yellow dashed box showing the Cr depleted zone. (c) EDX result highlighting O. (d) EDX result highlighting Si.

As discussed in Chapter VI, the Cr depletion and Cr carbide dissociation will induce a phase change (from martensite to ferrite) which will generate more equiaxed grains with low grain average misorientation as shown in Fig. 7.10. This phase change is expected in the oxidising environment and has been previously reported by other researchers [50]. The red dashed box in Fig. 7.10 highlights the region correlated with the red dashed box in Fig. 7.9 (a). The yellow dashed box in Fig. 7.10 highlights the region where the phase change happened. By comparing the yellow dashed boxes in Fig. 7.9 (b) and Fig. 7.10, it is reasonable to suggest that the phase-changed region measured with EBSD in Fig. 7.11 correlates with the GBs oxidised region and Cr depleted zone shown in Fig. 7.9. However, the GBs oxidised region and Cr depleted zone, show different size of recrystallised grains as shown in Fig. 7.10 (b) with the black dashed box. A layer of small grains is formed at the surface in the GBs oxidised region, while the grains in the Cr-depleted region are much larger.

A possible mechanism is as follows: The formation of Cr oxide initially draws Cr from the surface grains to the GBs, where oxides form. As a result, the surface grains undergo phase changes earlier as the surrounding GBs become oxidised. These oxidised GBs are stable and inhibit further growth of the surface grains. However, the GBs can continue to oxidise by attracting more Cr from deeper within the material, causing Cr to diffuse from greater distances. This leads to a Cr-depleted region, with all Cr carbides dissociated. The GBs in this Cr-depleted region remain unoxidised. Consequently, the recrystallised grains in the Cr-depleted zone grow larger.

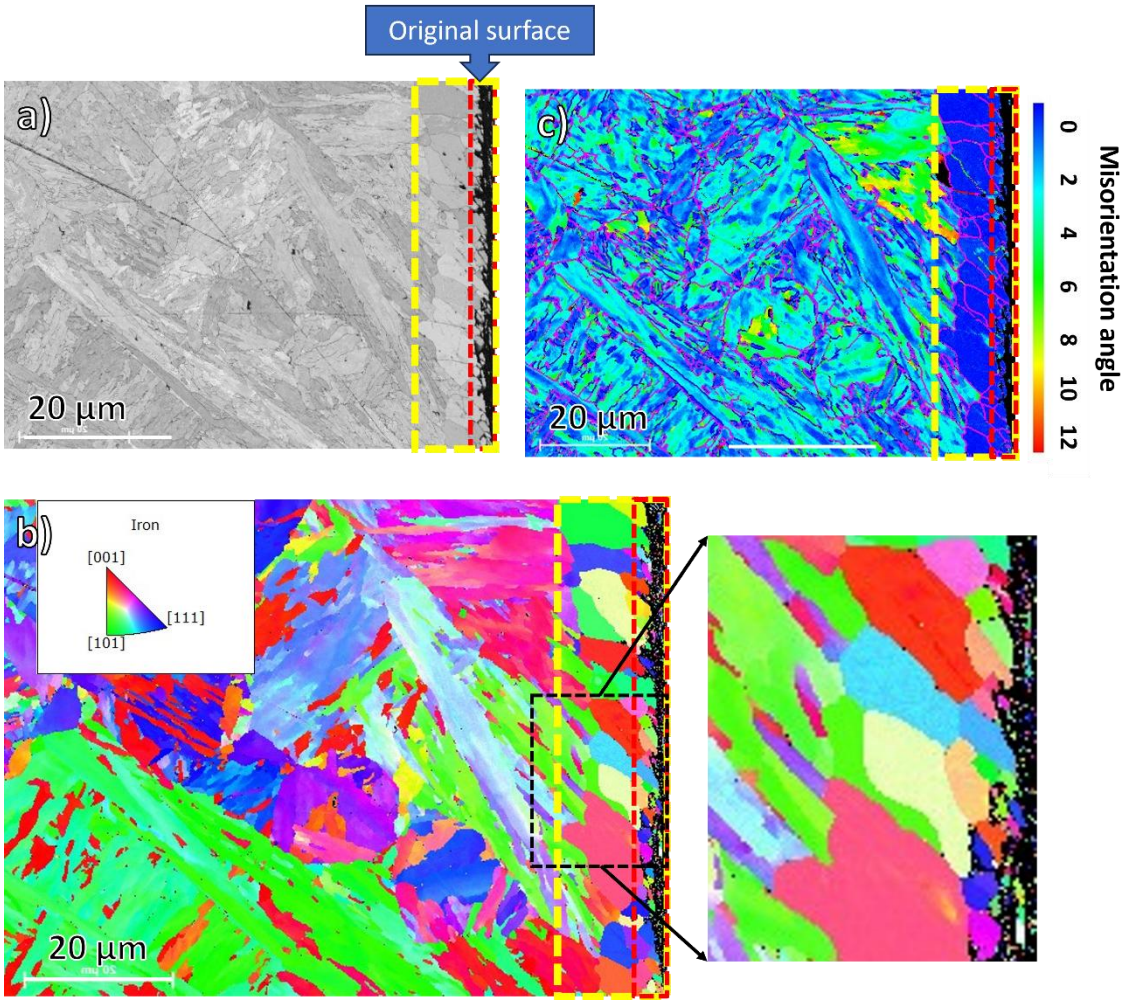

Fig. 7.10. SEM-EBSD results highlighting the phase changed region with yellow dashed box and GB oxidised region with red dashed box, corresponding to those shown in Fig. 7.10 [Sample: 245 h, oxidising environment, 700 °C, LBE]. (a) SEM result. (b) EBSD IPFZ map with the local region zoomed in for the black dashed box. (c) Grain average misorientation with scale bar.

Fig. 7.1 (g) shows that oxidisation happens in GBs but with a phase that has a different contrast appearing adjacent to the corrosion pattern. To further study the different contrast phases and the GBs oxide structure, an SEM-EDX line scan (20 KV) is used, with the result shown in Fig. 7.11. Firstly, the contrast difference between phases observed in the SEM image is detected as Mo from the EDX shown in Fig. 7.11 (b). However, the reason why Mo-enriched phases accumulate at the interface of oxidised GBs and unaffected T91 is unknown. At the same time, Pb-M energy

is 2.342 KeV and Bi-M energy is 2.419 KeV, similar to the Mo-Lα energy of 2.293 KeV. Thus, these phases may be LBE. There are previous studies that showed LBE underneath the oxide [50]. To further explore this, higher beam energy (for example, 30 KV) can be used to get the Mo- Kα peaks which can be used to distinguish Pb and Mo. The EDX results of 30 KV are shown in Fig. 7.12 proving the phase to be Mo-enriched rather than Pb or Bi. The linescan shows that Cr and O reach the highest content at the same place suggesting the formation of Cr oxides. Secondly, from Fig. 7.11 (c), the Si and Cr reach the peak content in different locations suggesting the formation of a layered oxide structure. This is consistent with the observations in the 506 h corroded sample shown in Fig. 7.8. The differences in stability and standard free energy of formation may influence the sequence of oxide formation [262].

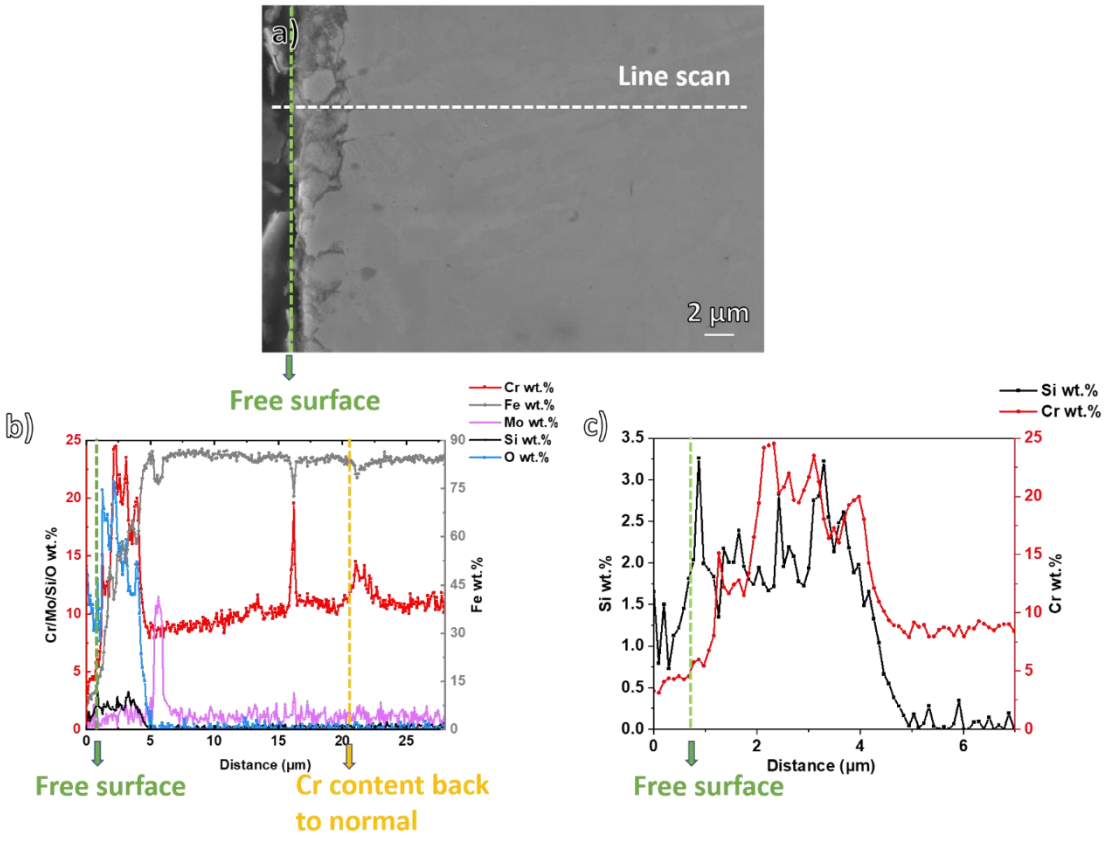

Fig. 7.11. SEM-EDX line scan results [Sample: 245 h, oxidising environment, 700 °C, LBE]. (a) SEM image showing the position of the line scan. (b) EDX line scan result showing content of Cr, Fe, Mo, Si, and O. (c) EDX line scan showing Si and Cr content at the surface region.

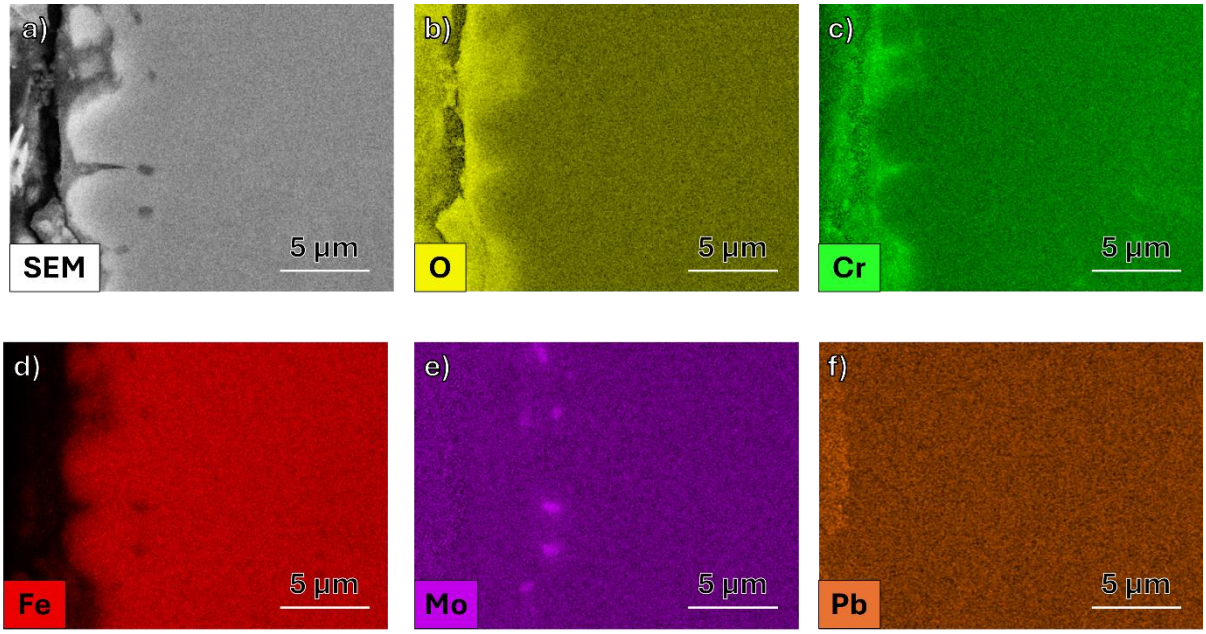

Fig. 7.12 30KV [Sample: 245 h, oxidising environment, 700 °C, LBE]. (a) SEM image. (b) – (f) EDX results highlight O, Cr, Fe, Mo, and Pb, respectively.

7.2.1.4 Corrosion occurring at PAGBs – part II: TEM based (245h)

As shown in Fig. 7.9 and Fig. 7.10, two distinct layers of phase-changed grains, with or without GB oxidation, are observed. However, it is challenging to explain the reason behind this phenomenon without higher-resolution characterisation methods. To further analyse the detailed structures of the oxidised PAGBs in the 245-hour corroded sample, one TEM sample and a set of APT samples were prepared.

Fig. 7.13 (a) provides an SEM overview of the whole sample, showing where it was lifted out. The right side of Fig. 7.13 (a) displays the Bakelite used to mount the sample, while the left side shows the T91. Fig. 7.13 (b) presents the STEM HAADF view of the TEM lift-out foil, and Fig. 7.13 (c) shows the STEM BF view. In both Fig. 7.13 (b) and (c), the oxidised GBs are clearly visible. Fig. 7.13 (d) is a zoomed-in HAADF image of the red box 1 from Fig. 7.13 (b), while the blue box 2

highlights a grain with oxidised GBs, with a higher magnification image of this area shown in Fig. 7.13 (f).

The ends of the oxidised GBs appear sharp, with a tendency for intergranular propagation rather than intragranular, suggesting that GBs may act as fast diffusion paths for oxidation. The growth of oxides from the original GBs into the grain interiors is visible in Fig. 7.13 (f). Fig. 7.13 (e) is a zoomed-in image of the blue box 3 from Fig. 7.13 (d). It is important to note that high-contrast features are also observed within the grains, not just along the GBs, suggesting the presence of intragranular oxidation.

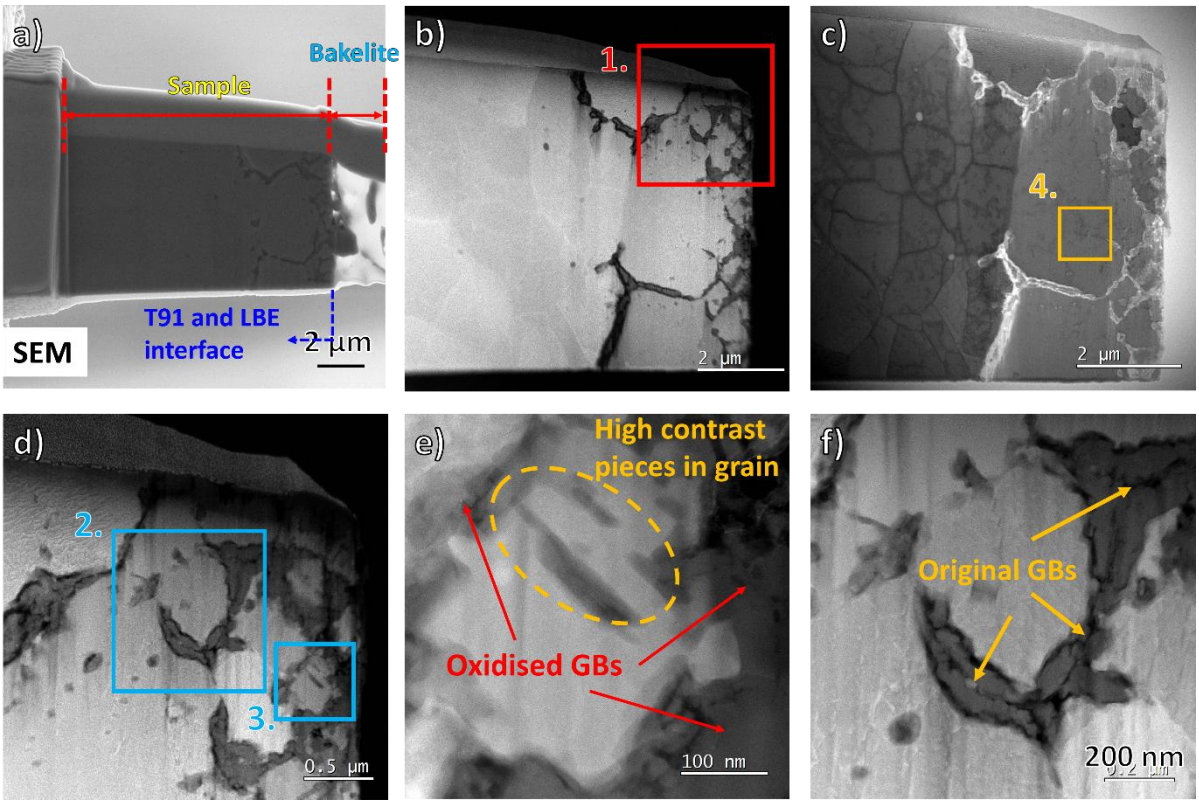

Fig. 7.13. [Sample: 245 h, oxidising environment, 700 ℃, LBE] (a) SEM overview of the TEM sample, showing the position of the lift-out. (b) STEM HAADF view, with red box 1 corresponding to Fig. 7.13 (d). (c) STEM BF view highlighting small features in the grains, with orange box 4 corresponding to Fig. 7.15. (d) STEM HAADF view of red box 1 from Fig. 7.13 (b). (e) STEM HAADF view of blue box 3 from Fig. 7.13 (d), showing the high-contrast region observed within the grains. (f) STEM HAADF view of blue box 2 from Fig. 7.13 (d), showing the oxidised GBs.

To investigate the high-contrast regions observed in Fig. 7.13 (e), STEM-EELS was performed on this area, and the results are shown in Fig. 7.14. From Figs. 7.14(b) - (d), the high-contrast regions in Fig. 7.14 (a) exhibit high Cr and O content with low Fe content, indicating that these high-contrast areas are Cr-enriched oxides. The STEM-EELS results suggest that oxidation occurs both at the PAGBs and within the martensite lath regions. Based on this and the earlier discussion, it is reasonable to propose that oxygen diffuses more rapidly along the GBs, forming oxides there. Over time, the oxygen continues to diffuse into the grains, leading to oxide formation within the grains as well.

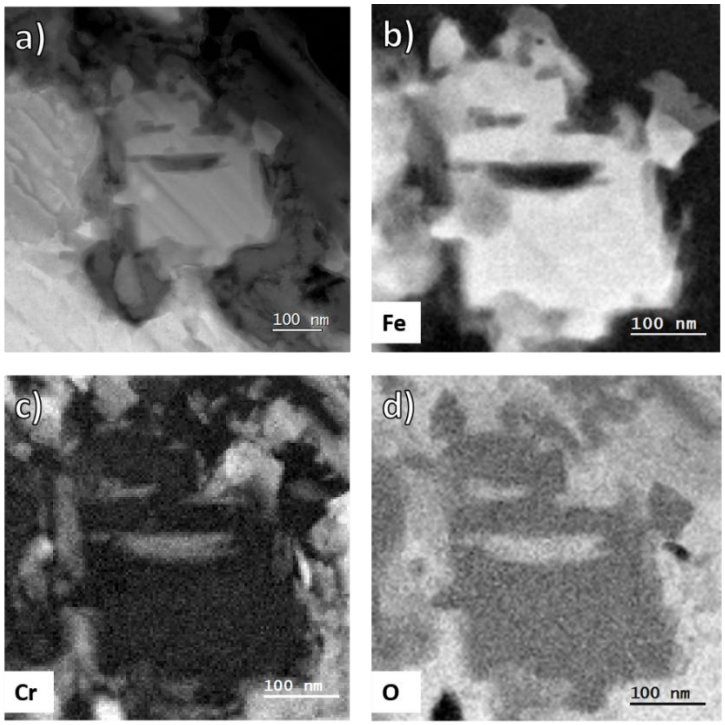

Fig. 7.14. [Sample: 245 h, oxidising environment, 700 ℃, LBE] (a) STEM HAADF view for grain with GBs and internal structure oxidised. (b) STEM-EELS result highlighting Fe. (c) STEM-EELS result highlighting Cr. (d) STEM-EELS result highlighting O.

Aside from the Cr-enriched oxides studied in Fig. 7.14, small features can be seen in the BF view in Fig. 7.13 (c), highlighted by the orange box 4. To further understand their chemical

composition, STEM-EELS was performed. To clarify the different structures, coloured boxes are used, as shown in Fig. 7.15 (a). Orange boxes 1 and 2 highlight the ends of GBs; blue boxes 3 and 4 highlight the dark lines observed near the oxidised GBs; and the red box 5 highlights particles linked to the oxidised GBs and the dark lines highlighted by the blue boxes.

The GBs in the orange boxes are enriched with O, Cr, Mn, and V, suggesting the formation of oxides containing Cr, Mn, and V within the GBs. The absence of Si is likely due to the high energy of the Si K-edge (1839 eV), making it difficult to detect. In the blue boxes, the lines are enriched with O, Cr, and Mn, indicating oxide formation. These lines may serve as fast diffusion pathways for oxygen, similar to GBs, and could represent internal lath boundaries or other defects, such as dislocations [263]. From Figs. 7.15 (b) and (f), the particles in the red box 5 are found to be enriched with O and V. As mentioned in section 5.2.2.3, VN exists at the interface between T91 and LBE. Based on the results, it is unclear whether these particles are fully oxidised VN or if they have formed an oxide shell around them. To further investigate this, APT, with its 3D chemical composition analysis, was employed.

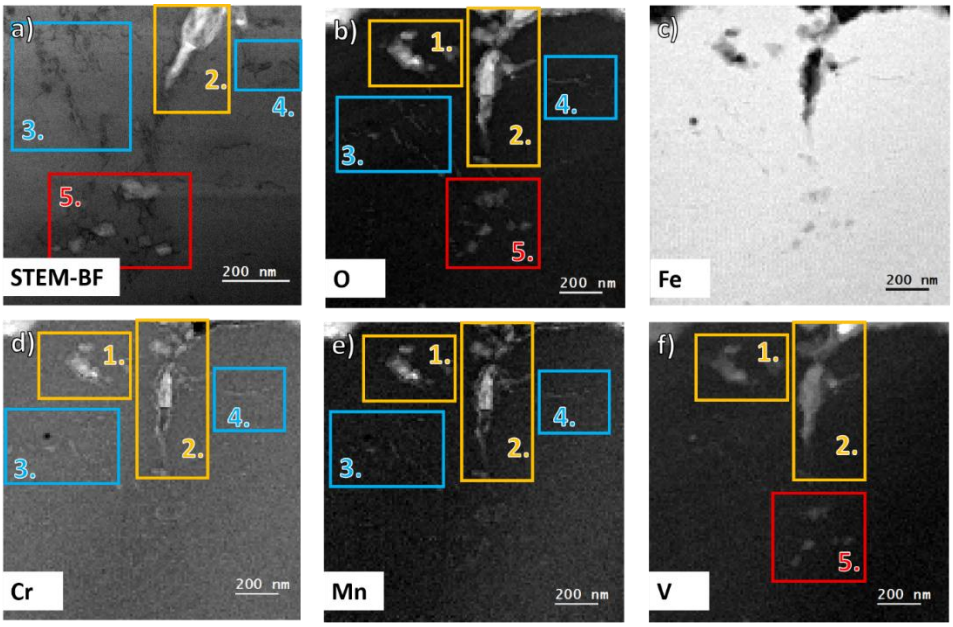

Fig. 7.15. [Sample: 245 h, oxidising environment, 700 ℃, LBE] (a) STEM HAADF view of the same area highlighted with orange box 4 in Fig. 7.13 (c). STEM EELS results highlight (b) O, (c) Fe, (d) Cr, (e) Mn, and (f) V with different coloured boxes to differentiate various structures.

As seen in Fig. 7.13 (f), the oxidation progresses from PAGBs into the grain interior. To verify this and analyse the distribution of the elements in this area, STEM-EELS and EDX are used, with the results presented in Fig. 7.16 and Fig. 7.17, respectively. In Fig. 7.16 (b), the high-contrast regions in Fig. 7.16 (a) (dark areas) are confirmed to be oxides, including the PAGBs and the surrounding fragments. Based on the Cr and Mn results in Fig. 7.16 (d) and (e), the central part of the oxidised GBs consists of Cr- and Mn-enriched oxides, while the composition of the outer layer remains unknown. The missing of this information can be caused by the corresponding fluorescent edges being at energies beyond the range of STEM-EELS used here. This finding is consistent with the observations in Fig. 7.15.

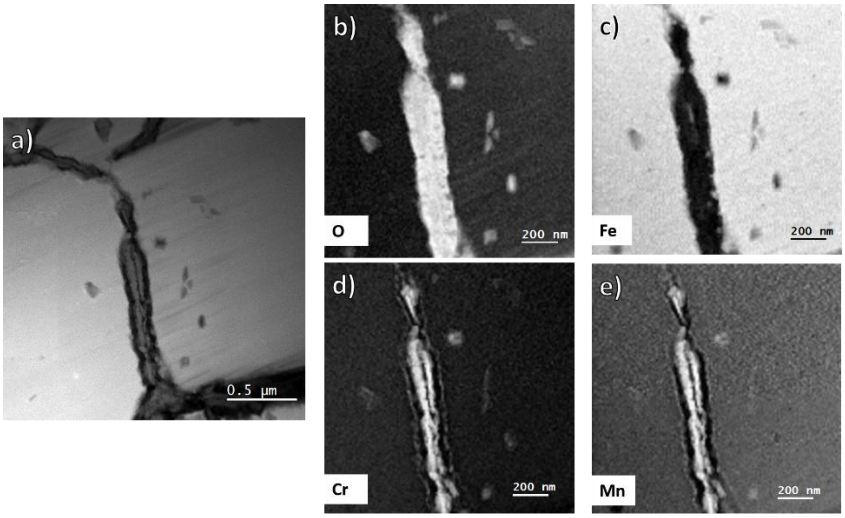

Fig. 7.16. STEM-EELS results [Sample: 245 h, oxidising environment, 700 ℃, LBE]. (a) STEM HAADF view for the oxidised GB. (b) EELS result highlighting O. (c) EELS result highlighting Fe. (d) EELS result highlighting Cr. (e) EELS result highlighting Mn.

To determine the composition of the missing part, STEM-EDX was used. Fig. 7.17 (a) and (b) show that the central portion of the oxidised PAGB consists of Cr-enriched oxide. Fig. 7.17 (c) confirms that the missing edge in the Fig. 7.16 EELS results is a Si-enriched region with a high oxygen content. Therefore, a layer of Si-enriched oxide formed around the Cr-enriched oxide core. This finding aligns with our SEM-EDX observations presented in Fig. 7.8 (e) and Fig. 7.11 (b) and (c).

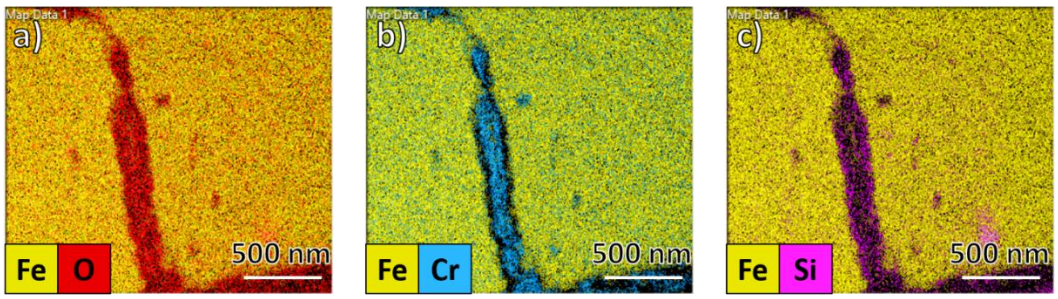

Fig. 7.17. STEM-EDX results for the same region are shown in Fig. 7.16 (a) [Sample: 245 h, oxidising environment, 700 ℃, LBE]. (a) EDX result highlighting Fe and O. (b) EDX result highlighting Fe and Cr. (c) EDX result highlighting Fe and Si.

7.2.1.5 Corrosion occurring at PAGBs – part II: APT based (245h)

To reveal the 3D structure of the oxidised GBs shown in Fig. 7.17, a set of APT samples was prepared. The sample preparation process is illustrated in Fig. 7.18. The lift-out was made parallel to the interface between the T91 material and the Bakelite used to mount the sample. Fig. 7.18 (a) and (b) show SEM images of the lift-out from both the front and back sides. To ensure the inclusion of the oxidised GBs in the lift-out, SEM-EDX was performed, with the results shown in Fig. 7.18 (c) and (d). The EDX results confirm that the GBs are oxidised, containing high levels of O and Cr. Following this, the lift-out was extracted from the sample and welded to the Si posts on the APT Si coupons, after which they were milled into a needle shape, as shown in Fig. 7.18 (e) and (f).

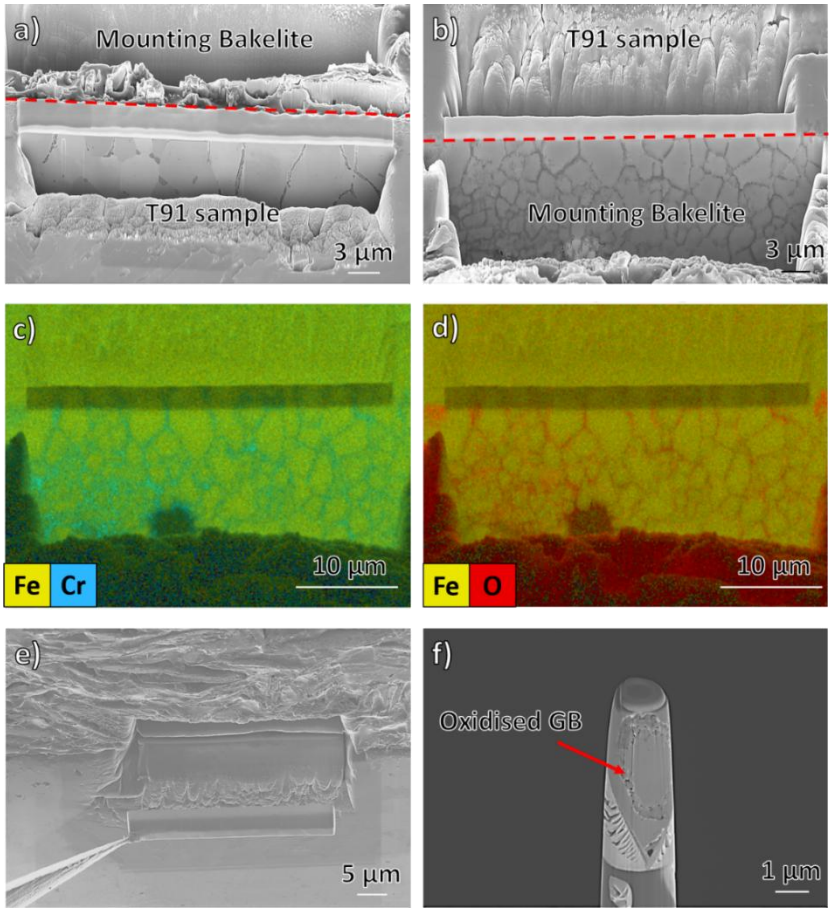

Fig. 7.18. APT sample preparation process [Sample: 245 h, oxidising environment, 700 °C, LBE]. (a) and (b) SEM views of the lift-out from two sides. (c) SEM-EDX result of Fig. 7.18 (b),

highlighting Fe and Cr. (d) SEM-EDX result of Fig. 7.18 (b), highlighting Fe and O. (e) The lift-out process. (f) Half-milled APT sample with the oxidised GB included.

Laser pulsed mode was used to analyse APT samples, and three of them contained oxides. The following section presents the results from the oxide-containing samples.

Fig. 7.19 shows a sample containing VN. Fig. 7.19 (a) provides the 3D reconstruction, highlighting the presence of SiO, CrO, and VN ions. This dataset demonstrates that Si and Cr form an oxide layer around VN precipitates rather than directly oxidising the VN itself, answering the question raised by Fig. 7.15.

Fig. 7.19 (b) shows the distribution of Cr ions within the reconstruction, highlighting the region where the O ion density exceeds 2.28/nm³ within the APT sample. To clearly illustrate the three regions of interest (ROIs) and the direction of the 1D concentration profiles, Fig. 7.19 (b) presents views from two different angles.

Focusing first on the red ROI in Fig. 7.19 (b), we observe from Fig. 7.19 (a) that this ROI spans from the T91 matrix through a thin layer of CrO, followed by SiO, and then VN. Fig. 7.19 (c) shows the 1D concentration profile of the red ROI, along the direction marked by the black dashed arrow. Based on the concentration changes of different elements, the 1D concentration profile is divided into five distinct regions, indicated by vertical black dashed lines: T91 matrix, CrO-1, SiO, CrO-2, and VN. In this ROI, SiO is surrounded by a shell of CrO, which differs from the sequence observed in Fig. 7.17.

Fig. 7.19 (d) provides the 1D concentration profile for the yellow ROI, which mainly consists of CrO with minor Si and V enrichment. Lastly, Fig. 7.19 (e) shows the 1D concentration profile for the orange ROI, extending from VN to the adjacent oxide. The oxide in this region displays a similar distribution to the yellow ROI in Fig. 7.19 (d), primarily consisting of CrO with slight accumulations of Si and V.

The ROIs from different locations reveal variations in oxide distribution types.

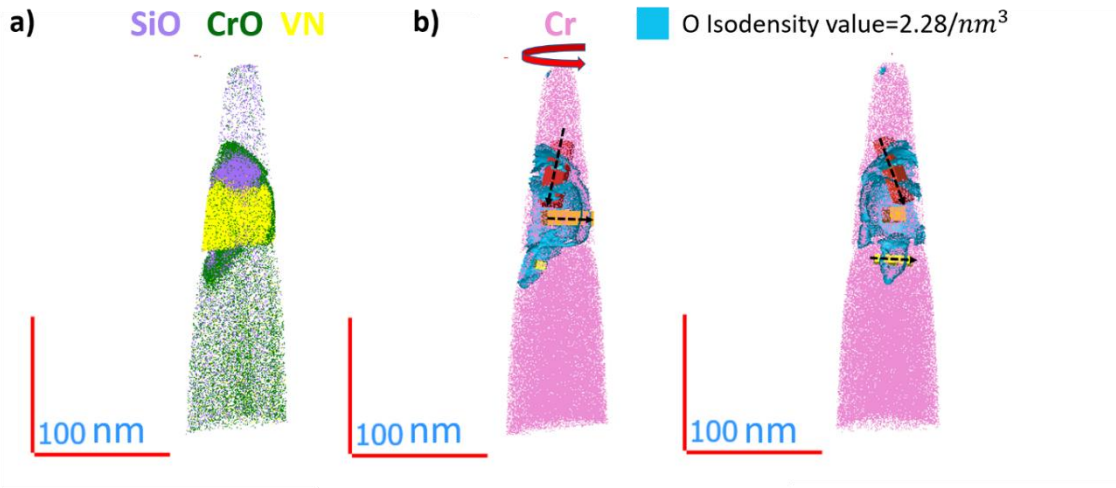

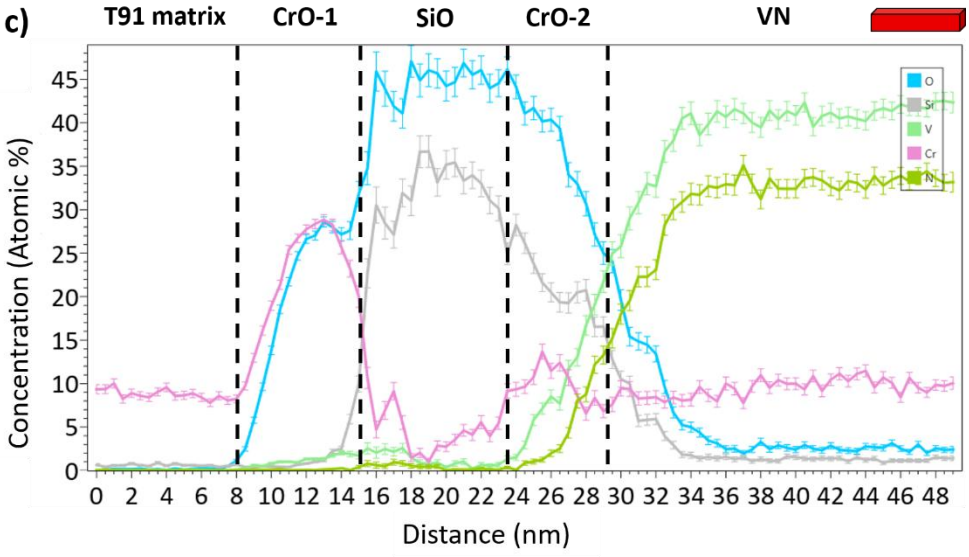

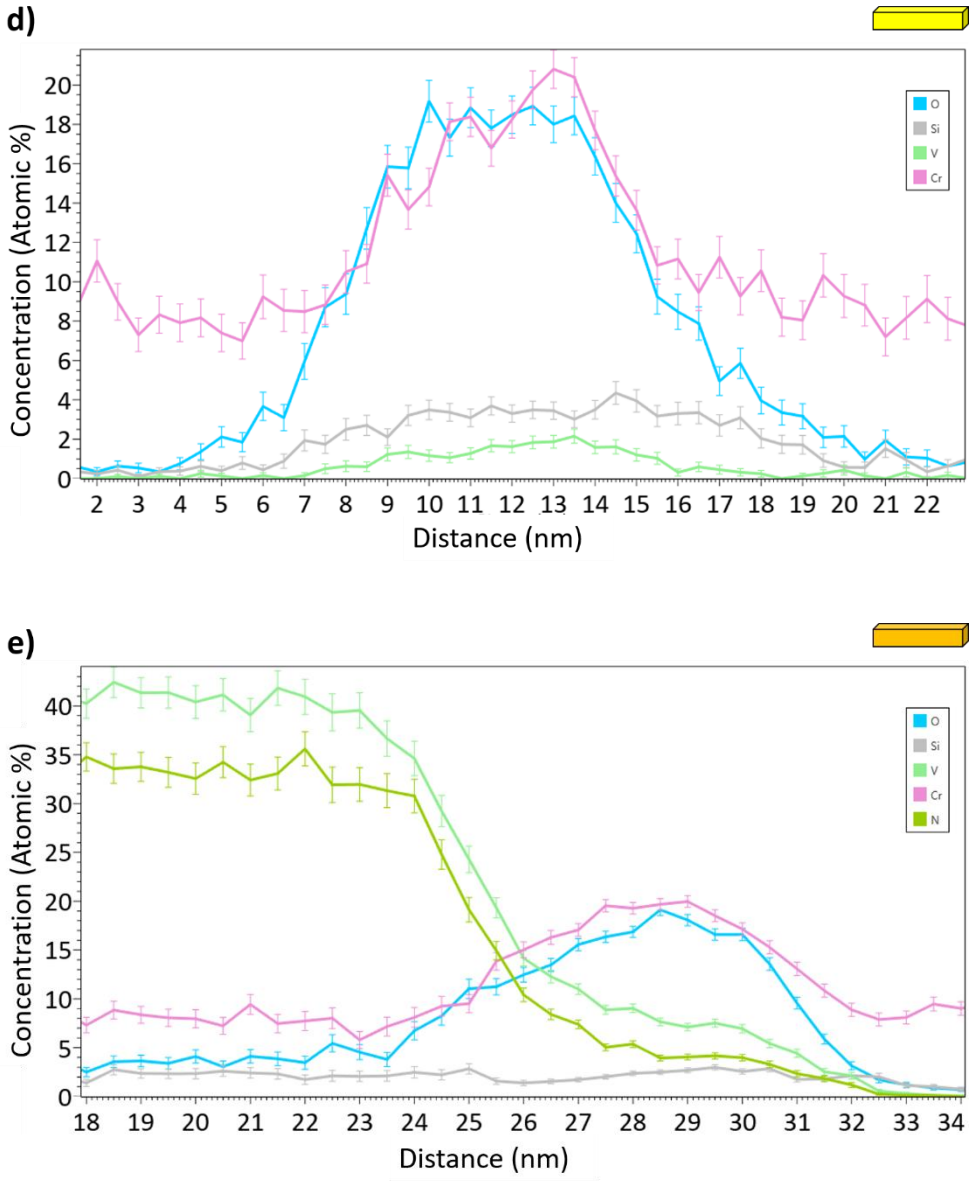

Fig. 7.19. APT characterisation of oxide formed around VN from the lift-out shown in Fig. 7.18 [Sample: 245 h, oxidising environment, 700 °C, LBE]. (a) 3D APT reconstruction showing SiO, CrO, and VN ions. (b) APT 3D reconstruction with O isosurface (isodensity = 2.28/nm³) and highlighting 3 ROIs with 1D concentration profile directions shown. (c) 1D concentration profile of the red ROI shown in Fig. 7.19 (b) with different regions marked. (d) 1D concentration profile of the yellow ROI shown in Fig. 7.19 (b). (e) 1D concentration profile of the orange ROI shown in Fig. 7.19 (b).

The second APT data set containing oxides is shown in Fig. 7.20. Fig. 7.20 (a) displays the APT 3D reconstruction highlighting Fe, Si, and CrO ions. Fig. 7.20 (b) shows the top-down view of Fig. 7.20 (a), with 2 ROIs indicated, along with the directions of the 1D concentration profiles. From the 1D concentration profiles in Fig. 7.20 (c) and (d), this APT 3D reconstruction reveals a 3-layered oxide structure consisting of Cr-enriched oxide, Fe-enriched oxide, and Si-enriched oxide. These oxides have clear boundaries with no mixing. Depending on the location, the content of each oxide layer varies, but the primary elements remain consistent.

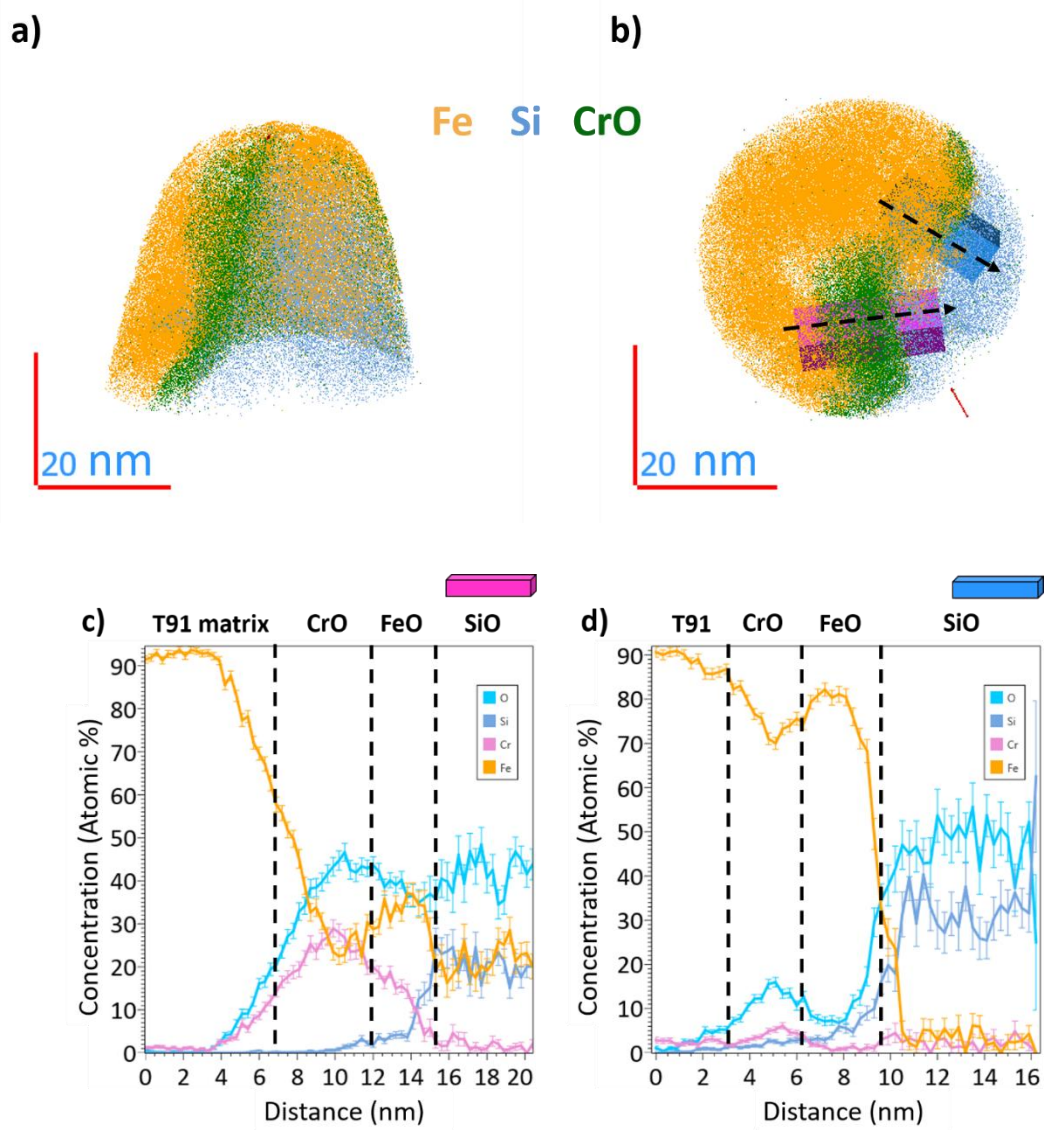

Fig. 7.20. APT characterisation of a 3-layered oxide [Sample: 245 h, oxidising environment, 700 °C, LBE]. (a) 3D APT reconstruction showing Fe, Si, and CrO ions. (b) 3D APT reconstruction

viewed from the top down of Fig. 7.20 (a), highlighting 2 ROIs with the direction of the 1D concentration profiles indicated. (c) 1D concentration profile of the pink ROI shown in Fig. 7.20 (b). (d) 1D concentration profile of the blue ROI shown in Fig. 7.20 (b).

To compare the elemental concentrations in different regions, the Si-enriched oxide area, Cr-enriched area, and T91 matrix were extracted separately from the 3D reconstruction as three new reconstructions based on the elemental concentrations. The threshold content was determined by adjusting the iso-content until a smooth interface formed between different phases. For the Si-enriched oxide, the threshold concentration was set at a Si concentration exceeding 8.09 at.%. The region that met this threshold was extracted to create a new 3D reconstruction containing only this region (or these regions). A similar method was applied to extract the T91 matrix and Cr-enriched oxide. The threshold for the T91 matrix was defined where the Fe concentration is greater than 80.25 at.%, while the Cr-enriched oxide was defined by a CrO concentration higher than 8.71 at.%. After these three reconstructions were extracted, the elemental compositions could be considered separately, with peak overlap taken into account during this process. The results are shown in Table 7.1 and Fig. 7.21.

The matrix mainly consists of Fe, with less than 3 at.% Cr. This is consistent with what was observed at a larger scale in Fig. 7.11 (b) and (c). This concentration is lower than the Cr concentration in the unaffected T91, which is around 9 wt.%. The Cr-enriched oxide has high contents of Fe (47 at.%), Cr (17 at.%), and O (29 at.%). The Si-enriched oxide has a high concentration of O (38 at%), Si (31 at%), and a lower content of Fe (19 at.%). Compared to the T91 matrix, the oxides exhibit higher levels of Ni, with the Si-enriched oxide having approximately 61 times the concentration in the matrix, and the Cr-enriched oxide around 18 times.

Table 7.1. The average composition of SiO (area Si concentration >8.09 at.%), CrO (area CrO concentration >8.71 at.%), and T91 matrix (area Fe concentration >80.25 at.%) [Sample: 245 h, oxidising environment, 700 ℃, LBE].

	Fe	O	Cr	Si	Ni	Others
SiO	0.18788	0.37734	0.01648	0.31206	0.10624	0
CrO	0.47459	0.28531	0.16948	0.02621	0.03085	0.01356
Matrix	0.95897	0.00729	0.02758	0.00243	0.00173	0.002

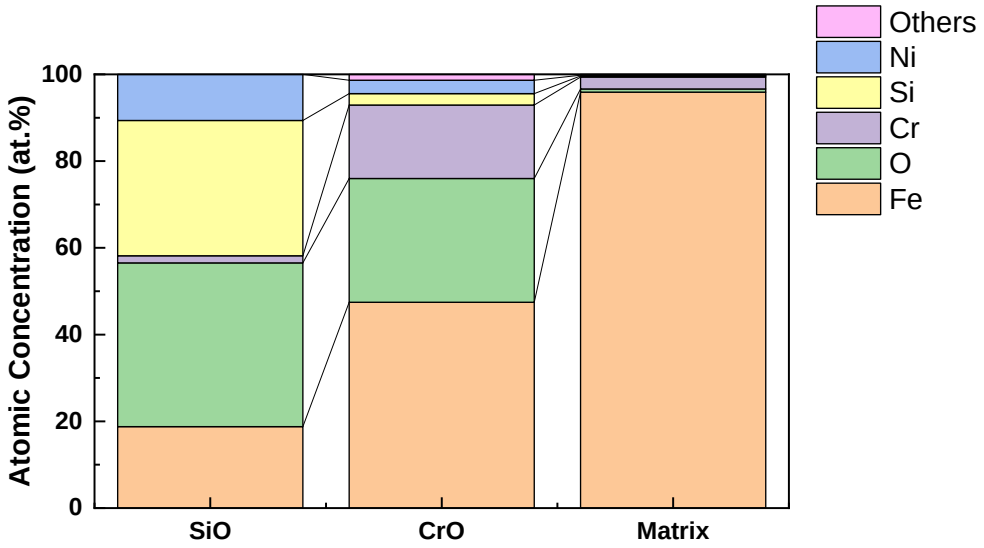

Fig. 7.21. The average composition of SiO, CrO, and T91 matrix according to Table 7.1 [Sample: 245 h, oxidising environment, 700 ℃, LBE].

The last APT sample containing oxides shows a similar structure to those observed in the STEM results presented in Fig. 7.13 to Fig. 7.16. The oxides appear separated from the GBs and are formed within the grains. APT reconstructions are illustrated in Fig. 7.22 (a), (b), (c), and (d), highlighting different ions. The various ions represent the atoms detected at their respective

positions without indicating the actual phases present. The 3D reconstructions show that SiO, CrO, FeO, and Fe_2O ions do not always occupy the same locations, suggesting that the positions of these oxides differ within the sample.

To further study the composition of the different oxides, four ROIs were selected from the areas highlighted in Fig. 7.22 (a), (b), (c), and (d), indicated by red dashed boxes. To better illustrate the directions of the 1D concentration profiles, the positions of the ROIs are shown superimposed on the larger 3D reconstructions and rotated according to the direction of the red arrow above the reconstruction.

The 1D concentration profile of the pink ROI in Fig. 7.22 (e) from Fig. 7.22 (a) shows that layers of Fe-enriched oxide are formed adjacent to the Si-enriched oxide, with negligible amounts of Cr-enriched oxide present. The brown ROI in Fig. 7.22 (b) consists of Cr and Fe oxides without any Si oxide, as indicated by the 3D reconstructions. Fig. 7.22 (f) provides similar results, with the positions of the Cr and Fe-enriched oxides aligning closely. The green ROI shown in Fig. 7.22 (c) exhibits a different oxide arrangement compared to the results shown in Fig. 7.22 (g), where multiple oxide layers are formed in the sequence of Si-enriched oxide, Fe-enriched oxide, V-enriched oxide, and then Cr-enriched oxide. The final ROI, the blue one shown in Fig. 7.22 (d), also reveals a layered oxide structure with Fe-enriched oxide followed by Cr-enriched oxide, as depicted in Fig. 7.22 (h).

From all the results presented in Fig. 7.22, we can confirm the formation of small-sized oxides within the grains. However, the oxide structures can vary. According to the Ellingham diagram [160], the oxide formation threshold for different elements is Si < Cr < Fe, indicating that Si is the easiest to oxidise. However, this only explains the presence of different oxides (Si, Cr, and Fe) and does not provide further insight into the various layers observed in Fig. 7.22. Local oxygen content, the concentration of different elements (Fe, Cr, Si, V, etc.), grain orientation, and defects in the material may all influence the sequence and composition of oxide formation.

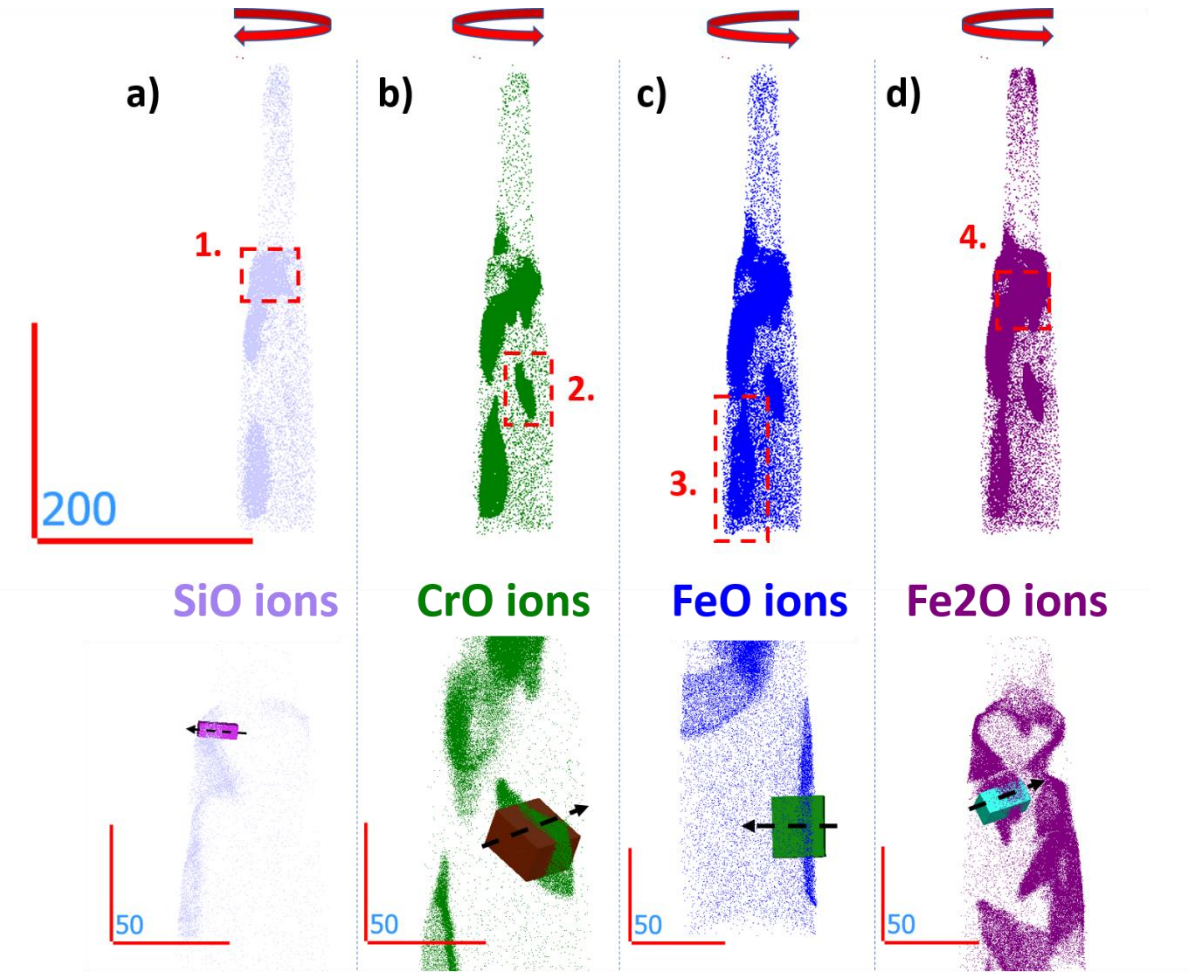
a)
b)
c)
d)
1.
2.
3.
4.
200
SiO ions
CrO ions
FeO ions
Fe2O ions
50
50
50
50

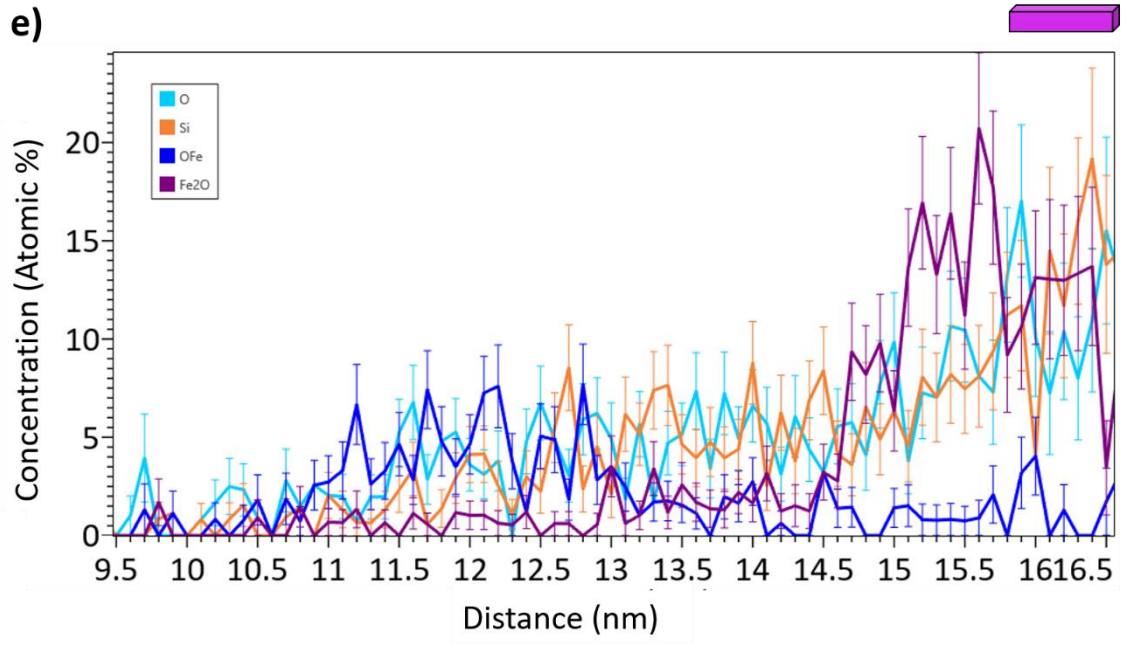
e)
O
Si
OFe
Fe2O
Concentration (Atomic %)
0
5
10
15
20
9.5
10
10.5
11
11.5
12
12.5
13
13.5
14
14.5
15
15.5
16
16.5
Distance (nm)

f)

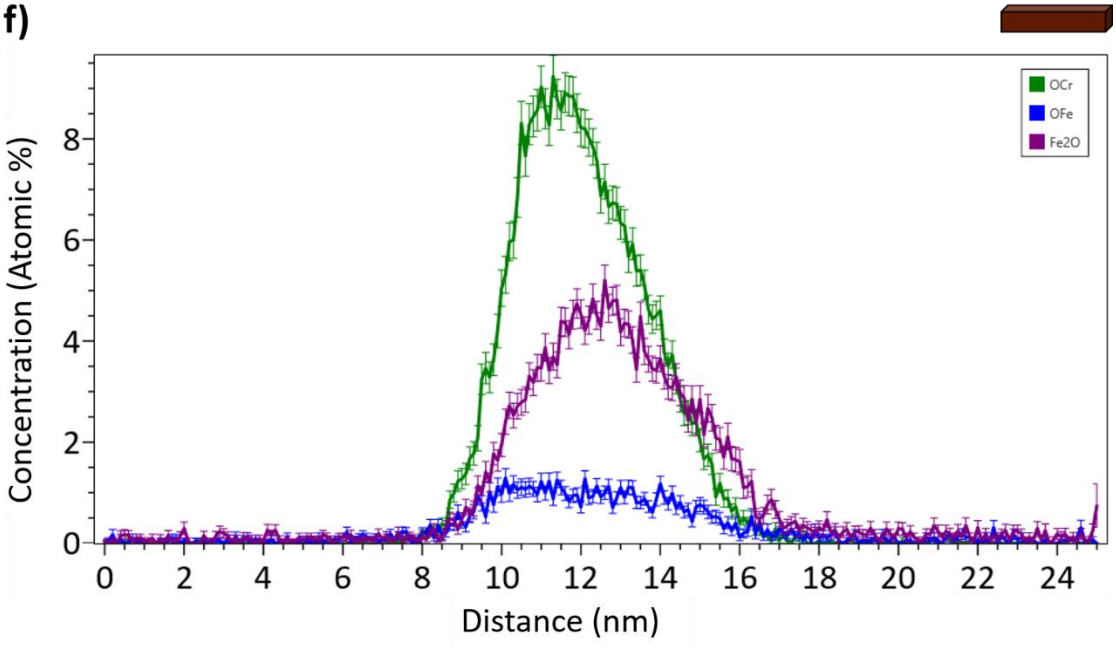
OCr
OFe
Fe2O
Concentration (Atomic %)
0
2
4
6
8
0
2
4
6
8
10
12
14
16
18
20
22
24
Distance (nm)

g)

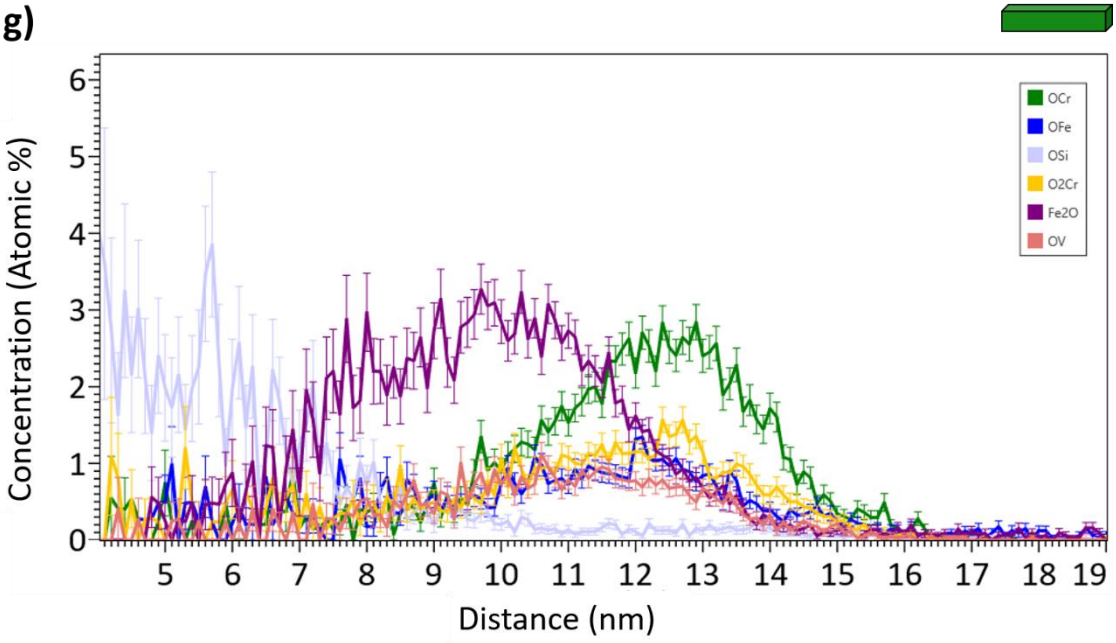
OCr
OFe
OSi
O2Cr
Fe2O
OV
Concentration (Atomic %)
0
1
2
3
4
5
6
5
6
7
8
9
10
11
12
13
14
15
16
17
18
19
Distance (nm)

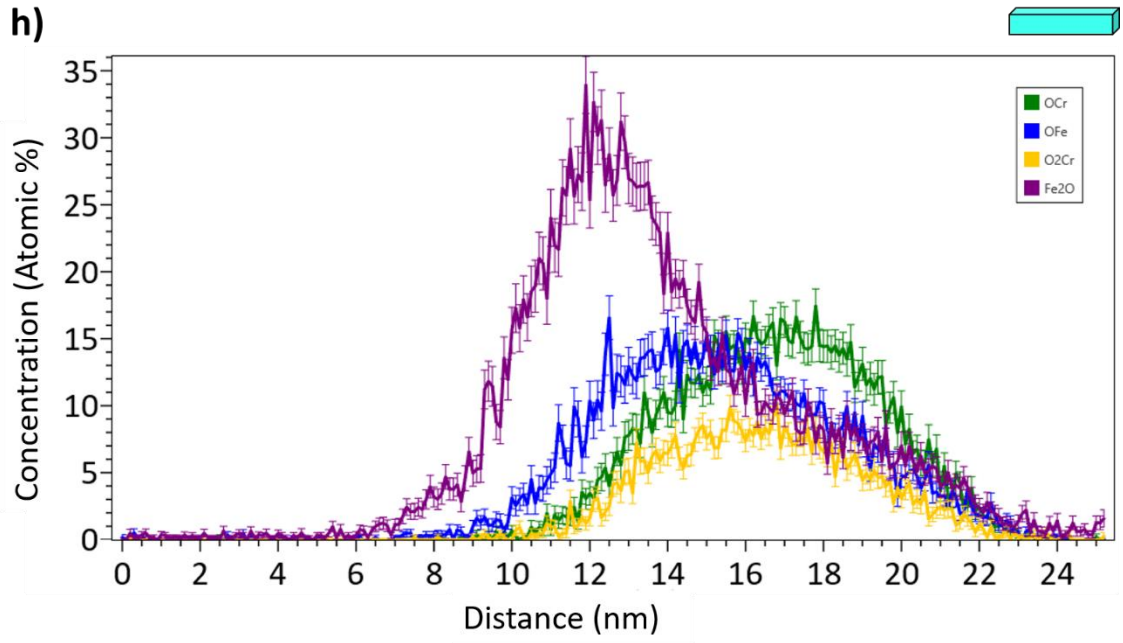

Fig. 7.22. APT analyses of the oxides formed inside grains [Sample: 245 h, oxidising environment, 700 ℃, LBE]. (a) APT 3D reconstruction highlighting SiO. (b) Highlighting CrO. (c) Highlighting FeO. (d) Highlighting Fe_2O, respectively, with the ROIs and directions of 1D concentration profiles highlighted. (e) 1D concentration profile for the pink ROI highlighted in Fig. 7.22 (a). (f) 1D concentration profile for the brown ROI highlighted in Fig. 7.22 (b). (g) 1D concentration profile for the green ROI highlighted in Fig. 7.22 (c). (h) 1D concentration profile for the blue ROI highlighted in Fig. 7.22 (d).

7.2.1.6 Corrosion occurring at PAGBs – part III: TKD based (245h)

Other than the oxides observed in GBs and the pieces within the grains, a change in grain morphology is also noted in Fig. 7.13 (b) and (c). As shown in Fig. 7.10, there are two types of phase-changed areas. The first is the region where the GBs are oxidised and recrystallised into smaller grains, followed by the region where no oxidation occurs, resulting in ferritization due to Cr depletion, which leads to larger grain sizes.

To further compare the differences between these two regions, on-axis TKD was performed on the TEM sample analysed in section 7.2.1.4, and the results are shown in Fig. 7.23. The dashed red box in Fig. 7.23 indicates where STEM-EELS and EDX analyses were conducted, which resulted in some carbon contamination; however, this does not affect the results.

With the higher resolution of on-axis TKD and increased magnification, we can not only compare the differences between the oxidised GB region and the Cr-depleted region but also reveal distinctions within the oxidised GB region. Both the pattern quality in Fig. 7.23 (a) and the Inverse Pole Figure (IPF) map in Fig. 7.23 (b) demonstrate that within the GBs oxidised region, the grain size near the T91 surface (marked as region 1 in Fig. 7.23 (b), referred to as R1) is smaller than that of the grains located deeper (marked as region 2 in Fig. 7.23 (b), referred to as R2).

Possible mechanisms for this observation are suggested. As mentioned earlier, the oxidation of the GBs limits the growth of ferritized grains, which can explain the grain size difference between R1 and R2 in comparison to region 3 (R3). However, we also noted a size difference between R1 and R2. One possible explanation is that the GBs of the surface grains (in R1) are oxidised first. With a high surrounding oxygen level, oxidation may also initiate within the grains, leading to the formation of new oxides that break the grains into smaller parts. We observed areas near the oxidised GBs in R2 where oxides appear within the grains adjacent to the GBs.

Combining these results with Fig. 7.10, we know that R3 is within the phase-change region, with Cr depletion but no oxidation of the GBs. Fig. 7.23 (c) shows the average misorientation of grains in R2 and R3, which is also indicated by a slight colour difference between the grains in R3, as seen in Fig. 7.23 (b), and the lines in Fig. 7.23 (a). If R1 and R2 are assumed to be fully ferritized regions, R3 can be recognised as an intermediate state between full ferritization and an unchanged martensite structure. It maintains a certain level of misorientation, but this is much lower than that of the unaffected martensite regions, indicating altered grain morphology.

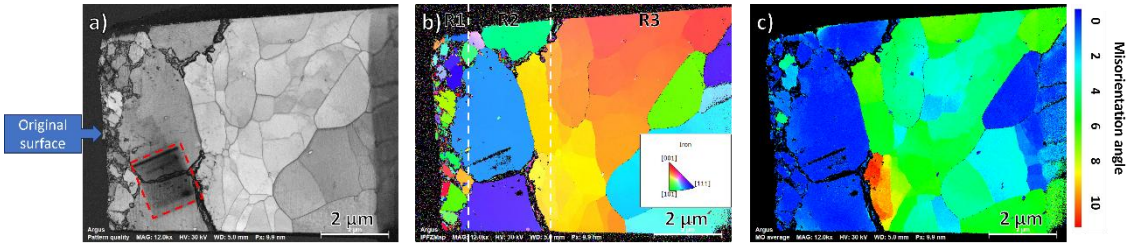

Fig. 7.23. On-axis TKD results for the TEM sample shown in Fig. 7.10 [Sample: 245 h, oxidising environment, 700 ℃, LBE]. (a) TKD pattern quality map, with a red dashed box highlighting the region affected by STEM-EELS/EDX contamination. (b) TKD-IPFZ map, with different areas divided into regions R1, R2, and R3. (c) Grain average misorientation, accompanied by a scale bar.

7.2.1.7 Corrosion occurring at PAGBs with crakes (245h)

The oxide layer with cracks is also observed in the 245 h corroded sample, as shown in Fig. 7.24, which is similar to the cracks observed in 70 h and 506 h mentioned in section 7.2.1.2. This oxide layer is enriched with Si and Cr, but lacks Fe. Beneath the surface oxide layer, the oxidation of the grain boundaries (GBs) is evident, highlighted in Fig. 7.24 (b), (c), and (e) with the dashed black rectangle. A Cr depletion zone is observed adjacent to the oxide, where Cr-enriched precipitates have dissociated. Fig. 7.24 (f) illustrates Pb penetrating into the unaffected T91 matrix through the cracks. This can be detrimental to the material's corrosion resistance, as the liquid metal can reach deeper areas of the material through these cracks, significantly accelerating the corrosion process.

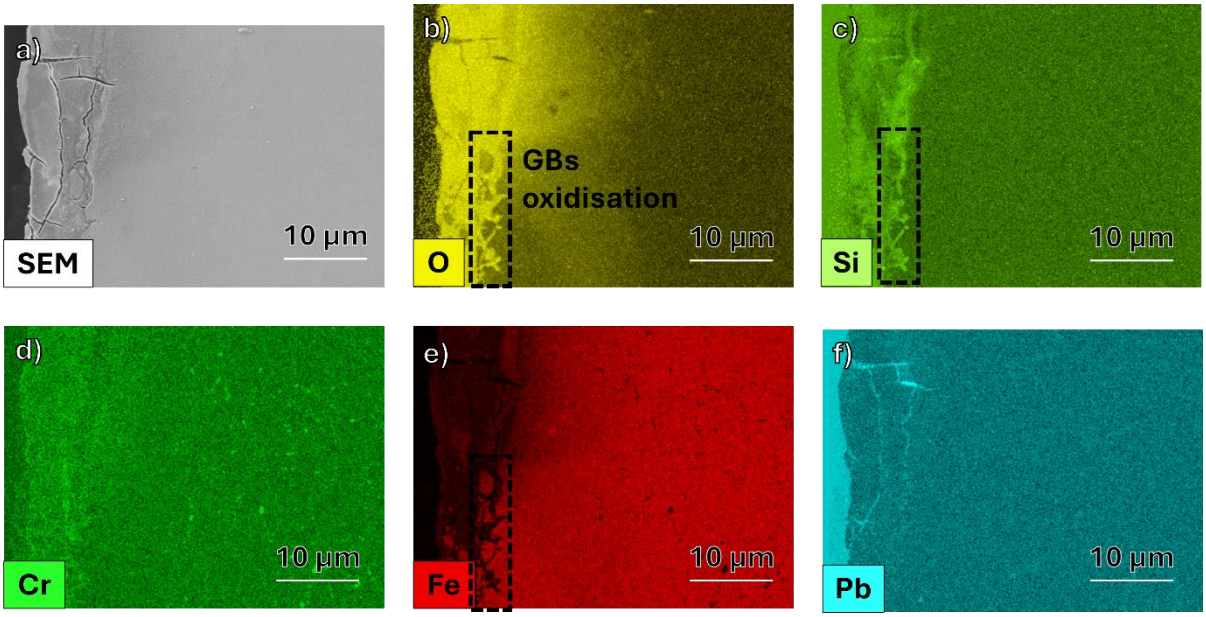

Fig. 7.24. SEM-EDX with cracks observed in the oxide layer [Sample: 245 h, oxidising environment, 700 °C, LBE]. (a) SEM image. (b)-(f) EDX results highlight O, Si, Fe, Cr, and Pb, respectively, with GBs oxidisation highlighted.

7.2.2 Area corrosion occurring within the grains

7.2.2.1 Area Corrosion with minimal LBE penetration

In addition to corrosion through GB oxidation, some regions of the sample show much more localized corrosion, as shown in Fig. 7.1 (d)-(f). SEM-EDX was used to study the element redistribution in these regions. Fig. 7.25 presents the SEM-EDX results corresponding to Fig. 7.1 (d), which depicts the 70 h corroded sample. To investigate the influence of accelerating voltage on resolution, the EDX results acquired at 25 kV are shown in Fig. 7.26. The EDX results in Fig. 7.25, obtained at 5 kV, demonstrate much better resolution. This improvement is expected, as reducing the accelerating voltage can enhance both the lateral and depth resolution of EDS maps [167].

The EDX results confirm that the significant chunk of corrosion is primarily due to oxidation, with only trace amounts of LBE present. Fig. 7.25 (b)-(d) illustrates the distribution of oxides, which are enriched with Cr and Si. In Fig. 7.25 (e), it can be observed that Fe has disappeared in the oxide area, although some remains within the corroded region. Furthermore, Fig. 7.25 (f) displays the distribution of Pb, which appears at the interface between the T91 matrix and the oxides. This observation is expected, as the LBE is a liquid phase with dissolved oxygen. If the formed oxides are porous, the LBE can penetrate through them and further corrode the deeper matrix. However, Fig. 7.26 (c) and (f) indicate that the observed enrichment corresponds to a Mo-enriched phase. It is important to note that spectrum overlaps between Mo and Pb are expected at 5 kV accelerating voltage, but a 25 kV setting should resolve this issue. Upon examining the spectrum in Fig. 7.26, no peaks were found at 10.550 eV (Pb-L). Thus, the Pb enrichment observed in Fig. 25 should be the artefacts caused by overlapping.

To determine the content of each element and the level of LBE penetration, an EDX line scan was performed along the white line shown in Fig. 7.25 (a), with results displayed in Fig. 7.25 (g). The Cr-enriched oxide is the dominant phase, while Si exhibits a relatively low level of enrichment. Minimal LBE penetration is observed, and Cr depletion is barely discernible in Fig. 7.25 (d), where Cr-enriched carbides are distributed around the corroded interface, suggesting little phase change, as discussed in Chapter 6. This conclusion is further supported by the EBSD results shown in Fig. 7.27 from a zoomed-out view.

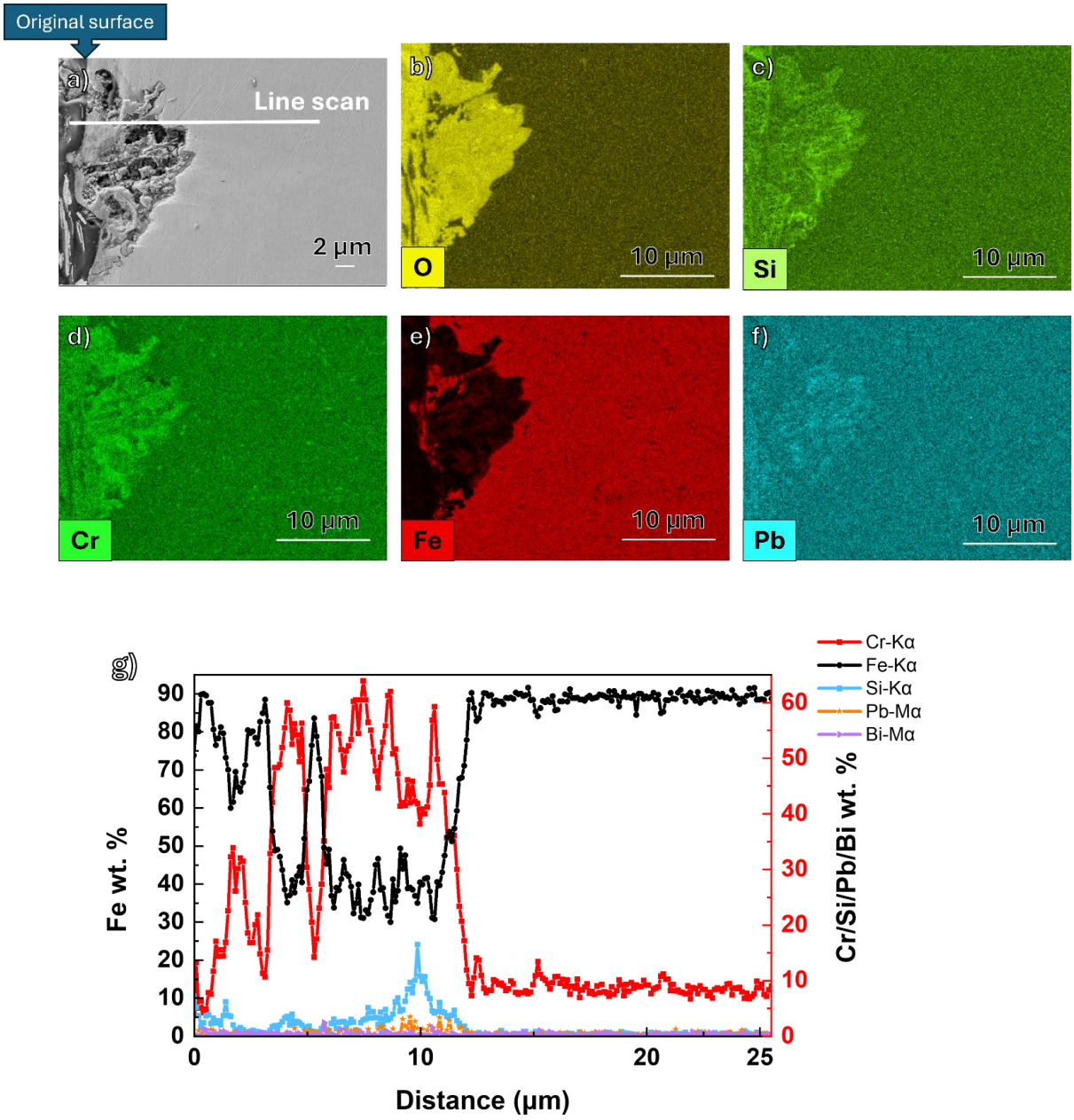

Fig. 7.25. SEM-EDX results acquired at 5 KV with area corrosion [Sample: 70 h, oxidising environment, 700 ℃, LBE]. (a) SEM image for Fig. 7.1 (d). (b)-(f) SEM-EDX results (5 KV) highlighting O, Si, Cr, Fe and Pb, respectively. (g) EDX line scan result for the white line in Fig. 7.24 (a).

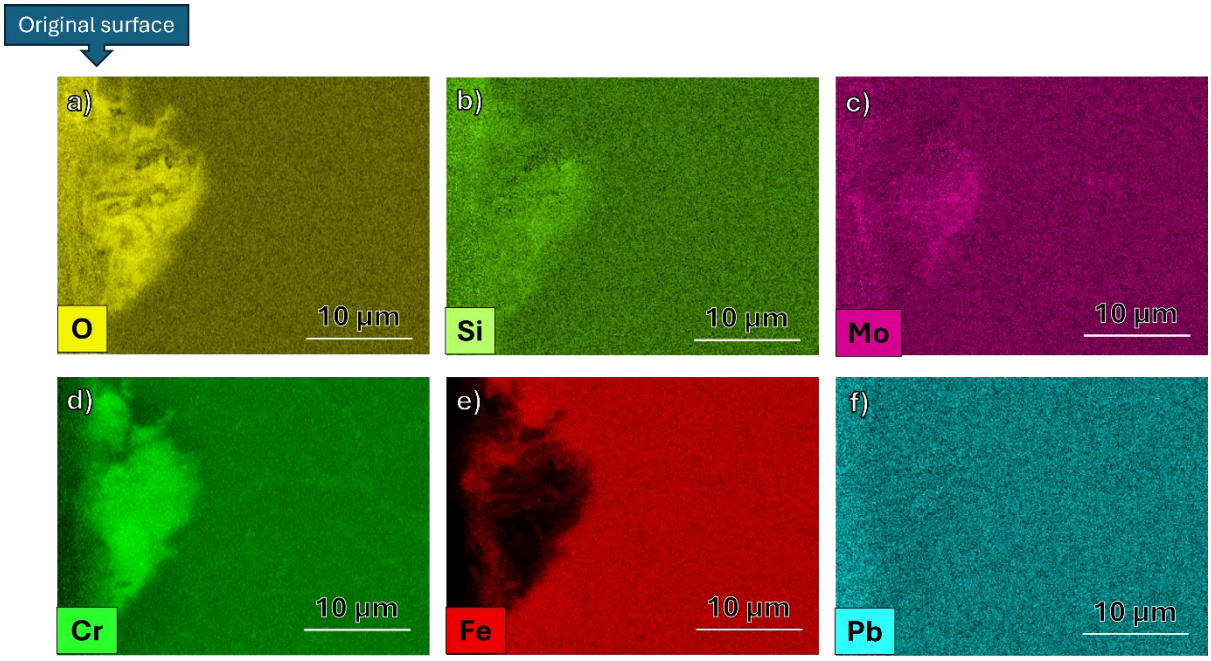

Fig. 7.26. SEM-EDX results acquired at 25 KV with area corrosion [Sample: 70 h, oxidising environment, 700 ℃, LBE]. (a) -(f) SEM-EDX results (25 KV) for Fig. 7.1 (d) highlighting O, Si, Mo, Cr, Fe and Pb, respectively.

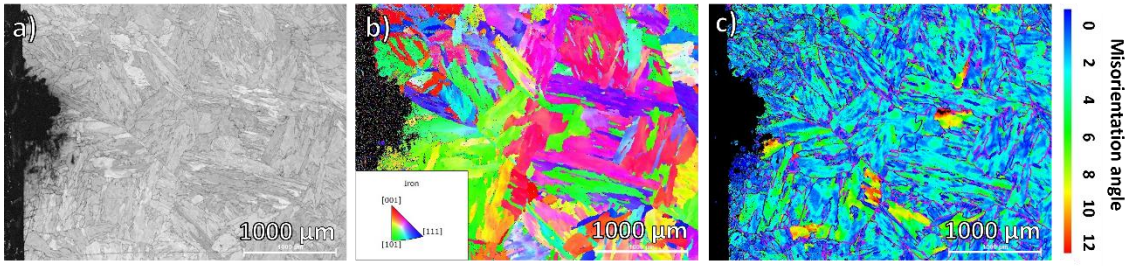

Fig. 7.27. SEM-EBSD results for Fig. 7.25 from a smaller magnification [Sample: 70 h, oxidising environment, 700 ℃, LBE]. (a) EBSD pattern quality map. (b) EBSD-IPFZ map. (c) EBSD grain average misorientation map with the scale bar.

7.2.2.2 Area Corrosion with LBE Detected Inside

Other than the oxide-dominated grain corrosion, LBE penetration is also observed in certain areas, as shown in Fig. 7.28 and Fig. 7.29.

A light level of LBE penetration is observed in Fig. 7.28 (f), primarily located at the interface between the T91 matrix and the formed oxide. The oxide is mainly Si-enriched, as indicated in Fig. 7.28 (c) and (d). The linescan in Fig. 7.28 (g), following the red line highlighted in Fig. 7.28 (a), confirms that the oxide and Pb are distributed in different locations.

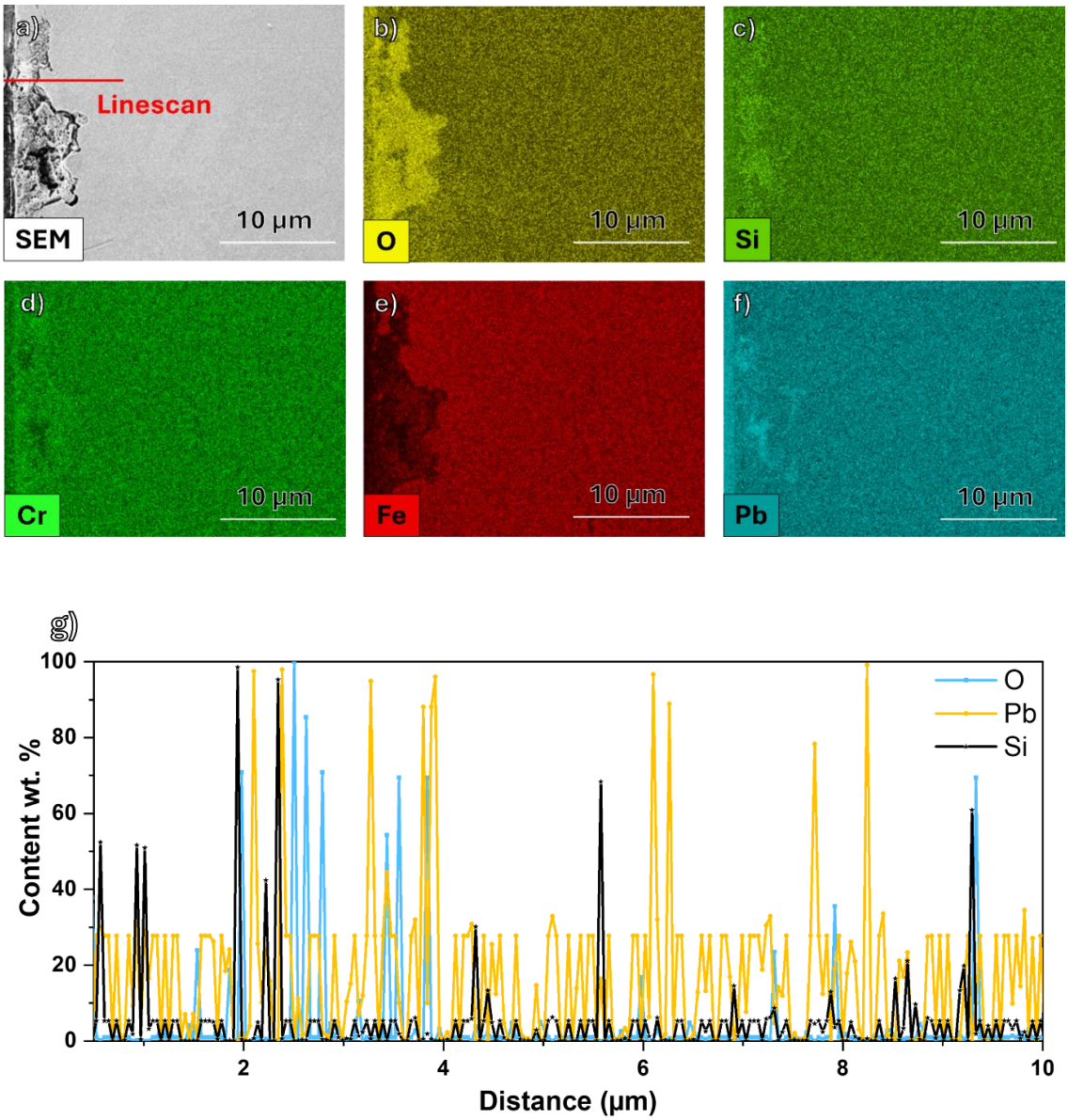

Fig. 7.28. SEM-EDX results acquired at 5 KV with area corrosion [Sample: 245 h, oxidising environment, 700 ℃, LBE]. (a) SEM image. (b)-(f) SEM-EDX results highlighting O, Si, Cr, Fe and Pb, respectively. (g) EDX line scan result for the red line in Fig. 7.28 (a).

Fig. 7.29 shows a region with more severe LBE penetration. The Cr depletion and lack of phase change shown in Fig. 7.29 (b) and (f) are similar to those observed in the 70 h corroded sample. However, in Fig. 7.29 (b), there is little Cr enrichment at the top surface, which differs from the pattern seen in Fig. 7.25 (d).

Fig. 7.29 (d) and (e) reveal that the corrosion primarily involves LBE intrusion, with high levels of Pb and Bi detected. This may explain the low Cr content detected in Fig. 7.29 (b), as the LBE intrusion may dissolve the surrounding Cr. Fig. 7.29 (c) highlights Si enrichment around the LBE intrusions. Si-enriched oxide forms adjacent to the LBE, with almost no Cr or Fe-enriched oxide surrounding it. This may suggest that Si-enriched oxide has higher resistance to LBE corrosion compared to other oxides.

To clarify the element distribution, a line scan was performed along the white line highlighted in Fig. 7.29 (a), and the results are shown in Fig. 7.29 (g). Cr dissolution is visible in the Pb- and Bi-enriched areas. Cr depletion is also observed, extending between 5 μm to 10 μm, as shown in Fig. 7.29 (g).

LBE is divided into two phases at room temperature due to its eutectic properties, as discussed in Chapter V. The line scan in Fig. 7.29 (g) and the EDX map in Fig. 7.29 (b) both show a layer of discontinuous Cr-enriched oxide formed at the surface, which appears to have no significant effect on obstructing LBE penetration. Additionally, Fig. 7.29 (g) indicates a layer of Fe-enriched phase formed at the surface, which could be the result of Fe diffusing outward and recrystallising as grains.

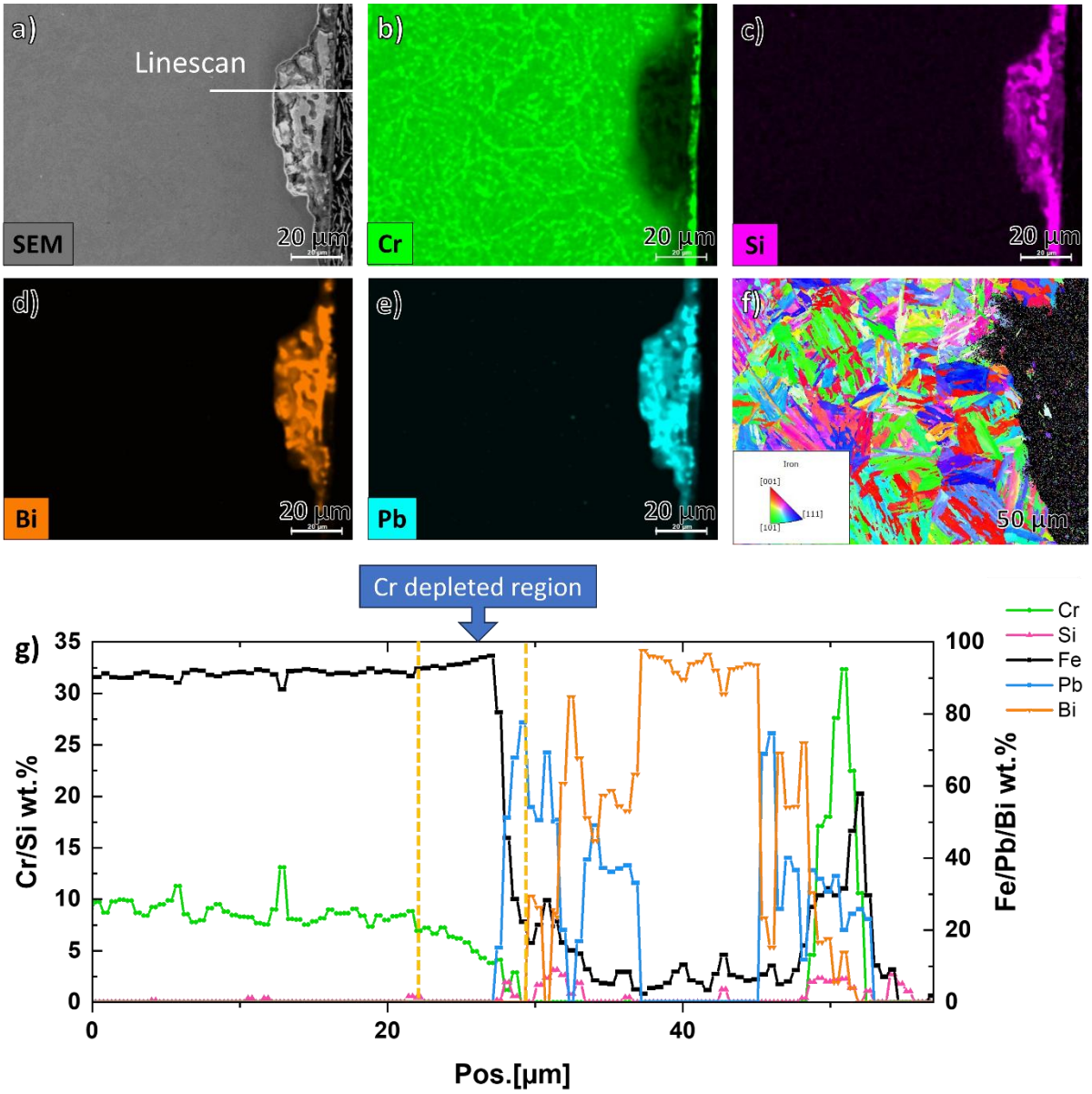

Fig. 7.29. The SEM-EDX and EBSD results acquired at 20 KV [Sample: 245 h, oxidising environment, 700 ℃, LBE]. (a) SEM view with the position of line-scan of Fig. 7.29 (g) highlighted with the white line. (b) (c) (d) (e) SEM-EDX results highlighting Cr, Si, Bi, and Pb, respectively. (f) SEM-EBSD IPFZ map. (g) Line-scan result for the white line in Fig. 7.29 (a).

7.2.3 No obvious corrosion observed

All the samples contain areas with no obvious corrosion, as shown in Fig. 7.1 (j)-(l). Studying these regions is crucial, as they may provide insights into improving the corrosion resistance of T91 steel. In this section, the 70 h and 506 h corroded samples are used as examples.

7.2.3.1 No obvious corrosion observed (70 h)

Fig. 7.30 shows the SEM-EDX results for the 70 h corroded sample. A layer is observed on the surface of T91 in Fig. 7.30 (a), which is confirmed to be an oxide layer based on the EDX results in Fig. 7.30 (b)-(d). This oxide layer primarily consists of Si and Cr oxides. A linescan was performed along the white line in Fig. 7.30 (a), and the results, shown in Fig. 7.30 (h), confirm that the layer is enriched in Si and depleted in Fe.

Cr does not show significant enrichment in the linescan results. Fig. 7.30 (d) shows that Cr carbides are dissociated in the region near the oxide layer, indicating the formation of Cr-enriched oxide. The Pb content remains consistent across the linescan, suggesting that any variation is likely due to noise in the scan.

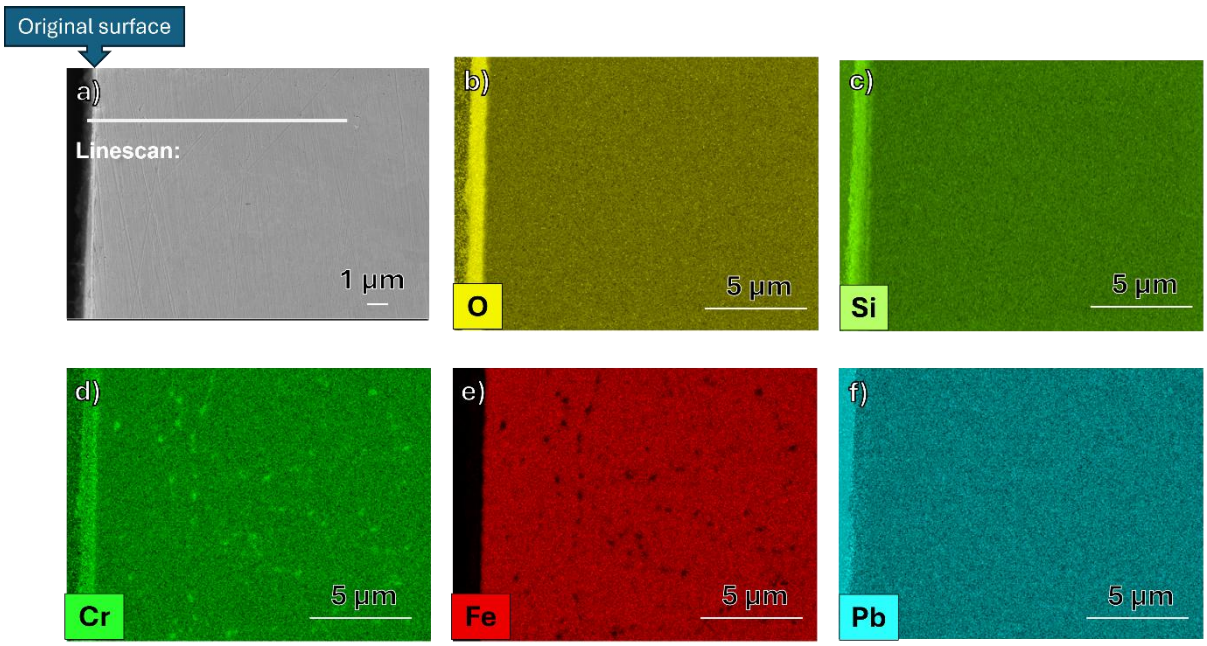

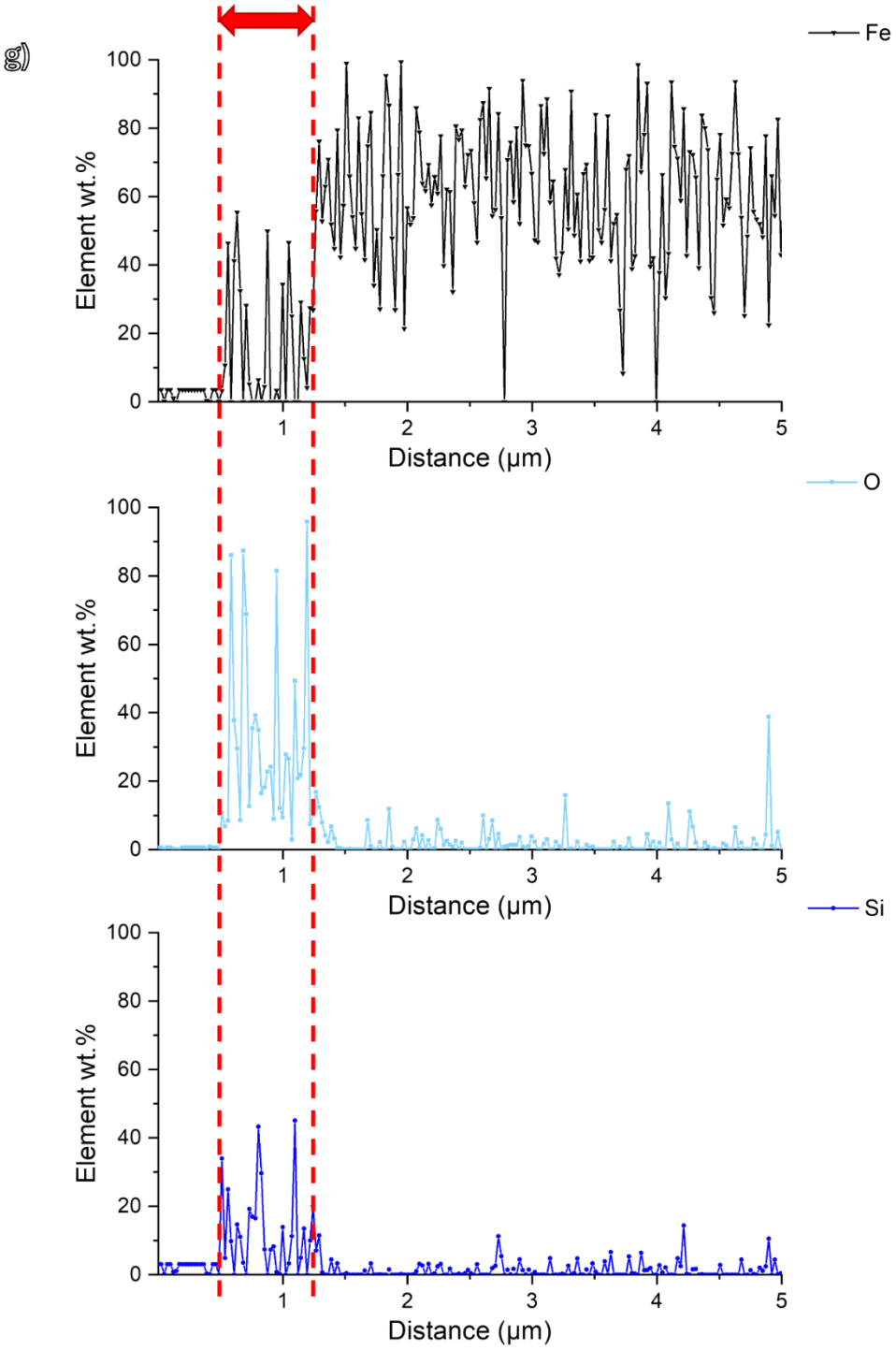
g)
Fe
O
Si
Element wt.%
Distance (μm)
0
20
40
60
80
100
1
2
3
4
5

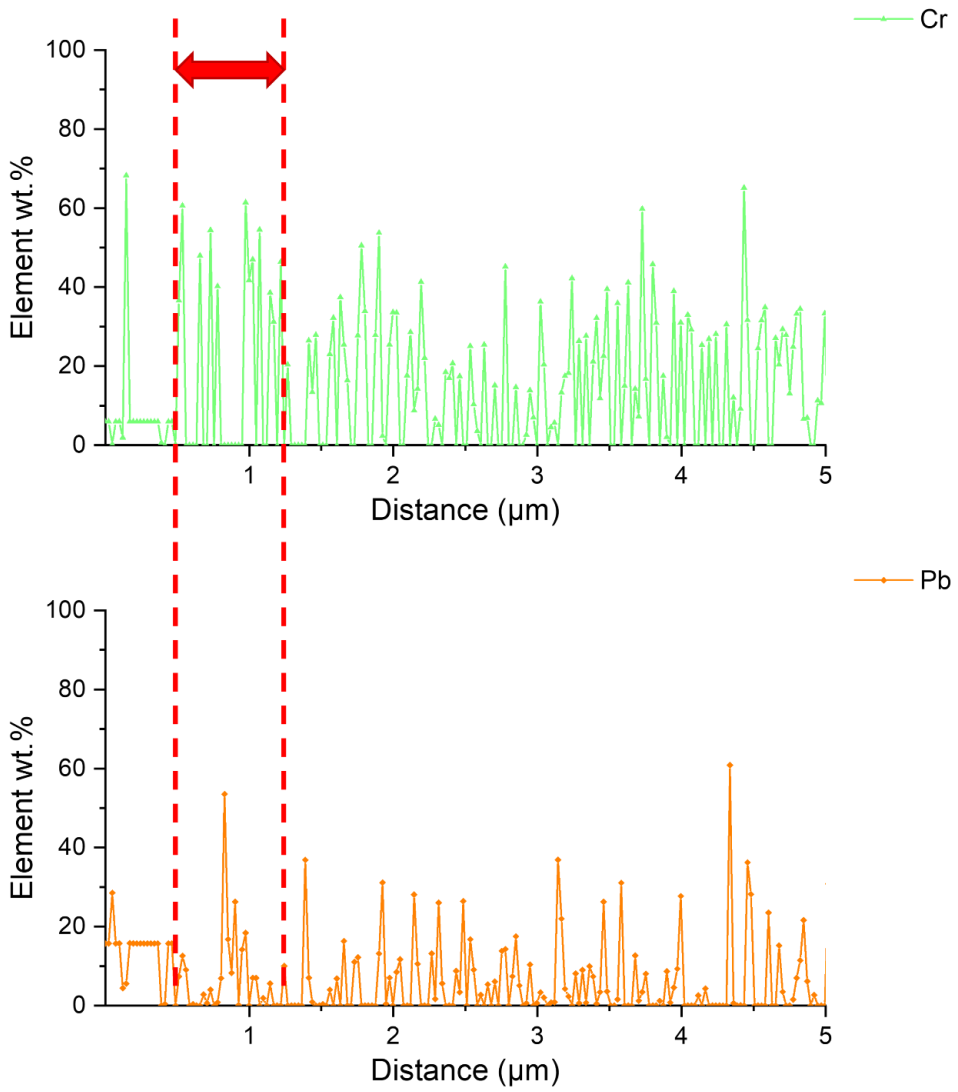

Fig. 7.30. The SEM-EDX results acquired at 5 KV [Sample: 70 h, oxidising environment, 700 ℃, LBE]. (a) SEM view with the position of line-scan of Fig. 7.30 (g) highlighted with the white line. (b)-(f) SEM-EDX results highlighting O, Si, Cr, Fe, and Pb, respectively. (g) Line-scan result for the white line in Fig. 7.30 (a).

7.2.3.1 No obvious corrosion observed (506 h)

Two distinct regions showing no obvious corrosion are analysed, as shown in Figs. 7.31 and 7.32, respectively. Fig. 7.31 corresponds to the area presented in Fig. 7.1 (l). In contrast, Fig. 7.32 depicts a region where a thicker oxide is present at the surface, accompanied by more Cr

depletion. The minimal Cr depletion observed in Fig. 31 (b) explains the limited phase change detected in Figs. 7.31 (d) and (e).

Compared to Fig. 7.31, the area in Fig. 7.32 exhibits a much thicker oxide layer at the surface, which is composed of Cr-enriched and Si-enriched oxides. The formation of this thicker oxide necessitates a greater diffusion of Cr to the surface, resulting in a larger Cr depletion zone. Consequently, this leads to a more pronounced phase change, as shown in Figs. 7.32 (d) and (e). These experimental results align well with the mechanism we proposed regarding the relationship between Cr depletion and phase change Chapter VI.

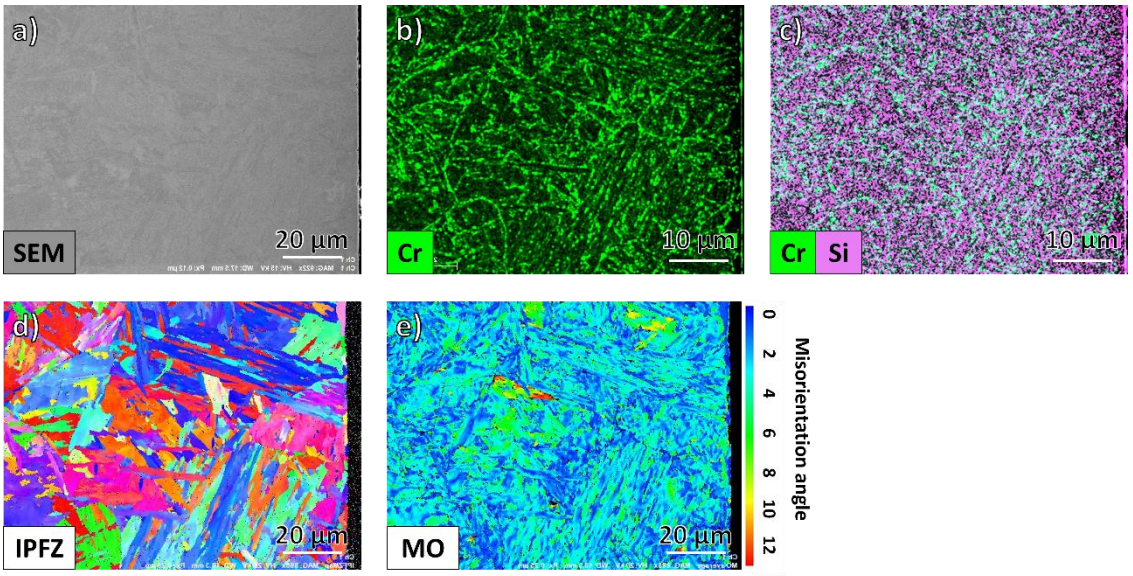

Fig. 7.31. The SEM-EDX and EBSD results for area with no obvious corrosion in SEM view [Sample: 506 h, oxidising environment, 700 ℃, LBE]. (a) SEM view. (b) SEM-EDX result highlighting the Cr. (c) SEM-EDX result highlighting Cr and Si. (d) SEM-EBSD IPFZ map. (e) SEM-EBSD grain average misorientation with the scale bar.

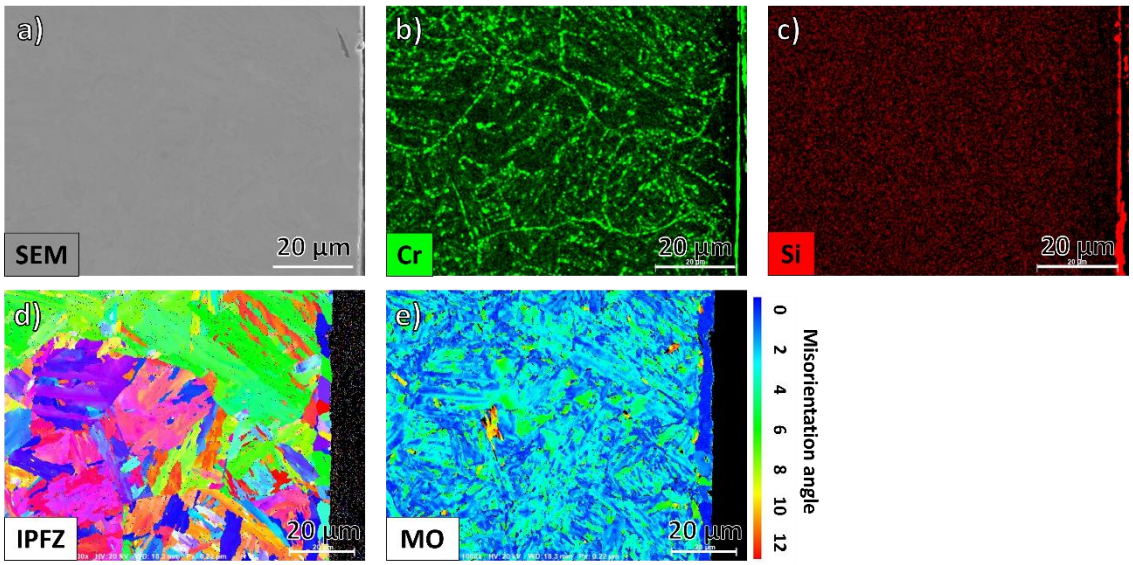

Fig. 7.32. The SEM-EDX and EBSD result for area with no obvious corrosion in SEM view [Sample: 506 h, oxidising environment, 700 °C, LBE]. (a) SEM view. (b) SEM-EDX result highlighting the Cr. (c) SEM-EDX result highlighting Si. (d) SEM-EBSD IPFZ map. (e) SEM-EBSD grain average misorientation with the scale bar.

Compared to the corroded areas, the non-corrosive regions all feature a continuous oxide layer. This oxide layer is enriched with Cr, potentially forming a spinel oxide as reported in other studies [113], and is also enriched with Si, likely comprising SiOx [160]. Excessive oxygen can lead to the oxidation of the liquid metal and uncontrollable oxidation of the material, which may result in coolant blockage. High temperatures complicate the formation of a dense oxide layer, while lower temperatures can diminish reactor efficiency. Additionally, a specific level of oxide-forming elements is necessary to produce a protective oxide layer. Nevertheless, an excessive amount of Si can reduce the ductility of the steel, while an overabundance of Al can adversely affect the weldability of the steel [160]. Therefore, a more detailed study is warranted to assess the feasibility of utilising an oxide layer as protection in liquid metal-cooled reactors.

7.3 Conclusion

In this chapter, the static corrosion of T91 in an oxidising environment at 700 °C was investigated. By combining the results from APT, TEM, EELS, EDX, EBSD, and SEM, a thorough study of the morphology and composition of the corroded samples was conducted, spanning atomic, nano-, and micro-scales. From the results, the following mechanistic insights and conclusions can be drawn:

Compared to corrosion in a reducing environment, oxidising corrosion exhibits a different pattern. The most significant difference is that GBs serve as rapid pathways for oxidation. The oxygen atoms, being much smaller than Pb and Bi atoms, can diffuse through GBs more easily. Oxidation can occur along both martensite lath boundaries and PAGBs.

The oxide structure varies depending on the location. It may form as a single layer rich in Cr, Fe, and O or appear as multiple layers. The Cr-enriched oxide can be Cr_xO or $FeCr_2O_4$ spinel oxide, as observed in previous studies [113, 260]. The Si-enriched oxide is primarily SiO. For the iron oxide, it predominantly appears in the GBs rather than on the surface. A layer of Fe-enriched phase with a BCC structure is present on the surface.

The formation of Cr-enriched oxide causes Cr to diffuse from the T91 matrix to the GBs and interfaces, leading to Cr depletion and Cr carbide dissociation. Phase changes (ferritization) were observed in different samples, which aligns well with the discussions in the previous chapter.

LBE penetration into the T91 in the oxidising environment requires more space than oxygen. Consequently, LBE may corrode the sample in a grain-by-grain manner, similar to that seen in reducing environments.

Continuous Si and Cr oxides can provide effective protection to T91, presenting a potential approach to enhance the anti-corrosion properties of structural materials during the design of LBE-cooled fast reactors.

Chapter VIII

Conclusions

This thesis focuses on the static corrosion mechanisms for T91 in LBE. To investigate the corrosion process, multiple research methods at different scales were used. Considering the influence of oxygen, corrosion is studied in reducing and oxidising environments (concerning FeO formation). The corrosion duration time effects are also researched by comparing the samples corroded for 70 h, 245 h, and 506 h. The main conclusions of this work are outlined as follows:

8.1 Sample preparation and APT parameters

During the sample preparation for APT and TEM, LBE is very sensitive to the Ga beam used in FIB machining. Even imaging will destroy the LBE part. The solutions are: (1) to put a sufficiently thick protective layer (either Pt, W, or C) on the lift-out to protect the LBE contained area; (2) to reduce the imaging and milling time; (3) the final polishing stage for TEM is not possible if the sample contains LBE because the sample needs to face the Ga beam directly without any protection. For APT samples, the polishing should be done precisely to the stage where the protection layer is just removed.

TEM sample preparation needs to consider that with the thinning, stresses in the sample will be released and may cause sample bending. This limits the sample length to approximately 10-15 µm.

Other than sample preparation, LBE also brings challenges for APT analysis. The evaporation fields of Fe and Pb/Bi are very different (for Fe it is 42 V/nm, and for Pb and Bi 20 V/nm and 18 V/nm, respectively), thus the sample will have less possibility to fracture if the LBE and T91 interface is paralleled to the sample height direction. Moreover, to reduce the chance of

fracture, laser mode should be used with a lower detection rate (maximum 0.4) to reduce the starting voltage. Considering the atomic mass difference between Pb/Bi and other elements, for example, Fe is 56 atomic mass unit (AMU), Cr is 52 AMU, Pb is 207 AMU, and Bi is 209 AMU, the pulse frequency should not be set higher than 125 kHz. Higher pulse frequency will cause a loss of Pb and Bi atoms.

8.2 Static corrosion of T91 in reducing environment

Reducing environment means the oxygen content is below the oxygen level required to form Fe oxide but above the threshold content to form Cr oxide and Si oxide according to the Ellingham diagram. In the reducing environment, the corrosion is mainly controlled by element dissolution in liquid LBE with a thin layer of oxide formed at the interface of T91 and LBE which mainly consists of FeO. Based on our observations, we propose the following corrosion sequence:

- Cr initially preferentially dissolves from T91 into liquid LBE creating a depletion zone adjacent to the corrosion interface.
- Cr precipitates dissociate in the region adjacent to the interface in response to the drop in Cr lattice content.
- The rate of Cr dissolution eventually slows, relative to that of Fe, with a decreasing concentration gradient.
- Constant Fe and Cr dissolution rates are reached which promotes the development of a stable Cr depletion distance.
- Fe dissolution into LBE progresses in a grain-by-grain fashion.

8.3 Static corrosion of T91 in the oxidising environment

The oxidising environment has enough oxygen to form Fe oxide but is still below the oxygen content required to form Pb/Bi oxides. By studying the corrosion of T91 in oxidising LBE, the following observations were made:

Firstly, the process is a mixture of oxidation and dissolution. The corrosion process begins with the oxygen penetrates GBs and forms oxides (Cr, Si, Fe, etc.). This is different to the reducing environment. At the same time, the oxide layer(s) shows different organisation ways.

Secondly, the Cr depletion and Cr carbide dissociation are also observed. The Cr diffused to the GBs and surfaces forming oxides.

Thirdly, LBE still penetrates the material in a grain-by-grain fashion with Si-enriched oxides retained at some martensite lath boundaries.

8.4 The correlation of Cr carbides dissociation and phase change

Both in reducing and oxidising environments, Cr depletion and Cr carbide dissociation in the region directly adjacent to the interface of T91 and LBE are observed. Based on the experimental observations, we proposed a possible process:

- The Cr content decreases at the surface of the T91 either because of dissolution in LBE or oxide formation at GBs or surfaces.
- The Cr carbides are unstable with lower Cr lattice content and start to dissociate.
- The Cr from dissociated Cr carbide also subsequently diffuses into the LBE, however, C partly diffuses in the opposite direction, away from the surface, potentially forming new Cr carbide, or growing existing precipitates, in the region not yet depleted in Cr. There is also C remaining within the recrystallised ferrite grains by forming C-enriched phases.

At a similar scale to the Cr depletion, the grains are observed to transform from a martensite laths structure to equiaxed grains. By comparing the Cr content in phase-changed areas to that of an untransformed region, we suggest that Cr depletion is the driving force for the phase change. The process may act as follows:

- The Cr and potentially C depletion reduces the recrystallisation temperature for these grains.
- With the test temperature of 715 ℃, the Cr and C depleted grains recover and recrystallise from martensite laths to equiaxed ferrite grains and grow to larger grains.
- There exists a middle region between the recrystallised region and the unaffected matrix where the grains are partly recrystallised. Within these grains, all the laths in one grain have very similar orientations.
- The recovery stage releases the strains and stress in the grain and the grain misorientation is greatly reduced.

8.4 Conclusion

The following table summarizes the main results for samples corroded in reducing and oxidizing environments, respectively.

Table 8.1 Summary of Corrosion Results in Reducing and Oxidizing Environments.

Materials	**T91**	**T91**
Temperature	715 ℃	700 ℃
Duration time	70h, 245h, 506h	70h, 245h, 506h
Oxygen Content	1×10^{-26} atm (1.8×10^{-9} wt.%)	1×10^{-21} atm (5.8×10^{-7} wt.%)
	Lower than the Fe oxides formation threshold	Higher than the Fe oxides formation threshold
Cr depletion and Cr carbides dissociation	Yes	Yes

Phase change detected (ferritization)	Yes	Yes
LBE penetration state	More areas	More localised
Dominated Corrosion Mechanism	Physical dissolution	GBs oxidation

Chapter IX

Future Work

Looking ahead, the work conducted in this thesis opens up several intriguing and unresolved questions that would be exciting to explore in future research.

First, T91, as a commercial steel, contains over ten alloying elements, making it challenging to determine precisely how each element modifies its behaviour. A more systematic and fundamental study could be conducted using model alloys. For example, multi-scale research could be performed on pure iron to elucidate its corrosion mechanism in static lead-bismuth eutectic (LBE). Previous studies have used modelling [264] and micro-scale analyses to investigate pure iron corrosion in LBE [29, 265, 266]; however, more detailed research is needed to reveal the atomic-scale corrosion mechanisms. Following this, Fe-Cr model alloys could be employed to analyse the effect of chromium. By testing model alloys with varying Cr content, the optimal Cr concentration could be determined. Other elements, such as Mo, Si, and Al, could then be added individually. Through this systematic approach, the influence of different alloying elements on corrosion could be elucidated, thereby clarifying the corrosion mechanisms and contributing to improvements in steel manufacturing processes.

Second, it would be beneficial to track grain characteristics more thoroughly. The results in this thesis indicate that grain orientation and morphology play a critical role in corrosion behaviour. Ideally, EBSD analysis could be performed on the sample before corrosion and repeated on the same area post-corrosion. However, a major challenge arises as LBE solidifies on the surface during cooling, and subsequent grinding and polishing could remove the pre-corrosion surface. Alternative methods for obtaining grain information should be considered, such as 3D X-ray diffraction (3D-XRD, Henning Poulsen's technique) or diffraction contrast tomography (Wolfgang Ludwig's technique), both of which use synchrotron radiation and can potentially

trace LBE infiltration paths post-corrosion. In-situ transmission electron microscopy (TEM) could also be explored, with a sealed sample holder designed to accommodate both the steel and a drop of LBE. This setup could allow direct observation of the corrosion process, providing insights into how grain orientation and morphology affect corrosion, and enabling real-time study of element redistribution. Potentially, preferential corrosion paths in LBE may be identified, and with atomic-resolution TEM, the atomic-scale interactions at the LBE-steel interface could be investigated.

Third, as discussed in this thesis, the stability of Cr-enriched carbides is theoretically influenced by the matrix Cr content. Molecular dynamics (MD) simulations [267] [268] could be developed to determine the threshold Cr content, which would indicate whether the dissociation or retention of Cr-enriched precipitates enhances corrosion resistance.

Fourth, it would be valuable to measure the average Fe and Cr concentrations at different stages, or even as gradients at varying distances from the sample surface, during exposure to liquid LBE. Such measurements could offer insights into how these elements gradually dissolve into LBE. More useful still would be position-sensitive concentration measurements of Fe and Cr within the liquid LBE or tracking their concentration as a function of time. However, obtaining this information from liquid LBE during static tests is challenging. Several factors contribute to this difficulty: first, the dissolution of Fe and Cr into LBE occurs at ppm levels, which are difficult to detect. Second, the interaction area is extremely small (on the order of several micrometres), further complicating measurement. Third, there is a lack of experimental methods capable of such precise measurements. Although MD simulations may offer a potential approach, it would be ideal to have comparable experimental data available.

Fifth, this study focuses on the static corrosion of steel in LBE. In practical applications, materials are typically exposed to circulating environments, which could alter the corrosion mechanisms. For instance, circulation may prevent the saturation of Fe and Cr in LBE. Previous studies have

investigated steel corrosion in circulating LBE [269-271]. It would be beneficial to combine the findings from those studies with the mechanisms proposed in this thesis to explore how circulation modifies the corrosion processes.

Finally, the material was tested for use in Generation IV reactors, where the combined effects of corrosion and irradiation must be considered. Radiation alters materials by increasing hardness and reducing ductility, while also accelerating atomic diffusion through defects. This process enhances corrosion by increasing the concentrations of interstitials and vacancies, leading to micro-cracking and grain boundary corrosion. Studies have shown that radiation can cause increased porosity, faster corrosion, and material degradation. Additionally, radiation-induced segregation and element redistribution further impact corrosion resistance. Therefore, it is crucial to examine both radiation and corrosion effects to ensure the material's performance in reactor environments. Methods for conducting simultaneous corrosion and irradiation tests have been developed, and these are listed in the appendix.

Chapter X

Bibliography

1. Davis, T.P., *Dispelling misconceptions of nuclear energy technology: How Generation IV nuclear reactors could become the key to achieving the Paris Agreement and the United Kingdom's net zero CO2 emissions target by 2050.* Saint Anne's Academic Review, 2019. **9**.
2. Alemberti, A., V. Smirnov, C.F. Smith, and M. Takahashi, *Overview of lead-cooled fast reactor activities.* Progress in Nuclear Energy, 2014. **77**: p. 300-307.
3. Van den Bosch, J., R.W. Bosch, D. Sapundjiev, and A. Almazouzi, *Liquid metal embrittlement susceptibility of ferritic–martensitic steel in liquid lead alloys.* Journal of Nuclear Materials, 2008. **376**(3): p. 322-329.
4. Zhang, J. and N. Li, *Review of the studies on fundamental issues in LBE corrosion.* Journal of Nuclear Materials, 2008. **373**(1-3): p. 351-377.
5. Gorse, D., T. Auger, J.B. Vogt, I. Serre, A. Weisenburger, A. Gessi, P. Agostini, C. Fazio, A. Hojna, F. Di Gabriele, J. Van Den Bosch, G. Coen, A. Almazouzi, and M. Serrano, *Influence of liquid lead and lead–bismuth eutectic on tensile, fatigue and creep properties of ferritic/martensitic and austenitic steels for transmutation systems.* Journal of Nuclear Materials, 2011. **415**(3): p. 284-292.
6. Zohuri, B., *Generation IV nuclear reactors*, in *Nuclear reactor technology development and utilization*. 2020, Elsevier. p. 213-246.
7. Garner, F.A., M.B. Toloczko, and B.H. Sencer, *Comparison of swelling and irradiation creep behavior of fcc-austenitic and bcc-ferritic/martensitic alloys at high neutron exposure.* Journal of Nuclear Materials, 2000. **276**(1-3): p. 123-142.

8. Davis, T.P., M.A. Auger, N. Almirall, P. Hosemann, G.R. Odette, P.A.J. Bagot, M.P. Moody, and D.E.J. Armstrong, *Atom probe characterisation of segregation driven Cu and Mn–Ni–Si co-precipitation in neutron irradiated T91 tempered-martensitic steel.* Materialia, 2020. **14**.

9. Kohyama, A., A. Hishinuma, D.S. Gelles, R.L. Klueh, W. Dietz, and K. Ehrlich, *Low-activation ferritic and martensitic steels for fusion application.* Journal of Nuclear Materials, 1996. **233**: p. 138-147.

10. Kurata, Y. and S. Saito, *Temperature Dependence of Corrosion of Ferritic/Martensitic and Austenitic Steels in Liquid Lead-Bismuth Eutectic.* Materials Transactions, 2009. **50**(10): p. 2410-2417.

11. Proriol Serre, I. and J.-B. Vogt, *Liquid metal embrittlement sensitivity of the T91 steel in lead, in bismuth and in lead-bismuth eutectic.* Journal of Nuclear Materials, 2020. **531**.

12. Gong, X., J. Chen, F. Hu, C. Xiang, Z. Yu, J. Xiao, H. Wang, H. Gong, H. Wang, C. Liu, Y. Deng, B. Pang, X. Huang, Y. Li, and Y. Yin, *Liquid metal embrittlement of an Fe10Cr4Al ferritic alloy exposed to oxygen-depleted and -saturated lead-bismuth eutectic at 350°C.* Corrosion Science, 2020. **165**.

13. Gordon, P. and H.H. An, *The mechanisms of crack initiation and crack propagation in metal-induced embrittlement of metals.* Metallurgical Transactions A, 1982. **13**(3): p. 457-472.

14. Nicholas, M.G. and C.F. Old, *Review Liquid metal embrittlement.* Joural of Materials Science, 1979(14): p. 1-18.

15. Klok, O., *Liquid Metal Corrosion Effects in MYRRHA candidate 316L Austenitic Stainless Steel.* Vrije Universiteit Brussel, 2018.

16. Hojná, A., F. Di Gabriele, M. Chocholoušek, L. Rozumová, and J. Vít, *Effect of applied stress on T91 steel performance in liquid lead at 400 C.* Materials, 2018. **11**(12): p. 2512.

17. Tsisar, V., S. Gavrilov, C. Schroer, and E. Stergar, *Long-term corrosion performance of T91 ferritic/martensitic steel at 400 °C in flowing Pb-Bi eutectic with 2 × 10−7 mass% dissolved oxygen.* Corrosion Science, 2020. **174**.

18. Hosemann, P., D. Frazer, E. Stergar, and K. Lambrinou, *Twin boundary-accelerated ferritization of austenitic stainless steels in liquid lead–bismuth eutectic.* Scripta Materialia, 2016. **118**: p. 37-40.

19. Allen, T.R., K. Sridharan, L. Tan, W.E. Windes, J.I. Cole, D.C. Crawford, and G.S. Was, *Materials Challenges for Generation IV Nuclear Energy Systems.* Nuclear Technology, 2017. **162**(3): p. 342-357.

20. Wolski, K. and V. Laporte, *Grain boundary diffusion and wetting in the analysis of intergranular penetration.* Materials Science and Engineering: A, 2008. **495**(1-2): p. 138-146.

21. Marie, N., K. Wolski, and M. Biscondi, *Intergranular penetration and embrittlement of solid nickel through bismuth vapour condensation at 700 C.* Journal of nuclear materials, 2001. **296**(1-3): p. 282-288.

22. Lambrinou, K., E. Charalampopoulou, T. Van der Donck, R. Delville, and D. Schryvers, *Dissolution corrosion of 316L austenitic stainless steels in contact with static liquid lead-bismuth eutectic (LBE) at 500 °C.* Journal of Nuclear Materials, 2017. **490**: p. 9-27.

23. Jalůvka, D., G. Van den Eynde, and S. Vandewalle, *Development of a core management tool for MYRRHA.* Energy Conversion and Management, 2013. **74**: p. 562-568.

24. Barbier, F., G. Benamati, C. Fazio, and A. Rusanov, *Compatibility tests of steels in flowing liquid lead–bismuth.* Journal of Nuclear Materials, 2001. **295**(2-3): p. 149-156.

25. Benamati, G., C. Fazio, H. Piankova, and A. Rusanov, *Temperature effect on the corrosion mechanism of austenitic and martensitic steels in lead–bismuth.* Journal of nuclear materials, 2002. **301**(1): p. 23-27.

26. Short, M.P., R.G. Ballinger, and H.E. Hänninen, *Corrosion resistance of alloys F91 and Fe–12Cr–2Si in lead–bismuth eutectic up to 715°C.* Journal of Nuclear Materials, 2013. **434**(1-3): p. 259-281.

27. Briceno, D.G., L.S. Crespo, F.J.M. Munoz, and F.H. Arroyo, *Influence of temperature on the oxidation/corrosion process of F82Hmod. martensitic steel in lead–bismuth.* Journal of nuclear materials, 2002. **303**(2-3): p. 137-146.

28. Lapington, M.T., M. Zhang, M.P. Moody, W.Y. Zhou, M.P. Short, and F. Hofmann, *Characterisation of corrosion damage in T91/F91 steel exposed to static liquid lead-bismuth eutectic at 700-715° C.* Journal of Nuclear Materials, 2023: p. 154687.

29. Kurata, Y., M. Futakawa, and S. Saito, *Corrosion behavior of steels in liquid lead–bismuth with low oxygen concentrations.* Journal of Nuclear Materials, 2008. **373**(1-3): p. 164-178.

30. Zhang, J., *Oxygen control technology in applications of liquid lead and lead–bismuth systems for mitigating materials corrosion.* Journal of Applied Electrochemistry, 2013. **43**(8): p. 755-771.

31. Hadjem-Hamouche, Z., T. Auger, and I. Guillot, *Temperature effect in the maximum propagation rate of a liquid metal filled crack: The T91 martensitic steel/Lead–Bismuth Eutectic system.* Corrosion Science, 2009. **51**(11): p. 2580-2587.

32. Kurata, Y., *Corrosion behavior of Si-enriched steels for nuclear applications in liquid lead–bismuth.* Journal of Nuclear Materials, 2013. **437**(1-3): p. 401-408.

33. McFarlane, H., *Special Section on Status of Generation IV Reactor Development Preface.* Progress in Nuclear Energy, 2014. **77**.

34. Kim, Y.M., *The National Promotion Strategy for the Development of the Generation IV Reactor Systems in the Republic of Korea.* Energy Sources, Part B: Economics, Planning, and Policy, 2012. **7**(4): p. 357-365.

35. *Uranium 2018: Resources, Production and Demand*. 2018, Organisation for Economic Cooperation and Development (OECD): Paris.

36. Board, N.I.a.R.A., *Clean Growth Through Innovation - the need for urgent action*. 2019, Nuclear Innovation and Research Advisory Board.

37. Zu, F., Z. Zhu, B. Zhang, Y. Feng, and J. Shui, *Post-melting anomaly of Pb-Bi alloys observed by internal friction technique.* Journal of Physics: Condensed Matter, 2001. **13**(50): p. 11435.

38. Zinkle, S.J. and G.S. Was, *Materials challenges in nuclear energy.* Acta Materialia, 2013. **61**(3): p. 735-758.

39. Weeks, J.R. and H.S. Isaacs, *Corrosion and deposition of steels and nickel-base alloys in liquid sodium*, in *Advances in corrosion science and technology*. 1973, Springer. p. 1-66.

40. Zhang, J., *A review of steel corrosion by liquid lead and lead–bismuth.* Corrosion Science, 2009. **51**(6): p. 1207-1227.

41. Cathcart, J.V. and W.D. Manly, *The mass transfer properties of various metals and alloys in liquid lead.* Corrosion, 1956. **12**(2): p. 43-47.

42. SHIMOTAKE, H. and J.C. HESSON, *Corrosion by fused salts and heavy liquid metals—A survey*. 1967, ACS Publications.

43. Ali-Khan, I., *Corrosion of steels and refractory metals in liquid lead*, in *Material Behavior and Physical Chemistry in Liquid Metal Systems*. 1982, Springer. p. 243-252.

44. James, J.A. and J. Trotman, *Corrosion of steels in liquid bismuth and lead.* J. Iron Steel Inst.(London), 1960. **194**.

45. Wilson, G.W., *Study of compatibility of some creep resistant steels with liquid bismuth in non isothermal systems.* Journal of the Iron and Steel Institute, 1958. **190**: p. 271-276.

46. Ilinčev, G., *Research results on the corrosion effects of liquid heavy metals Pb, Bi and Pb–Bi on structural materials with and without corrosion inhibitors.* Nuclear Engineering and Design, 2002. **217**(1-2): p. 167-177.

47. Gong, X., M.P. Short, T. Auger, E. Charalampopoulou, and K. Lambrinou, *Environmental degradation of structural materials in liquid lead-and lead-bismuth eutectic-cooled reactors.* Progress in Materials Science, 2022: p. 100920.

48. Charalampopoulou, E., K. Lambrinou, T. Van der Donck, B. Paladino, F. Di Fonzo, C. Azina, P. Eklund, S. Mráz, J.M. Schneider, and D. Schryvers, *Early stages of dissolution corrosion in 316L and DIN 1.4970 austenitic stainless steels with and without anticorrosion coatings in static liquid lead-bismuth eutectic (LBE) at 500 C.* Materials Characterization, 2021. **178**: p. 111234.

49. Zhu, Z., Q. Zhang, J. Tan, X. Wu, H. Ma, Z. Zhang, Q. Ren, E.-H. Han, and X. Wang, *Corrosion behavior of T91 steel in liquid lead-bismuth eutectic at 550° C: effects of exposure time and dissolved oxygen concentration.* Corrosion Science, 2022. **204**: p. 110405.

50. Sapundjiev, D., S. Van Dyck, and W. Bogaerts, *Liquid metal corrosion of T91 and A316L materials in Pb–Bi eutectic at temperatures 400–600°C.* Corrosion Science, 2006. **48**(3): p. 577-594.

51. Müller, G., G. Schumacher, and F. Zimmermann, *Investigation on oxygen controlled liquid lead corrosion of surface treated steels.* Journal of Nuclear Materials, 2000. **278**(1): p. 85-95.

52. Roy, M., L. Martinelli, K. Ginestar, J. Favergeon, and G. Moulin, *Dissolution and oxidation behaviour of various austenitic steels and Ni rich alloys in lead-bismuth eutectic at 520 C.* Journal of Nuclear Materials, 2016. **468**: p. 153-163.

53. Chhabra, R.P. and D.K. Sheth, *Viscosity of Molten Metals and its Temperature Dependence / Viscosity of Molten Metals and its Temperature Dependence.* International Journal of Materials Research, 1990. **81**(4): p. 264-271.

54. Grace, R.E. and G. Derge, *Diffusion in Liquid Lead-Bismuth Alloys.* JOM, 1955. **7**(7): p. 839-842.

55. Tas, H., S. Malang, F. Reiter, and J. Sannier, *Liquid breeder materials.* Journal of Nuclear Materials, 1988. **155**: p. 178-187.

56. Simon, N., A. Terlain, and T. Flament, *The compatibility of austenitic materials with liquid Pb–17Li.* Corrosion science, 2001. **43**(6): p. 1041-1052.

57. Fazio, C., G. Benamati, C. Martini, and G. Palombarini, *Compatibility tests on steels in molten lead and lead–bismuth.* Journal of nuclear materials, 2001. **296**(1-3): p. 243-248.

58. Fedirko, V.M., O.I. Eliseeva, V.I. Kalyandruk, and V.A. Lopushans' kyi, *Effect of admixtures of oxygen on the oxidation of iron and Fe− Cr alloys in lead melts.* Materials Science, 1997. **33**(3): p. 358-363.

59. Fazio, C., I. Ricapito, G. Scaddozzo, and G. Benamati, *Corrosion behaviour of steels and refractory metals and tensile features of steels exposed to flowing PbBi in the LECOR loop.* Journal of nuclear materials, 2003. **318**: p. 325-332.

60. Kurata, Y., M. Futakawa, and S. Saito, *Comparison of the corrosion behavior of austenitic and ferritic/martensitic steels exposed to static liquid Pb–Bi at 450 and 550°C.* Journal of Nuclear Materials, 2005. **343**(1-3): p. 333-340.

61. Kutateladze, S.S., *Liquid-metal heat transfer media*. Vol. 2. 1959: Consultants Bureau.

62. Marie, N., K. Wolski, and M. Biscondi, *Grain boundary penetration of nickel by liquid bismuth as a film of nanometric thickness.* Scripta materialia, 2000. **43**(10): p. 943-949.

63. Martinelli, L., F. Vanneroy, J.C.D. Rosado, D. L'Hermite, and M. Tabarant, *Nickel solubility limit in liquid lead–bismuth eutectic.* Journal of Nuclear Materials, 2010. **400**(3): p. 232-239.

64. Bhadeshia, H.K.D.H. and R.W.K. Honeycombe, *Steels: Structure, Properties, and Design*. 2024: Elsevier.

65. Chen, Z., K.-C. Chou, and K. Morita, *Mechanism of Metastable Wüstite Formation in the Reduction Process of Iron Oxide below 570^{o}C.* 2016.

66. Old, C.F., *Liquid metal embrittlement of nuclear materials.* Journal of nuclear materials, 1980. **92**(1): p. 2-25.

67. Gong, X., P. Marmy, A. Volodin, B. Amin-Ahmadi, L. Qin, D. Schryvers, S. Gavrilov, E. Stergar, B. Verlinden, M. Wevers, and M. Seefeldt, *Multiscale investigation of quasi-brittle fracture characteristics in a 9Cr–1Mo ferritic–martensitic steel embrittled by liquid lead–bismuth under low cycle fatigue.* Corrosion Science, 2016. **102**: p. 137-152.

68. Rostoker, W., J.M. McCaughey, and H. Markus, *Embrittlement by liquid metals*. 1960: Reinhold Publishing Corporation.

69. Westwood, A.R.C. and M.H. Kamdar, *Concerning liquid metal embrittlement, particularly of zinc monocrystals by mercury.* Philosophical Magazine, 1963. **8**(89): p. 787-804.

70. Lynch, S.P., *Environmentally assisted cracking: overview of evidence for an adsorption-induced localised-slip process.* Acta Metallurgica, 1988. **36**(10): p. 2639-2661.

71. Glickman, E.E., *Dissolution condensation mechanism of stress corrosion cracking in liquid metals: driving force and crack kinetics.* Metallurgical and materials transactions A, 2011. **42**(2): p. 250-266.

72. Dmukhovskaya, I.G. and V.V. Popovich, *A phenomenological model of embrittlement of metals under conditions of the adsorption action of liquid metal media.* Soviet materials science: a transl. of Fiziko-khimicheskaya mekhanika materialov/Academy of Sciences of the Ukrainian SSR, 1983. **18**(6): p. 461-467.

73. Long, B., Z. Tong, F. Gröschel, and Y. Dai, *Liquid Pb–Bi embrittlement effects on the T91 steel after different heat treatments.* Journal of nuclear materials, 2008. **377**(1): p. 219-224.

74. Holdsworth, S., *Creep-ductility of high temperature steels: a review.* Metals, 2019. **9**(3): p. 342.

75. Jianu, A., G. Müller, A. Weisenburger, A. Heinzel, C. Fazio, V.G. Markov, and A.D. Kashtanov, *Creep-to-rupture tests of T91 steel in flowing Pb–Bi eutectic melt at 550 C.* Journal of Nuclear Materials, 2009. **394**(1): p. 102-108.

76. Weisenburger, A., A. Jianu, W. An, R. Fetzer, M. Del Giacco, A. Heinzel, G. Müller, V.G. Markov, and A.D. Kasthanov, *Creep, creep-rupture tests of Al-surface-alloyed T91 steel in liquid lead bismuth at 500 and 550 C.* Journal of nuclear materials, 2012. **431**(1-3): p. 77-84.

77. Sizmann, R., *The effect of radiation upon diffusion in metals.* Journal of Nuclear Materials. **69-70**: p. 386-412.

78. Song, K., S. Das, A. Reza, N.W. Phillips, R. Xu, H. Yu, K. Mizohata, D.E.J. Armstrong, and F. Hofmann, *Characterising Ion-Irradiated FeCr: Hardness, Thermal Diffusivity and Lattice Strain.* Acta Materialia, 2020. **201**: p. 535-546.

79. Reza, A., H. Yu, K. Mizohata, and F. Hofmann, *Thermal diffusivity degradation and point defect density in self-ion implanted tungsten.* Acta Materialia, 2020. **193**: p. 270-279.

80. Reza, A., C.A. Dennett, M.P. Short, J. Waite, Y. Zayachuk, C.M. Magazzeni, S. Hills, and F. Hofmann, *Non-contact, non-destructive mapping of thermal diffusivity and surface acoustic wave speed using transient grating spectroscopy.* Rev Sci Instrum, 2020. **91**(5): p. 054902.

81. San Marchi, C., T. Michler, K.A. Nibur, and B.P. Somerday, *On the physical differences between tensile testing of type 304 and 316 austenitic stainless steels with internal hydrogen and in external hydrogen.* International Journal of Hydrogen Energy, 2010. **35**(18): p. 9736-9745.

82. Nastar, M. and F. Soisson, *Radiation-Induced Segregation*, in *Comprehensive Nuclear Materials*. 2012. p. 471-496.

83. Bruemmer, S.M., E.P. Simonen, P.M. Scott, P.L. Andresen, G.S. Was, and J.L. Nelson, *Radiation-induced material changes and susceptibility to*

intergranular failure of light-water-reactor core internals. Journal of Nuclear Materials, 1999. **274**: p. 299-314.

84. Nolfi, F.V., *Phase transformations during irradiation*. 1983: Applied Science Publishers.

85. Gusak, A.M. and K.N. Tu, *Interaction between the Kirkendall effect and the inverse Kirkendall effect in nanoscale particles.* Acta Materialia, 2009. **57**(11): p. 3367-3373.

86. Allen, T.R., J.T. Busby, G.S. Was, and E.A. Kenik, *On the mechanism of radiation-induced segregation in austenitic*

Fe–Cr–Ni alloys. Journal of Nuclear Materials, 1998. **255**: p. 44-58.

87. Brager, H.R. and J.L. Straalsund, *Defect development in neutron irradiated type 316 stainless steel.* Journal of Nuclear Materials, 1973. **46**(2): p. 134-158.

88. Okamoto, P.R. and L.E. Rehn, *Radiation-induced segregation in binary and ternary alloys.* Journal of Nuclear Materials, 1979. **83**(1): p. 2-23.

89. Bruemmer, S.M. and E.P. Simonen, *Radiation Hardening and Radiation-Induced Chromium Depletion Effects on Intergranular Stress Corrosion Cracking in Austenitic Stainless Steels.* Corrosion, 1994. **50**(12): p. 940-946.

90. Kenik, E.A. and J.T. Busby, *Radiation-induced degradation of stainless steel light water reactor internals.* Materials Science and Engineering: R: Reports, 2012. **73**(7-8): p. 67-83.

91. Maziasz, P.J., *Overview of microstructural evolution in neutron-irradiated austenitic stainless steels.* Journal of nuclear materials, 1993. **205**: p. 118-145.

92. Maziasz, P., *Formation and stability of radiation-induced phases in neutron-irradiated austenitic and ferritic steels.* Journal of Nuclear Materials, 1989. **169**: p. 95-115.

93. Kim, J.W. and T.S. Byun, *Analysis of tensile deformation and failure in austenitic stainless steels: Part II–Irradiation dose dependence.* Journal of nuclear materials, 2010. **396**(1): p. 10-19.

94. Grossbeck, M.L., *Effects of radiation on materials*. Vol. 1447. 2004: ASTM International.

95. Zhou, W., K.B. Woller, G. Zheng, P.W. Stahle, and M.P. Short, *A simultaneous corrosion/irradiation facility for testing molten salt-facing materials.* Nuclear Instruments and Methods in Physics Research Section B: Beam Interactions with Materials and Atoms, 2019. **440**: p. 54-59.

96. Wang, P. and G.S. Was, *Oxidation of Zircaloy-4 during in situ proton irradiation and corrosion in PWR primary water.* Journal of Materials Research, 2015. **30**(9): p. 1335-1348.

97. Iltis, X., F. Lefebvre, and C. Lemaignan. *Microstructure evolutions and iron redistribution in zircaloy oxide layers: Comparative effects of neutron irradiation flux and irradiation damages*. in *Zirconium in the Nuclear Industry: Eleventh International Symposium*. 1996. ASTM International.

98. Filippov, V.P., A.B. Bateev, Y.A. Lauer, A.F. Dykhuis, and M.P. Short, *The influence of reactor irradiation on the oxidation state of tin in Zr-0.76Fe-1.6Sn.* 2018. **239**.

99. Raiman, S.S., D.M. Bartels, and G.S. Was, *Radiolysis driven changes to oxide stability during irradiation-corrosion of 316L stainless steel in high temperature water.* Journal of Nuclear Materials, 2017. **493**: p. 40-52.

100. Raiman, S.S., A. Flick, O. Toader, P. Wang, N.A. Samad, Z. Jiao, and G.S. Was, *A facility for studying irradiation accelerated corrosion in high temperature water.* Journal of Nuclear Materials, 2014. **451**(1-3): p. 40-47.

101. Liu, C., T. Shen, P. Jin, J. Wang, H. Chang, Y. Zhu, M. Cui, J. Chai, and Z. Wang, *The role of He irradiation in the corrosion behaviour of T91 in high-temperature steam.* Corrosion Science, 2021. **189**: p. 109602.

102. Callister, W.D. and D.G. Rethwisch, *Materials science and engineering: an introduction*. Vol. 9. 2018: Wiley New York.

103. Totten, G.E., *Steel heat treatment: metallurgy and technologies*. 2006: CRC press.

104. Suryanarayana, C., *Experimental techniques in materials and mechanics*. 2011: Crc Press.

105. M., A.J. and J.C. Smith, *Metallurgy of Steel: A Handbook for Engineers*. 2008: ASM International.

106. Bhadeshia, H. and R. Honeycombe, *Steels: microstructure and properties*. 2017: Butterworth-Heinemann.

107. Winchell, P.G. and M. Cohen, *The effect of carbon on the hardness of martensite and austenite.* Transactions of the Metallurgical Society of AIME, 1962. **224**: p. 639.

108. Bhadeshia, H.K.D.H., *Theory of transformations in steels*. 2021: CRC Press.

109. Speich, G.R., *Tempering of low-carbon martensite.* Trans Met Soc AIME, 1969. **245**(12): p. 2553-2564.

110. Krauss, G., *Steels: processing, structure, and performance*. 2015: Asm International.

111. Hernández, M.J.Q., J.A. Pero-Sanz, and L.F. Verdeja, *Solidification and solid-state transformations of metals and alloys*. 2017: Elsevier.

112. Verhoeven, J.D., *Steel metallurgy for the non-metallurgist*. 2007: ASM International.

113. Shen, Z., K. Chen, H. Yu, B. Jenkins, Y. Ren, N. Saravanan, G. He, X. Luo, P.A.J. Bagot, M.P. Moody, L. Zhang, and S. Lozano-Perez, *New insights into the oxidation mechanisms of a Ferritic-Martensitic steel in high-temperature steam.* Acta Materialia, 2020. **194**: p. 522-539.

114. Marcus, P., *Surface science approach of corrosion phenomena.* Electrochimica Acta, 1998. **43**(1-2): p. 109-118.

115. Ueda, M. and A. Ikeda. *Effect of microstructure and Cr content in steel on CO2 corrosion*. in *NACE CORROSION*. 1996. NACE.

116. Diawara, B., Y.-A. Beh, and P. Marcus, *Nucleation and growth of oxide layers on stainless steels (FeCr) using a virtual oxide layer model.* The Journal of Physical Chemistry C, 2010. **114**(45): p. 19299-19307.

117. Legrand, M., B. Diawara, J.-J. Legendre, and P. Marcus, *Three-dimensional modelling of selective dissolution and passivation of iron–chromium alloys.* Corrosion Science, 2002. **44**(4): p. 773-790.

118. Diawara, B., M. Legrand, J.-J. Legendre, and P. Marcus, *Use of quantum chemistry results in 3D modeling of corrosion of iron-chromium alloys.* Journal of the Electrochemical Society, 2004. **151**(3): p. B172.

119. Łukaszczyk, A., J. Banaś, M. Pisarek, A. Seyeux, P. Marcus, and J. Światowska, *Effect of Cr content on corrosion resistance of low-Cr alloy steels studied by surface and electrochemical techniques.* Electrochem, 2021. **2**(4): p. 546-562.

120. Heusler, K.E., B. Kusian, and D. McPhail, *Kinetics of the Corrosion of Iron in Aqueous Electrolytes at Temperatures up to 300 C.* Berichte der Bunsengesellschaft für physikalische Chemie, 1990. **94**(12): p. 1443-1449.

121. Sato, N., K. Kudo, and T. Noda, *The anodic oxide film on iron in neutral solution.* Electrochimica Acta, 1971. **16**(11): p. 1909-1921.

122. Sato, N., K. Kudo, and R. Nishimura, *Depth analysis of passive films on iron in neutral borate solution.* Journal of the electrochemical society, 1976. **123**(10): p. 1419.

123. Fujii, C.T. and R.A. Meussner, *The mechanism of the high‐temperature oxidation of iron‐chromium alloys in water vapor.* Journal of the Electrochemical Society, 1964. **111**(11): p. 1215.

124. Col, A., V. Parry, and C. Pascal, *Oxidation of a Fe–18Cr–8Ni austenitic stainless steel at 850 C in O2: Microstructure evolution during breakaway oxidation.* Corrosion Science, 2017. **114**: p. 17-27.

125. Raman, R.K.S. and R.K. Gupta, *Oxidation resistance of nanocrystalline vis-à-vis microcrystalline Fe–Cr alloys.* Corrosion science, 2009. **51**(2): p. 316-321.

126. Li, Z., Z. Chai, L. Wang, Z. Wang, Q. Lu, J. Wang, and W. Xu, *Effect of Cr on high-temperature oxidation resistance of Cr–Si–Mn alloyed press-hardened steel during press hardening.* Journal of Materials Research and Technology, 2024. **32**: p. 1552-1564.

127. Lobb, R.C. and H.E. Evans, *An evaluation of the effect of surface chromium concentration on the oxidation of a stainless steel.* Corrosion Science, 1983. **23**(1): p. 55-73.

128. Basu, S.N. and G.J. Yurek, *Effect of alloy grain size and silicon content on the oxidation of austenitic Fe-Cr-Ni-Mn-Si alloys in pure O 2.* Oxidation of Metals, 1991. **36**: p. 281-315.

129. Zeng, J., J. Hu, X. Yang, H. Xu, H. Li, N. Guo, and Q. Dong, *Microstructure and formation mechanism of the Si-Cr dual-alloyed coating prepared by pack-cementation.* Surface and Coatings Technology, 2020. **399**: p. 126142.

130. Jin, X., S. Chen, and L. Rong, *Effects of Mn on the mechanical properties and high temperature oxidation of 9Cr2WVTa steel.* Journal of Nuclear Materials, 2017. **494**: p. 103-113.

131. Tunthawiroon, P., Y. Li, N. Tang, Y. Koizumi, and A. Chiba, *Effects of alloyed Si on the oxidation behaviour of Co–29Cr–6Mo alloy for solid-oxide fuel cell interconnects.* Corrosion Science, 2015. **95**: p. 88-99.

132. Wu, Q., Y. Liu, Z. Zhang, Y. Qi, C. Zhang, H. Zheng, and Y. Xu, *Oxidation behavior and high-temperature tensile properties of Fe-9Cr-(Mo, Mo/Ni) alloys.* Corrosion Science, 2021. **181**: p. 109243.

133. Li, C., X. Deng, Y. Li, and Z. Wang, *Adding Cr and Mo simultaneously enhances the strength and impact toughness of TiC microparticle-reinforced steel matrix composites at high temperatures.* Journal of Alloys and Compounds, 2023. **931**: p. 167531.

134. Han, Q.-h., Y.-l. Kang, X.-m. Zhao, L.-f. Gao, and X.-s. Qiu, *High-temperature properties and microstructure of Mo microalloyed ultra-high-strength steel.* International Journal of Minerals, Metallurgy, and Materials, 2011. **18**(4): p. 407-413.

135. Isasti, N., D. Jorge-Badiola, M.L. Taheri, and P. Uranga, *Microstructural features controlling mechanical properties in Nb-Mo microalloyed steels. Part II: Impact toughness.* Metallurgical and Materials Transactions A, 2014. **45**: p. 4972-4982.

136. Yun, D.W., H.S. Seo, J.H. Jun, J.M. Lee, and K.Y. Kim, *Molybdenum effect on oxidation resistance and electric conduction of ferritic stainless steel for SOFC interconnect.* International journal of hydrogen energy, 2012. **37**(13): p. 10328-10336.

137. Zhang, C., Y. Zhang, J. Hu, Z. Wang, J. Xue, H. Yu, X. Wang, Q. Cai, C. Wang, and T. Jiang, *Effect of Mo on the high-temperature oxidation behavior of Cr-Ni-Mo hot-work die steels.* Corrosion Science, 2023. **224**: p. 111487.

138. Clayton, C.R. and Y.C. Lu, *A bipolar model of the passivity of stainless steel: the role of Mo addition.* Journal of the Electrochemical Society, 1986. **133**(12): p. 2465.

139. Kaneko, M. and H.S. Isaacs, *Effects of molybdenum on the pitting of ferritic-and austenitic-stainless steels in bromide and chloride solutions.* Corrosion Science, 2002. **44**(8): p. 1825-1834.

140. Ha, H.-Y., T.-H. Lee, J.-H. Bae, and D.W. Chun, *Molybdenum effects on pitting corrosion resistance of FeCrMnMoNC austenitic stainless steels.* Metals, 2018. **8**(8): p. 653.

141. Zhang, G.J., Y. Zhou, J.F. Yang, H.Y. Yang, M.M. Wang, K. Jing, Z.M. Xie, L.C. Zhang, R. Liu, and G. Li, *Effect of Si content on the microstructure and mechanical properties of 9Cr-ferritic/martensitic steels.* Nuclear Materials and Energy, 2023. **35**: p. 101428.

142. Xu, Y., W. Cao, M. Huang, and F. Zhang, *First Principles Study of the Effects of Si, P, and S on the ∑ 5 (210)[001] Grain Boundary of γ-Fe.* Metals, 2024. **14**(4): p. 471.

143. Hu, Z. and H. Fu, *Effect of Si Content on Microstructure and Properties of Low-Carbon Medium-Manganese Steel after Intercritical Heat Treatment.* Metals, 2024. **14**(6): p. 675.

144. International, A., *Standard Terminology Relating to Stainless Ferritic and Martensitic Steels*. 2016, ASTM International.

145. Chen, T., G. Li, H. Wang, X. An, and X. Huang, *Effect of Si content on the mechanical behavior and microstructure of a 9Cr ferritic/martensitic steel.* Journal of Materials Research and Technology, 2024. **29**: p. 1542-1556.

146. Feng, S., H. Dai, X. Sun, K. Jiang, Z. Qiu, X. Chen, and G. Chen, *New insight of the enhanced oxidation resistance of T91 steel in 450° C liquid lead-bismuth eutectic by adding Al and Si element.* Journal of Materials Science & Technology, 2025. **204**: p. 29-46.

147. Chengxu, L., Y. Haoyu, L. Tian, W. Min, X. Hailong, M. Yingche, and L. Kui, *Effect of Si and Mn on microstructure and tensile properties of austenitic stainless steel.* Rare metal materials and engineering, 2021. **50**(1): p. 187-194.

148. Davis, J.R., *Metals Handbook, Desk Edition*. 2nd ed. 1998, Materials Park, Ohio: ASM International.

149. Allen, T.R. and D.C. Crawford, *Lead-Cooled Fast Reactor Systems and the Fuels and Materials Challenges.* Science and Technology of Nuclear Installations, 2007. **2007**: p. 1-11.

150. Was, G.S., D. Petti, S. Ukai, and S. Zinkle, *Materials for future nuclear energy systems.* Journal of Nuclear Materials, 2019. **527**: p. 151837.

151. Saini, N., C. Pandey, M.M. Mahapatra, H.K. Narang, R.S. Mulik, and P. Kumar, *A comparative study of ductile-brittle transition behavior and fractography of P91 and P92 steel.* Engineering Failure Analysis, 2017. **81**: p. 245-253.

152. Lancaster, J.F., *Engineering catastrophes: causes and effects of major accidents*. 2005: Elsevier.

153. Guguloth, K. and N. Roy, *Study on the creep deformation behavior and characterization of 9Cr-1Mo-V-Nb steel at elevated temperatures.* Materials Characterization, 2018. **146**: p. 279-298.

154. Qvist, S., A.M. Bolind, P. Hosemann, Y. Wang, J. Tesmer, M.S. De Caro, and M. Bourke, *Capability demonstration of simultaneous proton beam irradiation during exposure to molten lead–bismuth eutectic for HT9 steel.* Nuclear Instruments and Methods in Physics Research Section A: Accelerators, Spectrometers, Detectors and Associated Equipment, 2013. **698**: p. 98-105.

155. Hosemann, P., M. Hawley, G. Mori, N. Li, and S.A. Maloy, *AFM and MFM characterization of oxide layers grown on stainless steels in lead bismuth eutectic.* Journal of Nuclear Materials, 2008. **376**(3): p. 289-292.

156. Brierley, R.A., *Studies of the oxidation of 9 and 12 Cr steels in high temperature, high pressure CO2*, in *Corrosion of Steels in CO2*. 1974, Thomas Telford Publishing. p. 165-179.

157. Setia, P., T. Venkateswaran, K.T. Tharian, J. Jain, S.S. Singh, and S. Shekhar, *Influence of Si content on the microstructure and mechanical properties of silicon stainless steel.* Materials Science and Engineering: A, 2022. **829**: p. 142141.

158. Wolff, I.M., L.E. Iorio, T. Rumpf, P.V.T. Scheers, and J.H. Potgieter, *Oxidation and corrosion behaviour of Fe–Cr and Fe–Cr–Al alloys with minor alloying additions.* Materials Science and Engineering: A, 1998. **241**(1-2): p. 264-276.

159. Regina, J.R., J.N. Dupont, and A.R. Marder, *The effect of chromium on the weldability and microstructure of Fe-Cr-Al weld cladding.* WELDING JOURNAL-NEW YORK-, 2007. **86**(6): p. 170.

160. Short, M.P., R.G. Ballinger, and H.E. Hänninen, *Corrosion resistance of alloys F91 and Fe–12Cr–2Si in lead–bismuth eutectic up to 715 C.* Journal of nuclear materials, 2013. **434**(1-3): p. 259-281.

161. Hawkes, P.W. and J.C.H. Spence, *Springer handbook of microscopy*. 2019: Springer Nature.

162. Zhou, W., R. Apkarian, Z.L. Wang, and D. Joy, *Fundamentals of scanning electron microscopy (SEM).* Scanning microscopy for nanotechnology: techniques and applications, 2007: p. 1-40.

163. Goldstein, J.I., D.E. Newbury, J.R. Michael, N.W.M. Ritchie, J.H.J. Scott, D.C. Joy, J.I. Goldstein, D.E. Newbury, J.R. Michael, and N.W.M. Ritchie, *Electron beam—specimen interactions: Interaction volume.* Scanning electron microscopy and x-ray microanalysis, 2018: p. 1-14.

164. Thomas, S., R. Thomas, A.K. Zachariah, and R.K. Mishra, *Microscopy methods in nanomaterials characterization*. Vol. 1. 2017: Elsevier.

165. Hodoroaba, V.-D., *Energy-dispersive X-ray spectroscopy (EDS)*, in *Characterization of Nanoparticles*. 2020, Elsevier. p. 397-417.

166. Shindo, D., T. Oikawa, D. Shindo, and T. Oikawa, *Energy dispersive x-ray spectroscopy.* Analytical electron microscopy for materials science, 2002: p. 81-102.

167. Meisnar, M., S. Lozano-Perez, M. Moody, and J. Holland, *Low-energy EDX–A novel approach to study stress corrosion cracking in SUS304 stainless steel via scanning electron microscopy.* Micron, 2014. **66**: p. 16-22.

168. Schneider, R., *Energy‐Dispersive X‐Ray Spectroscopy (EDXS).* Surface and Thin Film Analysis: A Compendium of Principles, Instrumentation, and Applications, 2011: p. 293-310.

169. Wilkinson, A.J., T.B. Britton, J. Jiang, and P.S. Karamched. *A review of advances and challenges in EBSD strain mapping*. in *IOP Conference Series: Materials Science and Engineering*. 2014. IOP Publishing.

170. Venables, J.A. and C.J. Harland, *Electron back-scattering patterns—A new technique for obtaining crystallographic information in the scanning electron microscope.* Philosophical Magazine, 1973. **27**(5): p. 1193-1200.

171. Wilkinson, A.J. and P.B. Hirsch, *Electron diffraction based techniques in scanning electron microscopy of bulk materials.* Micron, 1997. **28**(4): p. 279-308.

172. Schwartz, A.J., M. Kumar, B.L. Adams, and D.P. Field, *Electron backscatter diffraction in materials science*. Vol. 2. 2009: Springer.

173. Charalampopoulou, E., N. Cautaerts, T. Van der Donck, D. Schryvers, K. Lambrinou, and R. Delville, *Orientation relationship of the austenite-to-ferrite transformation in austenitic stainless steels due to dissolution corrosion in contact with liquid Pb-Bi eutectic.* Scripta Materialia, 2019. **167**: p. 66-70.

174. Wilkinson, A.J. and T.B. Britton, *Strains, planes, and EBSD in materials science.* Materials today, 2012. **15**(9): p. 366-376.

175. Trimby and P. W., *Orientation mapping of nanostructured materials using transmission Kikuchi diffraction in the scanning electron microscope.* Ultramicroscopy, 2012. **120**: p. 16-24.

176. Niessen, F., A. Burrows, and A.B. da Silva Fanta, *A systematic comparison of on-axis and off-axis transmission Kikuchi diffraction.* Ultramicroscopy, 2018. **186**: p. 158-170.

177. Nye, J.F., *Some geometrical relations in dislocated crystals.* Acta metallurgica, 1953. **1**(2): p. 153-162.

178. Kröner, E., *Continuum theory of dislocations and self-stresses*. 1971: College of Engineering, University of Florida.

179. Wilkinson, A.J., E.E. Clarke, T.B. Britton, P. Littlewood, and P.S. Karamched, *High-resolution electron backscatter diffraction: an emerging tool for studying local deformation.* The Journal of Strain Analysis for Engineering Design, 2010. **45**(5): p. 365-376.

180. Birosca, S., G. Liu, R. Ding, J. Jiang, T. Simm, C. Deen, and M. Whittaker, *The dislocation behaviour and GND development in a nickel based superalloy during creep.* International Journal of Plasticity, 2019. **118**: p. 252-268.

181. Gao, S., Z. Hu, M. Duchamp, P.S.S.R. Krishnan, S. Tekumalla, X. Song, and M. Seita, *Recrystallization-based grain boundary engineering of 316L stainless steel produced via selective laser melting.* Acta Materialia, 2020. **200**: p. 366-377.

182. Linck, M., B. Freitag, S. Kujawa, M. Lehmann, and T. Niermann, *State of the art in atomic resolution off-axis electron holography.* Ultramicroscopy, 2012. **116**: p. 13-23.

183. Dekkers, N.H. and D.E. LANG, *DIFFERENTIAL PHASE CONTRAST IN A STEM.* 1974.

184. Shibata, N., S.D. Findlay, Y. Kohno, H. Sawada, Y. Kondo, and Y. Ikuhara, *Differential phase-contrast microscopy at atomic resolution.* Nature Physics, 2012. **8**(8): p. 611-615.

185. Yang, H., L. Jones, H. Ryll, M. Simson, H. Soltau, Y. Kondo, R. Sagawa, H. Banba, I. MacLaren, and P.D. Nellist. *4D STEM: High efficiency phase contrast imaging using a fast pixelated detector*. in *Journal of Physics: Conference Series*. 2015. IOP Publishing.

186. Crewe, A.V., J. Wall, and L.M. Welter, *A high-resolution scanning transmission electron microscope.* Journal of Applied Physics, 1968. **39**(13): p. 5861-5868.

187. Pennycook, S.J. and P.D. Nellist, *Scanning transmission electron microscopy: imaging and analysis*. 2011: Springer Science & Business Media.

188. JEOL. Available from: https://www.jeol.com/words/emterms/20121023.034459.php#gsc.tab=0.

189. Egerton, R.F., *Electron energy-loss spectroscopy in the TEM.* Reports on Progress in Physics, 2008. **72**(1): p. 016502.

190. Egerton, R.F., *Electron energy-loss spectroscopy in the electron microscope*. 2011: Springer Science & Business Media.

191. Zhang, M., G. He, M.T. Lapington, W. Zhou, M.P. Short, P.A.J. Bagot, F. Hofmann, and M.P. Moody, *Nano-scale corrosion mechanism of T91 steel in static lead-bismuth eutectic: A combined APT, EBSD, and STEM investigation.* Acta Materialia, 2024: p. 119883.

192. David, J.L., J.P. Ty, M.U. Robert, and P.G.T.F.K. Brian, *Local Electrode Atom Probe Tomography*. 2013.

193. Gault, B., M.P. Moody, J.M. Cairney, and S.P. Ringer, *Atom Probe Microscopy*. Springer Series in Materials Science ed. Springer-Verlag. 2012, New York.

194. Stephenson, L.T., M.P. Moody, P.V. Liddicoat, and S.P. Ringer, *New techniques for the analysis of fine-scaled clustering phenomena within atom probe tomography (APT) data.* Microsc Microanal, 2007. **13**(6): p. 448-63.

195. Li, C., C.D. Marioara, C. Hatzoglou, S.J. Andersen, R. Holmestad, and Y. Li, *Accelerating precipitation hardening by natural aging in a 6082 Al-Mg-Si alloy.* Acta Materialia, 2024. **281**: p. 120396.

196. Wheatley, L.E., T. Baumgartner, M. Eisterer, S.C. Speller, M.P. Moody, and C.R.M. Grovenor, *Understanding the nanoscale chemistry of as-received and fast neutron irradiated Nb3Sn RRP® wires using atom probe tomography.* Superconductor Science and Technology, 2023. **36**(8): p. 085006.

197. Diagne, A., L.G. Garcia, S. Ndiaye, N. Gogneau, M. Vrellou, J. Houard, and L. Rigutti, *Field‐dependent abundances of hydride molecular ions in atom probe tomography of III‐N semiconductors.* Journal of Microscopy, 2024. **293**(3): p. 153-159.

198. Jenkins, B.M., J.O. Douglas, H.M. Gardner, D. Tweddle, A. Kareer, P.S. Karamched, N. Riddle, J.M. Hyde, P.A.J. Bagot, G.R. Odette, and M.P. Moody, *A more holistic characterisation of internal interfaces in a variety of materials via complementary use of transmission Kikuchi diffraction and Atom probe tomography.* Applied Surface Science, 2020. **528**.

199. Larson, B.C., W. Yang, G.E. Ice, J.D. Budai, and J.Z. Tischler, *Three-dimensional X-ray structural microscopy with submicrometre resolution.* Nature, 2002. **415**(6874): p. 887-890.

200. Yang, W., B.C. Larson, J.Z. Tischler, G.E. Ice, J.D. Budai, and W. Liu, *Differential-aperture X-ray structural microscopy: a submicron-resolution three-dimensional probe of local microstructure and strain.* Micron, 2004. **35**(6): p. 431-439.

201. Yang, W., B.C. Larson, G.E. Ice, J.Z. Tischler, J.D. Budai, K.-S. Chung, and W.P. Lowe, *Spatially resolved Poisson strain and anticlastic curvature measurements in Si under large deflection bending.* Applied physics letters, 2003. **82**(22): p. 3856-3858.

202. Ice, G.E. and B.C. Larson, *3D X-Ray Crystal Microscope.* Advanced Engineering Materials, 2000. **2**(10): p. 643-646.

203. Zhang, Y. and R.I. Barabash, *High resolution mapping of orientation and strain gradients in metals by synchrotron 3D X-ray Laue microdiffraction.* Quantum Beam Science, 2019. **3**(1): p. 6.

204. Ohashi, T., R.I. Barabash, J.W.L. Pang, G.E. Ice, and O.M. Barabash, *X-ray microdiffraction and strain gradient crystal plasticity studies of geometrically necessary dislocations near a Ni bicrystal grain boundary.* International Journal of Plasticity, 2009. **25**(5): p. 920-941.

205. Wang, L., M. Li, J. Almer, T. Bieler, and R. Barabash, *Microstructural characterization of polycrystalline materials by synchrotron X-rays.* Frontiers of Materials Science, 2013. **7**: p. 156-169.

206. Burgess, S., J. Holland, C. Collins, and S. Sharp, *X-ray nano-analysis of sub-100nm particles using EDS in conjunction with SEM.* Microscopy and Microanalysis, 2008. **14**(S2): p. 1098-1099.

207. Lozano-Perez, S., *A guide on FIB preparation of samples containing stress corrosion crack tips for TEM and atom-probe analysis.* Micron, 2008. **39**(3): p. 320-8.

208. London, A.J., *Quantifying Uncertainty from Mass-Peak Overlaps in Atom Probe Microscopy*, in *Microscopy and Microanalysis*, M.-. John Mansfield 4304 Spring Lake Boulevard|Ann Arbor, Editor. 2019, Microscopy Society of America: US. p. 378-388.

209. London, A.J. *AtomProbeLab*. 2021; Available from: https://sourceforge.net/projects/atomprobelab/.

210. Britton, T.B. and A.J. Wilkinson, *Measurement of residual elastic strain and lattice rotations with high resolution electron backscatter diffraction.* Ultramicroscopy, 2011. **111**(8): p. 1395-1404.

211. Liu, W., G.E. Ice, B.C. Larson, W. Yang, J.Z. Tischler, and J.D. Budai, *The three-dimensional X-ray crystal microscope: A new tool for materials characterization.* Metallurgical and Materials Transactions A, 2004. **35**: p. 1963-1967.

212. Jenkins, B., *Improving the safety and reliability of reactor pressure vessel steels*. 2019, University of Oxford.

213. Thuvander, M., J. Weidow, J. Angseryd, L.K.L. Falk, F. Liu, M. Sonestedt, K. Stiller, and H.-O. Andrén, *Quantitative atom probe analysis of carbides.* Ultramicroscopy, 2011. **111**(6): p. 604-608.

214. Schaffer, M., B. Schaffer, and Q. Ramasse, *Sample preparation for atomic-resolution STEM at low voltages by FIB.* Ultramicroscopy, 2012. **114**: p. 62-71.

215. Hudson, D., G.D.W. Smith, and B. Gault, *Optimisation of mass ranging for atom probe microanalysis and application to the corrosion processes in Zr alloys.* Ultramicroscopy, 2011. **111**(6): p. 480-486.

216. Lorenzin, N. and A. Abanades, *A review on the application of liquid metals as heat transfer fluid in Concentrated Solar Power technologies.* International journal of hydrogen energy, 2016. **41**(17): p. 6990-6995.

217. Morito, S., H. Tanaka, R. Konishi, T. Furuhara, and T. Maki, *The morphology and crystallography of lath martensite in Fe-C alloys.* Acta materialia, 2003. **51**(6): p. 1789-1799.

218. Bachmann, F., R. Hielscher, and H. Schaeben, *Grain detection from 2d and 3d EBSD data—Specification of the MTEX algorithm.* Ultramicroscopy, 2011. **111**(12): p. 1720-1733.

219. Scully, J.C., *Fundamentals of corrosion.* 1975.

220. Zhou, W., Y. Yang, G. Zheng, K.B. Woller, P.W. Stahle, A.M. Minor, and M.P. Short, *Proton irradiation-decelerated intergranular corrosion of Ni-Cr alloys in molten salt.* Nat Commun, 2020. **11**(1): p. 3430.

221. Tan, H., J. Verbeeck, A. Abakumov, and G. Van Tendeloo, *Oxidation state and chemical shift investigation in transition metal oxides by EELS.* Ultramicroscopy, 2012. **116**: p. 24-33.

222. Lapington, M.T., D.J. Crudden, R.C. Reed, M.P. Moody, and P.A.J. Bagot, *Characterization of oxidation mechanisms in a family of polycrystalline chromia-forming nickel-base superalloys.* Acta Materialia, 2021. **206**.

223. Di Gianfrancesco, A., *Materials for ultra-supercritical and advanced ultra-supercritical power plants*. 2016: woodhead Publishing.

224. Pint, B.A., Y.-F. Su, D. Sulejmanovic, and R. Pillai, *Characterization of Fe and Cr Dissolution and Reaction Product Formation in Molten Chloride Salts With and Without Impurities.* Materials at High Temperatures, 2023: p. 1-11.

225. Sankar, K.M. and P.M. Singh, *Effect of metal fluorides on the corrosion of structural materials in molten LiF-NaF-KF.* Corrosion Science, 2023. **213**: p. 110977.

226. Yang, Y., W. Zhou, S. Yin, S.Y. Wang, Q. Yu, M.J. Olszta, Y.-Q. Zhang, S.E. Zeltmann, M. Li, and M. Jin, *One dimensional wormhole corrosion in metals.* Nature Communications, 2023. **14**(1): p. 988.

227. Schroer, C., O. Wedemeyer, J. Novotny, A. Skrypnik, and J. Konys, *Selective leaching of nickel and chromium from Type 316 austenitic steel in oxygen-containing lead–bismuth eutectic (LBE).* Corrosion Science, 2014. **84**: p. 113-124.

228. Tsisar, V., C. Schroer, O. Wedemeyer, A. Skrypnik, and J. Konys, *Characterization of corrosion phenomena and kinetics on T91 ferritic/martensitic steel exposed at 450 and 550 °C to flowing Pb-Bi eutectic with 10−7 mass% dissolved oxygen.* Journal of Nuclear Materials, 2017. **494**: p. 422-438.

229. Kitahara, H., R. Ueji, N. Tsuji, and Y. Minamino, *Crystallographic features of lath martensite in low-carbon steel.* Acta materialia, 2006. **54**(5): p. 1279-1288.

230. Jiang, L., K. Wang, B. Leng, X.-X. Ye, S.-J. Chen, R.-D. Liu, J.-P. Liang, C.-W. Li, and Z.-J. Li, *Tellurium segregation-induced intergranular corrosion of GH3535 alloys in molten salt.* Corrosion Science, 2022. **194**.

231. Popovic, M.P., A.M. Bolind, Y. Aussat, A.J. Gubser, and P. Hosemann, *Oxidative passivation of Fe–Cr–Al steels in lead-bismuth eutectic under oxygen-controlled static conditions at 700° and 800° C.* Journal of Nuclear Materials, 2019. **523**: p. 172-181.

232. Weisenburger, A., G. Mueller, A. Heinzel, A. Kazumi, and F. Tomohiro. *Stability of oxide layer formed on high-chromium steels in LBE under oxygen content and temperature fluctuation*. in *The 13th international conference on nuclear engineering abstracts*. 2005.

233. Ellingham, H.J.T., *Transactions and Communications.* Journal of the Society of Chemical Industry, 1944. **63**(5): p. 125-160.

234. Tien, R.H. and E.T. Turkdogan, *Gaseous reduction of iron oxides: Part IV. Mathematical analysis of partial internal reduction-diffusion control.* Metallurgical Transactions, 1972. **3**: p. 2039-2048.

235. Li, Y., J. Du, L. Li, K. Gao, X. Pang, and A.A. Volinsky, *Mechanical properties and phases evolution in T91 steel during long-term high-temperature exposure.* Engineering Failure Analysis, 2020. **111**: p. 104451.

236. Liu, J., Q. Shi, H. Luan, W. Yan, W. Sha, W. Wang, Y. Shan, and K. Yang, *Lead–bismuth eutectic corrosion behaviors of ferritic/martensitic steels in low oxygen concentration environment.* Oxidation of Metals, 2015. **84**: p. 383-395.

237. Was, G.S. and T.R. Allen, *Corrosion issues in current and next-generation nuclear reactors.* Structural Alloys for Nuclear Energy Applications, 2019: p. 211-246.

238. Cabet, C. and F. Rouillard, *Corrosion issues of high temperature reactor structural metallic materials.* Journal of engineering for gas turbines and power, 2009. **131**(6).

239. Durham, R.N., B. Gleeson, and D.J. Young, *Factors affecting chromium carbide precipitate dissolution during alloy oxidation.* Oxidation of Metals, 1998. **50**: p. 139-165.

240. Liao, Q., B. Li, F. Ge, R. Wang, H. Zhang, V. Krsjak, and Y. Sheng, *Investigation into creep‐to‐rupture of SIMP steel in stagnant LBE at 300–450 °C.* Materials and Corrosion, 2022. **73**(5): p. 784-797.

241. Schroer, C., V. Koch, O. Wedemeyer, A. Skrypnik, and J. Konys, *Silicon-containing ferritic/martensitic steel after exposure to oxygen-containing flowing lead–bismuth eutectic at 450 and 550 °C.* Journal of Nuclear Materials, 2016. **469**: p. 162-176.

242. Berry, W.E. and C.V. King, *Corrosion in nuclear applications.* Journal of The Electrochemical Society, 1971. **118**(12): p. 311C.

243. Nowell, M.M., S.I. Wright, and J.O. Carpenter, *Differentiating ferrite and martensite in steel microstructures using electron backscatter diffraction.* Proceedings of the Materials Science and Technology (MS&T), Pittsburgh, PA, USA, 2009: p. 25-29.

244. Barabash, R.I., G.E. Ice, B.C. Larson, G.M. Pharr, K.-S. Chung, and W. Yang, *White microbeam diffraction from distorted crystals.* Applied Physics Letters, 2001. **79**(6): p. 749-751.

245. Barabash, R.I., G.E. Ice, N. Tamura, B.C. Valek, J.C. Bravman, R. Spolenak, and J.R. Patel, *Quantitative analysis of dislocation arrangements induced by electromigration in a passivated Al (0.5 wt% Cu) interconnect.* Journal of Applied Physics, 2003. **93**(9): p. 5701-5706.

246. Barabash, R.I., G.E. Ice, W. Liu, and O.M. Barabash, *Polychromatic microdiffraction characterization of defect gradients in severely deformed materials.* Micron, 2009. **40**(1): p. 28-36.

247. Hofmann, F., S. Keegan, and A.M. Korsunsky, *Diffraction post-processing of 3D dislocation dynamics simulations for direct comparison with micro-beam Laue experiments.* Materials Letters, 2012. **89**: p. 66-69.

248. Chen, X., C. Dejoie, T. Jiang, C.-S. Ku, and N. Tamura, *Quantitative microstructural imaging by scanning Laue x-ray micro-and nanodiffraction.* MRS bulletin, 2016. **41**(6): p. 445-453.

249. Abe, F., *Precipitate design for creep strengthening of 9% Cr tempered martensitic steel for ultra-supercritical power plants.* Science and Technology of Advanced Materials, 2008. **9**(1): p. 013002.

250. Zeman, A., L. Debarberis, J. Kočík, V. Slugeň, and E. Keilová, *Microstructural analysis of candidate steels pre-selected for new advanced reactor systems.* Journal of nuclear materials, 2007. **362**(2-3): p. 259-267.

251. Challa, V.S.A., R.D.K. Misra, R. O'Malley, and S.G. Jansto, *The Effect of Coiling Temperature on the Mechanical Properties of Ultrahigh-Strength 700 MPa Grade Processed via Thin-Slab Casting.* Proceedings of the AISTech, 2014: p. 2987-2997.

252. Griffith, C.B. and M.W. Mallett, *The solubility of carbon and oxygen in liquid bismuth.* Journal of the American Chemical Society, 1953. **75**(8): p. 1832-1834.

253. YAMAMOTO, S., T. SAKIYAMA, and C. OUCHI, *Effect of alloying elements on recrystallization kinetics after hot deformation in austenitic stainless steels.* Transactions of the Iron and Steel Institute of Japan, 1987. **27**(6): p. 446-452.

254. Ma, L., S. Hu, J. Shen, J. Han, and Z. Zhu, *Effects of Cr content on the microstructure and properties of 26Cr–3.5 Mo–2Ni and 29Cr–3.5 Mo–2Ni super ferritic stainless steels.* Journal of Materials Science & Technology, 2016. **32**(6): p. 552-560.

255. Moorthy, C.M.D. and J.N. Reddy, *Recovery of interlaminar stresses and strain energy release rates in composite laminates.* Finite elements in analysis and design, 1999. **33**(1): p. 1-27.

256. Rebak, R.B. and D.D. Ellis. *Passivation Characteristics of Ferritic Stainless Materials in Simulated Reactor Environments*. in *NACE CORROSION*. 2016. NACE.

257. Li, N., *Active control of oxygen in molten lead–bismuth eutectic systems to prevent steel corrosion and coolant contamination.* Journal of Nuclear materials, 2002. **300**(1): p. 73-81.

258. Courouau, J.-L., P. Trabuc, G. Laplanche, P. Deloffre, P. Taraud, M. Ollivier, R. Adriano, and S. Trambaud, *Impurities and oxygen control in lead alloys.* Journal of Nuclear Materials, 2002. **301**(1): p. 53-59.

259. Laverde, D., T. Gomez-Acebo, and F. Castro, *Continuous and cyclic oxidation of T91 ferritic steel under steam.* Corrosion science, 2004. **46**(3): p. 613-631.

260. Chen, G., J. Zhao, K. Chen, S. Liu, M. Zhang, Y. He, and J. Luo, *Ultrastable lubricating properties of robust self-repairing tribofilms enabled by in situ-assembled polydopamine nanoparticles.* Langmuir, 2020. **36**(4): p. 852-861.

261. Bruemmer, S.M. and G.S. Was, *Microstructural and microchemical mechanisms controlling intergranular stress corrosion cracking in light-water-reactor systems.* Journal of Nuclear Materials, 1994. **216**: p. 348-363.

262. Hsieh, K.C., S.S. Babu, J.M. Vitek, and S.A. David, *Calculation of inclusion formation in low-alloy-steel welds.* Materials Science and Engineering: A, 1996. **215**(1-2): p. 84-91.

263. Yurimoto, H., M. Morioka, and H. Nagasawa, *Oxygen self-diffusion along high diffusivity paths in forsterite.* Geochemical Journal, 1992. **26**(4): p. 181-188.

264. Martinelli, L., K. Ginestar, V. Botton, C. Delisle, and F. Balbaud-Célérier, *Corrosion of T91 and pure iron in flowing and static Pb-Bi alloy between 450° C and 540° C: experiments, modelling and mechanism.* Corrosion Science, 2020. **176**: p. 108897.

265. Qiu, J., J. Han, R. Schoell, M. Popovic, E. Ghanbari, D. Kaoumi, J.R. Scully, D.D. Macdonald, and P. Hosemann, *Electrical properties of thermal oxide scales on pure iron in liquid lead-bismuth eutectic.* Corrosion Science, 2020. **176**: p. 109052.

266. Schroer, C., A. Skrypnik, O. Wedemeyer, and J. Konys, *Oxidation and dissolution of iron in flowing lead–bismuth eutectic at 450 C.* Corrosion science, 2012. **61**: p. 63-71.

267. Guo, T., Y. Chen, H. Shao, Q. Zhao, and Z. Liang, *Molecular dynamics, thermodynamics and experimental studies on the corrosion mechanism of T92 and TP347H steels in high-pressure CO2 and H2O at 600° C.* Applied Surface Science, 2023. **621**: p. 156879.

268. Buggenhoudt, O., *Modelling and simulation of carbides in alpha-Fe alloys from first principles: alloying elements, diffusion and nucleation*. 2021, Université Paris-Saclay.

269. Schroer, C., V. Tsisar, A. Durand, O. Wedemeyer, A. Skrypnik, and J. Konys, *Corrosion in iron and Steel T91 caused by flowing lead–bismuth eutectic at 400 C and 10− 7 mass% dissolved oxygen.* Journal of Nuclear Engineering and Radiation Science, 2019. **5**(1): p. 011006.

270. Tian, S.J., Z.Z. Jiang, and L. Luo, *Oxidation behavior of T91 steel in flowing oxygen‐containing lead‐bismuth eutectic at 500°C.* Materials and Corrosion, 2016. **67**(12): p. 1274-1285.

271. Tsisar, V., C. Schroer, O. Wedemeyer, A. Skrypnik, and J. Konys, *Corrosion interaction of 9% Cr ferritic/martensitic steels at 450 and 550° C with flowing Pb–Bi eutectic containing 10− 7 mass% dissolved oxygen.* Journal of Nuclear Engineering and Radiation Science, 2019. **5**(3): p. 031201.

272. Was, G.S., *Challenges to the use of ion irradiation for emulating reactor irradiation.* Journal of Materials Research, 2015. **30**(9): p. 1158-1182.

273. Jepeal, S.J., L. Snead, and Z.S. Hartwig, *Intermediate energy proton irradiation: Rapid, high-fidelity materials testing for fusion and fission energy systems.* Materials & Design, 2021. **200**.

274. Abromeit, C., *Aspects of simulation of neutron damage by ion irradiation.* Journal of nuclear materials, 1994. **216**: p. 78-96.

275. Kiener, D., P. Hosemann, S.A. Maloy, and A.M. Minor, *In situ nanocompression testing of irradiated copper.* Nature materials, 2011. **10**(8): p. 608-613.

276. Son, N.T., E. Janzén, J. Isoya, N. Morishita, H. Hanaya, H. Takizawa, T. Ohshima, and A. Gali, *Identification of a Frenkel-pair defect in electron-irradiated 3 C SiC.* Physical Review B, 2009. **80**(12): p. 125201.

277. Kinchin, G.H. and R.S. Pease, *The displacement of atoms in solids by radiation.* Reports on progress in physics, 1955. **18**(1): p. 1.

278. Enrique, R.A., K. Nordlund, R.S. Averback, and P. Bellon, *Simulations of dynamical stabilization of Ag–Cu nanocomposites by ion-beam processing.* Journal of Applied physics, 2003. **93**(5): p. 2917-2923.

279. Was, G.S., J.T. Busby, T. Allen, E.A. Kenik, A. Jenssen, S.M. Bruemmer, J. Gan, A.D. Edwards, P.M. Scott, and P.L. Andresen, *Emulation of neutron irradiation effects with protons: validation of principle.* Journal of Nuclear Materials, 2002. **300**: p. 198-216.

280. Was, G.S., Z. Jiao, E. Getto, K. Sun, A.M. Monterrosa, S.A. Maloy, O. Anderoglu, B.H. Sencer, and M. Hackett, *Emulation of reactor irradiation damage using ion beams.* Scripta Materialia, 2014. **88**: p. 33-36.

281. Jiao, Z., G.S. Was, T. Miura, and K. Fukuya, *Aspects of ion irradiations to study localized deformation in austenitic stainless steels.* Journal of Nuclear Materials, 2014. **452**(1-3): p. 328-334.

282. Sencer, B.H., G.S. Was, H. Yuya, Y. Isobe, M. Sagisaka, and F.A. Garner, *Cross-sectional TEM and X-ray examination of radiation-induced stress relaxation of peened stainless steel surfaces.* Journal of Nuclear Materials, 2005. **336**(2-3): p. 314-322.

283. Xu, C. and G.S. Was, *Proton irradiation creep of FM steel T91.* Journal of Nuclear Materials, 2015. **459**: p. 183-193.

284. Mansur, L.K., *Correlation of neutron and heavy-ion damage: II. The predicted temperature shift if swelling with changes in radiation dose rate.* Journal of Nuclear Materials, 1978. **78**(1): p. 156-160.

285. Hasegawa, A., M. Ejiri, S. Nogami, M. Ishiga, R. Kasada, A. Kimura, K. Abe, and S. Jitsukawa, *Effects of helium on ductile-brittle transition behavior of reduced-activation ferritic steels after high-concentration helium implantation at high temperature.* Journal of nuclear materials, 2009. **386**: p. 241-244.

286. Dai, Y., X.J. Jia, and K. Farrell, *Mechanical properties of modified 9Cr–1Mo (T91) irradiated at ⩽300 °C in SINQ Target-3.* Journal of Nuclear Materials, 2003. **318**: p. 192-199.

287. Zhou, W., K.B. Woller, G.T. Zheng, P.W. Stahle, and M.P. Short, *A simultaneous corrosion/irradiation facility for testing molten salt-facing materials.* Nuclear Instruments and Methods in Physics Research Section B: Beam Interactions with Materials and Atoms, 2019. **440**: p. 54-59.

Chapter XI

Appendix

11.1 The challenge of investigating neutron irradiation

As part of future work, there are limitations preventing progress currently. In addition to alloy development, rapidly testing their performance is equally important. Currently, the main mechanisms of material degradation (such as embrittlement, RIS, void swelling, and precipitate formation) and the relationship between corrosion and radiation require lengthy experiments. These experiments involve exposing materials to various conditions and then performing detailed property testing. This gap in knowledge and testing capabilities highlights the need for an experimental facility that can assess how irradiation affects corrosion in structural materials, particularly for Gen IV reactor coolants like lead and LBE.

One way to achieve this is by constructing LFR/LBEFR test reactors, which currently only exist in Russia, or by using in-core loops to simultaneously expose materials to Gen IV coolants and neutrons. However, the fastest test reactors in the world can only reach 20 dpa/yr, much slower than a real reactor. As a result, research cannot progress faster than the operational reactors, and such experiments typically take years due to construction, in-core insertion, cool-down, and post-irradiation examination [272]. This long material development cycle is impractical. Moreover, building and licensing a test reactor requires an initial understanding of material performance, which is challenging without prior data. Additionally, test reactors differ from real reactors in several ways, such as the amount of helium and the impact of thermal neutrons on dissolving impurities and forming embrittling precipitates [273].

11.2 The feasibility of using ion irradiation to emulate neutron irradiation

As a surrogate to emulate the effects of neutron irradiation, ion irradiation has its obvious advantages. Compared with neutron irradiation, ion irradiation enables rapid damage rates and much less activation [274]. Low activation rates mean less time is needed for decay [272]. Furthermore, ion irradiation experiments are easy to control. The damage can even be observed in situ [275]. Electron irradiation is suitable to investigate the mechanism of vacancy formation due to only single Frenkel pairs formed at one time [276].

Ion irradiation mainly includes three species: electron irradiation, light ion irradiation (usually mainly referring to proton irradiation), and heavy ion irradiation (usually referring to self-ion irradiation). Different ion irradiation can cover a wide primary recoil spectrum by varying the accelerate voltage which can be used to modify the fission neutron effect.

Neither electron nor proton irradiation produces the collision cascades which happen during neutron irradiation. However, heavy ion irradiation can trigger collision cascades. Atoms which are displaced by direct collision with the bombarding radiation are called 'primary knock-ons' (PKA), to distinguish them from those atoms displaced as a consequence of subsequent collision [277]. If it possesses sufficient energy (threshold displacement energy), it will cause collision cascades. Compared to neutron irradiation, heavy ion irradiation is most suitable for gaining insight into defect formation due to neutron irradiation [278]. Table 11.1 shows a comparison of ion beam irradiation and neutron irradiation, which is concluded from different references.

Table 11.1. Comparison of attributes of irradiation using ion beams and neutron [272, 273, 279, 280]. Reprinted with permission from Elsevier.

Variable	Ion beams			Neutron
	Electrons	Light ion	Heavy ion	
Energy	~1 MeV	Few MeV	Up to 10s of MeV	Up to 14 MeV (varies for fission and fusion reactors)
PKA energy		Low and wider	High and wider	High and narrower
Dose	>500 dpa			Max 10-20 dpa
Dose rate	High	Accelerate	High	Low
Temperature shift	High	Modest	High	No
Cascade production	No	Smaller	Can produce	Can produce
Transmutation	No			Have
Penetration depth (1 MeV)	500 μm	10 μm	Less than 1 μm	Mean free path
Surface effect	High		High	No
Test time	Short	Short	Adjustable	Long
Expense	Low			High
Residual activity	Low or none	Minor	Low or none	High

Was researched the comparison between ion irradiation and neutron irradiation [272, 279, 280]. From the test results of 304 and 316 stainless steel, they concluded that the microchemistry, microstructure, hardening, and stress corrosion cracking behaviour of neutron and proton irradiated materials are in good agreement. For example, there is a similar tendency of RIS (for instance, the Cr depletion form 'W' profile with low dose and 'V' form with high dose) and dose dependency of yield strength was found between 275℃ neutron irradiation and 360℃ proton irradiation. The higher temperature will allow faster diffusion. It was used for proton irradiation to balance the increased displacement. Irradiation-assisted stress corrosion cracking of proton and neutron-irradiated materials was also similar. Fig. 11.1 gives the resulting elemental distribution, irradiation assistant stress corrosion crack potential and yield strength for both irradiations. The reduction of work hardening and reduction of uniform ductility are observed in both proton-irradiated and neutron-irradiated steels [281].

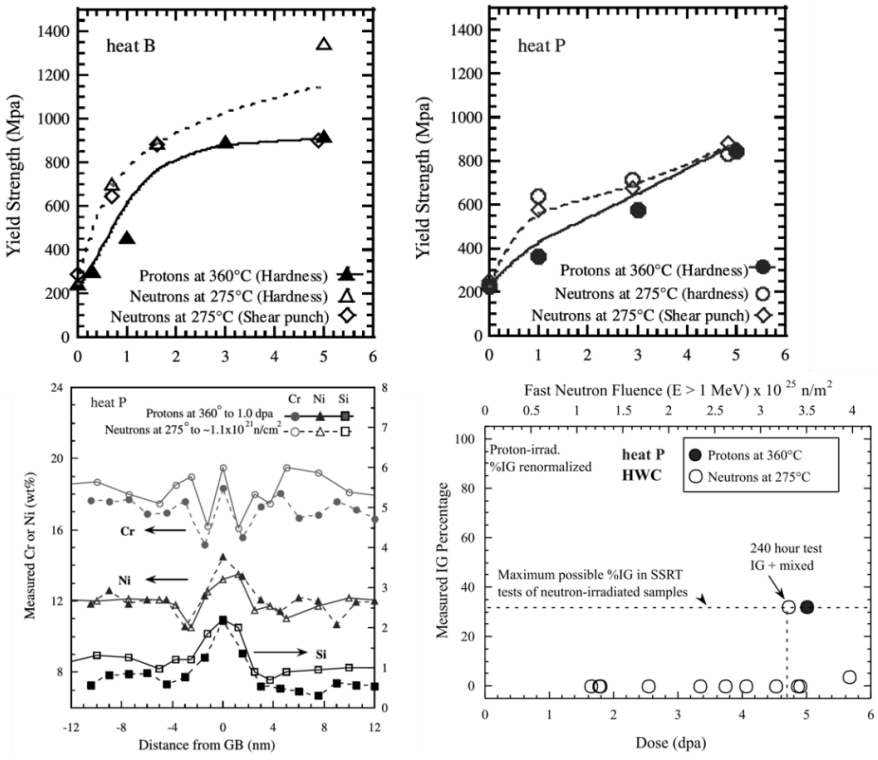

Fig. 11.1 Comparison of Cr, Ni, and Si segregation profiles and dose dependence of yield strength as determined from hardness and shear punch [279]. Reprinted with permission from Elsevier.

Irradiation-induced creep and stress relaxation also matched closely for proton and neutron irradiation. Sencer [282]investigated stress relaxation in 304 stainless steel with irradiation at 288 ℃ using 3.2 MeV protons of 2.0 dpa. Xu [283] researched the effect of temperature on the creep behaviour of T91 with 3 MeV protons of 1.0 dpa under the stress between 100-200 MPa. The similarity between proton and neutron is apparent in Fig. 11.2.

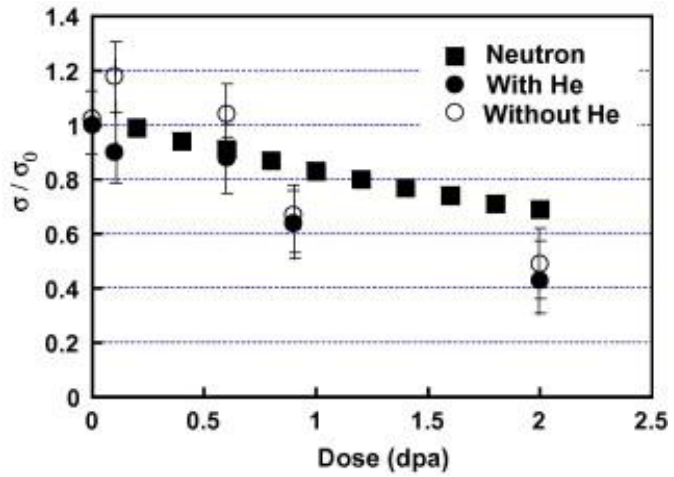

Fig. 11.2 Comparison of the neutron-based prediction with the proton-induced relaxation after removal of thermally induced relaxation component [282]. Reprinted with permission from Elsevier.

Heavy-ion irradiation (self-ion irradiation) is used to gain insight into defect formation due to neutron irradiation. Was used Fe++ irradiation on HT9 steel and compared it with the neutron irradiation. They concluded that heavy-ion irradiation can produce similar defects and defect-solute clusters with analogous size and density to the test reactor, which is shown in Fig. 11.3 [284].

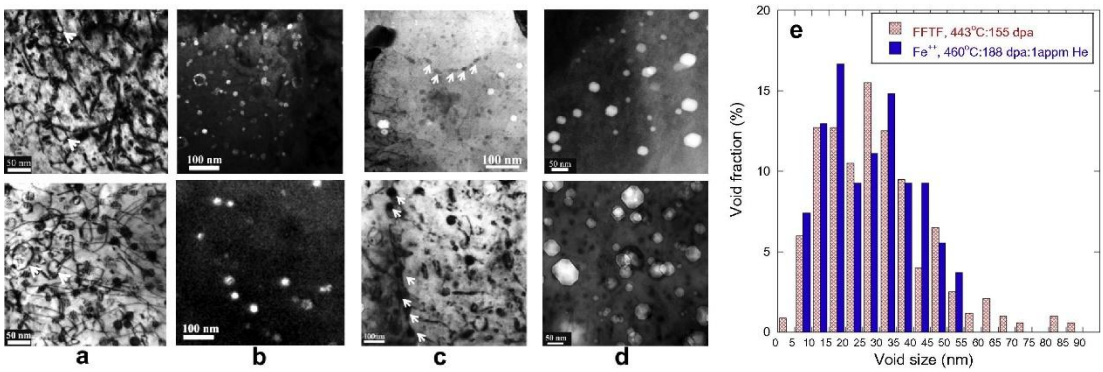

Fig. 11.3 Comparison of irradiation microstructure in HT9 with 460 °C:155 dpa Fe++ irradiation (top images) and 443 °C:155 dpa in test reactor irradiation (Fast Flux Test Facility, Hanford, WA) (bottom images): (a) line dislocations and loops (b) G-phase precipitates (c) G-phase precipitates along grain boundary (d) voids (e) voids size distribution comparison [280]. Reprinted with permission from Elsevier.

Mimicking all aspects of irradiated microstructure is rarely possible since the PKA energy spectra of incoming neutrons and protons are intrinsically different. As previously discussed, the trends show similarity, but it is still difficult to give quantitative information about freely migrating defects. Meanwhile, there exist some microstructure differences between neutron and proton-irradiated materials [272]. The neutron irradiation possesses a long mean-free path (~cm) in materials, and the damage induced is inherently in the bulk. However, for ion irradiation, even proton irradiation only can penetrate a few μm. For austenitic stainless steels, the denuded zones are only observed in neutron-irradiated conditions, they are absent in proton-irradiated samples [279]. The variation of loop diameter and density with the dose between two irradiations is also not the same. Due to the energy difference between neutrons and protons, transmutation reactions which produce H, He and other mobile light elements can only happen with neutron irradiation. The appearance of He will stabilize voids and thus promote swelling [279]. He is also an essential element which influences the ductile-brittle transition temperature

changes ($\Delta DBTT_{SP}$) after irradiation [285]. Dai illustrated this with neutron irradiated T-91, where they found that $\Delta DBTT_{SP}$ depended linearly on the He content as shown in Fig. 11.4 [286].

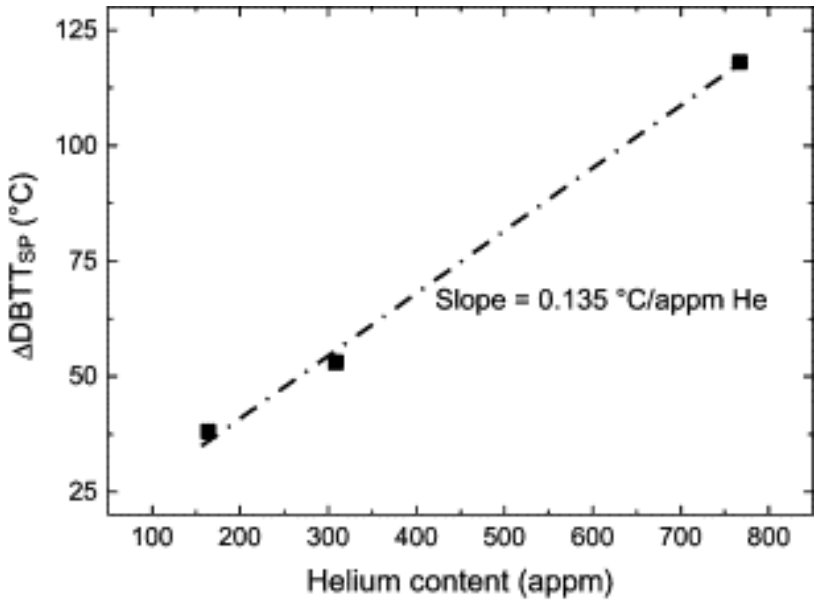

Fig. 11.4 Helium content dependence on the $\Delta DBTT_{SP}$ of T91 [286]. Reprinted with permission from Elsevier.

Proton irradiation may affect the chemistry with the addition of foreign atoms, while self-ion irradiation injects additional interstitial atoms and suppresses void nucleation. Electron irradiation has a Gaussian shape electron beam which induces strong dose rate gradients [272].

11.3 Intermediate energy proton irradiation method

As we discussed previously, though low-energy proton irradiation has many advantages, the lack of cascades and transmutation, a low penetration depth and the sharp spatial gradient of damage present some problems.

Jepeal proposed a method to solve these shortcomings; intermediate energy proton irradiation [273]. With higher energy protons, a similar PKA energy spectrum as produced by neutron irradiation can be achieved and the transmutation and cascades can also be produced, which

allows the study of the impact of helium and hydrogen production. With 12 MeV protons, the access range will be over 100 μm, making macroscale testing feasible. At the same time, after the radiation of high-energy protons, the residual activity of the specimen is very low, and the temperature difference induced by irradiation is also small.

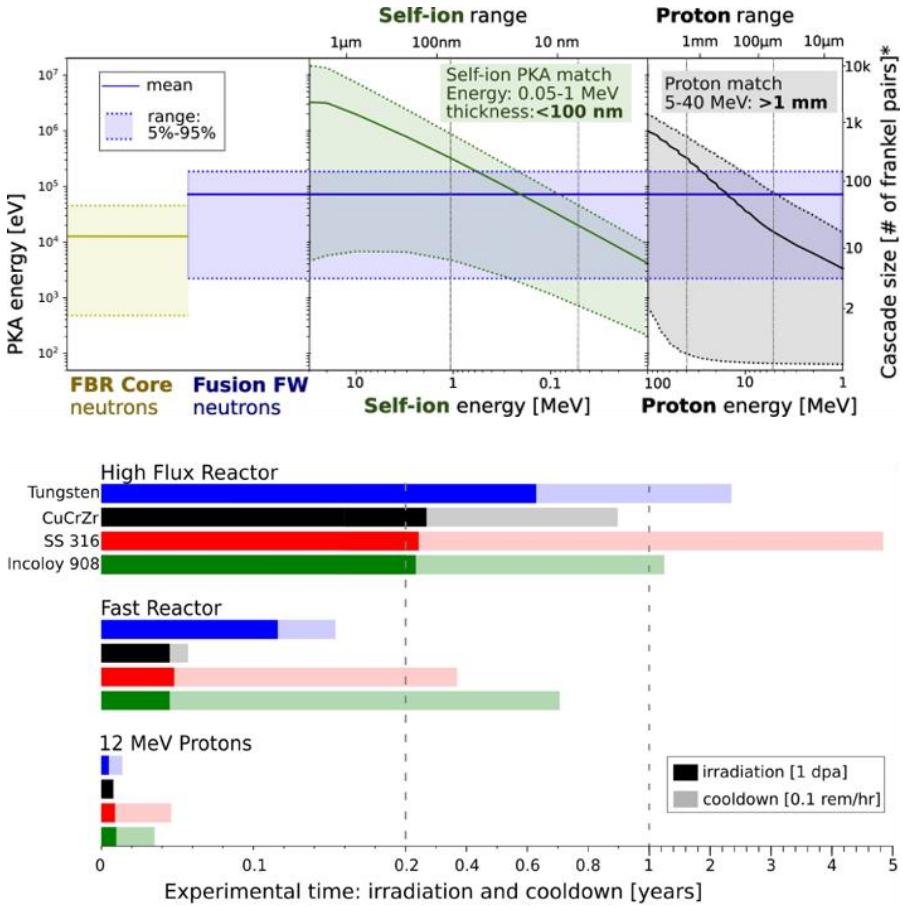

Fig. 11.5 Comparison of tungsten recoil energies from four different irradiation scenarios and the experimental time compared to reactor irradiation [273]. Reprinted with permission from Elsevier.

11.4 Proton irradiation facility used to study simultaneous irradiation and corrosion

There are facilities to investigate the combined effect of radiation and corrosion using proton beams. Raiman designed a facility to study simultaneous irradiation and corrosion properties in 316 stainless steels used in high-temperature water reactors using 3.2 MeV proton irradiation. They suggested that the irradiation will accelerate the corrosion by creating radiolysis products in high-temperature water [100].

To prepare for the upcoming LFR and LBEFR, equipment has been built to investigate the simultaneous effect of irradiation and corrosion of steels in liquid lead and LBE. There are facilities built at Los Alamos National Laboratory and Massachusetts Institute of Technology (MIT). At Los Alamos National Laboratory, the first irradiation and corrosion experiment (ICE-I) was built with a proton beam as a radiation source. The experiment temperature was set to 300℃ and could not control oxygen content. The beam current was only able to reach 500 nA, which limited the dose rate. All these aspects cannot match the expected operating condition. Then ICE-II was set up with a temperature of 550℃ and 3-6 MeV proton beam. The corrosion medium could be changed and the beam spot size adjusted. The structure is shown in Fig. 11.6.

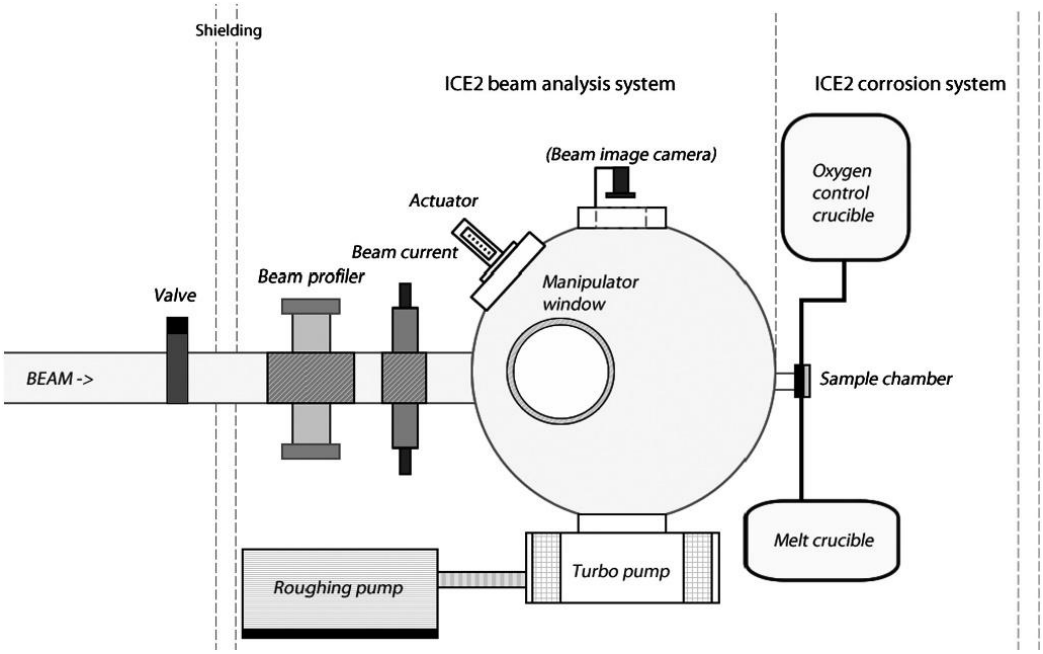

Fig. 11.6. The conceptual structure of the ICE-II station [154]. Reprinted with permission from Elsevier.

At MIT, there is also a new accelerator-based facility for rapid, simultaneous testing of coolant-facing materials utilizing a proton beam as the radiation source built [95]. The overall design is shown in Fig. 11.7 [287].

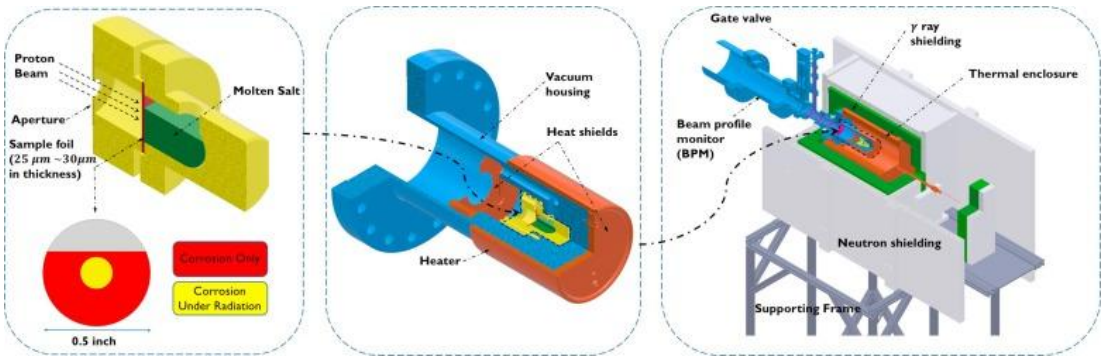

Fig. 11.7 The overall design of the simultaneous corrosion/irradiation facility [287]. Reprinted with permission from Elsevier.

11.5 Conclusion

Proton irradiation offers significant benefits as a surrogate for neutron irradiation, enabling rapid damage rates, lower activation, and controlled experiments. It facilitates the study of critical mechanisms like radiation-induced segregation, void swelling, and stress corrosion cracking. With intermediate energy protons, similar PKA energy spectra and transmutation effects can be achieved, overcoming limitations of low-energy irradiation. Facilities like ICE-II and MIT's accelerator-based setup already demonstrate the feasibility of simultaneous corrosion and irradiation testing. These advancements pave the way for developing materials for Gen IV reactors, allowing accelerated and cost-effective testing, ultimately bridging the gap between fundamental research and real-world reactor applications.